

INFORMATION TO USERS

This manuscript has been reproduced from the microfilm master. UMI films the text directly from the original or copy submitted. Thus, some thesis and dissertation copies are in typewriter face, while others may be from any type of computer printer.

The quality of this reproduction is dependent upon the quality of the copy submitted. Broken or indistinct print, colored or poor quality illustrations and photographs, print bleedthrough, substandard margins, and improper alignment can adversely affect reproduction.

In the unlikely event that the author did not send UMI a complete manuscript and there are missing pages, these will be noted. Also, if unauthorized copyright material had to be removed, a note will indicate the deletion.

Oversize materials (e.g., maps, drawings, charts) are reproduced by sectioning the original, beginning at the upper left-hand corner and continuing from left to right in equal sections with small overlaps. Each original is also photographed in one exposure and is included in reduced form at the back of the book.

Photographs included in the original manuscript have been reproduced xerographically in this copy. Higher quality 6" x 9" black and white photographic prints are available for any photographs or illustrations appearing in this copy for an additional charge. Contact UMI directly to order.

UMI

A Bell & Howell Information Company
300 North Zeeb Road, Ann Arbor MI 48106-1346 USA
313/761-4700 800/521-0600

LiV₂O₄: a heavy fermion transition metal oxide

by

Shinichiro Kondo

A dissertation submitted to the graduate faculty
in partial fulfillment of the requirements for the degree of
DOCTOR OF PHILOSOPHY

Major: Condensed Matter Physics

Major Professor: David C. Johnston

Iowa State University

Ames, Iowa

1998

Copyright © Shinichiro Kondo, 1998. All rights reserved.

UMI Number: 9841061


**UMI Microform 9841061
Copyright 1998, by UMI Company. All rights reserved.**

**This microform edition is protected against unauthorized
copying under Title 17, United States Code.**

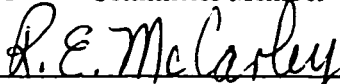
UMI
300 North Zeeb Road
Ann Arbor, MI 48103

Graduate College
Iowa State University

This is to certify that the Doctoral dissertation of
Shinichiro Kondo
has met the dissertation requirements of Iowa State University



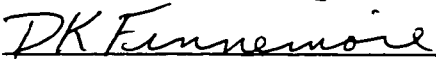
Committee Member



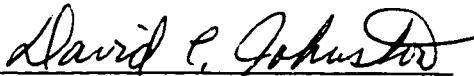
Committee Member




Committee Member



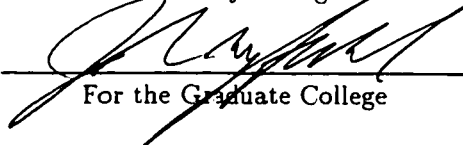
Committee Member



Major Professor



For the Major Program



For the Graduate College

To my wife and son

TABLE OF CONTENTS

1	INTRODUCTION	1
	Motivation of the study and introduction of LiV_2O_4	1
	Scope of this study and dissertation organization	5
	Reviews of important concepts	7
	Reviews of frustration	7
	Reviews of heavy fermion systems	10
	Reviews of spinels	18
2	Overview of LiV_2O_4: A HEAVY FERMION TRANSITION METAL OXIDE . .	30
	Abstract	30
	Introduction	30
	Sample preparations	32
	X-ray and neutron diffraction measurements	32
	Magnetic susceptibility measurements	32
	^7Li nuclear magnetic resonance measurements	34
	Heat capacity measurements	34
	Muon spin relaxation measurements	36
	Conclusion	38
3	SYNTHESIS AND CHARACTERIZATION	40
	Synthesis of LiV_2O_4 and $\text{Li}_{1+x}\text{Ti}_{2-x}\text{O}_4$ ($x = 0$ and $1/3$)	40
	LiV_2O_4 preparations	40
	LiTi_2O_4 and $\text{Li}_{4/3}\text{Ti}_{5/3}\text{O}_4$ preparations	41
	Characterization	41
	X-ray diffraction measurement results	41
	Introduction of Rietveld analyses	44
	Structure analyses by Rietveld method and thermogravimetric analysis results	56

4	MAGNETIZATION	58
	Magnetization measurements	58
	Overview of observed magnetic susceptibility	58
	Isothermal magnetization versus magnetic field	60
	Magnetization versus temperature measurements	68
	Modeling of the intrinsic magnetic susceptibility	70
	The Van Vleck susceptibility	70
	High-temperature series expansion analysis of the susceptibility	74
	Crystal field model	82
	Spin-1/2 Kondo model and Coqblin-Schrieffer model	83
5	RESISTIVITY	90
	Resistivity measurements using powder samples	90
	Analysis of single crystal resistivity measurements	90
6	HEAT CAPACITY	95
	Heat capacity measurement results	95
	Overview	95
	$\text{Li}_{1+x}\text{Ti}_{2-x}\text{O}_4$ ($x = 0$ and $1/3$)	97
	LiV_2O_4	103
	Theoretical modeling of electronic heat capacity of LiV_2O_4	108
	Single-band spin $S = 1/2$ Fermi liquid	108
	Quantum-disordered antiferromagnetically coupled metal	110
	Spin-1/2 Kondo model	113
	Local moment high-temperature description	117
7	THERMAL EXPANSION	121
	Neutron diffraction	121
	Capacitance dilatometry	122
8	NUCLEAR MAGNETIC RESONANCE	131
	Linewidths	131
	^7Li linewidth	131
	^{51}V linewidth	133
	Knight shifts	135

^7Li Knight shift	135
^{51}V Knight shift	140
Nuclear spin-lattice relaxation rates	142
^7Li nuclear spin-lattice relaxation rate	142
^{51}V nuclear spin-lattice relaxation rate	150
9 SUMMARY AND DISCUSSIONS	153
APPENDIX. RIETAN-97β INPUT FILE EXAMPLE	160
BIBLIOGRAPHY	169
ACKNOWLEDGMENTS	181

1 INTRODUCTION

Motivation of the study and introduction of LiV_2O_4

The cubic spinel compound LiV_2O_4 (see Fig. 1.1) is unusual since among a great deal of existing spinels [1] it is one of the two oxide spinel compounds [2] which sustain a metallic transport behavior [3] to low temperatures (Fig. 1.2), aside from the isostructural superconducting LiTi_2O_4 ($T_c \leq 13.7$ K) [4]. The formal oxidation number of vanadium and titanium in the respective spinels are both +3.5, assuming that Li has +1 and O -2. These correspond to 1.5 d electrons per V ion and 0.5 d electron per Ti ion available, respectively. In the normal spinel structure there is only one crystallographic site that V and Ti occupy in the respective compounds. From this and the half-integer valences, the observed metallic behaviors are readily anticipated.

LiV_2O_4 is unusual in its magnetic susceptibility. LiTi_2O_4 in the normal state shows a comparatively temperature T -independent susceptibility up to 300 K [4], whereas the observed susceptibility $\chi^{\text{obs}}(T)$ of LiV_2O_4 is strongly T -dependent [2, 5, 6, 7, 8, 9]. The observed susceptibilities of both LiTi_2O_4 and LiV_2O_4 are given in Fig. 1.3 [9]. It is reasonable to consider that the 0.5 d -valence electron per Ti site in LiTi_2O_4 is responsible for both of the metallic and paramagnetic behaviors. By the same token, by assuming that 0.5 d -electron/V plays the role of metallic conduction electrons in LiV_2O_4 and that the remaining 1 d -electron/V is localized, would this be feasible for the observed transport and magnetic measurement results? Is there something more taking place to make this V spinel more exotic? Having 1.5 d -valence electrons per V ion, LiV_2O_4 can also be considered to be a (dynamic) equal mixture of V^{+3} (d^2) and V^{+4} (d^1) states. This may be regarded as an electron-analogue of the high temperature cuprate superconductors which formally contain one to two holes per Cu.

LiV_2O_4 is unusual since it has built-in geometric frustration in the antiferromagnetic coupling between V local spins. As the name suggests, due to the frustration a system cannot achieve long-range magnetic order [10]. In fact, no long-range magnetic ordering is observed in frustrated compounds, including LiV_2O_4 down to 20 mK [11], unless something else (*e.g.* a structural distortion) takes place. Frustration by itself has already drawn much attention from both theoretical and experimental physi-

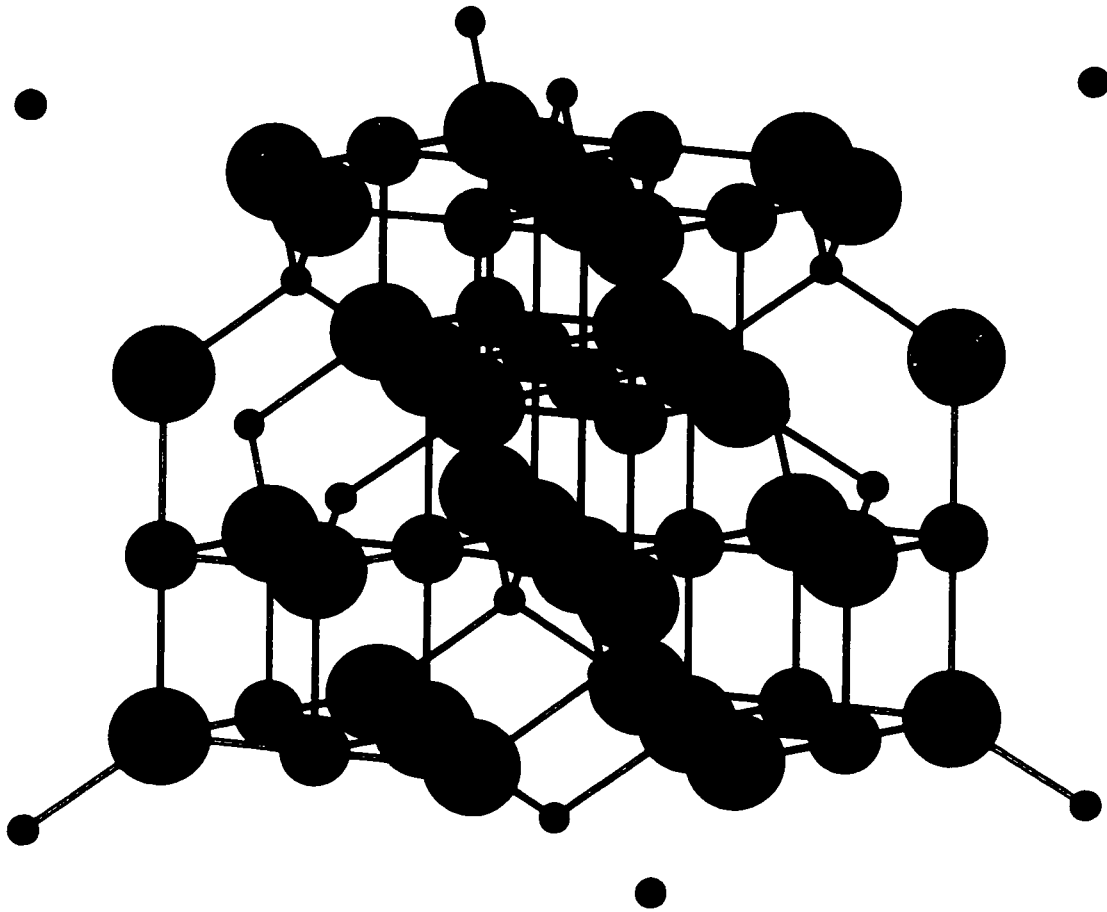


Figure 1.1 Normal spinel structure $\text{Li}[\text{V}_2]\text{O}_4$. Li, V and O atoms are represented in blue, red and green, respectively.

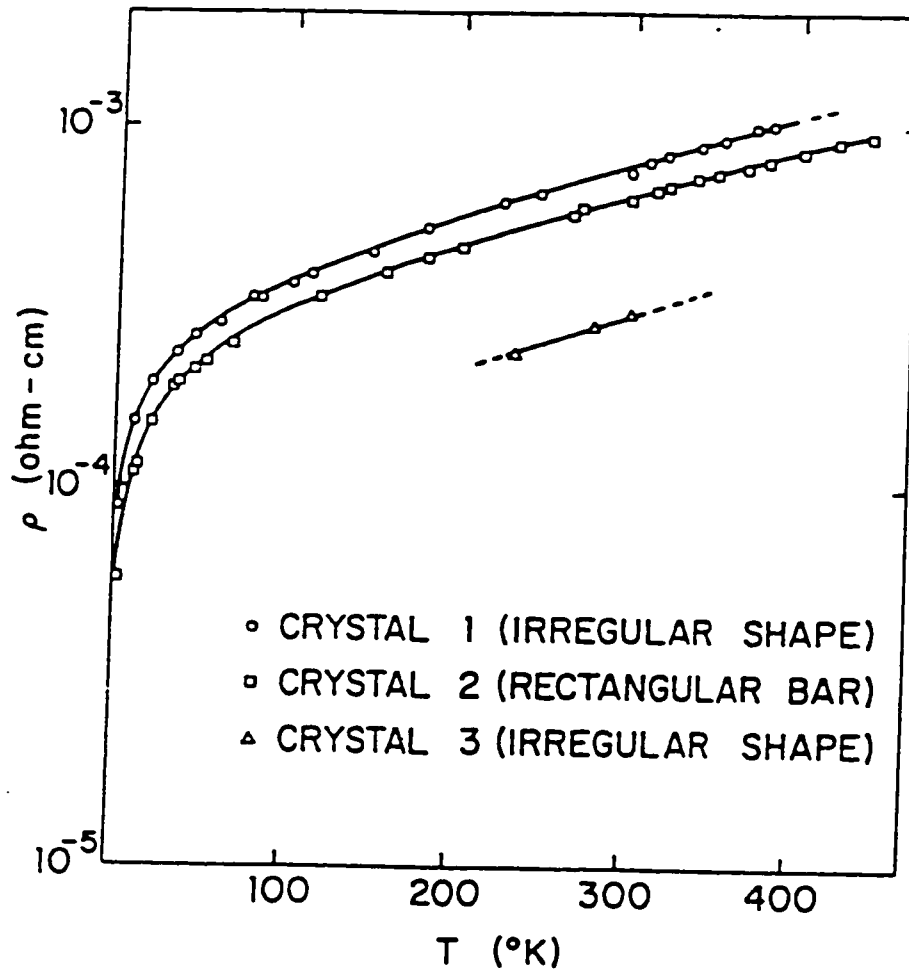


Figure 1.2 Resistivity ρ versus temperature T of hydrothermally-grown single crystals of LiV_2O_4 . Note the use of a logarithmic scale for the ordinate (from [3]).

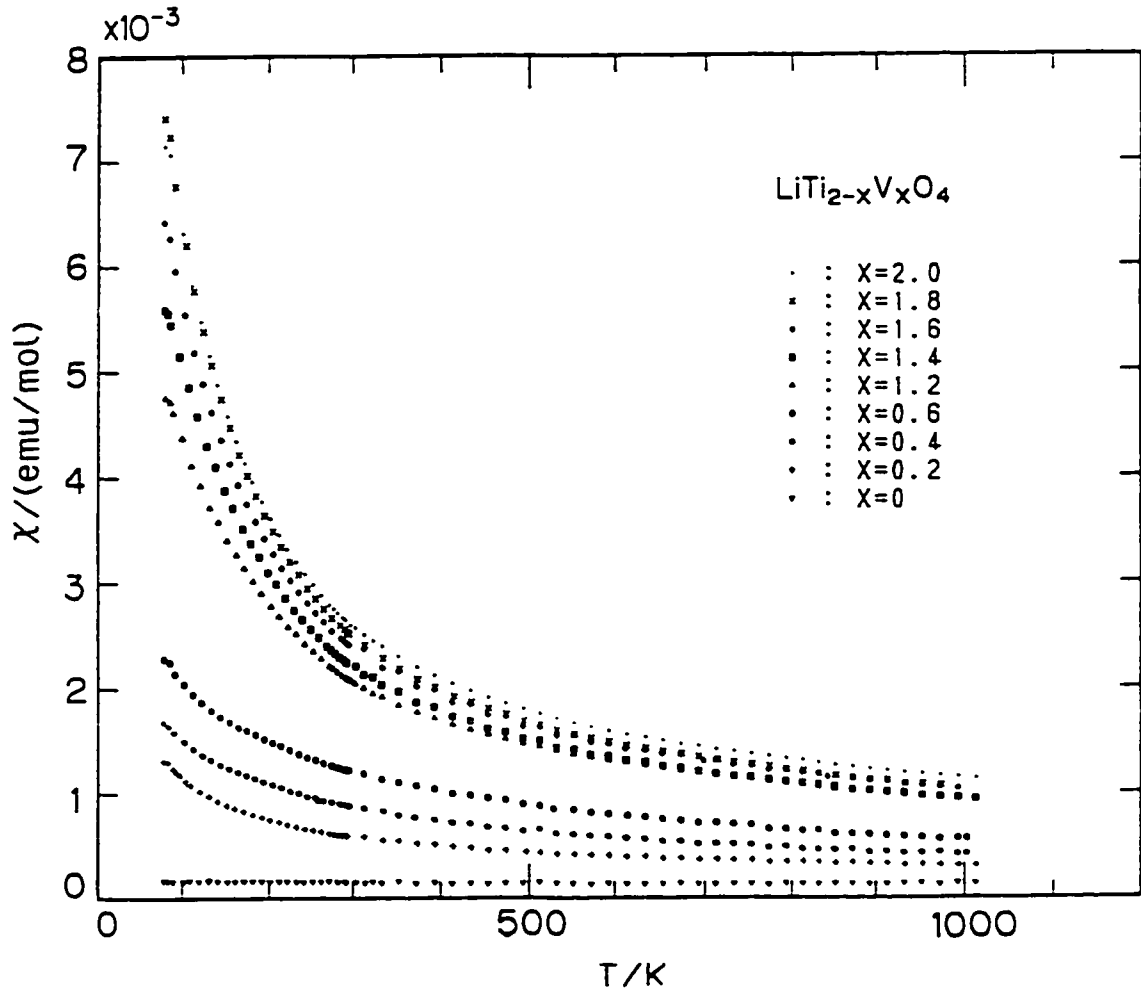


Figure 1.3 Temperature T variations of the magnetic susceptibility χ in $\text{LiTi}_{2-x}\text{V}_x\text{O}_4$ (from [9]). The core diamagnetic susceptibility contributions were already subtracted in the shown data.

cists for over a decade. In particular, the frustration effect due to doped holes in a CuO_2 plane in high temperature superconducting compounds is probably one of the most well-known and recent topics [12]. Another intriguing group of compounds in which frustration plays a major role is a spin glass [13]. What interesting feature would frustration bring to LiV_2O_4 ?

Last not but least, LiV_2O_4 is extremely unusual since it shows the largest electronic heat capacity coefficient $\gamma(T)$ at low T as a transition metal compound, to our knowledge [11, 14]. The low T part of $\gamma(T)$ is plotted in Fig. 1.4. This large γ corresponds to a large quasiparticle effective mass m^* of approximately 180 times as heavy as the bare electron mass m_e [14]. In other words, LiV_2O_4 is a heavy fermion (HF) $3d$ compound. Although the quasiparticle effective mass is relatively smaller than those seen in the heaviest-mass f -electron HF compounds (for example, for CeAl_3 $\gamma = 1.62 \text{ J/mol K}^2$ corresponding to $m^*/m_e \approx 860$ [15]), the value of $\gamma(1 \text{ K}) = 0.42 \text{ J/mol K}^2$ for LiV_2O_4 is still more than a factor of two larger than that of the “heaviest” previously known transition metal compound $\text{Y}_{0.97}\text{Sc}_{0.03}\text{Mn}_2$ ($\lesssim 0.2 \text{ J/mol K}^2$) [16].

The first three unique characters of LiV_2O_4 motivated this work and led us to the discovery of the last important feature [11].

Scope of this study and dissertation organization

The format of this dissertation is as follows. In the remainder of Chapter 1, brief introductions and reviews are given to the topics of frustration, heavy fermions and spinels including the precedent work of LiV_2O_4 . In Chapter 2, as a general overview of this work the important publication in *Physical Review Letters* by the author of this dissertation and collaborators [11] regarding the discovery of the heavy fermion behavior in LiV_2O_4 is introduced. The preparation methods employed by the author for nine LiV_2O_4 and two $\text{Li}_{1+x}\text{Ti}_{2-x}\text{O}_4$ ($x = 0$ and $1/3$) polycrystalline samples are introduced in Chapter 3. The subsequent structural characterization of the LiV_2O_4 and $\text{Li}_{1+x}\text{Ti}_{2-x}\text{O}_4$ samples was done by the author using thermogravimetric analysis (TGA), x-ray diffraction measurements and their structural refinements by the Rietveld analysis. The results of the characterization are detailed in Chapter 3. In Chapter 4 magnetization measurements carried out by the author are detailed [17].

In Chapter 5, after briefly discussing the resistivity measurement results including the single-crystal work by Rogers *et al.*[3], for the purpose of clear characterization of LiV_2O_4 it is of great importance to introduce in the following chapters the experiments and subsequent data analyses done by our collaborators. Heat capacity measurements (Chapter 6) were carried out and analyzed by Dr. C. A. Swenson, and modeled theoretically by Dr. D. C. Johnston [11, 14]. In Chapter 7 a thermal expansion study

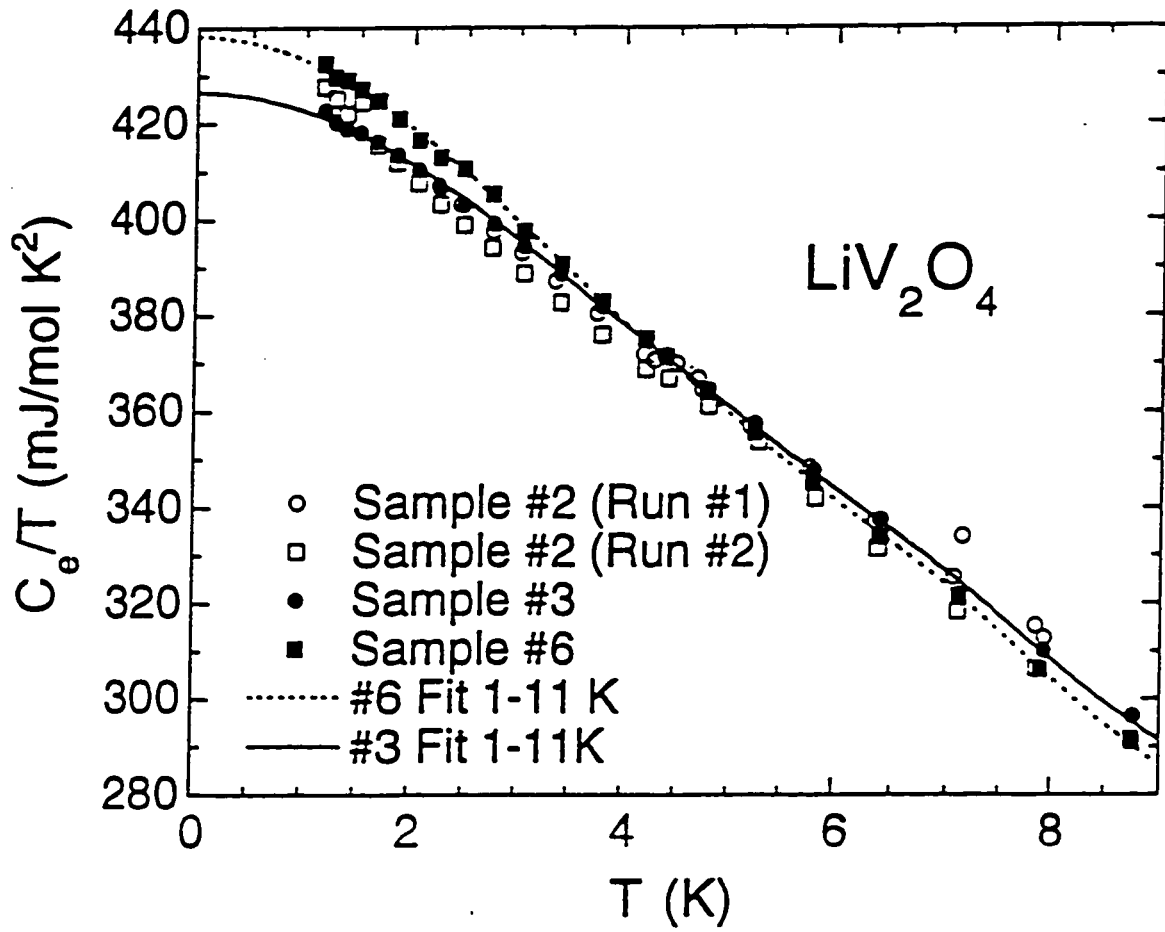


Figure 1.4 Electronic heat capacity coefficient $\gamma(T) \equiv C_e/T$ versus temperature T below 9K for LiV_2O_4 samples 2, 3 and 6 (from [14]).

using neutron diffraction by Dr. O. Chmaissem *et al.* [11, 18] and capacitance dilatometry measurements by Dr. C. A. Swenson [14] are introduced. The data analyses for the thermal expansion study were mainly done by Dr. O. Chmaissem (for neutron diffraction) and Dr. C. A. Swenson (for dilatometry), with assistances by Dr. J. D. Jorgensen, Dr. D. C. Johnston, and S. Kondo the author of this dissertation. Chapter 8 describes nuclear magnetic resonance (NMR) measurements and analyses by Dr. A. V. Mahajan, R. Sala, E. Lee and Dr. F. Borsa [11, 19].

Detailed reports of the neutron diffraction and NMR work were already published as [18] and [19], respectively. Detailed reports of magnetization [17], heat capacity and dilatometry thermal expansion measurements [14] are currently being prepared by the author of this dissertation and Dr. D. C. Johnston, respectively. The other important measurements reported in the above *Physical Review Letters* paper, but not detailed in a separate chapter in this dissertation, are muon spin rotation measurements at TRIUMF by J. Merrin *et al.* and low- T (≈ 0.45 to ≈ 5.5 K) heat capacity measurements under finite external magnetic fields (up to 6 T) by Dr. M. B. Maple *et al.* Without their collaboration work, this important discovery of the 3d heavy fermion compound would have never been realized. In the final chapter, a summary and discussion are given.

Reviews of important concepts

Reviews of frustration

The concept of frustration is not new. The various anomalous phenomena of frustration have fascinated many physicists, and still provide us with important unsolved problems. The term frustration accounts for a situation of a spin system in which a single ground state with a certain spin configuration cannot be determined definitively because of the presence of frustrated spin-spin interaction bonds.

The causes of frustration can essentially be placed into two categories: by the geometry of an ordered lattice and by randomness. The simplest example which explains the first one is shown in Fig. 1.5(a) [13], a plaquette of a triangular lattice with the nearest-neighbor (NN) antiferromagnetic (AF) coupling in all the three bonds. For the sake of convenience, the Ising model is considered here, in which the spins on the triangle can point only up or down. It is evident that in this model it is impossible to satisfy all three bonds in the AF fashion simultaneously. At most, two bonds may be antiferromagnetically coupled, but the spins on the remaining bond are coupled ferromagnetically. In this single triangular plaquette, six different configurations, *i.e.* six-fold degenerate ground states, exist. This is frustration: in particular, frustration in an ordered magnetic lattice is called geometric frustration. A triangle with

AF bonds is the key to this type of frustration. In real materials, there are several lattice structures which contain triangles. The triangular and Kagomé lattices are two-dimensional examples. Triangular plaquettes are also inherent in the fcc lattice; this can be easily recognized if the nearest-neighbor (NN) pairs are connected. Other three-dimensional examples of frustrating lattices are the garnet, and the transition metal sublattice of the pyrochlore structure which is identical to the B sublattice of a normal spinel $A[B_2]O_4$. In Table 1.1 some specific compounds are given for each frustrated structure type.

Table 1.1 Some examples of geometrically frustrated compounds. The ion in bold face represents a magnetic species that causes frustration in the compound. θ is the Weiss temperature (where the Curie-Weiss law is defined as $\chi = C/(T - \theta)$), and T_c the ordering temperature (Néel and spin freezing temperatures for AF and SG, respectively). AF, SG and HF respectively stand for antiferromagnet, spin-glass and heavy fermion low temperature states.

Compound	Magnetic lattice	$-\theta$ (K)	T_c (K)	Low T state	Ref.
VCl_2	triangular	437	36	AF	[21]
$NaTiO_2$	triangular	1000	< 2	—	[22]
$LiCrO_2$	triangular	490	15	AF	[23]
$SrCr_8Ga_4O_{19}$	kagomé	515	3.5	SG	[24]
$KCr_3(OH)_6(SO_4)_2$	kagomé	70	1.8	AF	[25]
K_2IrCl_6	fcc	321	3.1	AF	[26]
$Gd_3Ga_5O_{12}$	garnet	2.3	< 0.03	—	[27]
$ZnCr_2O_4$	pyrochlore	390	16	AF	[28]
LiV_2O_4	pyrochlore	40	< 0.02	HF	[11]

The other cause of frustration is randomness. Randomness in magnetism may originate from bond disorder or site disorder. First, in a magnetic ordered lattice with bond disorder, NN couplings are randomly varied between $+J$ and $-J$. This mixed-interaction case is illustrated in Fig. 1.5(b) where the presence of frustration is obvious. Second, site disorder comes from varied spatial distances between spin pairs due to, for instance, structural defects. Also, by diluting a non-magnetic metal with a small amount of magnetic elements (~ 0.05 to ~ 10 at. % [29]), one may have an alloy with a random spatial distribution of moments. The Ruderman-Kittel-Kasuya-Yosida (RKKY) interaction couples the magnetic moments via conduction electrons. However, the coupling constant J_{RKKY} between the local moments via the RKKY interaction is oscillatory in space with a power-law damping amplitude. Therefore, the spatial random distribution of spins results in a corresponding random mixture of coupling

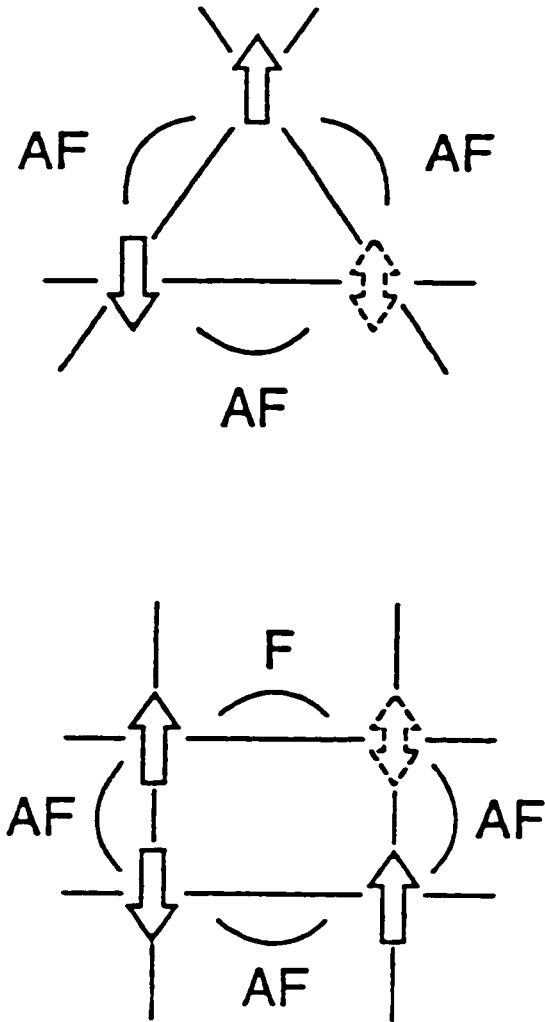


Figure 1.5 Two simple examples typifying the two different categories of frustration [13]. The geometric frustration is shown in the triangular plaquette in (a), whereas the frustration via randomness (mixed interactions) in (b).

constants which vary not only in size, but also in sign.

This second type of frustration, frustration induced by randomness, leads to a unique ordered state, called a spin glass state [29, 30] under favorable circumstances. A typical example is Mn-doped Cu (Fig. 1.6) [31]. As temperature T decreases from above a transition temperature, namely, a spin glass temperature (or spin freezing temperature) T_g , widely and randomly spread spins begin to form clusters in each of which spins are aligned along a direction of some magnetic moment anisotropy (*e.g.*, arising from Ising anisotropy, single-ion anisotropy, or Dzyaloshinskii-Moriya interactions). Clusters correlate with each other via the RKKY interactions, rotating themselves as a whole. As the system is further cooled toward T_g , thermal disorder becomes less, and the spins begin to freeze over a larger range. However, frustration via randomness hinders the system from finding one single spin configuration as $T \rightarrow 0$. Therefore, the spins have to settle down to one of many nearly degenerate ground states. Since these states have nearly, but not exactly, the same energy, the system may be only metastable (like ordinary glass). Spin glass behaviors in specific experiments such as dc/ac-susceptibility, heat capacity, resistivity, neutron scattering, etc. are detailed in Mydosh's book [29]. Among the most noticeable spin glass features is the temperature dependence of the uniform susceptibility $\chi(T)$ for low $T < T_g$, which is different depending on whether a sample is cooled in an applied magnetic field (field-cooled = "FC") or in zero field (zero-field-cooled = "ZFC"). This is shown in Fig. 1.6. ZFC $\chi(T)$ presents a cusp at T_g , while FC $\chi(T)$ becomes flat for $T < T_g$.

Reviews of heavy fermion systems

One usually imagines that heavy fermion (HF) materials are f -electron intermetallic compounds, more specifically those containing Ce or U (and Yb for some). In fact, almost all reported HF compounds are f -electron systems since the first reported HF CeAl_3 by Andres *et al.* [15] in 1975. In Table 1.2 several known f -electron HF materials are listed with characteristic quantities. At low temperatures T , some HF compounds become superconducting, some antiferromagnetic, and others remain nonmagnetic. In Fig. 1.7 are sketched temperature dependences of the electrical resistivity ρ , magnetic susceptibility χ and electronic heat capacity coefficient C/T (at the low T shown, the lattice contribution $C^{\text{lat}}(T)$ is negligible, so this C/T represents the electronic part essentially) for the HF compound CeCu_6 . This compound is a good representative to show the general behaviors of these quantities for HF materials in the normal state. There are several extensive reviews of the topic available [32, 33, 34, 35]. HF compounds have the following general peculiarities [32] (see Table 1.2).

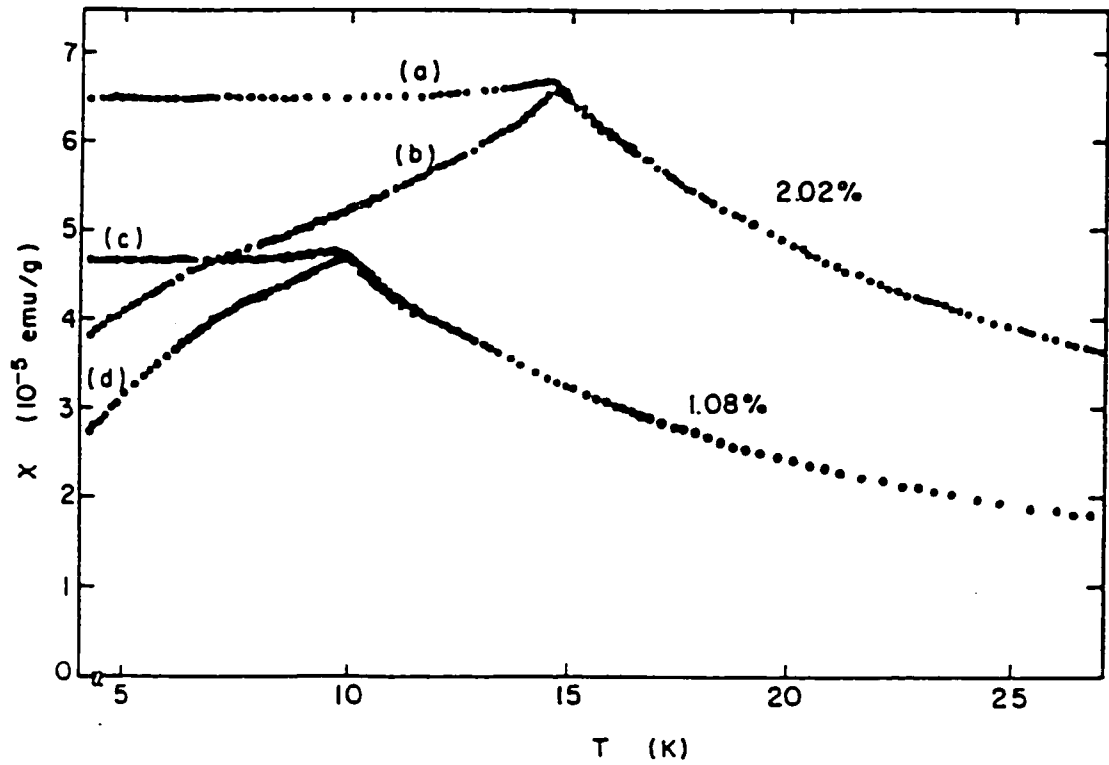


Figure 1.6 Field-cooled [(a) and (c)] and zero-field-cooled [(b) and (d)] susceptibility χ versus temperature T for Cu alloys containing 1.08 and 2.02 at. % of Mn (from [31]).

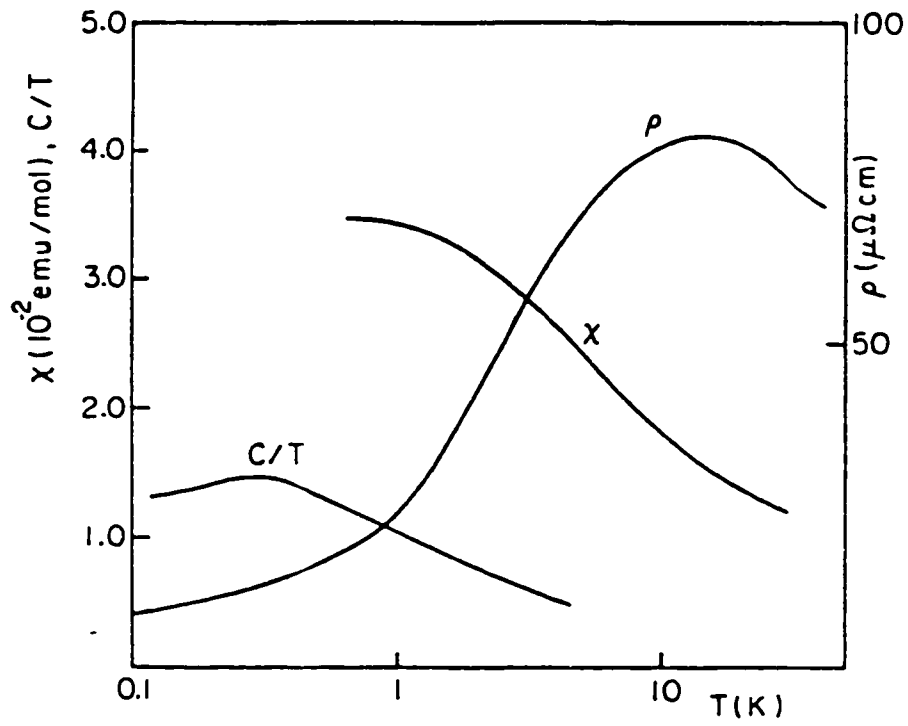


Figure 1.7 Temperature variations of the electrical resistivity $\rho(T)$, uniform magnetic susceptibility $\chi(T)$ and linear heat capacity coefficient C/T of a heavy fermion compound CeCu_6 (from [36, 37]).

Table 1.2 Comparisons of low temperature T electronic heat capacity coefficient γ , magnetic susceptibility χ and T^2 -coefficient of resistivity ρ for some f -electron heavy fermion compounds and elemental metals. These quantities are inferred from the lowest T measurements for the normal states. The symbol “mol” refers to a mole of a given formula unit.

	Material	$\gamma(0)$ [mJ/(molK)]	$\chi(0)$ (10^{-3} cm ³ /mol)	A ($\mu\Omega$ cm/K ²)
Paramagnet	CeCu ₆	1530 [38]	27 [39]	111 [38]
	CeAl ₃	1362 [40]	36 [15]	35 [15]
Superconducting	CeCu ₂ Si ₂	728 [40]	82 [41]	≈ 10 [41]
	UBe ₁₃	1100 [42]	15 [42]	—
	UPt ₃	450 [43]	103 [44]	1.2 [45]
Magnetic	U ₂ Zn ₁₇	1070 [46]	23 [47]	—
Elemental metal	Pd	9.9 [48]	0.6 [49]	3.3×10^{-5} [48]
	Na	1.4 [50]	0.03 [51]	1.0×10^{-6} [52]

- An extraordinarily large coefficient of electronic heat capacity, $\gamma(T) \equiv C_e/T$. γ is proportional to the density of states $\mathcal{D}^*(E_F)$ at the Fermi level E_F , and then $\mathcal{D}^*(E_F)$ to the quasiparticle effective mass m^* in the Fermi liquid picture (see Chapter 6). Therefore, a large γ implies a large m^* . This is the origin of the term “heavy” fermions. The real electron mass does not actually increase, but it is a way of stating in the Fermi liquid the unique character caused by many-body effects. As in Fig. 1.7, $\gamma(T)$ is strongly T dependent at low T ($\lesssim 10$ K) unlike the constant γ observed in a conventional metal. This suggests a T -dependent $\mathcal{D}^*(E_F)$. $\gamma(0)$ values inferred from the lowest temperature measurements are listed in Table 1.2.
- The magnetic susceptibility $\chi(T)$ shows a large value at low T on the order of 10^{-2} cm³/mol which is two or more orders of magnitude larger than that of a conventional metal, as illustrated in Table 1.2. A HF compound displays Curie-Weiss-like localized moment behavior in $\chi(T)$ at high T with a negative Weiss temperature θ , while the T dependence becomes much less at low T (see Fig. 1.7).
- The low- T resistivity $\rho(T)$ follows a T^2 dependence, thus obeying the Fermi liquid prediction (see Fig. 1.8(a)). A notable feature in $\rho(T)$ in this relation is that the T^2 coefficient of a HF compound is much larger than that of a conventional metal. The T^2 coefficients are given for some HF compounds in Table 1.2. Except for UPt₃ [see Fig. 1.8(c)] and UAl₂, $\rho(T)$ exhibits a peak and then decreases as T increases, as shown in Fig. 1.8(b), in sharp contrast to conventional

metals.

- It seems necessary that the inter- f -atom distance be larger than the so-called “Hill limit” of 3.25–3.5 Å [53] for a compound to be a HF [32, 33]. When the f - f atom spacing is above the Hill limit, the material is expected to display local moment magnetism due to the absence of f - f orbital overlaps, unless the hybridization of f electrons with conduction electrons prevents that from occurring. Therefore, the presence of nonmagnetic (at low T) HF compounds suggests the importance of the hybridization. Furthermore, Fisk [32] remarks that i) HF materials with very large γ do not have an f atom as a nearest neighbors of an f -atom. ii) uranium tends to form HF compounds with an element from “the end of d -block and the beginning of the sp -blocks where few states are available for hybridization with the f -electrons.” This last point implies that the hybridization tends to suppress the heavy fermion formation, which is opposite to the above notion. However, this superficial contradiction is not problematic. It is known that in the (periodic) Anderson model the hybridization V is necessary to establish a virtual-bound state around a local f energy level, and with the interelectronic on-site Coulomb interaction U a local moment appears in the metal. In addition, the many-body scattering resonance of the conduction electrons by the local moments yields a large electronic density of states at the Fermi level, called the Kondo (or Abrikosov-Suhl) resonance, which in turn causes a large effective mass. In other words, for a large effective electron mass, the presence of hybridization is essential (without hybridization, f electrons will be uncoupled and show magnetism at low T , which is contrary to the observed nonmagnetic ground state; see below). However, it is known that charge configurations become unstable and fluctuate (resulting in an “intermediate valence” system) if the degree of hybridization (strictly speaking the size of V/U) becomes large.

The nearly T -independent $\chi(T)$ and rapidly varying $\gamma(T)$ at low T of HF compounds are often analyzed by and found to follow the predictions of the single spin $S = 1/2$ -impurity Kondo model (or the Coqblin-Schrieffer model, an extended model of the Kondo model to angular momentum $J > 1/2$). HF compounds are lattices formed by f -electron ions and therefore are often called “Kondo lattices” or “dense Kondo systems” for their Kondo-like behaviors. On the other hand, the resistivity $\rho(T)$ of HF compounds which decreases with decreasing T at low T (\ll the Kondo temperature T_K) cannot be explained by the dilute impurity model. This decrease is normally considered as the development of a “coherent state” at the Fermi level (*i.e.* Kondo peak) which corresponds to a Fermi-liquid (*i.e.* metallic) quasiparticle state made from coupled local spins and conduction electrons (as detailed in the next paragraph). As a Fermi liquid, ρ is proportional to T^2 in this coherent region.

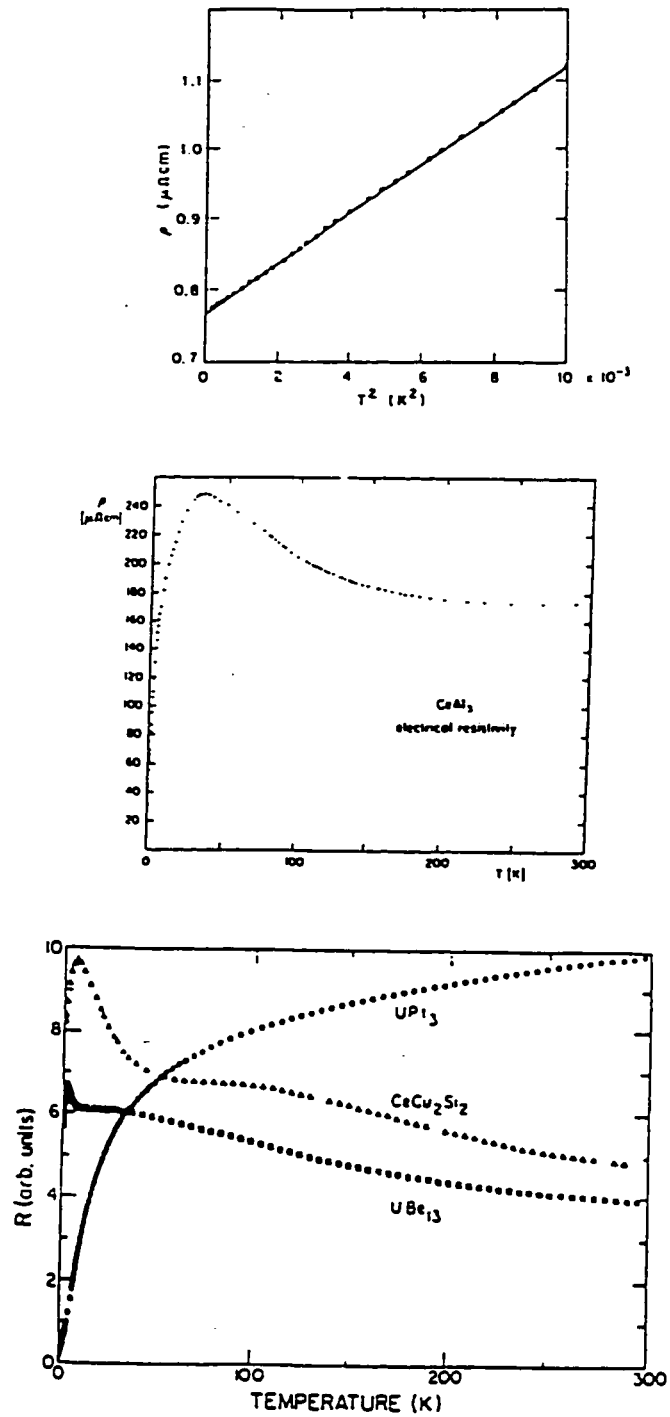


Figure 1.8 Temperature T dependences of the electrical resistivity ρ of some heavy fermion materials. The low- T T^2 dependence of CeAl_3 is given in (a) (from [15]), and the overall ρ behavior in (b) (from [46]). In (c), the anomalous T dependence of UPt_3 is shown along with two HF superconducting compounds (from [33]).

The $S = 1/2$ Kondo model was invented in 1964 [54] in order to solve the long-standing (since 1930s) theoretical mystery of the origin of the resistivity minimum in nonmagnetic alloy systems (such as Cu, Ag, Pt) with small amounts of magnetic impurities (like Cr, Fe, Co). Starting with the s - d Hamiltonian $\mathcal{H} = J_{s-d} \sum_i \vec{s}_i \cdot \vec{S}$ where \vec{s}_i is a conduction electron spin, Kondo extended the previous perturbative calculation of $\rho(T)$ to the second-order Born approximation term which includes up to the third order in the exchange coupling constant J_{s-d} . This new term gives rise to a logarithmically increasing $\rho(T)$ with decreasing T , which when combined with the lattice T^5 contribution then causes the resistivity minimum to occur. However, although this Kondo model succeeded in accounting for the resistivity minima, the logarithmically diverging low- T ρ became another theoretical challenge (Kondo problem). Abrikosov [55] computed even higher-order terms, but found again that the resulting ρ diverged as $T \rightarrow 0$. The susceptibility derived by Yosida and Okiji [56] in the same way was found to be diverging again, but to the negative direction, in the zero T limit. All these results suggested that the perturbative calculation could not work even qualitatively for the description of low- T properties of Kondo alloys. The ultimate theoretical solution to this problem had to wait until Wilson [57] devised the numerical renormalization group theory and the exact solution based upon the Bethe ansatz [58, 59, 60] became available.

Starting with the s - d model, Yosida [61, 62] successfully accounted for the observed T -independent low- T susceptibility. He postulated a singlet ground-state wavefunction from which he found that a local moment is coupled by a pair of one half of a conduction electron and one half of a hole. For instance, around one "up" local spin $S = 1/2$, one half of a "down" conduction electron spin and one half of an "up" conduction hole spin gather, forming a spin singlet. In other words, the local spin is screened locally by a conduction electron-hole pair, while the charge is conserved. Hence, the spin doublet ($S = 1/2$) uncoupled with conduction electrons at high T (which gives the Curie-Weiss $\chi(T)$) is, upon cooling, transformed to the spin singlet formed by local spins and conduction electron/hole spins which leads to the saturating $\chi(T)$ at low T . In addition, by using the Friedel sum rule [63], Yosida's theory [62] yields a finite residual resistivity, called the unitarity limit; thus, the divergence problem is removed. The resistivity $\rho(T)$ is found to decrease like T^2 from this maximum value as T increases.

The general temperature dependences of the resistivity $\rho(T)$, inverse susceptibility $\chi^{-1}(T)$, electronic heat capacity C_e and thermoelectric power S of a typical dilute Kondo alloy system are presented in Fig. 1.9 [64].

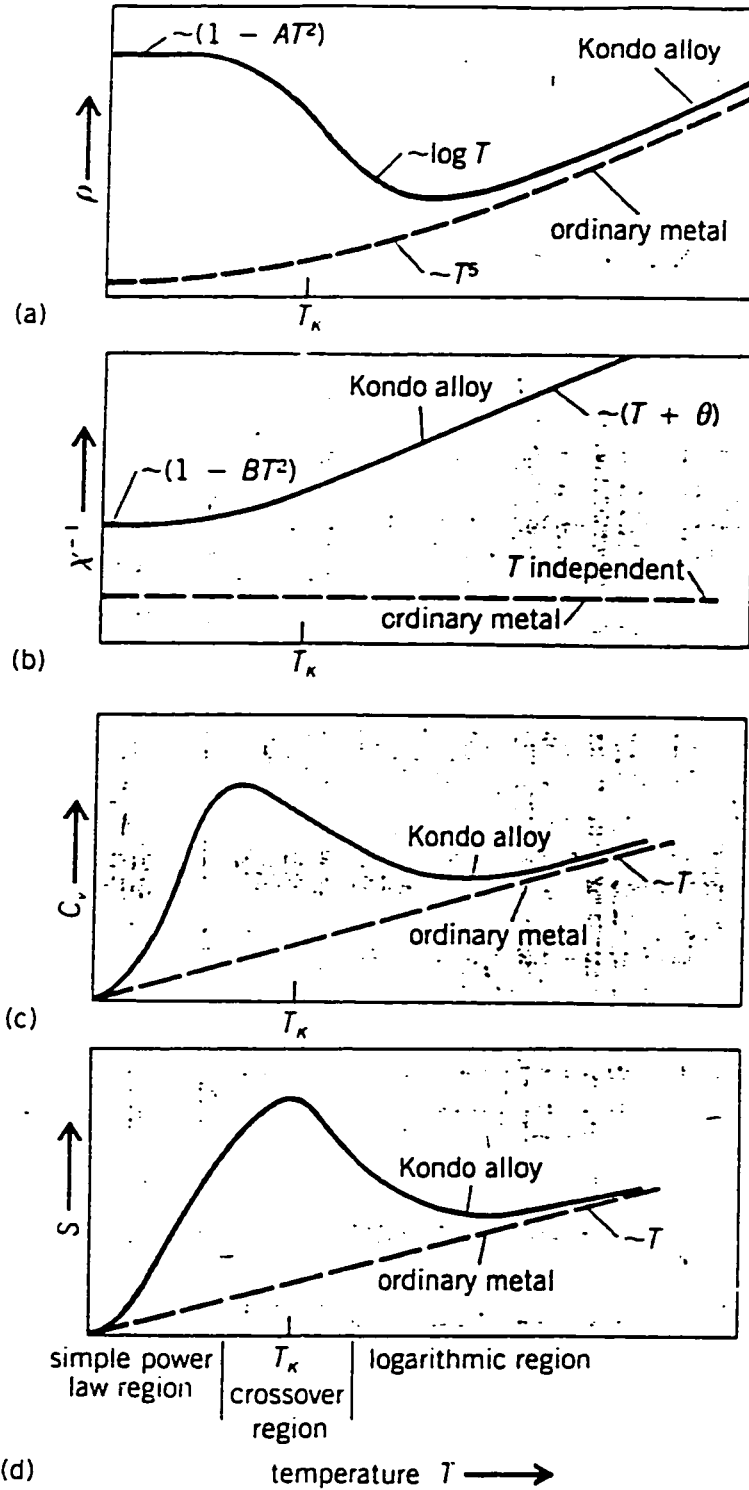


Figure 1.9 Temperature variations of a typical Kondo alloy and a normal metal for (a) electrical resistivity ρ , (b) inverse magnetic susceptibility χ^{-1} , (c) electronic heat capacity C_e and (d) thermoelectric power S (from [64]).

The periodic Anderson model [65] is usually employed to describe HF materials since it may incorporate the strong electronic correlation via the intra-atomic Coulomb repulsion U between f -electrons in a lattice. Both the electronic heat capacity coefficient γ and magnetic susceptibility χ are enhanced via many-body effects (*i.e.* U). The normalized ratio of χ to γ is called the Wilson ratio R_W , and may signify the degree of many-body effects. For quasiparticles with $S = 1/2$, R_W is defined as

$$R_W = \frac{\chi(0)/(\frac{1}{4}g^2\mu_B^2)}{\gamma(0)/(\frac{1}{3}\pi^2k_B^2)} \quad (1.1)$$

where g is the g -factor of the quasiparticles, and μ_B is the Bohr magneton. This Wilson ratio can be considered as the ratio of the two densities of states at the Fermi level probed by susceptibility and heat capacity measurements. That is,

$$R_W = \frac{D^{\chi}(E_F)}{D^C(E_F)} \quad (1.2)$$

In almost all HF metals, R_W is roughly unity, so χ and C_e are probing the same low- T quasiparticle excitations.

The T^2 coefficient A of the electrical resistivity $\rho(T) = \rho_0 + AT^2$ at low T in HF compounds is found to be proportional to $\gamma^2(0)$ with a universal proportionality constant. The plot of A versus γ showing this proportionality is called the Kadowaki-Woods plot [66]. See Chapter 5 for $\rho(T)$ of LiV_2O_4 .

Reviews of spinels

Spinel crystal structure

The conventional unit cell of an oxide spinel AB_2O_4 shown in Fig. 1.1 is a face-centered-cubic (fcc) structure. Both A and B are cations. In addition to oxide spinels, chalcogenide spinels with S^{-2} , Se^{-2} and Te^{-2} anions exist. The cations occupying the octahedral sites (called $16d$ sites) are customarily enclosed in a pair of square brackets. $A[B_2]O_4$ is called a normal spinel. Meanwhile, $B[AB]O_4$ is called an inverse spinel because the two types of atoms occupy the octahedral site with an equal probability. There are also intermediate spinels which are between the normal and inverse spinels. Excellent reviews of spinel structures are [1, 67]. The spinel compound studied in this work is normal, *i.e.* $\text{Li}[\text{V}_2]\text{O}_4$.

The space group of a normal spinel is $Fd\bar{3}m (O_h^7)$. The oxygen ions constitute a nearly close-packed fcc array. Lithium occupies the $8a$ sites, which correspond to one-eighth of the 64 tetrahedral holes formed by the closed-packed oxygen sublattice in the Bravais unit cell that contains eight formula units. Vanadium occupies the $16d$ sites which correspond to one half of the 32 octahedral holes in the oxygen sublattice per unit cell. All the V ions are crystallographically equivalent, as are the Li ions and the O ions.

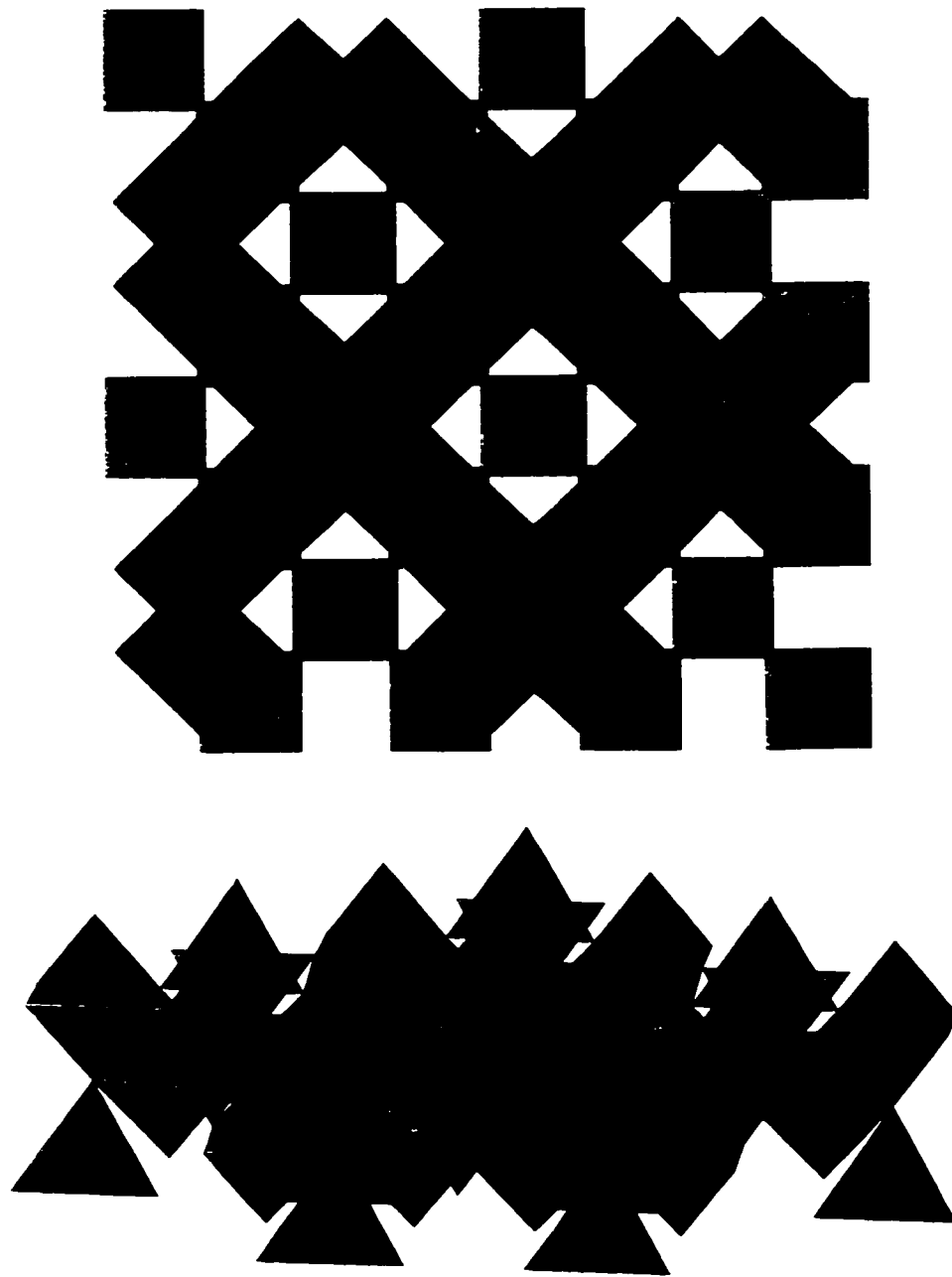


Figure 1.10 Alternative polyhedron illustration of a spinel structure from different viewpoints. (S). Tetrahedra in blue are LiO_4 , while octahedra in pink are VO_6 . In each polyhedron, a cation (Li or V) is located at the center. Only a few layers are shown.

Figure 1.10 is an alternative picture of a cubic spinel in terms of LiO_4 tetrahedra and VO_6 octahedra [18]. It is evident that the edge-sharing VO_6 octahedra constitute linear chains parallel to each other along one of the $\langle 110 \rangle$ directions within the plane. In the layers immediately above and below, the VO_6 chains alter the direction by 90° . These octahedron chains are separated from one another by LiO_4 tetrahedra. Interestingly, these tetrahedra are arranged in such a way that they are not touching each other.

Out of the six possible $\langle 110 \rangle$ axes, each octahedron is edge-shared with neighboring octahedra along only three of these axes, one from the two axes in each $\{110\}$ plane. Discarding all the oxygens from the VO_6 octahedron chains in Fig. 1.10, we now see V chains. These V chains form a three-dimensional network of corner-shared tetrahedra, as shown in Fig. 1.11.

The positions of Li, V and O ions in terms of fractional coordinates with respect to the cubic lattice parameter a_0 are given in Table 1.3. The positions of the oxygen atoms can be varied depending on

Table 1.3 Lattice positions of the normal oxide spinel LiV_2O_4 [68]. Note the use of the second choice of the origin.

Space Group No. 227, $Fd\bar{3}m (O_h^-)$, Origin choice 2		For equivalent coordinates			
		$(0, 0, 0)+ . (0, \frac{1}{2}, \frac{1}{2})+ . (\frac{1}{2}, 0, \frac{1}{2})+ . (\frac{1}{2}, \frac{1}{2}, 0)+$			
Li	$8a$	$(\frac{1}{8}, \frac{1}{8}, \frac{1}{8})$	$(\frac{7}{8}, \frac{3}{8}, \frac{3}{8})$		
V	$16d$	$(\frac{1}{2}, \frac{1}{2}, \frac{1}{2})$	$(\frac{1}{4}, \frac{3}{4}, 0)$	$(\frac{3}{4}, 0, \frac{1}{4})$	$(0, \frac{1}{4}, \frac{3}{4})$
O	$32e$	(u, u, u)	$(\bar{u} + \frac{3}{4}, \bar{u} + \frac{1}{4}, u + \frac{1}{2})$	$(\bar{u} + \frac{1}{4}, u + \frac{1}{2}, \bar{u} + \frac{3}{4})$	$(u + \frac{1}{2}, \bar{u} + \frac{3}{4}, \bar{u} + \frac{1}{4})$
		$(u + \frac{3}{4}, u + \frac{1}{4}, \bar{u} + \frac{1}{2})$	$(\bar{u}, \bar{u}, \bar{u})$	$(u + \frac{1}{4}, \bar{u} + \frac{1}{2}, u + \frac{3}{4})$	$(\bar{u} + \frac{1}{2}, u + \frac{3}{4}, u + \frac{1}{4})$

the oxygen parameter u . For an ideal cubic-close-packed oxygen array, u becomes equal to $1/4$. If the first choice of the origin was used, the oxygen parameter in the ideal case becomes $3/8$ due to the shift of the origin. In a real spinel, usually $u \neq 1/4$, and in the hard-sphere model u increases linearly with the reduced difference $(r_A - r_B)/a_0$ of ionic radii r_A and r_B [1], as illustrated in Fig. 1.12. From Shannon's radius table [69], we have $r(\text{V}^{+3}) = 0.640 \text{ \AA}$ (CN = 6), $r(\text{V}^{+4}) = 0.58 \text{ \AA}$ (CN = 6), $r(\text{Li}^{+1}) = 0.59 \text{ \AA}$ (CN = 4), $r(\text{O}^{-2}) = 1.38 \text{ \AA}$ (CN = 4), where CN stands for the coordination number of a given ion. Since the V in LiV_2O_4 has the effective valence of $+3.5$, the average of $r(\text{V}^{+3})$ and $r(\text{V}^{+4})$, which is 0.61 \AA , is used. Then the above reduced difference can be calculated

$$\frac{r(\text{Li}^{+1}) - r(\text{V}^{+3.5})}{a_0} = -0.0024 \quad (1.3)$$

where $a_0 = 8.24039 \text{ \AA}$ (at $T = 295 \text{ K}$) from Chmaissem *et al.* [18] is used. With the obtained oxygen parameter $u = 0.26127$ [18], the location of LiV_2O_4 in Fig. 1.12 calculated from the above ionic radii is

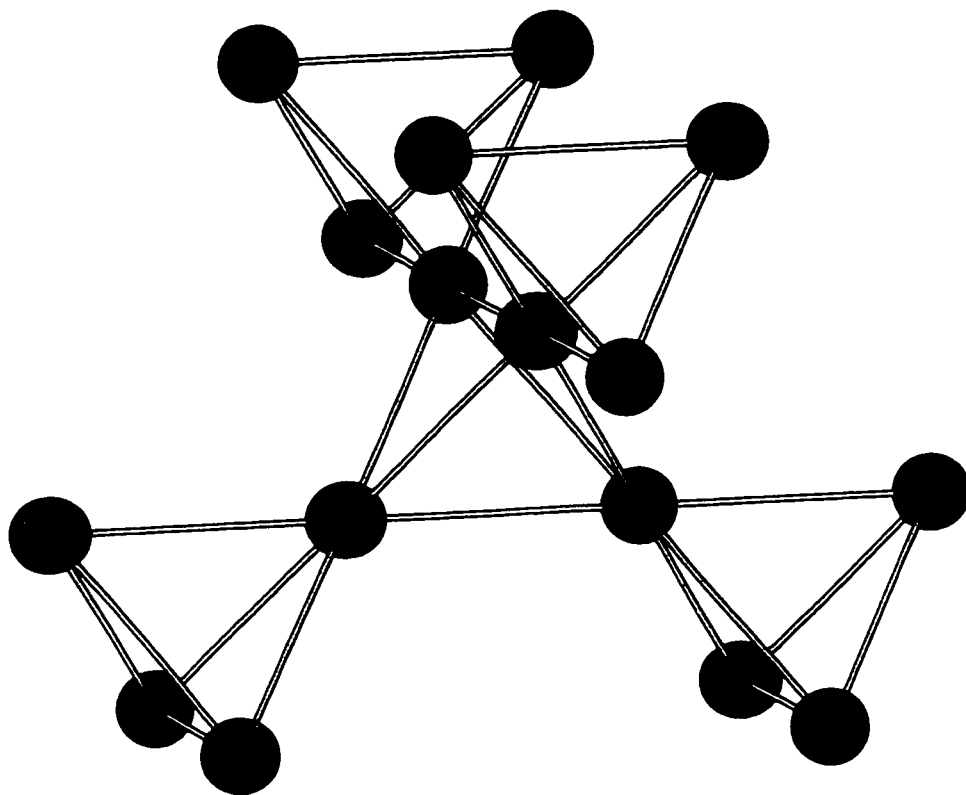


Figure 1.11 Vanadium atom sublattice of the LiV_2O_4 spinel structure.

found to be in good agreement with other spinel compounds.

As introduced below in Chapter 3, the oxygen parameter u for all of our samples was found larger than the ideal close-packed oxygen value of $1/4$. Compared to the "ideal" structure with this u value, the volumes of an oxygen tetrahedron and an octahedron become larger and smaller, respectively. The increase of the tetrahedron volume takes place in such a way that each of the four Li-O bonds are lengthened along one of the $\langle 111 \rangle$ axes, so that the tetrahedron remains undistorted. Each of the oxygen atoms in a tetrahedron is also bonded to three V atoms. This elongation of a Li-O bond is illustrated in Fig. 1.13. As a result of this elongation, the tetrahedral and octahedral holes in the oxygen sublattice become respectively larger and smaller [67]. Since the fractional coordinates of both Li and V are fixed in terms of the unit cell edge, an octahedron centered by a V atom is accordingly distorted. The point symmetry of the Li $8a$ sites remains cubic, no matter how large the distortion is. However, for $u \neq 1/4$ the point symmetry of V $16d$ sites becomes trigonal. In Figs. 1.14 the ideal undistorted and real distorted V octahedra are compared.

The interatomic distances d between nearest-neighbor pairs can be calculated readily. Since it is only oxygen that slightly alters position depending on the value of u , the cation-cation distances (Li-Li, V-V and Li-V) do not depend on the distortion, but only on the lattice parameter a_0 . Defining the deviation of u from its ideal closed-packed oxygen array value of $1/4$ as $\Delta \equiv u - 1/4$, one obtains

$$d_{\text{Li-Li}} = \frac{\sqrt{3}}{4} a_0 \quad (1.4)$$

$$d_{\text{V-V}} = \frac{1}{2\sqrt{2}} a_0 \quad (1.5)$$

$$d_{\text{Li-V}} = \frac{\sqrt{11}}{8} a_0 \quad (1.6)$$

$$d_{\text{Li-O}} = \frac{\sqrt{3}}{8} (1 + 8\Delta) a_0 \quad (1.7)$$

$$d_{\text{V-O}} = \frac{1}{4} \sqrt{1 - 8\Delta + 48\Delta^2} a_0 \quad (1.8)$$

These equations are used to derive the interatomic distances. The cation-anion distances ($d_{\text{Li-O}}$ and $d_{\text{V-O}}$) are parameters which may be used to quantify the influences of the distortion in the oxygen array on various properties.

Reviews of oxide spinels

The spinel structure has its origin in the mineral spinel MgAl_2O_4 . Numerous compounds exist which have this spinel AB_2O_4 structure. Among the existing spinels, the ferrites $MO \cdot \text{Fe}_2\text{O}_3$ ($M =$ a divalent cation = Fe, Co, Ni, Cu, Zn, Mg, Cd, etc. [70]) are probably the most intensively investigated.

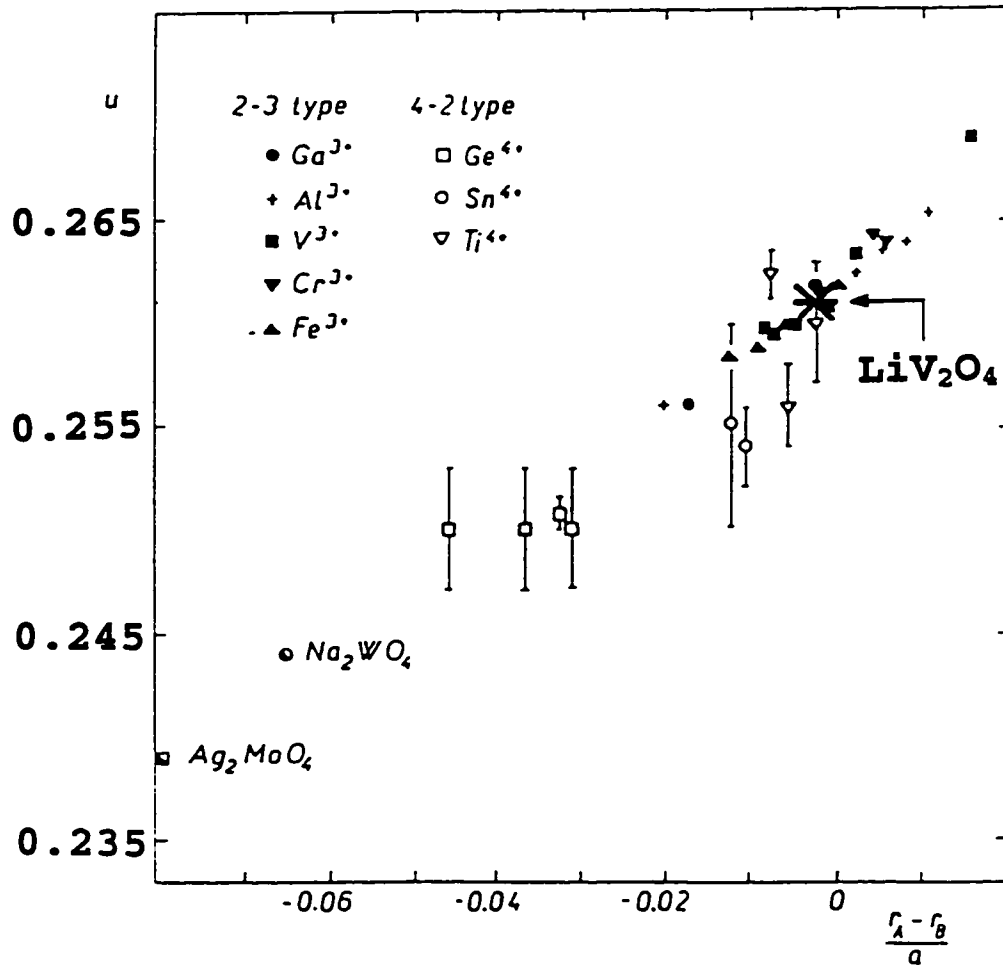


Figure 1.12 Linear dependence of the oxygen parameter u versus the reduced difference of radii of A and B ions in various oxide spinels [1]. Listed are so-called 2-3 type spinels ($A^{+2}B_2^{+3}O_4$ with $B=Ga, Al, V, Cr$ and Fe) and 4-2 type spinels ($A^{+4}B_2^{+2}O_2$ with $A=Ge, Sn,$ and Ti).

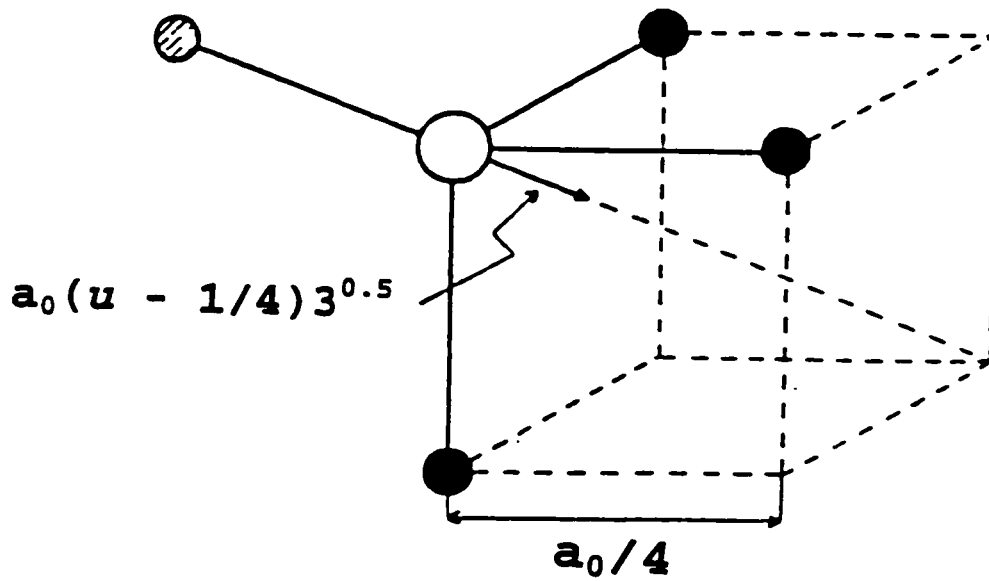


Figure 1.13 Illustration of how an elongation of a Li-O bond takes place [1]. Lithium is the shaded circle, vanadium the filled circles and oxygen the open circle. The elongation is achieved without displacements of lithium and vanadium ions.

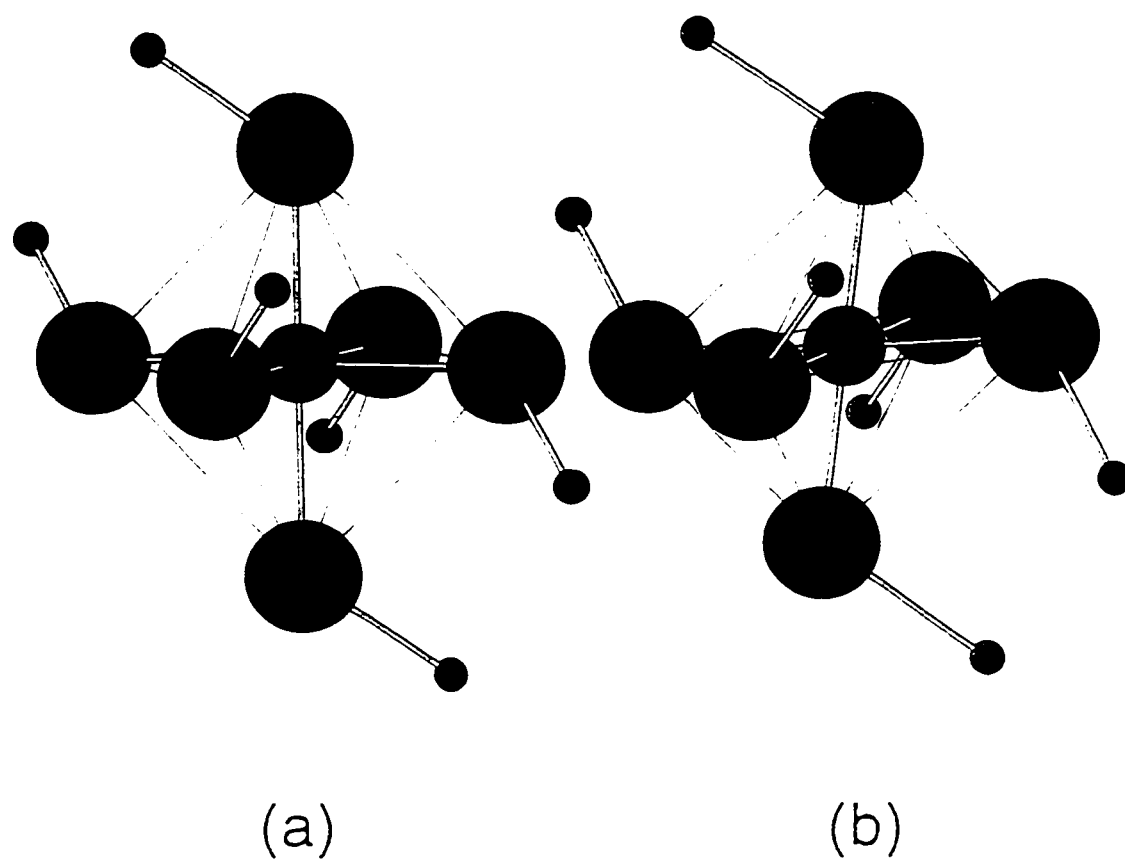


Figure 1.11 An undistorted (a) and distorted (b) VO_4 tetrahedron. The distortion in (b) is a consequence of the elongation of each La-O bond as shown. The distortion in (b) is exaggerated ($\alpha = 127^\circ$) compared to the actual distortion.

In particular, Zn ferrites have an engineering application as a high-frequency magnetic core material [70], and Cr-doped LiMn_2O_4 as a secondary battery [71]. Spinel compounds possess a variety of magnetic behaviors; especially prominent is the ferrimagnetism in the ferrites (for a review see [72]).

The large electronegativity of oxygen has a tendency to make spinels have ionic-type bonds. In general, this tends to yield high resistivity in oxide spinels [1]. When the A cation is non-magnetic and B is integral-valent, this high resistivity can be expected from the viewpoint of the nearest-neighbor B - B distance. The 3-fold orbital degenerate t_{2g} orbitals are partially filled by valence d electrons for a spinel with a non-magnetic A and a magnetic transition metal element B . These t_{2g} orbitals of a B ion are extending their lobes toward the nearest-neighboring B ions, as shown in Fig. 1.15. Assuming no conduction electrons, the transport properties are then dependent upon the direct overlaps of these occupied d orbitals. Over the years Goodenough and his coworkers prepared a series of V^{+3} spinel compounds (MV_2O_4 where $M = \text{Mn, Fe, Mg, Zn, and Co}$) [73] and studied how the V-V distance influences their electronic transport properties. In the order of the metal elements M listed in the Table 1.4, the activation energy decreased as the V-V distance decreased in these semiconducting compounds, suggesting that V t_{2g} wavefunctions overlap more. By observing this decreasing activation energy, they established an estimate of a critical V-V distance R_c below which the transport is transformed from semiconductive to metallic. The most recent estimate of this distance is $R_c = 2.90(1) \text{ \AA}$ for V^{+3} [74]. The value of the nearest neighbor V-V distance in LiV_2O_4 , calculated from the lattice parameters at $T = 295 \text{ K}$ and 4 K [18], are 2.913 and 2.909 \AA , respectively, which is on the verge of the transition, and, in fact, LiV_2O_4 is a metal [3] (also see Fig. 1.2). However, it is not clear if this approach of the critical V-V distance is appropriate for LiV_2O_4 since it is not a purely V^{+3} system. In this mixed-valence system it appears trivial that LiV_2O_4 is a metal by the reasons of the non-integral valence at crystallographically equivalent V sites, as already mentioned. The question is why LiV_2O_4 does not distort to a lower symmetry structure containing a static distribution of V^{+3} and V^{+4} .

Reviews of the past work on LiV_2O_4

In spite of being a metal (see Fig. 1.2), LiV_2O_4 exhibits strong temperature dependence in its magnetic susceptibility, indicating strong electron correlations. In all work reported before 1997, $\chi(T)$ was found to increase monotonically with decreasing T down to $\approx 4 \text{ K}$ and to approximately follow the Curie-Weiss law, as shown in Fig. 1.3 [2, 5, 6, 7, 8, 9]. Kessler and Sienko [5] interpreted their susceptibility data as the sum of a Curie-Weiss term $2C/(T - \theta)$ and temperature-independent term $\chi_0 = 0.4 \times 10^{-4} \text{ cm}^3/\text{mol}$. Their Curie constant C was $0.468 \text{ cm}^3 \text{ K}/(\text{mol V})$, corresponding to a $V^{+4} g$ -

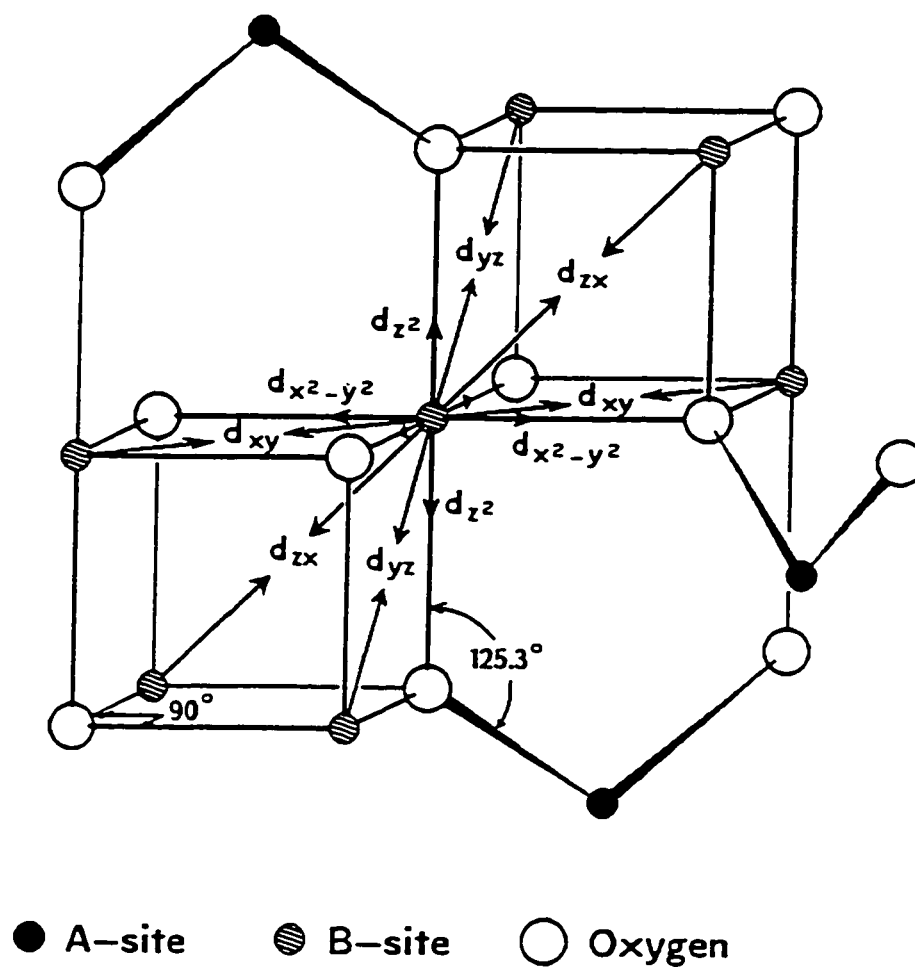


Figure 1.15 Spatial directions of the d orbitals of a B cation in a spinel AB_2O_4 (from [20]).

Table 1.4 Physical properties of vanadium spinels. a_0 is the lattice parameter, and "V-V" is the distance between a nearest vanadium pair (both at room temperature). q is the activation energy from resistivity measurements for 113–473 K. A number in parentheses is the error in the last digit of a quantity (reproduced from [73]).

Formula	a_0 (Å)	V-V (Å)	q (eV)
MnV ₂ O ₄	8.522(2)	3.013	0.37(1)
FeV ₂ O ₄	8.454(2)	2.990	0.25(1)
MgV ₂ O ₄	8.418(2)	2.976	0.18(1)
ZnV ₂ O ₄	8.410(2)	2.973	0.16(1)
CoV ₂ O ₄	8.407(2)	2.972	0.07(1)

factor of 2.23 with spin $S = 1/2$. The negative Weiss temperature $\theta = -63$ K suggests antiferromagnetic (AF) interactions between the V spins. However, no magnetic ordering was found above 4.2 K. This may be understood in terms of the possible suppression of long-range magnetic ordering due to the geometric frustration among the AF-coupled V spins in their tetrahedra network. Similar values of C and θ have also been obtained by subsequent workers [2, 6, 7, 8, 9], as shown in Table 1.5. This local magnetic moment behavior of LiV₂O₄ is in marked contrast to the magnetic properties of isostructural LiTi₂O₄ which manifests a comparatively temperature independent Pauli paramagnetism and superconductivity ($T_c \leq 13.7$ K) [4].

Strong electron correlations in LiV₂O₄ were inferred by Fujimori *et al.* [75, 76] from their ultraviolet (UPS) and x-ray (XPS) photoemission spectroscopy measurements. An anomalously small density of states at the Fermi level was observed at room temperature which they attributed to the effect of long-range Coulomb interactions. They interpreted the observed spectra assuming charge fluctuations between d^1 (V⁴⁺) and d^2 (V³⁺) configurations on a time scale longer than that of photoemission ($\sim 10^{-15}$ sec). Moreover, the intra-atomic Coulomb interaction energy, U , was found to be ~ 2 eV. This value is close to the calculated width of the t_{2g} conduction band for LiTi₂O₄, $W \sim 2$ eV [77]. From these observations, one might infer that $U \sim W$ for LiV₂O₄, suggesting possible proximity to a metal-insulator transition.

Table 1.5 Lattice parameter a_0 , oxygen parameter u , and magnetic parameters χ_0 , C and θ reported in the literature for LiV_2O_4 . The u values are shown using the second setting for the space group $Fd\bar{3}m$ from the *International Tables for Crystallography, Vol. A*. [68] The "T range" is the temperature range over which the fits to the susceptibility data were done. χ_0 is the temperature-independent contribution. C is the Curie constant and θ is the Weiss temperature. The error in the last digit of a quantity is given in parentheses. Unless otherwise noted, all measurements were done on polycrystalline samples.

a_0 (Å)	u	T range (K)	χ_0 ($10^{-6} \frac{\text{cm}^3}{\text{mol LiV}_2\text{O}_4}$)	C ($\frac{\text{cm}^3 \text{K}}{\text{mol V}}$)	θ (K)	Ref.
8.22						[78]
8.2403(12)	0.260(1)					[79]
8.240(2)						[80]
8.22		4.2-308	37	0.468	-63	[5]
8.240(2)	0.253(1)					[81]
8.25 ^a						[82]
8.255(6)	0.260	50-380 ^a	37	0.460	-34	[7]
		50-380 ^a	37	0.471	-42	[7] ^b
		80-300	43	0.441 ^a	-31 ^a	[8]
8.241(3) ^a		80-300	43	0.434 ^a	-39 ^a	[9]
				0.473		[6]
8.235		10-300	0	0.535	-35.4	[2]
8.2408(9)		100-300	230	0.35	-33	[83]

^aThis value was digitized from the published figure.

^bSingle crystal susceptibility data, corrected for the contribution of 10% V_4O_7 .

2 Overview of LiV_2O_4 : A HEAVY FERMION TRANSITION METAL OXIDE

The text of a paper published in Physical Review Letters¹

S. Kondo,² D. C. Johnston,² C. A. Swenson,² F. Borsa,² A. V. Mahajan,^{2,3} L. L. Miller,² T. Gu,²
 A. I. Goldman,² M. B. Maple,⁴ D. A. Gajewski,⁴ E. J. Freeman,⁴ N. R. Dilley,⁴ R. P. Dickey,⁴
 J. Merrin,⁵ K. Kojima,⁵ G. M. Luke,⁵ Y. J. Uemura,⁵ O. Chmaissem,^{6,7} and J. D. Jorgensen⁷

Abstract

A crossover with decreasing temperature T from localized moment magnetism to heavy Fermi liquid behavior is reported for the metallic compound LiV_2O_4 with the fcc normal-spinel structure. At $T = 1$ K, the electronic heat capacity coefficient $\gamma \approx 0.42 \text{ J/mol K}^2$ is exceptionally large for a transition metal compound, the Wilson ratio ≈ 1.7 and the Korringa ratio ≈ 0.7 . Our sample with the lowest level of paramagnetic defects showed no static magnetic order above 0.02 K. Superconductivity was not observed above 0.01 K.

Introduction

The current interest in highly correlated electron systems has been sparked by several discoveries: These include f -electron intermetallics with heavy Fermi liquid (FL) ground states [heavy fermion (HF) compounds] [33, 35] or non-FL ground states [84], and high T_c cuprate superconductors. The above HF f -electron compounds (e.g., CeAl_3 , UPt_3) have enormous electronic heat capacity coefficients $\gamma(T) \equiv C(T)/T \sim 1 \text{ J/mol K}^2$, where $C(T)$ is the electronic heat capacity, from which quasiparticle

¹ Reprinted with permission of Phys. Rev. Lett. **78**, 3729 (1997).

² Ames Laboratory and Department of Physics and Astronomy, Iowa State University, Ames, Iowa 50011

³ Permanent address: Department of Physics, Indian Institute of Technology, Powai, Bombay 400076, India

⁴ Department of Physics and Institute for Pure and Applied Physical Sciences, University of California at San Diego, La Jolla, California 92093

⁵ Physics Department, Columbia University, New York, New York 10027

⁶ Science and Technology Center for Superconductivity, Argonne National Laboratory, Argonne, Illinois 60439

⁷ Materials Science Division, Argonne National Laboratory, Argonne, Illinois 60439

effective masses of several hundred times the free electron mass have been inferred. In this Letter, we report the discovery of HF behavior in the transition metal oxide LiV_2O_4 . To our knowledge, this is the first report of a d -electron material exhibiting HF behavior characteristic of those of the heaviest-mass f -electron systems. In such systems a high and narrow (~ 10 meV) peak occurs at low T in the quasiparticle density of states \mathcal{D} near the Fermi energy E_F , a many-body effect [33, 35]. The large $\mathcal{D}(E_F)$ is reflected in a large nearly T -independent magnetic spin susceptibility χ^{spin} and γ compared with the respective predictions of conventional band structure calculations [33, 35]. The normalized ratio of these two quantities, the Wilson ratio R_W , is on the order of unity as in conventional metals (FLs), where $R_W \equiv \pi^2 k_B^2 \chi^{\text{spin}} / 3\mu_B^2 \gamma$. k_B is Boltzmann's constant and μ_B is the Bohr magneton. However, at higher T the $\mathcal{D}(E)$ peak height decreases strongly [33, 35], on the scale of a low characteristic temperature ~ 1 –100 K. This results in a corresponding strong decrease in γ with T , as we observe for LiV_2O_4 above ~ 4 K, but which is not observed for conventional metals or, to our knowledge, reported for any metallic oxide in which γ is enhanced by proximity to a metal-insulator phase boundary.

LiV_2O_4 is metallic [3] with the fcc normal-spinel structure [78, 79], containing equivalent V ions in slightly distorted octahedral coordination by O. LiV_2O_4 manifestly exhibits strong electron correlations (local moment magnetism). The magnetic susceptibility $\chi(T)$ (4.2–308 K) was found to be the sum of a T -independent term $\chi_0 = 0.4 \times 10^{-4} \text{ cm}^3/\text{mol}$ and a Curie-Weiss term $C/(T - \theta)$ due to local V magnetic moments [2, 5, 6]. The Curie constant C is consistent with a V^{+4} spin $S = 1/2$ with g -factor 2.23. The negative Weiss temperature $\theta = -63$ K indicates antiferromagnetic (AF) V spin interactions. However, no evidence for magnetic ordering above 4.2 K was found. The local moment behavior strongly contrasts with the relatively T -independent Pauli paramagnetism and superconductivity ($T_c \leq 13.7$ K) of isostructural LiTi_2O_4 [4]. Band structure calculations for LiTi_2O_4 yield a t_{2g} conduction band width $W \sim 2$ eV [77]. Photoemission measurements on LiV_2O_4 revealed strongly correlated electron behavior with a V intra-atomic Coulomb repulsion parameter $U \sim 2$ eV $\sim W$ [75]. The nature of the ground state is unknown up to now.

We carried out crystallography, electrical resistivity ρ , magnetization M , heat capacity C_p , ^7Li nuclear magnetic resonance NMR and positive-muon spin relaxation (μSR) measurements on LiV_2O_4 . We report a crossover with decreasing T from the local moment behavior to heavy FL behavior. We find an enormous $\gamma(1 \text{ K}) \approx 0.42 \text{ J/molK}^2$, much larger than those of other metallic transition metal compounds, e.g., $\text{Y}_{1-x}\text{Sc}_x\text{Mn}_2$ ($\lesssim 0.2 \text{ J/molK}^2$ [16]) and V_{2-y}O_3 ($\lesssim 0.07 \text{ J/molK}^2$ [85]). The magnitudes and T -dependences of γ and χ and the T -dependence of ρ [3] for LiV_2O_4 are remarkably similar to those of the HF f -electron superconductor UPt_3 ($T_c = 0.54$ K) [33, 35, 39, 86, 87]. We infer that

paramagnetic defects seen in $\chi(T)$ can strongly influence the $C_p(T)$ and spin dynamics of LiV_2O_4 below 1 K.

Sample preparations

Polycrystalline LiV_2O_4 samples were made using techniques in [4] and were single-phase or very nearly so by x-ray and neutron diffraction. Neutron diffraction measurements were carried out at the Intense Pulsed Neutron Source at Argonne National Laboratory. $M(H, T)$ data (H = applied magnetic field) were obtained with SQUID and Faraday magnetometers at Ames and La Jolla, and $C_p(H, T)$ data using heat-pulse calorimeters at Ames and La Jolla. ^7Li NMR measurements were done at 17 and 135 MHz with a pulse Fourier transform spectrometer: the recovery of the nuclear magnetization, measured by the echo signal after a saturating radio frequency pulse sequence, was exponential. μSR time spectra in zero and longitudinal H were obtained at TRIUMF.

X-ray and neutron diffraction measurements

X-ray and neutron diffraction data on three LiV_2O_4 samples revealed no distortion from the spinel structure (space group $Fd3m$) between 295 and 9 K. Rietveld refinements of the neutron data for sample 5 yielded the lattice and oxygen parameters $a_0 = 8.23932(3)$ Å, $x = 0.26125(2)$ at 295 K and $a_0 = 8.22694(3)$ Å, $x = 0.26109(2)$ at 12 K. $\rho(T)$ measurements down to 0.01 K showed no evidence for superconductivity.

Magnetic susceptibility measurements

$\chi(T)$ data from 2 to 400 K are shown for LiV_2O_4 sample 1 in Fig. 2.1. Above ~ 50 K, Curie-Weiss-like behavior is seen as previously reported. We assumed that $\chi(T) = \chi_o + \chi_{\text{loc}}^{\text{spin}}(T)$, where $\chi_{\text{loc}}^{\text{spin}}(T)$ was the high- T series expansion to sixth order in $1/T$ of the $S = 1/2$ nearest-neighbor AF Heisenberg model for the V sublattice of the spinel structure [88]. The fit parameters depended on the T region of the fits as previously found assuming $\chi_{\text{loc}}^{\text{spin}}(T) = C/(T - \theta)$ [7, 89]. Our fit for the range 50–400 K (solid curve in Fig. 2.1) yielded $\chi_o = 0.57 \times 10^{-4} \text{ cm}^3/\text{mol}$, $g = 2.19$ and $\theta = -40$ K, similar to values cited above.

Contrary to previous reports [2, 5, 6], we find that $\chi(T)$ becomes nearly independent of T below ~ 30 K, with a shallow broad maximum at ≈ 16 K (Fig. 2.1 inset). Field-cooled and zero-field-cooled $M(H = 10 \text{ G}, T)$ data above 2 K showed no evidence for spin-glass ordering. A Curie-like C_{imp}/T upturn

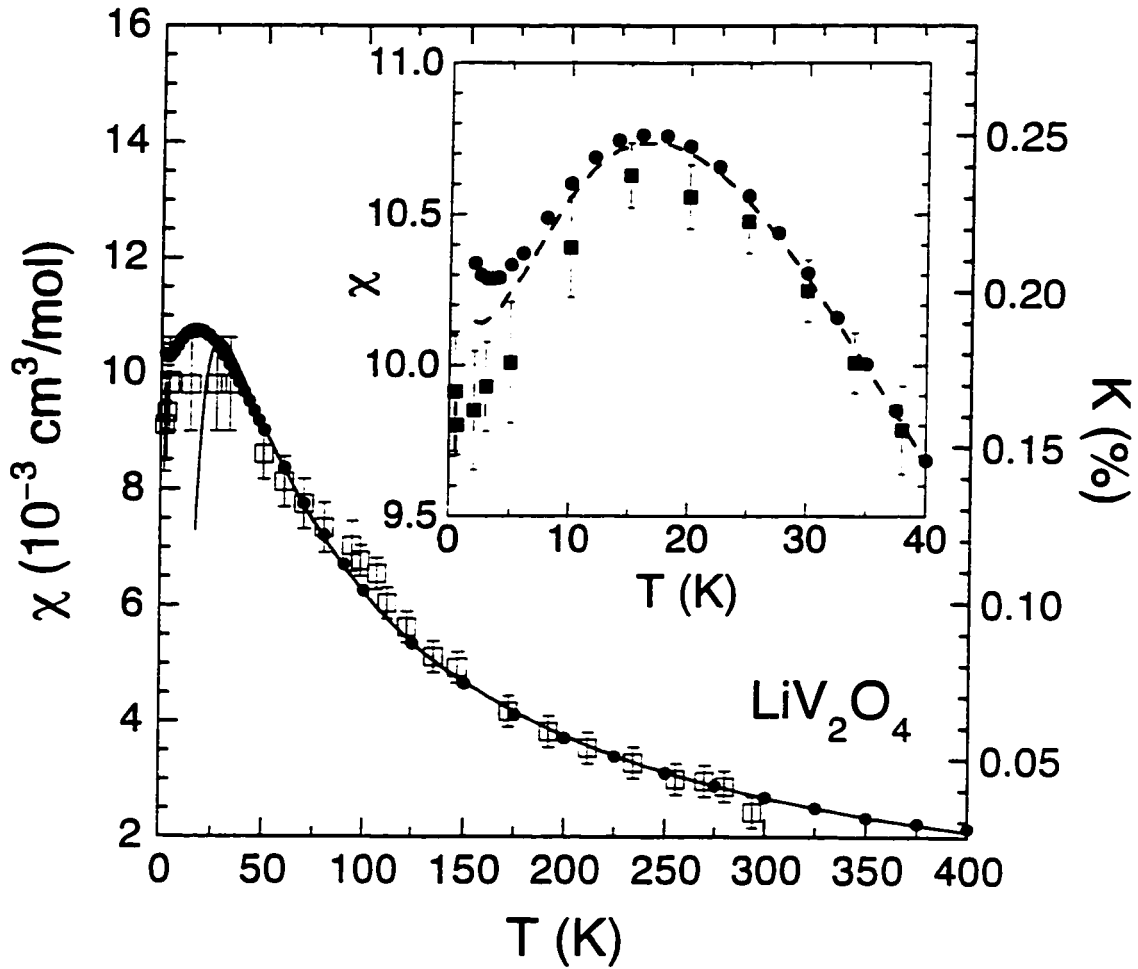


Figure 2.1 $\chi \equiv M/H$ ($H = 10 \text{ kG}$) vs. T for LiV_2O_4 sample 1 (\bullet) and ^7Li $K(T)$ for sample 2 (open squares, right-hand scale). The solid curve is a theoretical fit to $\chi(T)$ for $T > 50 \text{ K}$. The dashed curve and filled squares (inset) denote the intrinsic $\chi(T)$ of LiV_2O_4 inferred from $M(H, T)$ data for samples 1 and 4, respectively (see text).

in $\chi(T)$ is seen in Fig. 2.1 below ~ 5 K, found to be sample-dependent. $M(H \leq 55 \text{ kG})$ isotherms above 15 K were linear, but at 2 K exhibited negative curvature which increased with increasing C_{imp} in various samples, indicating that this curvature and the Curie term arise from paramagnetic impurities/defects. The $M(H, T)$ data yielded the impurity $S_{\text{imp}} \approx 2$ and $g_{\text{imp}} \approx 2$, with concentrations 0.03, 0.35, 0.15, 0.08, and 0.70 mol% in samples 1–5, respectively. The intrinsic $\chi(T)$ for LiV_2O_4 inferred by subtracting the impurity contributions in samples 1 and 4 is shown in the inset of Fig. 2.1, where $\chi(0.4\text{--}2 \text{ K}) = 0.0100(2) \text{ cm}^3/\text{mol}$.

^7Li nuclear magnetic resonance measurements

The ^7Li $K(T)$ (Fig. 2.1) approximately scales linearly with $\chi(T)$ as found above 30 K in [2, 90]. $1/T_1(T)$ (Fig. 2.2) shows an unusual maximum (at 30–50 K), also seen in ^{27}Al $1/T_1(T)$ for the HF compound CeAl_3 [91] with $\gamma \sim 1.6 \text{ J/molK}^2$ [33, 35], evidently reflecting the crossover from FL (low T) to local moment (high T) behaviors. From Fig. 2.2 inset, $1/T_1 \approx (2.4 \text{ sec}^{-1} \text{ K}^{-1})T$. From Fig. 2.1, $K(T)$ is nearly constant ($\approx 0.17\%$) below 30 K. Thus, the Korringa ratio $K^2 T_1 / S_{\text{Li}}$, where $S_{\text{Li}} = 1.74 \times 10^{-5} \text{ sec K}$, is constant (≈ 0.7) below 4 K. These low- T observations are consistent with expectations for a FL. Our 1.6–4.2 K value of ^7Li $1/T_1 T$ in LiV_2O_4 is a factor of ~ 6000 greater than that in LiTi_2O_4 [92, 93], implying an enhancement of the dressed density of states $\mathcal{D}(E_F)$ by a factor $\sqrt{6000} \sim 80$. However, comparison of this ratio of 80 with the ratio ~ 20 of the $\gamma(1 \text{ K})$ values for the two compounds (below) suggests a difference in the ^7Li hyperfine coupling constants.

Heat capacity measurements

$C_p(T)$ data up to 80 K for LiV_2O_4 are shown in Fig. 2.3(a). Also shown are data for the isostructural nonmagnetic insulator $\text{Li}_{4/3}\text{Ti}_{5/3}\text{O}_4$ obtained to estimate the lattice contribution. After multiplying the T scale of $C_p(T)$ for $\text{Li}_{4/3}\text{Ti}_{5/3}\text{O}_4$ by 0.941 to take into account the different masses of $\text{Li}_{4/3}\text{Ti}_{5/3}\text{O}_4$ and LiV_2O_4 and subtracting this corrected lattice contribution from the data for LiV_2O_4 , the inferred electronic heat capacity $\Delta C_p(T)$ for LiV_2O_4 was obtained (inset). $\Delta C_p(T)$ shows a broad peak near 16 K, and a distinct additional contribution above ~ 25 K also seen in LiTi_2O_4 [94]. Figure 2.3(b) shows $\gamma(T) \equiv \Delta C_p(T)/T$ below 30 K, where a strong increase with decreasing T is observed. We obtain $\gamma(1 \text{ K}) \approx 0.42 \text{ J/molK}^2$, about twenty times larger than in LiTi_2O_4 [94]. Using $\chi^{\text{spin}}(1 \text{ K}) = 0.01 \text{ cm}^3/\text{mol}$, the Wilson ratio $R_W(1 \text{ K}) \approx 1.7$. These low- T results indicate heavy FL behavior [33, 35]. In this interpretation, the nearly T -independent $\chi(T)$ and $K(T)$ for $T \lesssim 30$ K in Fig. 2.1 is a reflection

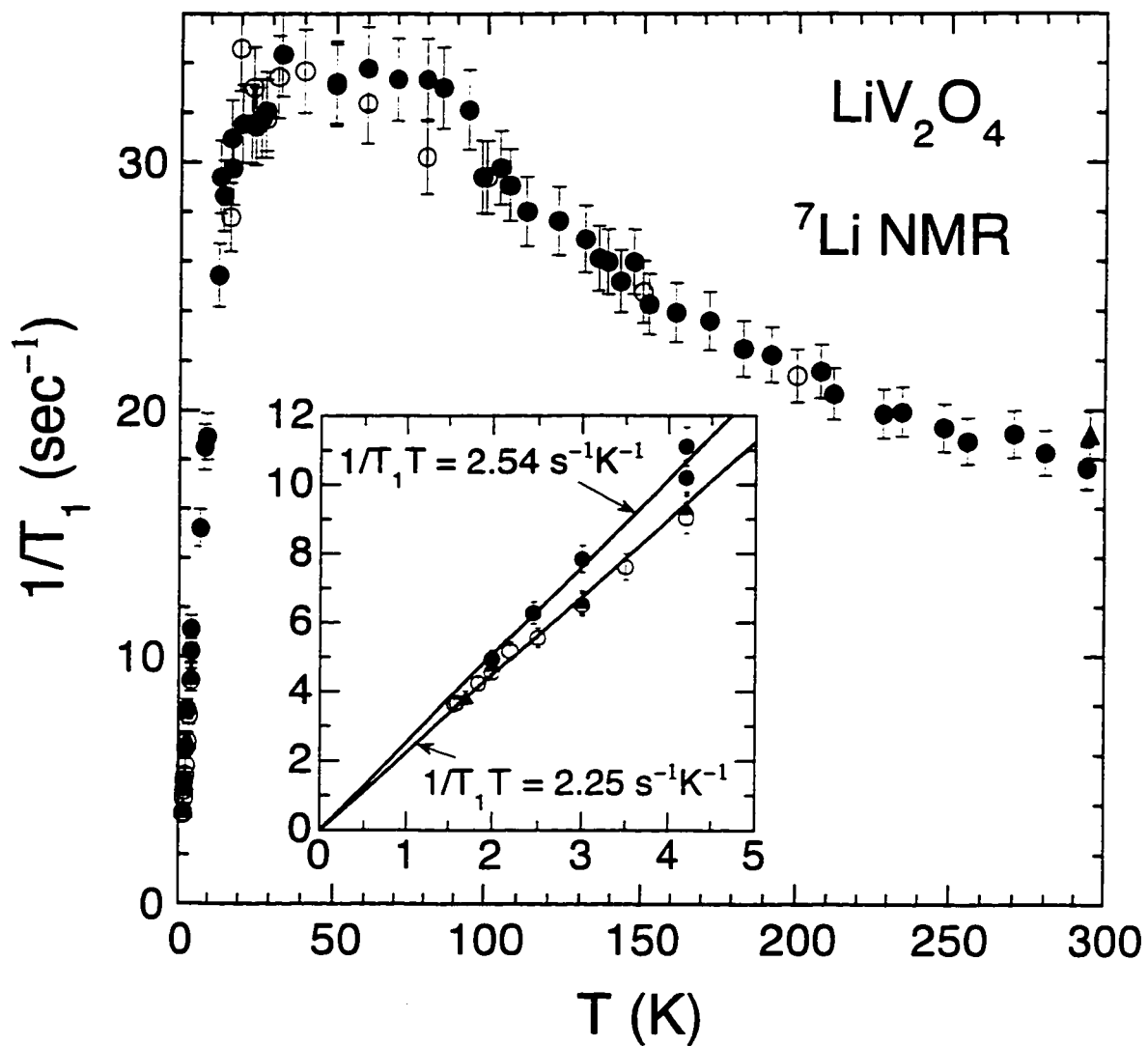


Figure 2.2 ${}^7\text{Li } 1/T_1$ vs. T for LiV_2O_4 samples 1 (filled triangles), 2 (\bullet) and 4 (\circ). The lowest- T data are shown in the inset, along with proportional fits.

of the disappearance of the V local moments.

$\gamma(T = 1.2\text{--}5\text{ K})$ for LiV_2O_4 was fitted by the prediction for the $S = 1/2$ Kondo model ($R_W = 2$) [33, 35], yielding a Kondo temperature $T_K = 27.5\text{ K}$ [solid curves in Figs. 2.3(a) inset and 2.3(b)]. This single-parameter fit extrapolated to higher T also describes well the $\Delta C_p(T)$ data up to $\sim 30\text{ K}$, including the magnitude and temperature of the broad maximum near 16 K [Fig. 2.3(a) inset]. A 1–10 K fit of $\gamma(T)$ by the FL prediction $\gamma(T) = \gamma(0) + \delta T^2 \ln(T/T_0)$ [33, 35] is shown by the short-dashed curve in Fig. 2.3(b), for which $\gamma(0) = 428\text{ mJ/molK}^2$, $\delta = 1.6\text{ mJ/molK}^4$ and $T_0 = 25\text{ K}$, parameters remarkably similar to those of UPt_3 [39, 86]. $\gamma(T)$ is also consistent with theory [95] for a three-dimensional AF-coupled quantum-disordered FL. A 1–10 K fit by the theory [long-dashed curve in Fig. 2.3(b)] gave parameters [95] $N = 3$, $\gamma_0 = 810\text{ mJ/molK}^2$, $r = 0.78$ and $T^* = 9.7\text{ K}$.

Low- T $\gamma(T)$ data and the above theoretical fits for LiV_2O_4 sample 3 are shown in Fig. 2.3(c). The data exhibit a plateau with $\gamma \approx 0.42\text{ J/molK}^2$ from $\sim 1.3\text{--}0.8\text{ K}$ and an upturn at lower T . The $\gamma(T)$ data in Fig. 2.3(c) for sample 5, which contains a higher level of magnetic defects (above), increase monotonically down to $\approx 0.5\text{ K}$ where the data appear to exhibit a maximum with value $\approx 0.6\text{ J/molK}^2$. Below $\sim 2\text{ K}$, $\gamma(T, H = 20\text{ kG})$ for sample 5 in Fig. 2.3(c) is suppressed relative to $\gamma(T, H = 0)$. The $H = 0$ results indicate that the presence of magnetic defects increases $C_p(T)$, especially at low T .

Muon spin relaxation measurements

Zero-field (ZF) μSR spectra for sample 1 exhibit a single-exponential decay $\exp(-t/T_1)$ (after correction for effects due to nuclear dipolar fields). $1/T_1$ at 20 mK in ZF and in longitudinal field LF = 50 G show little difference (see Fig. 2.4 inset), indicating that the depolarization is mostly due to fluctuating dynamic local fields. The average fluctuation rate at 20 mK , obtained from the LF dependence, is $\nu \sim \gamma_\mu \times 150\text{ G} \sim 12\ \mu\text{s}^{-1}$, where γ_μ is the positive muon (μ^+) gyromagnetic ratio. The instantaneous random local field H_r inferred from $1/T_1 \sim (\gamma_\mu H_r)^2/\nu$ is then $H_r \sim 30\text{ G}$. This H_r is about 50 times smaller than $H_r \sim 1.5\text{ kG}$ which we observed in the AF state of isostructural ZnV_2O_4 , suggesting that H_r in LiV_2O_4 sample 1 is due to dilute (% level) paramagnetic impurities. The $1/T_1(T)$ in Fig. 2.4 indicates slowing down of impurity spin fluctuations with decreasing T , yet we found no signature of static spin freezing in sample 1 down to 20 mK . In contrast, the ZF- μSR spectra in sample 3 (with a larger Curie term in χ) showed two-component relaxation below $T \sim 0.8\text{ K}$, with a fast 2/3 component and slow 1/3 component, characteristic of static spin freezing. This behavior correlates with the C_p anomaly at $T \sim 0.8\text{ K}$ observed for sample 3 in Fig. 2.3(c). Unfortunately, $1/T_1$ for μ^+ due to itinerant HF quasiparticles, as inferred from NMR in Fig. 2.2, is not clearly visible in Fig. 2.4, overshadowed by

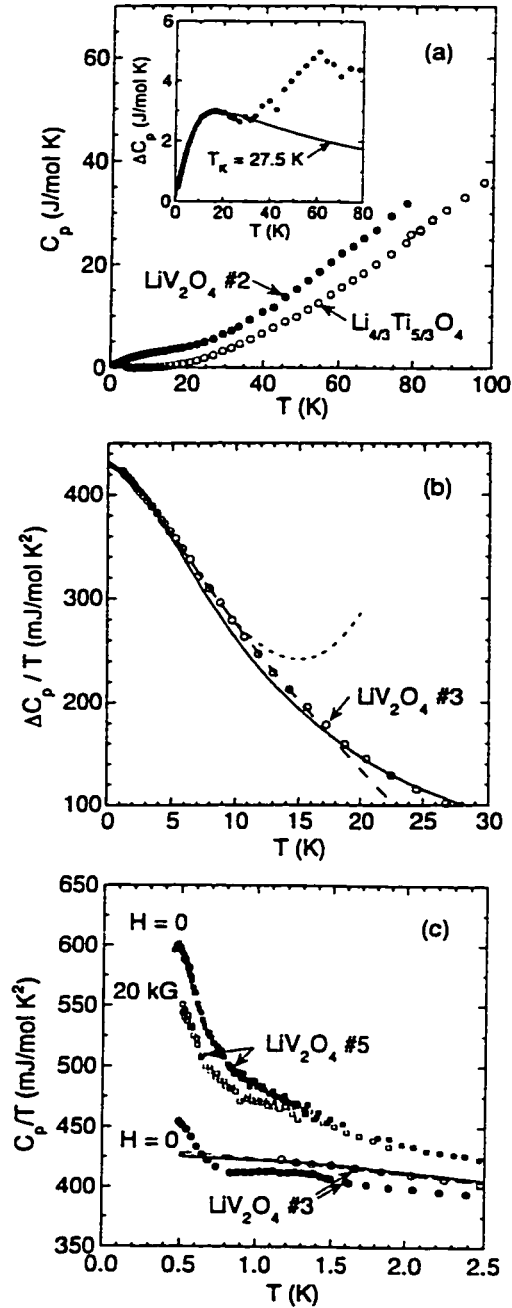


Figure 2.3 (a) Heat capacity C_p vs. temperature T for LiV_2O_4 sample 2 (\bullet) and $\text{Li}_{4/3}\text{Ti}_{5/3}\text{O}_4$ (\circ). Inset: electronic contribution $\Delta C_p(T)$ for sample 2 (\bullet). The solid curve is a 1–5 K fit by Kondo theory. (b) $\Delta C_p(T)/T \equiv \gamma(T)$ for sample 3 below 30 K (\circ) (the data for samples 2 and 3 are nearly identical). (c) $\gamma(T \leq 2.5$ K) data for sample 3 from Ames [\circ from (b)] and La Jolla (\bullet), and for sample 5 at $H = 0$ and 20 kG from La Jolla (squares). The curves in (b) and (c) are fits to the Ames data for sample 3 above 1.2 K by theories for Fermi liquids (see text).

the depolarization due to fluctuating/freezing local fields. However, this is not surprising in view of the unobservably small $1/T_1$ for μ^+ in the HF compounds UPt_3 [96] and UBe_{13} .

Conclusion

In conclusion, our $\chi(T)$, $C_p(T)$ and ^7Li NMR measurements on LiV_2O_4 demonstrate a crossover with decreasing T from localized moment to heavy FL behavior, with a Kondo or spin-fluctuation temperature $T_K \sim 28\text{K}$. The $\rho(T)$ data show a pronounced smooth downturn below $\sim 30\text{K}$ [3], consistent with Kondo lattice behavior in which the onset of electronic coherence below T_K reduces ρ [33, 35]. $\rho(T)$ data on single crystals at low $T \lesssim 4\text{K}$ are needed to test whether a T^2 temperature dependence is observed as expected for a FL. The geometric frustration for AF ordering inherent in the V sublattice of the spinel structure may help to destabilize the local moments in LiV_2O_4 at low T [16] and lead to the FL behavior.

Note added.— Ueda *et al.* and Fujiwara *et al.*, respectively, have independently obtained $\chi(T)$ and ^7Li NMR data on LiV_2O_4 [83, 97] similar to ours.

Acknowledgements We thank K. H. Kim and R. Sala for assistance with the NMR measurements and Z. Fisk, R. J. Gooding, A. J. Millis, J. Röhler and C. M. Varma for helpful discussions. Ames Laboratory is operated for the U.S. Department of Energy (USDOE) by Iowa State University under Contract No. W-7405-Eng-82. The work at Ames was supported by the Director for Energy Research, Office of Basic Energy Sciences (BES), at UCSD by the USDOE under Grant No. DE-FG03-86ER-45230, at Columbia by Grants NSF-95-10454, NSF-DMR-95-10453 and a NEDO International Joint Research Grant (Japan), and at Argonne by the NSF Office of Science and Technology Centers, Grant No. DMR 91-20000 (O.C.) and the USDOE, BES, Division of Materials Sciences, Contract No. W-31-109-ENG-38 (J.D.J. and operation of the IPNS).

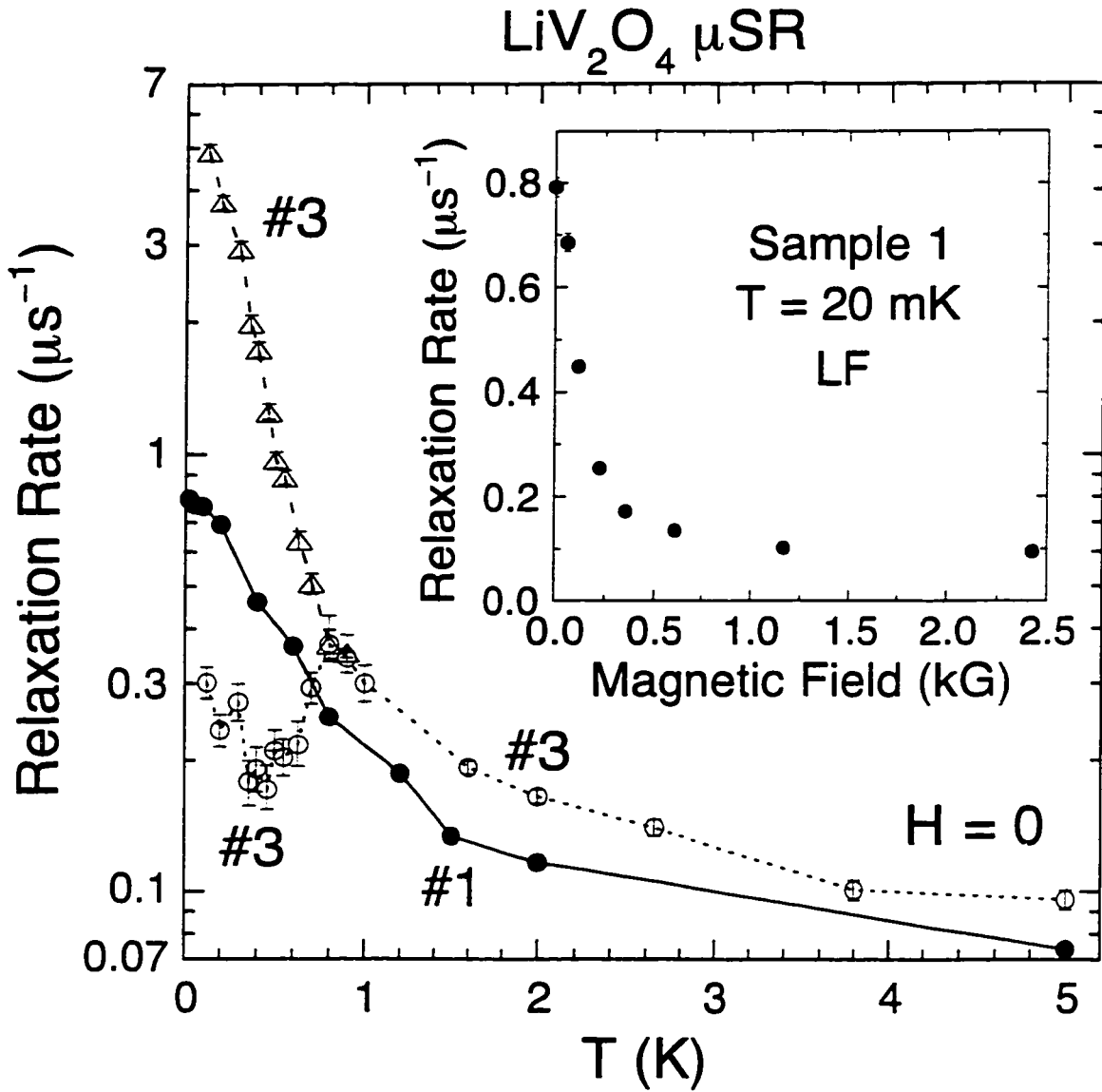


Figure 2.4 Muon spin relaxation (μSR) rate in LiV_2O_4 obtained in $H = 0$ vs. temperature T (main figure) and vs. longitudinal field (LF) at $T = 20$ mK (inset). Rates for sample 1 at all T and LF (\bullet) and sample 3 for $T \gtrsim 0.8$ K (\circ) represent $1/T_1$ in fits of the μSR time t spectra by $\exp(-t/T_1)$, while two rates for sample 3 for $T \lesssim 0.8$ K represent $1/T_2$ (Δ) and $1/T_1$ (\circ) in fits by $0.67 \exp(-t/T_2) + 0.33 \exp(-t/T_1)$.

3 SYNTHESIS AND CHARACTERIZATION

Synthesis of LiV_2O_4 and $\text{Li}_{1+x}\text{Ti}_{2-x}\text{O}_4$ ($x = 0$ and $1/3$)

LiV_2O_4 preparations

Polycrystalline samples of LiV_2O_4 were prepared using conventional solid-state reaction techniques with two slightly different paths to the products. The five samples used in the paper by Kondo *et al.* (samples 1 through 5) (see Chapter 2) [11] were prepared by the method in [4]. Two additional samples (samples 6 and 7) were synthesized by the method of Ueda *et al* [83]. Different precursors are used in the two methods: “ $\text{Li}_2\text{VO}_{3.5}$ ” (see below) and Li_3VO_4 , respectively. Both methods successfully yielded high-quality LiV_2O_4 samples which showed a broad peak in the observed susceptibility $\chi^{\text{obs}}(T)$ at ≈ 16 K. Here only the first synthesis method is explained in detail, and the reader is referred to [83] for details of the second method.

The starting materials were Li_2CO_3 (99.999%, Johnson Matthey), V_2O_3 , and V_2O_5 (99.995%, Johnson Matthey). Oxygen vacancies tend to be present in commercially obtained V_2O_5 [98]. Therefore, the V_2O_5 was heated in an oxygen stream at 500-550 °C in order to fully oxidize and also dry it. V_2O_3 was made by reduction of either V_2O_5 or NH_4VO_3 (99.995%, Johnson Matthey) in a tube furnace under 5% H_2 /95% He gas flow. The heating was done in two steps: at 635 °C for ≈ 1 day and then at 900-1000 °C for up to 3 days. The oxygen content of the nominal V_{2-y}O_3 obtained was then determined by thermogravimetric analysis (TGA, see below). The precursor “ $\text{Li}_2\text{VO}_{3.5}$ ” (found to be a mixture of Li_3VO_4 and LiVO_3 from an x-ray diffraction measurement) was prepared by heating a mixture of Li_2CO_3 and V_2O_5 in a tube furnace under an oxygen stream at ≈ 525 °C until the expected weight decrease due to the loss of carbon dioxide was obtained. Ideally the molar ratio of Li_2CO_3 to V_2O_5 for the nominal composition $\text{Li}_2\text{VO}_{3.5}$ is 2 to 1. A slight adjustment was, however, made to this ratio according to the actual measured oxygen content of the V_{2-y}O_3 ($y \simeq 0.005$ to 0.017) so that the final product is stoichiometric LiV_2O_4 . This precursor and V_{2-y}O_3 were ground thoroughly inside a helium-filled glovebox. The mixture was then pelletized, wrapped in a piece of gold foil, sealed into a quartz

tube under vacuum, and heated between 570 °C and 700 °C for $\lesssim 2$ weeks. The as-prepared samples were all removed from the oven at the final furnace temperature and air-cooled to room temperature. For samples 2 and 3 additional heating at a higher $T = 750$ °C was given (with a repeated sequence of grinding, repelletizing and reheating for sample 2). From ≈ 725 °C different methods of cooling, liquid-nitrogen or ice-water quenching or slow-oven cooling, were applied to pieces from sample 2, yielding samples 4, 4A and 4B, respectively.

LiTi₂O₄ and Li_{4/3}Ti_{5/3}O₄ preparations

Polycrystalline LiTi₂O₄ and Li_{4/3}Ti_{5/3}O₄ samples were synthesized in essentially the same way as for LiV₂O₄, using solid-state reaction techniques [4]. TiO₂ (Johnson Matthey, 99.99%) was dried under a pure oxygen stream at 900 °C before use. This was mixed with Li₂CO₃ (Alfa, 99.999%) in an appropriate ratio to produce either Li_{4/3}Ti_{5/3}O₄ or a precursor "LiTiO_{2.5}" for LiTi₂O₄. The mixture was then pressed into pellets, and heated at 670 °C in a pure oxygen atmosphere for ≈ 1 day. The weight loss due to release of CO₂ was within 0.04 wt.% of the theoretical value for LiTiO_{2.5}. However, for Li_{4/3}Ti_{5/3}O₄ additional firings at higher temperatures (up to 800 °C), after being reground and repelletized, were necessary. LiTi₂O₄ was prepared by heating pressed pellets of a ground mixture of the LiTiO_{2.5} precursor and Ti₂O₃ in an evacuated and sealed quartz tube at 700 °C for one week and then air-cooling. The Ti₂O₃ was prepared by heating a mixture of TiO₂ and titanium metal powder (Johnson Matthey) at 1000 °C for one week in an evacuated and sealed quartz tube.

Characterization

Using a Rigaku Geigerflex diffractometer with a curved graphite crystal monochromator, x-ray diffraction patterns were obtained at room temperature with Cu K α radiation. Rietveld analyses of the diffraction patterns were carried out using the angle-dispersive x-ray diffraction version of the RIETAN-973 program [99].

TGA measurements were done using a Perkin-Elmer TGA 7 Thermogravimetric Analyzer. Oxygen contents of the samples were calculated from weight gains after heating in an oxygen flow to 540-600 °C for LiV₂O₄ and 620 °C for V_{2-y}O₃, assuming that the oxidized products contained vanadium as V⁺⁵.

X-ray diffraction measurement results

X-ray diffraction patterns of our LiV₂O₄ samples revealed that the samples were single-phase or very nearly so. Figure 3.1 shows the diffraction pattern of sample 7 which has no detectable impurities. The

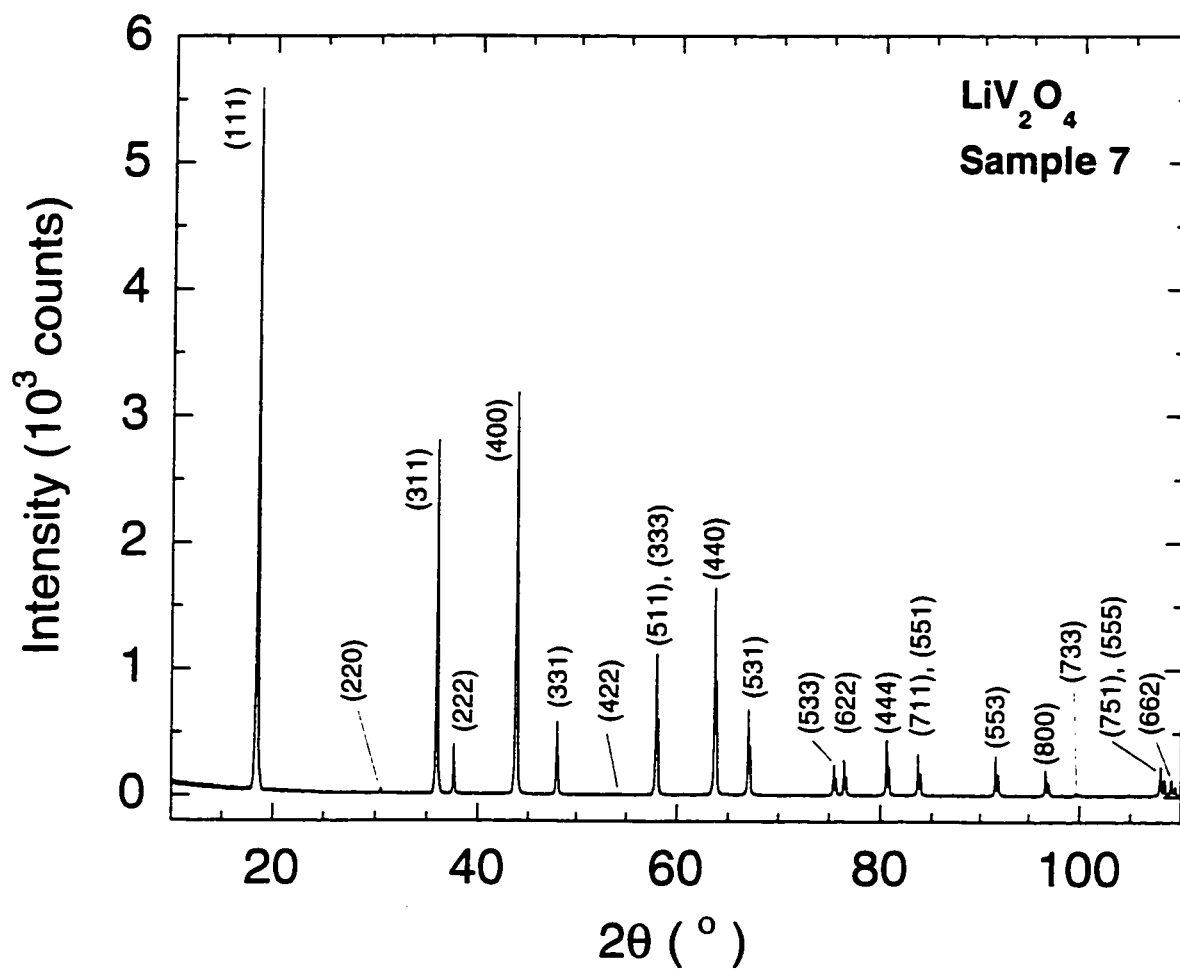


Figure 3.1 X-ray diffraction pattern of LiV₂O₄ sample 7. The spinel-phase peaks are indexed as shown.

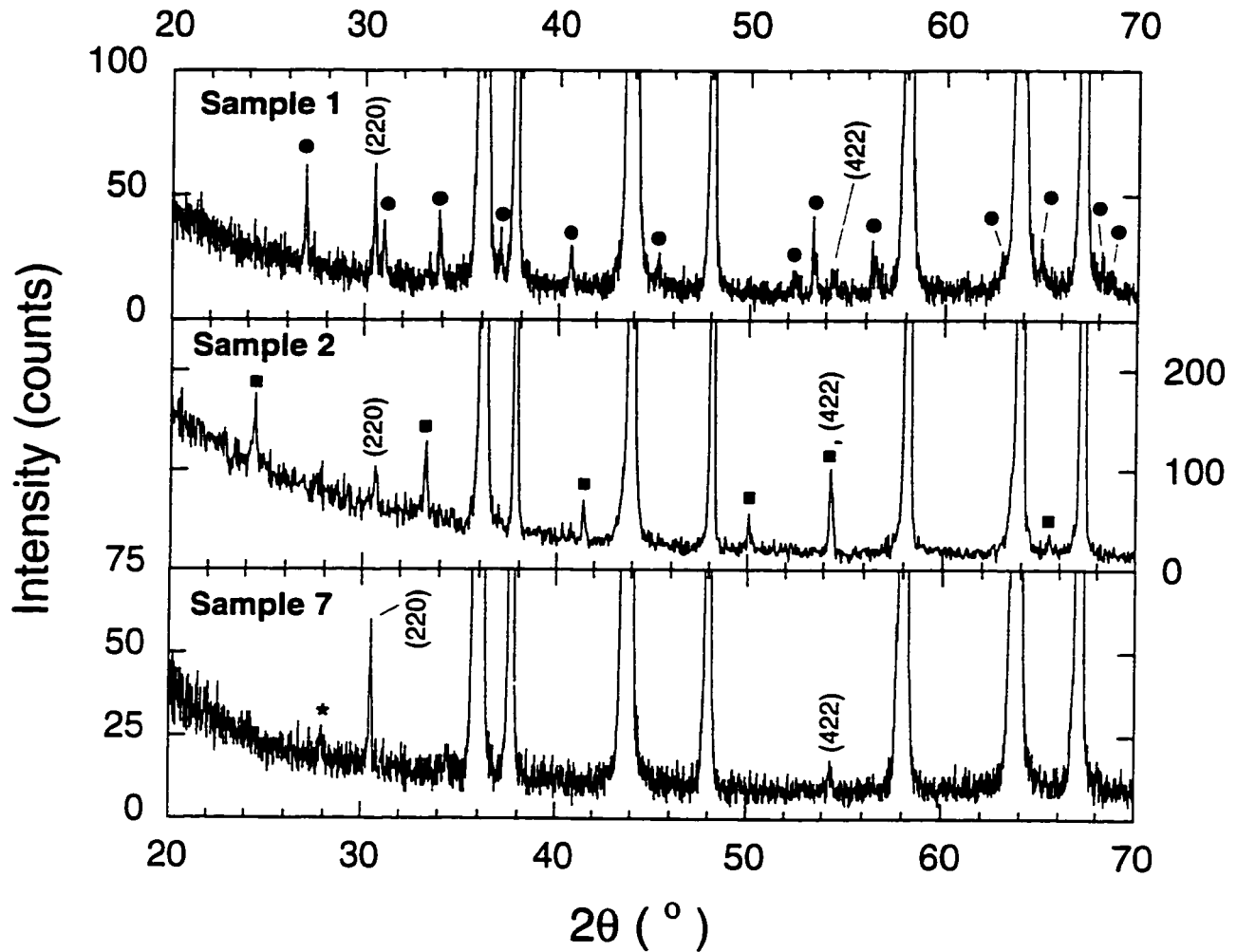


Figure 3.2 Expanded plots of the X-ray patterns of samples 1 (top), 2 (middle) and 7 (bottom). Indexed peaks are those of LiV_2O_4 spinel phase. Sample 1 has V_3O_5 impurity (filled circles), whereas sample 2 has V_2O_3 impurity (filled squares). Sample 7 has no impurity peaks except possibly the very weak unidentified one marked with a star.

nine samples described in detail in this dissertation are categorized into three groups in terms of purity: essentially impurity-free (samples 3 and 7), V_3O_5 impurity (samples 1, 4 and 6) and V_2O_3 impurity (samples 2, 4A, 4B and 5). The presence of these impurity phases is detected in magnified views of the diffraction patterns as shown in Fig. 3.2. The powerful structural refinement method “Rietveld analysis” is introduced to some extent in the next section. The refinements were carried out for all nine LiV_2O_4 samples and two Ti spinel samples, and the results for the different samples are discussed and compared.

Introduction of Rietveld analyses

Introduction

The so-called Rietveld method was introduced by Dr. Rietveld in the 1960s [100, 101]. The real potential power of the method was not realized until years after his invention. The history of the method and its versatility are detailed in an excellent review entitled *The Rietveld Method* [102]. The discovery and the subsequent intense investigation of high-temperature superconductors helped the method to prevail as the necessary tool for structure analysis studies among solid-state physicists all over the world. It had been thought that powder-sample diffraction data could not give as much information as single-crystal data. However, in combination with the Rietveld method, powder-sample data were able to show its superiority for some cases. For example, in the early stage of studying the high-temperature superconductor $YBa_2Cu_3O_{7-\delta}$, the sample quality was not very good, because it had two phases (superconducting orthorhombic and non-superconducting tetragonal phases). It was the powder neutron diffraction data analyzed by the Rietveld method that revealed for the first time that the distribution of oxygen and its occupancy at the copper-oxygen plane cause the creation of the two different phases in the compound [103]. Meanwhile, a single-crystal X-ray diffraction study on the same compound failed to identify the important role of oxygen in the one-dimensional copper-oxygen chain, mainly because of the presence of twin structure in the crystal [104]. The appreciation of the Rietveld method and the development of one of the Rietveld method programs, RIETAN [99], are reviewed by Izumi [105].

Some basics of the Rietveld method

In a typical angle-dispersive, fixed-wavelength X-ray powder diffraction measurement, thousands of data points are collected in steps of 2θ (Bragg) angle, normally 0.01° to 0.05° . For many simple analysis methods, only the peak angles are utilized to identify the structure of a sample. The strong advantage

of the Rietveld method was due to its capability of distinguishing structure parameters in greater detail. Moreover, it makes use of an entire diffraction pattern: in other words, it uses *all* data points including background signals for analyses. For instance, in this work with LiV_2O_4 it was important to have some knowledge of the oxygen parameter u . A few, rather simple computer programs for structure refinements that were tried required the parameter u as an input. Hence, it would be tedious to iterate the whole process by trial-and-error to narrow down possible values of u in such programs.

In the following section, some basics of the Rietveld method are introduced, which essentially follow the discussions by Young [102] and Izumi [106].

The principle of the method is to minimize the weighted sum of squared residuals

$$S_{\text{Riet}}(\vec{x}) = \sum_i w_i [y_i - f_i(\vec{x})]^2 \quad . \quad (3.1)$$

by altering variable parameters (x_1, x_2, \dots) in \vec{x} , where i is a data point number, w_i the weight equal to $1/y_i$, y_i the observed intensity, and f_i the calculated intensity for the i -th point. The calculated intensity is then defined as the sum of Bragg reflection and background terms like the following model function

$$f_i = \Phi(2\theta_i) A(2\theta_i) s \sum_K m_K |F_K|^2 P_K L(2\theta_K) \phi(2\theta_i - 2\theta_K) + y_b(2\theta_i) \quad . \quad (3.2)$$

where $\Phi(2\theta_i)$ is the incident intensity, $A(2\theta_i)$ the absorption factor, s the scale factor, K the Miller indices for a Bragg reflection, m_K the multiplicity, F_K the structure factor, P_K the preferred orientation function, $L(2\theta_K)$ the Lorentz and polarization factors, and $\phi(2\theta_i - 2\theta_K)$ the profile function. The structure factor for a reflection with Miller indices $K = hkl$ is defined by

$$F_K = \sum_j g_j f_j T_j \exp[2\pi i(hx_j + ky_j + lz_j)] \quad . \quad (3.3)$$

where j is the site number, g_j the occupancy, f_j the atomic scattering factor, T_j the temperature factor, and x_j , y_j and z_j the fractional coordinates. The temperature factor for the isotropic thermal displacement case is

$$T_j = \exp\left[-B_j \left(\frac{\sin \theta_K}{\lambda}\right)^2\right] \quad . \quad (3.4)$$

where B_j is the isotropic thermal-displacement parameter. The absorption factor $A(2\theta_i)$ is constant for a typical X-ray diffractometer with a flat sample (so-called Bragg-Brentano type), so it is irrelevant for the refinement processes. The Lorentz-polarization factor $L(2\theta_K)$ is

$$L(2\theta_K) = \frac{1 + \cos^2 2\zeta \cos^2 2\theta_K}{\sin 2\theta_K \sin 2\theta_K} \quad , \quad (3.5)$$

when a monochromator is employed and ζ is the diffraction angle of the monochromator.

Most of the Rietveld method programs adopt either the pseudo-Voigt function [107, 108] or the Pearson VII function [109] for the profile function ϕ . The Rietveld-method computer program utilized in this work is RIETAN-97 β by Dr. Izumi at the National Institute for Research in Inorganic Materials (NIRIM) in Japan [99, 110]. His RIETAN-97 β program utilizes the pseudo-Voigt function of Thompson, Cox and Hastings [107] which is a combination of the Lorentz (ϕ_L) and Gaussian functions (ϕ_G) with the fraction η of the former.

$$\begin{aligned}\phi(\delta 2\theta) &= \eta\phi_L(\delta 2\theta) + (1 - \eta)\phi_G(\delta 2\theta) \\ &= \eta \frac{2}{\pi H_K} \left[1 + 4 \left(\frac{\delta 2\theta}{H_K} \right)^2 \right]^{-1} + (1 - \eta) \frac{2\sqrt{\ln 2}}{\sqrt{\pi} H_K} \exp \left[-4 \ln 2 \left(\frac{\delta 2\theta}{H_K} \right)^2 \right] .\end{aligned}\quad (3.6)$$

where η is given by Thompson *et al.* [107]

$$\eta = 1.36603 \left(\frac{H_{KL}}{H_K} \right) - 0.47719 \left(\frac{H_{KL}}{H_K} \right)^2 + 0.11116 \left(\frac{H_{KL}}{H_K} \right)^3 .\quad (3.7)$$

where $\delta 2\theta = 2\theta_i - 2\theta_K$. H_K is the full-width-at-half-maximum (FWHM) of the profile function, and H_{KL} (H_{KG}) is the FWHM of the Lorentz (Gaussian) function. They numerically obtained the following relation among H_K , H_{KL} and H_{KG}

$$\begin{aligned}H_K &= (H_{KG}^5 + 2.69269H_{KG}^4 H_{KL} + 2.42843H_{KG}^3 H_{KL}^2 + 4.47163H_{KG}^2 H_{KL}^3 \\ &\quad + 0.07842H_{KG} H_{KL}^4 + H_{KL}^5)^{0.2} .\end{aligned}\quad (3.8)$$

Therefore, once H_{KG} and H_{KL} are determined, both η and H_K can be calculated by Eqs. (3.7 and 3.8). These two FWHMs can be represented in terms of physically meaningful parameters

$$H_{KG} = [8 \ln 2 (U \tan^2 \theta_K + V \tan \theta_K + W + P \sec^2 \theta_K)]^{\frac{1}{2}} ,\quad (3.9)$$

and

$$H_{KL} = (X + X_e \cos \phi_K) \sec \theta_K + (Y + Y_e \cos \phi_K) \tan \theta_K .\quad (3.10)$$

U , V and Y_e are parameters for microstrain broadening, which is proportional to $\tan \phi_K$ (ϕ_K is the angle between the scattering vector and the broadening axis). The crystalline size broadening is also taken into consideration in terms of X , X_e and P . Both X and Y are isotropic broadening parameters, whereas the corresponding symbols with the subscript e are anisotropic. V and W are diffractometer-dependent.

These profile functions are all symmetric with respect to $\delta 2\theta$. But due to several unavoidable reasons [106], the profile shape is normally asymmetric. This is particularly noticeable for low 2θ in which a lower- 2θ tail of a peak tends to be spread longer. This asymmetry is approximately corrected in

the program RIETAN-97 β by using the multi-term Simpson's rule integration [111]. This adjustment involves four refinable parameters (A_s , Z , D_s , and T_s), each of which has a physical meaning. The details of this adjustment are not described here, but are referred to in the original paper.

For preferred orientation functions, P_K , there are two types of functions available: Sasa-Uda [112, 113], and March-Dollase [114, 115] functions. The latter has superiority in overall performance for structural refinement [110].

The background function, $y_b(2\theta_i)$, in RIETAN-97 β is a finite sum of Legendre polynomials with a refinable parameter b_n for each term [110]. Up to 12 background parameters ($n = 1-12$) can be employed.

All the refinable parameters in the angle-dispersive version of RIETAN-97 β are tabulated in Table 3.1.

Table 3.1 Parameters that can be refined in the Rietveld analysis using RIETAN-97 β .

Parameters common to all phases	
1	Zero-point shift, Z
2	Specimen-displacement parameter, D_s
3	Specimen-transparency parameter, T_s
4	Background parameters, b_1, b_2, \dots, b_{12}
Parameters assigned to each phase	
5	Scale factor, s
6	Profile parameters, $U, V, W, P, X, X_e, Y, Y_e, A_s$
7	Preferred orientation parameter, r
8	Lattice parameters, $a, b, c, \alpha, \beta, \gamma$
9	Fractional coordinates, x_j, y_j, z_j
10	Thermal-displacement parameter, B_j^a

^aIn case of anisotropic thermal displacement cases, the six β_j .

The criteria used to judge the agreement between the observed and calculated intensities for the entire pattern are various R -factors listed in Table 3.2. R is very similar to the R -factor which is used in single-crystal structure analysis ($R = \sum[|F_o| - |F_c|] / \sum|F_o|$, where F_o and F_c are observed and calculated structure factors, respectively). Both R -Bragg and R -structure factors are model-dependent since these two use the observed intensities deduced by the model, not the actual observed intensities. In the Rietveld analysis, it is R_{wp} among the R -factors that is influenced most significantly by the fitting agreement. This is because R_{wp} has S_{Riet} itself (see Eq. 3.1) in the numerator inside the squared

bracket. As a direct guide to determine the effectiveness of a given refinement, this R_{wp} is compared to R_e , the statistically estimated minimum R_{wp} , which can be written

$$R_e = \left[\frac{N - P}{\sum_i w_i y_i^2} \right]^{\frac{1}{2}} \quad (3.11)$$

S is defined as R_{wp}/R_e . An S value of 1.3 or less indicates a satisfactory refinement. ($S = 1.0$ corresponds to perfect agreement.) Nonetheless, if an S value too close to 1.0 is obtained during the relatively early stages of a refinement, it might suggest either that the diffraction data have poor counting statistics, or that the background is too high, which may cause R_{wp} to be smaller than necessary. For further details including the meaning of the Durbin-Watson d -statistic, see references [102, 116, 117].

Practical know-how on the Rietveld refinements

The Rietveld refinement might appear to be too difficult for inexperienced graduate students. This fear could be even larger if Rietveld refinement computer programs were not easy to use, or without helpful and practical manuals. What follows is some practical know-how that was learned through doing the Rietveld refinements and studying them from related papers and books.

It is quite natural to think that one can get a better quality in the measurement by increasing the count time and/or the number of measurement steps. However, this improvement cannot go on indefinitely. When the counting error becomes as small as other kinds of errors, no further improvement can be made. At this point, further measurements would just be a waste of machine time. This is very well presented by R. J. Hill in the book *The Rietveld Method* [117]. If one either increases the count time or uses a smaller step size, Hill suggests that there is greater benefit to choose the latter. Moreover, as a rule of thumb, one should aim to have 5000–10000 counts at the maximum intensity, and approximately $1/5$ – $1/3$ of the minimum full-width-at-half-maximum (FWHM) of the peaks as the measurement step.

In addition, due caution has to be taken for the width of the slits in the diffractometer. For instance, when a divergence slit (DS) with a slit width of 1 degree is used in the Bragg-Brentano X-ray diffractometer with a goniometer radius of 185 mm (as in our *Rigaku* machine), for $2\theta \leq 20^\circ$ the effective area with which incoming X-rays impinge on a flat sample surface becomes wider than the usual sample width of 20 mm. In this case, unnecessary reflections from the sample holder material are recorded, giving uncertainty to the measured intensities. As a reference, Fig. 3.3 explicitly shows the relation of the DS width to the apparent X-ray width on a sample plate. Therefore, in this work, all the X-ray diffraction measurements done with $DS = 1^\circ$ were analyzed by the Rietveld method without

Table 3.2 Numerical criteria of the fitting results (reproduced from Table 7-1 of Izumi [106]): σ_i is the standard deviation of the observed intensity for the i th data point; $I_K(\text{"o"})$ and $I_K(c)$ are the estimated observed ("o") and calculated integrated intensities for reflection K , respectively; N is the number of data points; P is the number of refinable parameters.

$R_{wp} = \left[\frac{\sum_i w_i [y_i - f_i(\bar{x})]^2}{\sum_i w_i y_i^2} \right]^{\frac{1}{2}}$	R-weighted pattern
$R_p = \frac{\sum_i y_i - f_i(\bar{x}) }{\sum_i y_i}$	R-pattern
$R_B = \frac{\sum_K I_K(\text{"o"}) - I_K(c) }{\sum_K I_K(\text{"o"})}$	R-Bragg factor
$R_F = \frac{\sum_K \sqrt{I_K(\text{"o"})} - \sqrt{I_K(c)} }{\sum_K \sqrt{I_K(\text{"o"})}}$	R-structure factor
$S = \left[\frac{\sum_i w_i [y_i - f_i(\bar{x})]^2}{N - P} \right]^{\frac{1}{2}}$	Goodness-of-fit indicator
$d = \frac{\sum_{i=2}^N \left[\frac{y_i - f_i(\bar{x})}{\sigma_i} - \frac{y_{i-1} - f_{i-1}(\bar{x})}{\sigma_{i-1}} \right]^2}{\sum_{i=1}^N \left[\frac{y_i - f_i(\bar{x})}{\sigma_i} \right]^2}$	Durbin-Watson d -statistic

using the data below $2\theta = 20^\circ$.

Before starting the Rietveld analysis, one has to have a reasonable starting model for the crystal structure to be determined. If the structure has been well studied in the past, the available literature should be used. The Rietveld method will not yield convergent parameters without a good starting model. In this sense, the method cannot be a versatile, omnipotent structure solver; rather, its maximum potential power is to pursue and obtain details that cannot be obtained with simpler analysis methods. Hence, the Rietveld method is a structure *refinement* program, not a solution program. Initial values of the diffractometer-dependent values such as V and W may be pre-determined from a well-characterized standard material such as silicon powder from *NIST*. Other parameters such as D_s , T_s (usually these two are set to zero), U , X and Y may be started with values determined from a standard, too.

Normally $U > 0$, $V < 0$ and $W > 0$, but among these three a strong correlation always exists. Various combinations of the three parameters can give the same Gaussian FWHM. Hence, it is advisable not to refine all three at the same time in the early stages of refinement. Instead, it is best to fix V to the value determined from a standard sample. Nevertheless, one must start with a combination of these three parameters so that they give a positive, hence physically meaningful value of H_{KG} for the entire 2θ range. In a similar manner, it can be readily seen that both X and Y must be positive to make H_{KL} physically meaningful, assuming that the corresponding anisotropic parameters X_e and Y_e are set to zero, which is not an uncommon way to begin. Later, if an anisotropic profile is seen on plotted calculated intensities, set X_e and/or Y_e to nonzero values for the first time. Moreover, since the crystalline-size effect is usually Lorentzian [119], set $P = 0$ unless the profile is obviously Gaussian. It is not desirable to use more background parameters than necessary; an excess of parameters would simply increase the value of S as can be seen from its definition in the table above.

For x-ray diffraction, the lighter the atom is, the weaker the diffracted intensity. This obviously makes the Rietveld analysis more difficult. Sometimes for such a light element a value of thermal-displacement parameter B would become very large, or negative which is unphysical. This can also happen if an occupancy at a site is very small. Thermal-displacement parameters can readily be a sink for all other incorrect fitting results, making the value unreasonable. In such a case there is no other choice than to give up the refinement on B and very often other parameters, too, and to fix them to literature values if available. In the latter case, if the same element exists at a different site with a larger occupancy, set both B values to one value with a linear constraint between them. Dr. Izumi's RIETAN-97 β is capable of applying linear and nonlinear constraints between parameters [110]. This fragile state of thermal-displacement parameters B comes partly from a strong correlation with occupancy parameters.

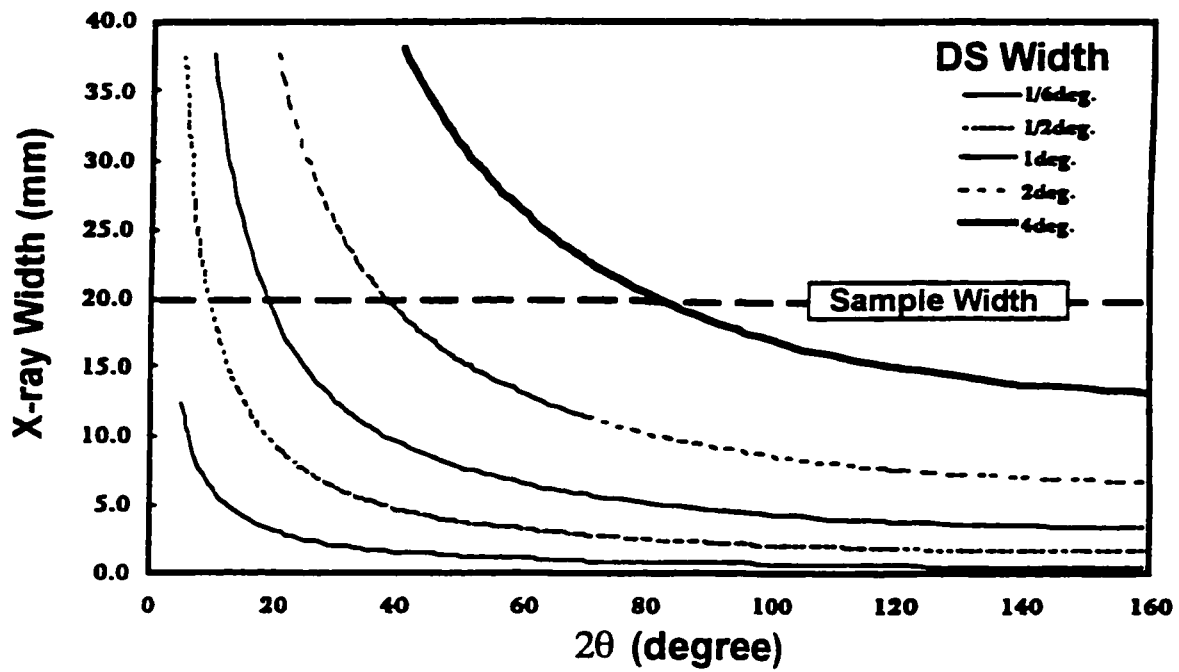


Figure 3.3 X-ray beam width on the sample plate versus the diffraction angle 2θ using a divergence slit (DS) with different angular widths for an X-ray diffractometer with a goniometer radius of 185 mm. (excerpted from [118])

In general, conventional x-ray diffractometers are not as capable of determining values of B as well (the case of anisotropic thermal-displacement parameters is even worse) as, *e.g.*, neutron diffraction.

In the Rietveld method, one "switches on" only some of all the refinable parameters at one time. Until the later stage of refinement, it is never a good idea to turn on all the parameters for refinement. An important question, therefore, is in what order parameters are supposed to be switched on. Young discusses this issue and makes a suggestion of the order, which is reproduced in Table 3.3 [102]. The Rietveld method program RIETAN-973 has its unique and fairly reliable function that automatically selects an order of parameters to be turned on during repetitive refinement cycles. This is very useful and can save much time.

Table 3.3 A suggested parameter turn-on sequence. (Context: constant wavelength x-ray or neutron powder diffractometer data.) (reproduced from Table 1.5 of Young [102])

Parameters	Linear	Stable	Comment	Sequence
s	Yes	Yes	Note 1	1
D_s	No	Yes	Note 2	1
Flat background	Yes	Yes		2
$a, b, c, \alpha, \beta, \gamma$	No	Yes	Note 3	2
More background	No	Yes(?)	Note 4	2 or 3
W	No	Poorly	Note 5	3 or 4
x, y, z	No	Fairly	Note 6	3
g 's and B 's	No	?	Correlated	4
U, V , etc.	No	No	Note 5	Last
β_{ij}	No	No?		Last
Z	No	Yes	Note 2	1, 4 or not

Note 1: if the scale factor is very far off or the structural model is very bad, the scale factor may get worse, *e.g.* smaller, during refinement because the difference between a pattern and nothing is less than the difference between two badly mismatched patterns.

Note 2: for properly aligned and mechanically stable diffractometers, the zero point error should be and remain inconsequential. In any event, it cannot change from sample to sample whereas the effective specimen displacement can and does. The displacement parameter will also take up some of the effect of specimen transparency which occurs in non-infinitely absorbing specimens.

Note 3: beware lest one or more incorrect lattice parameters cause one or more calculated peaks to 'lock on' to the wrong observed peaks. The result can be a very solid false minimum. Artificially broadening the calculated profiles (temporarily) may help. A parameter for wavelength may be turned on instead of one of the lattice parameters if the wavelength is not as well known as are the lattice parameters.

Note 4: if more background parameters are turned on than needed to model the angular dependence of the background, the result will be high correlations and, often, large shifts that are mostly mutually compensating but may lead to erratic behaviour and failure of the refinement. The higher order ones should be turned off sequentially until the problem is corrected.

Note 5: U, V, W tend to be highly correlated. Various combinations of quite different values can lead to essentially the same profile breadth. In Chapter 3, Prince points out that the problem can be greatly ameliorated by offsetting the origin of the Caglioti *et al.* [120] polynomial expression for the angular dependence of U, V, W as he shows in Eq. (3.12).

Note 6: graphics and the reflection indices should be used now to assess whether preferred orientation should be modelled at this point.

It is important to remember that when a value of S is not going below 1.3, then plotting the fitting result often helps to identify a possible reason for the poor S value. Even if a value of S becomes small enough, there is always the potential danger that a refinement is not actually converging to the global minimum in the entire parameter space, but to a so-called false minimum. One of methods to confirm convergence to the global minimum is to repeat the refinement process using a different least-square algorithm. In the program RIETAN-97 β , three different algorithms are available for use: the Gauss-Newton, modified Marquardt, and conjugate direction methods. The modified Marquardt method is used for most refinement steps because of its overall performance quality and its speed. However, a choice can be made in an input file to RIETAN-97 β so that the program automatically alters one algorithm to another subsequently. It is a good custom to execute this choice at the last stage of a refinement to double check its convergence to the global minimum. A caution is given when too small a value of S (< 1) is obtained even after confirming the global minimum of the solution. Rietveld analysis computer programs cannot give a perfect estimate of S ; therefore, S could become less than 1 for a correct solution.

Example of the Rietveld refinement

In this section, an example of the Rietveld refinement is given for sample 4A of LiV_2O_4 . A piece of sample 2 was given additional heating at 725°C for approximately one day before quenching the sample tube into ice water, which was labeled as sample 4A. The x-ray diffraction measurement revealed that this sample had V_2O_3 as an impurity phase. The Rietveld analysis computer program RIETAN-97 β is not a menu-driven software, but uses an input file as a batch file that executes the application. Compared to the GUI-based (Graphical User Interface) input method seen in many recent applications, this CUI-based (Character User Interface) input method might appear less sophisticated. However, a GUI-based input system often has a hierachial menu which has many layers below. A user usually has to respond at each layer to go further below in the menu, or to execute a subprogram. The result is that the user tends to get lost while moving up and down between different levels of the menu. However, the CUI-based input method is more direct and probably requires less time if one uses one's favorite editor. The creator of RIETAN97 β calls this input system F^3IS (Flat, Flexible and Friendly Input System) [105].

An input file of Dr. Izumi's F^3IS consists of equation-like assignment lines

$$\text{variable} = \text{value} : \text{comment} \quad . \quad (3.12)$$

in which a user can write any comment after a colon as long as the number of characters in the line

does not exceed 80. If such a colon is replaced with an exclamation point, the whole assignment line becomes void and will be ignored on execution. In this way one can leave choices in the input file lines for future use. In addition, the “If... then...” command is available, as seen in an example input file for LiV_2O_4 sample 4A given in the Appendix. Also one can put a # sign at the beginning of a line to make the rest of a line a comment. Multiple lines can be grouped in a pair of braces, and a comment can be added outside the braces. A template file which is available as a sample of the program is, therefore, very useful. A beginner can start a refinement, without studying the details before use, by simply validating and nullifying given selections.

Refinable parameters have flags to identify whether they are to be fixed (set to 0) or refined (1). Furthermore, linear and nonlinear constraints can be given between refinable parameters by setting a flag to 2. For instance, on the line beginning with ASYM2 a flag of 2 is attached to the value (= 0.110906). A constraint of such a parameter is given in the next section. For ASYM2, it is set $A(\text{ASYM2.1})=A(\text{ASYM1.1})$, where “A” itself means nothing, but the first argument in the parentheses tells which variables are to be constraints, and the second argument specifies a variable number for the given parameter. In this example of sample 4A, all the profile parameters of the impurity phase are set equal to the corresponding values in the main phase. All structure parameters except lattice parameters are fixed to literature values. Refinements usually cannot be done for a very minor second phase.

By making a choice of $\text{NEXC} = 1$, the data points in the $2\theta = 15\text{--}19.98^\circ$ range were not used for the refinement. The normal setting in our Rigaku x-ray diffractometer has a divergence slit with a width of 1 degree, so the measured intensity values for $2\theta < 20^\circ$ include reflections from the sample holder. Often such low angle data are discarded simply because a peak shape exhibits more asymmetry at low angle, which makes the refinement process more difficult.

The best way to know the preferred-orientation vector is to view the crystalline shape under an electron microscope. When this is unavailable, various choices of this vector and also anisotropic-broadening axis ought to be tested.

The results of the Rietveld analyses for all nine LiV_2O_4 samples are listed in Table 3.4 below (the information for the two Ti spinel samples are in Table 6.2), and are discussed in the next section. The fit curve to thousands of data points between $2\theta = 20$ and 80° for this example of LiV_2O_4 sample 4A is shown in Fig. 3.4.

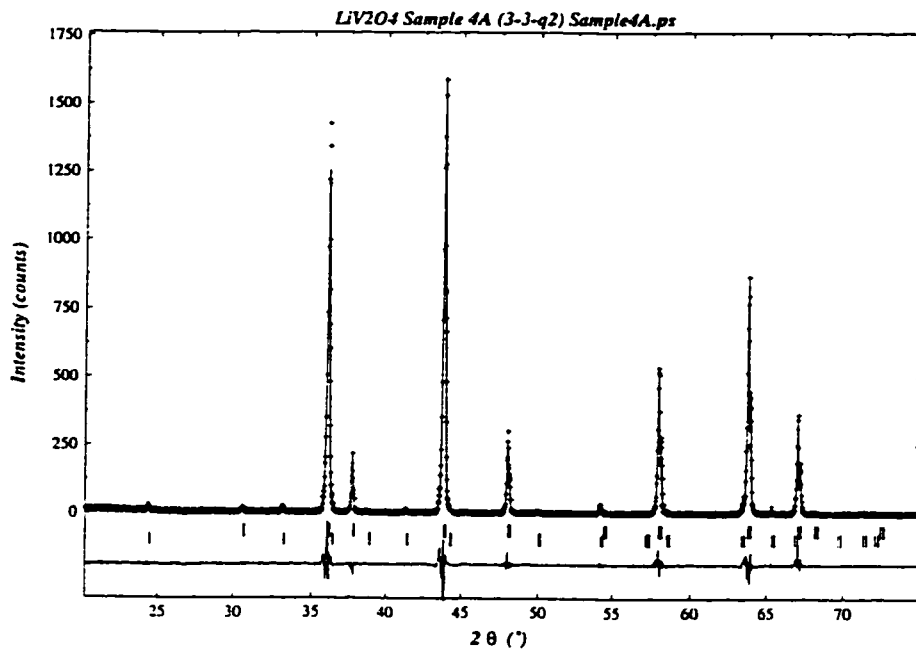


Figure 3.4 Rietveld refinement fit to the x-ray diffraction pattern of LiV_2O_4 sample 4A for diffraction angles $2\theta = 20\text{--}80^\circ$. Diffraction data points are indicated by crosses, while the calculated intensity is the solid curve. Right below the diffraction pattern, there are two sets of ticks, overlapping somewhat in the vertical direction. The upper ticks represents expected 2θ angles for LiV_2O_4 diffraction peaks, and the lower ticks are those for V_2O_3 impurity phase. The difference between the observed and calculated intensity is shown at the bottom.

Structure analyses by Rietveld method and thermogravimetric analysis results

The results from Rietveld analyses of the x-ray diffraction patterns for the nine LiV_2O_4 samples are given in Table 3.4. The refinements of the spinel phase were based on the assumption of exact LiV_2O_4 stoichiometry. The peaks of this main phase can be indexed on the space group $Fd\bar{3}m$. The values of the isotropic thermal-displacement parameters B of lithium and oxygen were taken from the Rietveld analysis of neutron diffraction measurements on our LiV_2O_4 sample 5 by Chmaissem *et al.* [18], and fixed throughout to $B_{\text{Li}} = 1.1 \text{ \AA}$ and $B_{\text{O}} = 0.48 \text{ \AA}$, respectively. These atoms do not scatter x-rays strongly enough to allow accurate determinations of the B values from Rietveld refinements of our x-ray diffraction data.

Table 3.4 Results of Rietveld refinements of x-ray diffraction measurements for nine LiV_2O_4 samples. The oxygen parameter (u) is shown using the second setting for the space group $Fd\bar{3}m$ from the *International Tables for Crystallography, Vol. A* [68]. $f_{\text{str imp}}$ is the impurity concentration. The error in the last digit of a quantity is given in parentheses. The x-ray detection limit for the impurity concentration is assumed to be 1% [121]. For samples 3 and 7 in which no discernable impurities were seen, this detection limit is listed. Also, the Rietveld refinement for sample 5 yielded a concentration less than 1%, which is replaced with the detection limit below.

Sample No.	Alt. Sample No.	Cooling	Impurity	a_0 (\AA)	u	$f_{\text{str imp}}$ (mol%)
1	4-0-1	air	V_3O_5	8.24062(11)	0.26115(17)	2.01
2	3-3	air	V_2O_3	8.23997(4)	0.2612(20)	1.83
3	4-E-2	air	pure	8.24100(15)	0.26032(99)	< 1
4	3-3-q1	LN_2	V_3O_5	8.24622(23)	0.26179(36)	3.83
4A	3-3-q2	ice H_2O	V_2O_3	8.24705(29)	0.26198(39)	1.71
4B	3-3-a2	slow cool	V_2O_3	8.24734(20)	0.26106(32)	1.46
5	6-1	air	V_2O_3	8.24347(25)	0.26149(39)	< 1
6	12-1	air	V_3O_5	8.23854(11)	0.26087(23)	2.20
7	13-1	air	pure	8.24114(9)	0.26182(19)	< 1

The nine LiV_2O_4 samples were given three different heat treatments after heating to 700 to 750 °C: air-cooling (samples 1, 2, 3, 5, 6 and 7), liquid-nitrogen quenching (sample 4), ice-water quenching (sample 4A) or oven-slow cooling at $\approx 20 \text{ }^\circ\text{C/hr}$ (sample 4B). Possible loss of Li at the high synthesis temperature, perhaps in the form of a lithium oxide, was a concern. This lithium loss would cause a deficiency of lithium (or lithium and oxygen) relative to the composition LiV_2O_4 . In a detailed neutron

diffraction study. Dalton *et al.* [93] determined the lithium contents in their samples of $\text{Li}_{1+x}\text{Ti}_{2-x}\text{O}_4$ ($0 \leq x \leq 0.33$), and found lithium deficiency in the 8a site of the spinel phase of all four samples studied. If the spinel phase in the Li-V-O system is similarly Li-deficient, then samples of exact stoichiometry LiV_2O_4 would contain V-O impurity phase(s), which might then explain the presence of small amounts of V_2O_3 or V_3O_5 impurity phases in most of our samples.

Sample 3 was intentionally made slightly off-stoichiometric, with the nominal composition $\text{LiV}_{1.92}\text{O}_{3.89}$. A TGA measurement in oxygen showed a weight gain of 12.804% to the fully oxidized state. If one assumes an actual initial composition $\text{LiV}_{1.92}\text{O}_{3.89+\delta}$, this weight gain corresponds to $\delta = 0.08$ and an actual initial composition of $\text{LiV}_{1.92}\text{O}_{3.97}$, which can be rewritten as $\text{Li}_{1.01}\text{V}_{1.93}\text{O}_4$ assuming no oxygen vacancies on the oxygen sublattice. On the other hand, if one assumes an actual initial composition of $\text{Li}_{1-x}\text{V}_{1.92}\text{O}_{3.89}$, then the weight gain yields $x = 0.19$, and an initial composition $\text{Li}_{0.81}\text{V}_{1.92}\text{O}_{3.89}$, which can be similarly rewritten as $\text{Li}_{0.83}\text{V}_{1.97}\text{O}_4$. Our Rietveld refinements could not distinguish these possibilities from an assumed stoichiometric composition of $\text{Li}[\text{V}_2]\text{O}_4$ for the spinel phase.

Sample 4, which was given a liquid-nitrogen quench from the final heating temperature of $\simeq 725^\circ\text{C}$ (labelled “LN₂” in Table 3.4), is one of the structurally least pure samples (see Table 3.4). Our Rietveld refinement of the x-ray diffraction pattern for this sample did not reveal any discernable deviation of the cation occupancy from that of ideal $\text{Li}[\text{V}_2]\text{O}_4$. There is a strong similarity among samples 4, 4A (ice-water quenched) and 4B (oven-slow cooled), despite their different heat treatments. These samples all have much larger lattice parameters ($a_0 \gtrsim 8.246 \text{ \AA}$) than the other samples. The as-prepared sample 2, from which all three samples 4, 4A and 4B were obtained by the above quenching heat treatments, has a much smaller lattice parameter. On the other hand, the oxygen parameters u of these four samples are similar to each other and to those of the other samples in Table 3.4.

The weight gains upon the oxidization of our samples in pure oxygen in the TGA can be converted to values of the average oxidation state per vanadium atom, assuming the ideal stoichiometry LiV_2O_4 for the initial composition. The values, to an accuracy of ± 0.01 , are 3.57, 3.55, 3.60, 3.56, 3.56, 3.57, 3.57, 3.55 for samples 1–7 and 4B, respectively. This measurement was not done for sample 4A. We do not currently understand why these values are systematically higher than the expected value of 3.50.

4 MAGNETIZATION

Magnetization measurements

Overview of observed magnetic susceptibility

An overview of the observed zero-field-cooled (ZFC) magnetic susceptibilities $\chi^{\text{obs}}(T) \equiv M^{\text{obs}}(T)/H$ at $H = 1.0\text{ T}$ from 1.8–2 K to 400 K of the nine LiV_2O_4 samples is shown in Figs. 4.1(a), (b) and (c). The $\chi^{\text{obs}}(T)$ data for the various samples are very similar for $T \gtrsim 50\text{ K}$. Differences in $\chi^{\text{obs}}(T)$ between the samples appear at lower T , where variable Curie-like C_{imp}/T upturns occur.

Samples 1 and 6 clearly exhibit shallow broad peaks in χ^{obs} at $T \approx 16\text{ K}$. The $\chi^{\text{obs}}(T)$ of sample 6 is systematically slightly larger than that of sample 1; the reason for this shift is not known. Samples 3 and 4 also show the broad peak with a relatively small Curie-like upturn. Samples 2 and 7 show some evidence of the broad peak but the peak is partially masked by the upturn. For the other three samples, the broad peak is evidently masked by larger Curie impurity contributions. From Fig. 4.1 and Table 3.4, the samples 1, 4 and 6 with the smallest Curie-like impurity contributions contain V_3O_5 impurities, whereas the other samples, with larger paramagnetic impurity contributions, contain V_2O_3 impurities. The reason for this correlation is not clear. The presence of the vanadium oxide impurities by itself should not be a direct cause of the Curie-like upturns. The susceptibility of pure V_2O_3 follows the Curie-Weiss law in the metallic T region above $\sim 170\text{ K}$, but for $T \lesssim 170\text{ K}$ it becomes an antiferromagnetic insulator, showing a decrease in $\chi(T)$ [122]. V_{2-y}O_3 ($y \approx 0.03$), on the other hand, sustains its high- T metallic state down to low temperatures, and at its Néel temperature $T_N \sim 10\text{ K}$ it undergoes a transition to an antiferromagnetic phase with a cusp in $\chi(T)$ [122]. V_3O_5 also orders antiferromagnetically at $T_N = 75.5\text{ K}$, but $\chi(T)$ shows a broad maximum at a higher $T = 125\text{ K}$ [123]. Though not detected in our x-ray diffraction measurements, V_4O_7 , which has the same V oxidation state as in LiV_2O_4 , also displays a cusp in $\chi^{\text{obs}}(T)$ at $T_N \approx 33\text{ K}$ and $\chi^{\text{obs}}(T)$ follows the Curie-Weiss law for $T \gtrsim 50\text{ K}$ [31]. The susceptibilities of these V-O phases are all on the order of 10^{-4} to $10^{-3}\text{ cm}^3/\text{mol}$ at low T [31, 122]. Moreover, the T variations of $\chi^{\text{obs}}(T)$ in these vanadium oxides for $T \lesssim 10\text{ K}$ are,

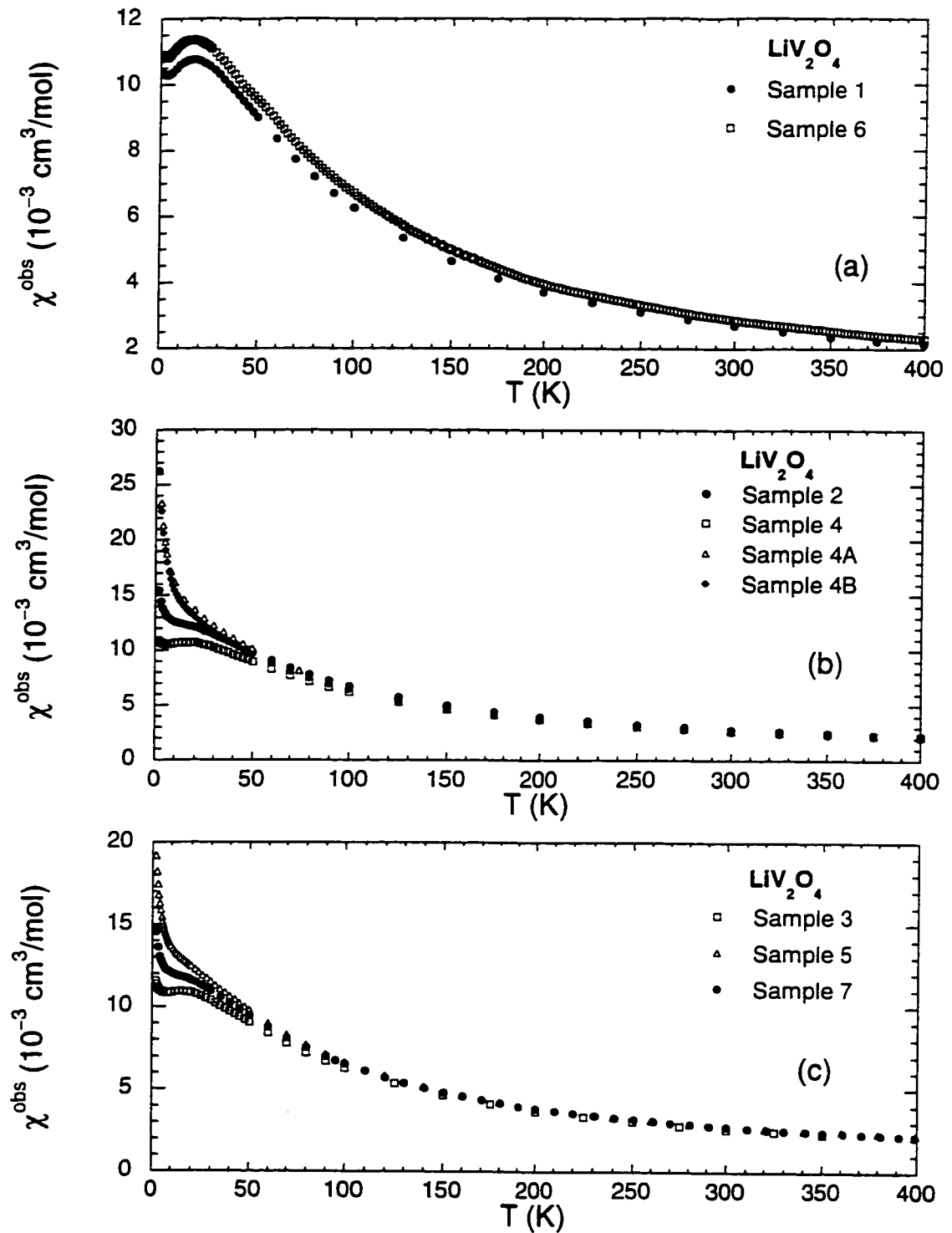


Figure 4.1 Observed magnetic susceptibility $\chi^{\text{obs}}(T)$ ($\equiv M^{\text{obs}}/H$) of all the nine samples studied, measured with $H = 1$ T after being zero-field cooled to the lowest T : (a) Samples 1 and 6; (b) samples 2, 4, 4A and 4B; (c) samples 3, 5 and 7.

upon decreasing T , decreasing ($V_{2-y}O_3$) or nearly T independent (V_3O_5 and V_4O_7), in contrast to the increasing behavior of the observed Curie-like magnetic impurity contribution. From the above discussion and the very small amounts of V-O impurity phases found from the Rietveld refinements of our x-ray diffraction measurements, we conclude that the V-O impurity phases cannot give rise to the observed Curie-like upturns in our $\chi^{\text{obs}}(T)$ data at low T . These Curie-like terms therefore most likely arise from paramagnetic defects in the spinel phase and/or from a very small concentration of an unidentified impurity phase.

Figure 4.1(b) shows how the additional heat treatments of the as-prepared sample 2, to produce samples 4, 4A and 4B, yielded different behaviors of $\chi^{\text{obs}}(T)$ at low T . Only liquid-nitrogen quenching (sample 4) caused a decrease in the Curie-like upturn of sample 2. On the contrary, ice water quenching (sample 4A) and oven-slow cooling (sample 4B) caused $\chi^{\text{obs}}(T)$ to have an even larger upturn. However, the size of the Curie-like upturn in $\chi^{\text{obs}}(T)$ of sample 4 was found to be irreproducible when the same liquid-nitrogen quenching procedure was applied to another piece from sample 2: in this case the Curie-like upturn was larger, not smaller, than in sample 2. The observed susceptibility (not shown) of this latter liquid nitrogen-quenched sample is very similar to those of samples 4A and 4B. The $\chi^{\text{obs}}(T)$ of samples 4A and 4B resemble those reported previously [2, 5, 6, 7, 8, 9].

Isothermal magnetization versus magnetic field

Larger Curie-like upturns were found in samples with larger curvatures in the isothermal $M^{\text{obs}}(H)$ data at low T . A few representative $M^{\text{obs}}(H, 2\text{ K})$ data for samples showing various extents of curvatures in $M^{\text{obs}}(H)$ are shown in Fig. 4.2, which may be compared with the corresponding $\chi^{\text{obs}}(T)$ data at low T in Figs. 4.1. This correlation suggests that the Curie-like upturns in $\chi^{\text{obs}}(T)$ arise from paramagnetic (field-saturable) impurities/defects in the samples. On the other hand, there is no obvious correlation between the magnetic impurity concentration and the structural V_2O_3 or V_3O_5 impurity concentration, as noted above.

The isothermal $M^{\text{obs}}(H)$ data for $H \leq 5.5\text{ T}$ displayed negative curvature for $T \lesssim 10\text{--}20\text{ K}$ and linear behavior for higher T , as illustrated for sample 1 in Fig. 4.3. The concentrations of magnetic impurities in the various samples were obtained from analyses of $M^{\text{obs}}(H)$ isotherms, as follows. From high-field measurements, the intrinsic magnetization $M(H, 0.5\text{ K})$ of LiV_2O_4 is proportional to H up to $H \sim 16\text{ T}$ [124]. Therefore, the observed molar magnetization $M^{\text{obs}}(H, T)$ isotherm data for each sample were fitted by the equation

$$M^{\text{obs}}(H, T) = M_{\text{imp}}(H, T) + M(H, T)$$

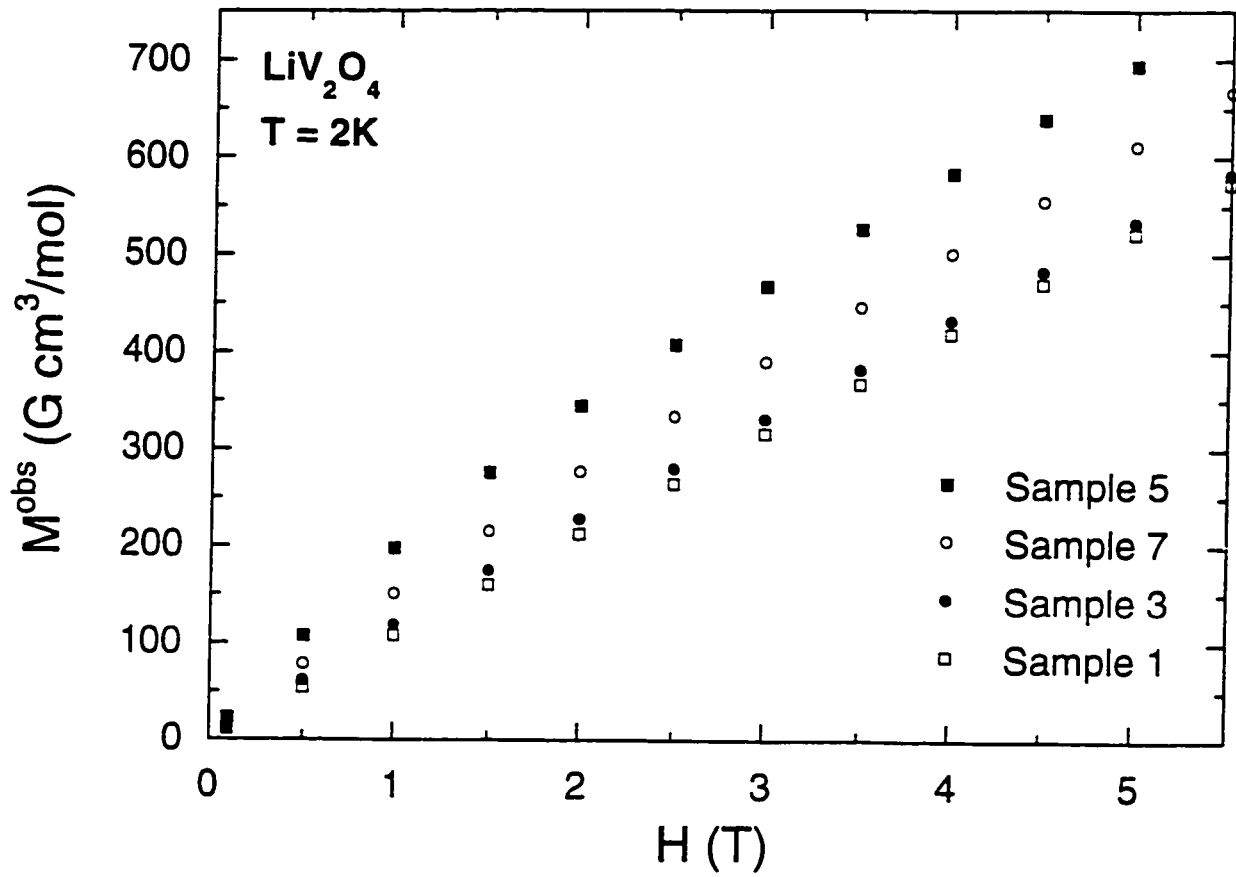


Figure 4.2 Comparison of the negative curvatures of observed magnetization isotherms M^{obs} at $T = 2\text{K}$ versus applied magnetic field H for samples 1, 3, 5 and 7.

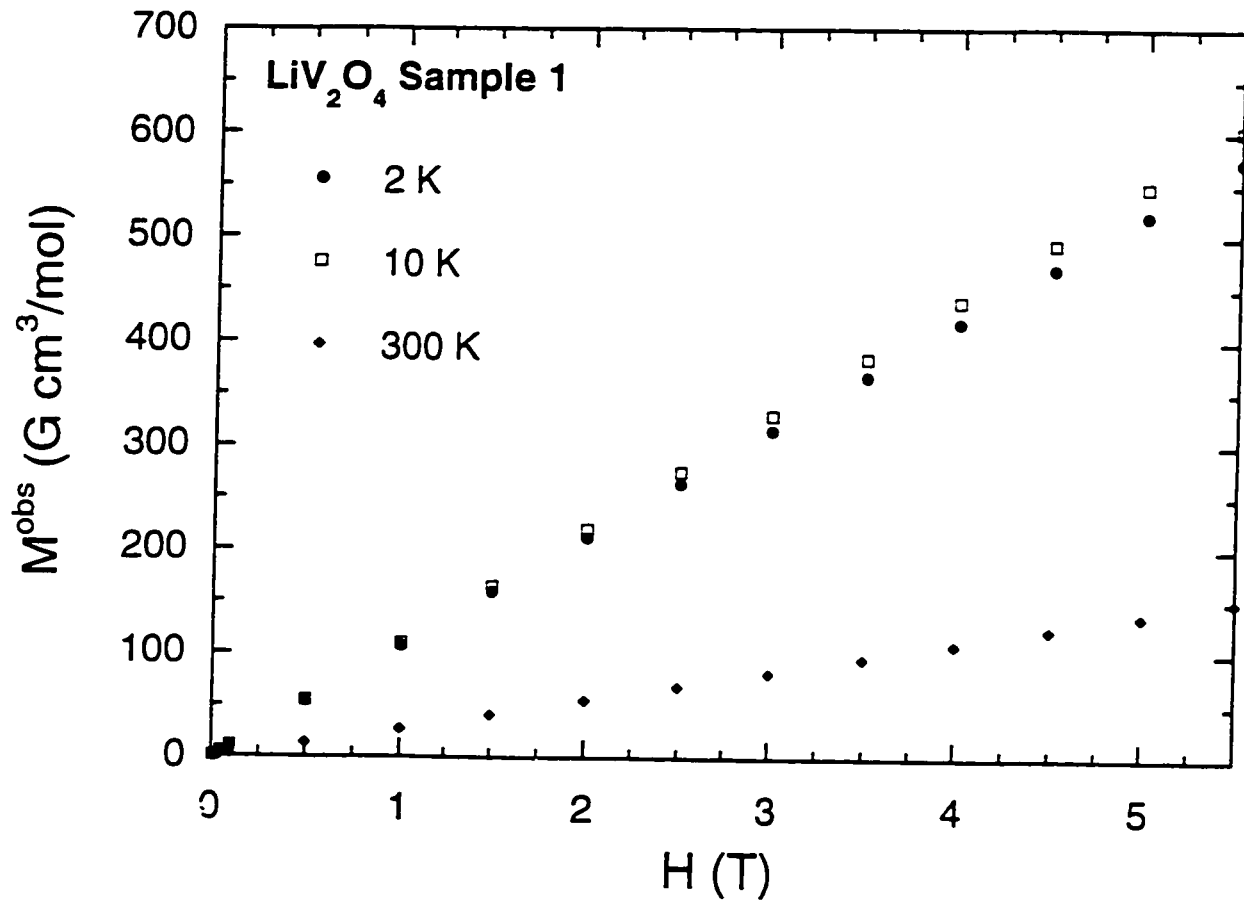


Figure 4.3 Observed magnetization M^{obs} versus applied magnetic field H isotherms at temperatures $T = 2, 10$ and 300 K for LiV_2O_4 sample 1. Negative curvature in $M^{\text{obs}}(H)$ is not present for $T > 10$ K for this sample.

$$= f_{\text{imp}} N_{\text{A}} g_{\text{imp}} \mu_{\text{B}} S_{\text{imp}} B_{S_{\text{imp}}}(x) + \chi(T) H \quad (4.1)$$

where f_{imp} is the magnetic impurity concentration, N_{A} Avogadro's number, g_{imp} the impurity g -factor, μ_{B} the Bohr magneton, S_{imp} the impurity spin, $B_{S_{\text{imp}}}$ the Brillouin function, χ the intrinsic susceptibility of the LiV_2O_4 spinel phase and H the applied magnetic field. The argument of the Brillouin function is $x = g_{\text{imp}} \mu_{\text{B}} S_{\text{imp}} H / [k_{\text{B}}(T - \theta_{\text{imp}})]$. θ_{imp} represents the Weiss temperature of the Curie-Weiss law when the susceptibility is obtained by expanding the Brillouin function in the limit of small $H/(T - \theta_{\text{imp}})$. Incorporating the parameter $\theta_{\text{imp}} \neq 0$ takes account of possible interactions between magnetic impurities in a mean-field way. To improve the precision of the obtained fitting parameters, we fitted $M^{\text{obs}}(H)$ isotherm data measured at more than one low temperature simultaneously by Eq. (4.1). Since the negative curvature of the isothermal $M^{\text{obs}}(H, T)$ data diminishes rapidly with increasing T , only low T (1.8–6 K) data were used. Furthermore, a linear T dependence of $\chi(T)$ in this T range was assumed [see Fig. 4.1(a)] in order to reduce the number of free parameters. However, $\chi(T = 2 \text{ K})$ and the linear slope $d\chi/dT$ still have to be determined. Hence up to six free parameters were to be determined by fitting Eq. (4.1) to the data: f_{imp} , g_{imp} , S_{imp} , θ_{imp} , $\chi(T = 2 \text{ K})$ and $d\chi/dT$.

With all six parameters varied as free parameters, fits of $M^{\text{obs}}(H, T)$ by Eq. (4.1) produced unsatisfactory results, yielding parameters with large estimated standard deviations. Therefore, we fixed S_{imp} to various half-integer values starting from 1/2, thereby reducing the number of free parameters of each fit to five. With regard to the g_{imp} values, g -factors of slightly less than 2 are observed in V^{4+} compounds: VO_2 (1.964) [125], $(\text{NH}_4)_x\text{V}_2\text{O}_5$ (1.962) [126] and $\text{Li}_x\text{V}_2\text{O}_5$ (1.96) [127]. Having $g_{\text{imp}} \approx 2$ as a guide, we selected a few values of S_{imp} which resulted in $g_{\text{imp}} \sim 2$ in the five-parameter fit. Then using the obtained parameter values we calculated and plotted the impurity magnetization M_{imp} ($\equiv M^{\text{obs}} - \chi H$) versus $H/(T - \theta_{\text{imp}})$ for all the low T data utilized in the fit by Eq. (4.1). If a fit is valid, then all the $M_{\text{imp}}[H/(T - \theta_{\text{imp}})]$ data points obtained at the various isothermal temperatures for each sample should collapse onto a universal curve described by $M_{\text{imp}} = f_{\text{imp}} N_{\text{A}} g_{\text{imp}} \mu_{\text{B}} S_{\text{imp}} B_{S_{\text{imp}}}(x)$. The fixed value of S_{imp} which gave the best universal behavior for a given sample was chosen. Then, using this S_{imp} , we fixed the value of g_{imp} to 2 to see if the resultant $M_{\text{imp}}[H/(T - \theta_{\text{imp}})]$ data yielded a similar universal behavior. For the purpose of reducing the number of free parameters as much as possible, if this fixed- g fit did yield a comparable result, the parameters obtained were taken as the final fitting parameters and are reported in this paper. For sample 1 only, the fit parameters obtained by further fixing $\theta_{\text{imp}} = 0$ are reported here. To estimate the goodness of a fit, the χ^2 per degree of freedom (DOF) was obtained, which is defined as $(N_{\text{p}} - P)^{-1} \sum_{i=1}^{N_{\text{p}}} (M_i - M_i^{\text{calc}})^2 / \sigma_i^2$, where N_{p} is the number of data points, P is the number of free parameters, and σ_i is the standard deviation of the

observed value M_i . A fit is regarded as satisfactory if $\chi^2/\text{DOF} \lesssim 1$, and this criterion was achieved for each of the nine samples.

The magnetic parameters for each sample, obtained as described above, are listed in Table 4.1. Plots of M_{imp} versus $H/(T - \theta_{\text{imp}})$ for the nine samples are given in Figs. 4.4, 4.5 and 4.6, where an excellent universal behavior for each sample at different temperatures is seen. The two magnetically purest samples 1 and 6 have the largest relative deviations of the data from the respective fit curves, especially at the larger values of $H/(T - \theta_{\text{imp}})$. Since these two samples contain extremely small amounts of paramagnetic saturable impurities, the magnetic parameters of the impurities could not be determined to high precision. The impurity spins S_{imp} obtained for the nine samples vary from 3/2 to 4. In general, the magnetic impurity Weiss temperature $|\theta_{\text{imp}}|$ increased with magnetic impurity concentration $f_{\text{mag imp}}$. From the chemical analyses of the starting materials (V_2O_5 , NH_4VO_3 and Li_2CO_3) supplied by the manufacturer, magnetic impurity concentrations of 0.0024 mol% Cr and 0.0033 mol% Fe are inferred with respect to a mole of LiV_2O_4 , which are too small to account for the paramagnetic impurity concentrations we derived for our samples.

Table 4.1 Results of magnetization $M^{\text{obs}}(H, T)$ isotherm analyses, where the T values used are listed in the second column. $f_{\text{mag imp}}$ is the magnetic impurity concentrations. The error in the last digit of a quantity is given in parentheses. A number without an error listed was fixed in the data fit.

Sample No.	T (K)	fixed S_{imp}	g_{imp}	θ_{imp} (K)	$f_{\text{mag imp}}$ (mol%)	χ (2 K) ($10^{-2} \text{ cm}^3/\text{mol}$)	$d\chi/dT$ ($\text{cm}^3/\text{mol K}$)
1	2.3,4.5	3/2	2	0	0.049(2)	1.026(1)	7.3(1)
2	2.4,6	3	2.00(6)	-0.6(2)	0.22(1)	1.034(5)	6.7(4)
3	2.5	5/2	2.10(2)	-0.51(5)	0.118(2)	0.9979(6)	7.46(7)
4	2.3,4.5	5/2	2	-0.2(1)	0.066(2)	0.9909(9)	6.7(1)
4A	2.5	3	2	-0.5(1)	0.77(2)	1.145(9)	6.5(9)
4B	2.3,4.5	7/2	2	-1.2(1)	0.74(2)	1.13(1)	4.4(7)
5	2.5	5/2	2.31(3)	-0.59(4)	0.472(8)	1.091(2)	5(3)
6	2.5	4	2	-0.9(14)	0.0113(6)	1.067	5.6(2)
7	2.5	3	2	-0.2(2)	0.194(7)	1.094(4)	5.4(4)

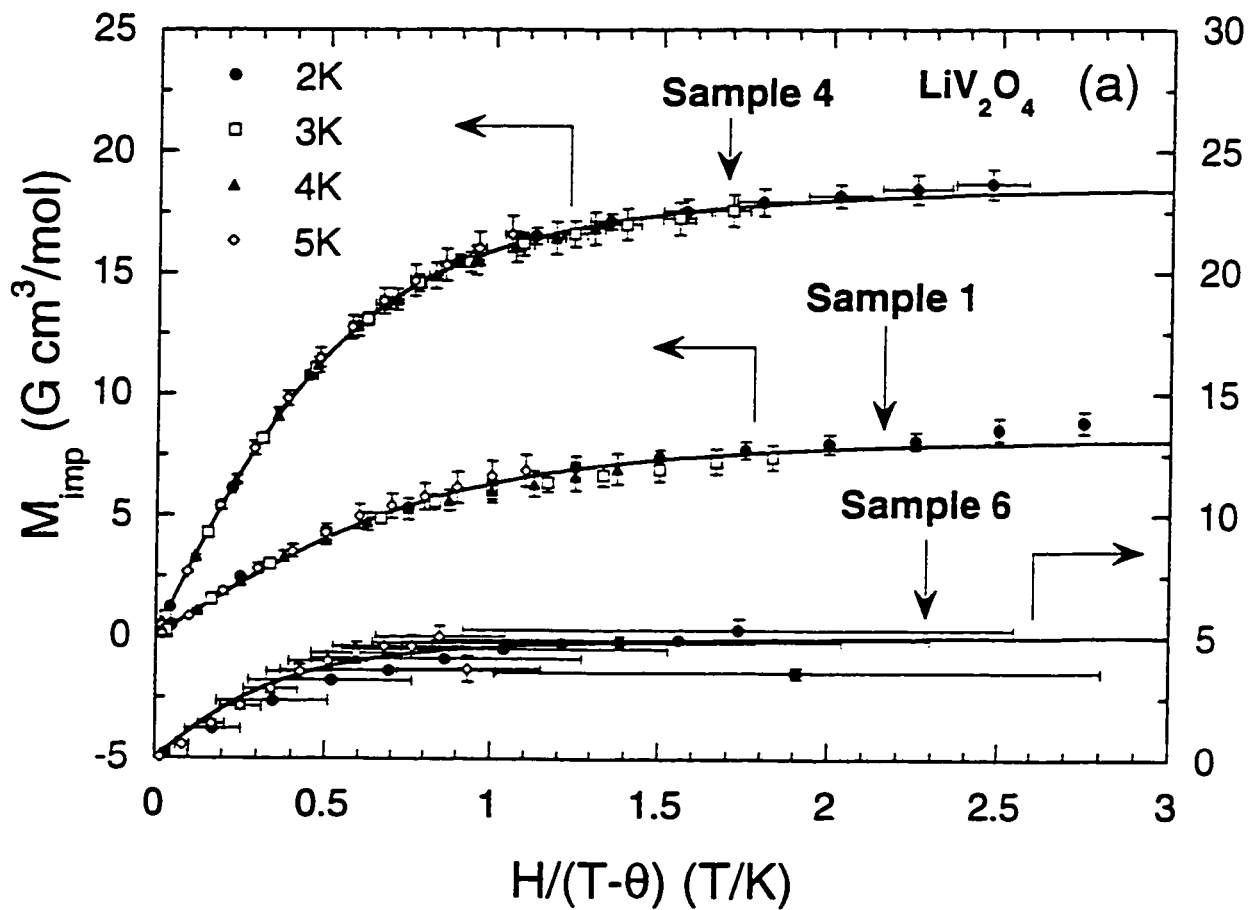


Figure 4.4 Calculated impurity magnetizations $M_{\text{imp}} \equiv M^{\text{obs}} - \chi H$ versus $H/(T - \theta_{\text{imp}})$ for LiV_2O_4 samples 1, 4 and 6. For each sample, the solid curve is the best-fit Brillouin function Eq. (4.1).

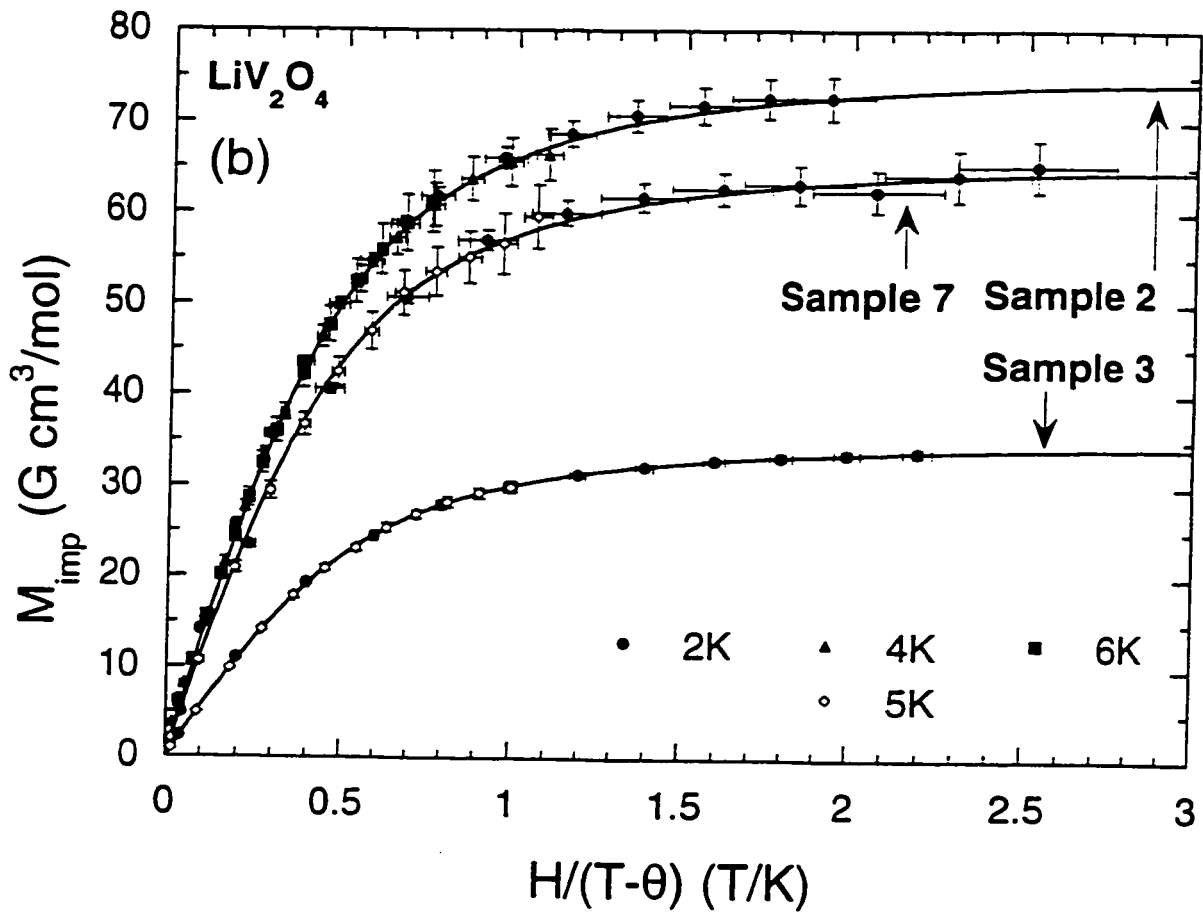


Figure 4.5 Calculated impurity magnetizations $M_{\text{imp}} \equiv M^{\text{obs}} - \chi H$ versus $H/(T - \theta_{\text{imp}})$ for LiV_2O_4 samples 2, 3 and 7. For each sample, the solid curve is the best-fit Brillouin function Eq. (4.1).

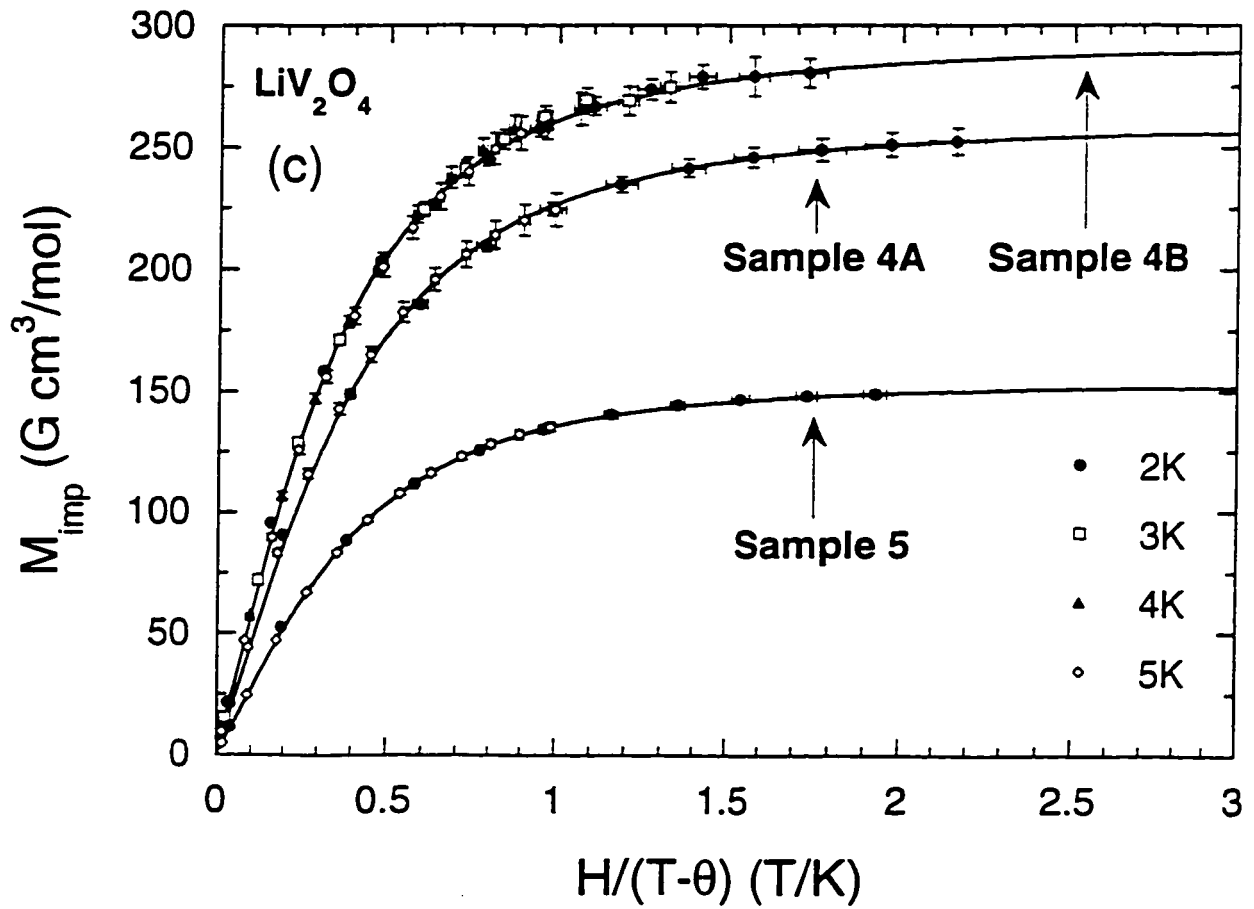


Figure 4.6 Calculated impurity magnetizations $M_{\text{imp}} \equiv M^{\text{obs}} - \chi H$ versus $H/(T - \theta_{\text{imp}})$ for LiV_2O_4 samples 4A, 4B and 5. For each sample, the solid curve is the best-fit Brillouin function Eq. (4.1).

Magnetization versus temperature measurements

Low magnetic field ZFC and FC measurements

The zero-field-cooled (ZFC) $\chi^{\text{obs}}(T)$ data in Fig. 4.1(a) for our highest magnetic purity samples 1 and 6 show a broad maximum at $T^{\text{peak}} \approx 16$ K. One interpretation might be that static short-range (spin-glass) ordering sets in below this temperature. To check for spin-glass ordering, we carried out low-field (10–100 G) ZFC and field-cooled (FC) magnetization measurements from 1.8–2 K to 50 K on all samples except samples 2 and 4B. For each sample, there was no hysteresis between the ZFC and FC measurements, as illustrated for sample 4 in Fig. 4.7, and thus no evidence for spin-glass ordering above 1.8–2 K [29].

Ueda *et al.* [83] reported that spin-glass ordering occurs in the zinc-doped lithium vanadium oxide spinel $\text{Li}_{1-x}\text{Zn}_x\text{V}_2\text{O}_4$ for $0.1 < x \leq 0.9$. However, spin-glass ordering was not seen in the pure compound LiV_2O_4 , consistent with our results. Further, positive-muon spin relaxation μSR measurements for sample 1 did not detect static magnetic ordering down to 20 mK [11]. However, the μSR measurements did indicate the presence of static spin-glass ordering in the off-stoichiometric sample 3 below 0.8 K [11]. As mentioned in Chapter 3, the stoichiometry of sample 3 was intentionally made slightly cation-deficient, and may contain cation vacancies. Such a defective structure could facilitate the occurrence of the spin-glass behavior, relieving the geometric frustration among the V spins. Whether the nature of the spin-glass ordering in sample 3 is similar to or different from that in $\text{Li}_{1-x}\text{Zn}_x\text{V}_2\text{O}_4$ noted above is at present unclear.

Intrinsic susceptibility

The intrinsic susceptibility $\chi(T)$ was derived from the observed $M^{\text{obs}}(T)$ data at fixed $H = 1$ T using

$$\chi(T) = \frac{M^{\text{obs}}(T) - M_{\text{imp}}(H, T)}{H} \quad (4.2)$$

where $M_{\text{imp}}(H, T)$ is given by Eq. (4.1) with $H = 1$ T and by the parameters for each sample given in Table 4.1, and T is the only variable. The $\chi(T)$ for each of the nine samples is shown in Figs. 4.8(a) and (b), along with $\chi^{\text{obs}}(T)$ for samples 1 and 6. A shallow broad peak in $\chi(T)$ is seen at a temperature $T_{\text{peak}} = 18, 16, 18, 18, 15, 17, 17, 5, 14$ K for samples 1–7, 4A and 4B, respectively. The peak profiles seen in $\chi(T)$ for the two magnetically purest samples 1 and 6 are regarded as most closely reflecting the intrinsic susceptibility of LiV_2O_4 . This peak shape is obtained in the derived $\chi(T)$ of all the samples except for sample 4A, as seen in Fig. 4.8(b). The physical nature of the magnetic impurities in sample

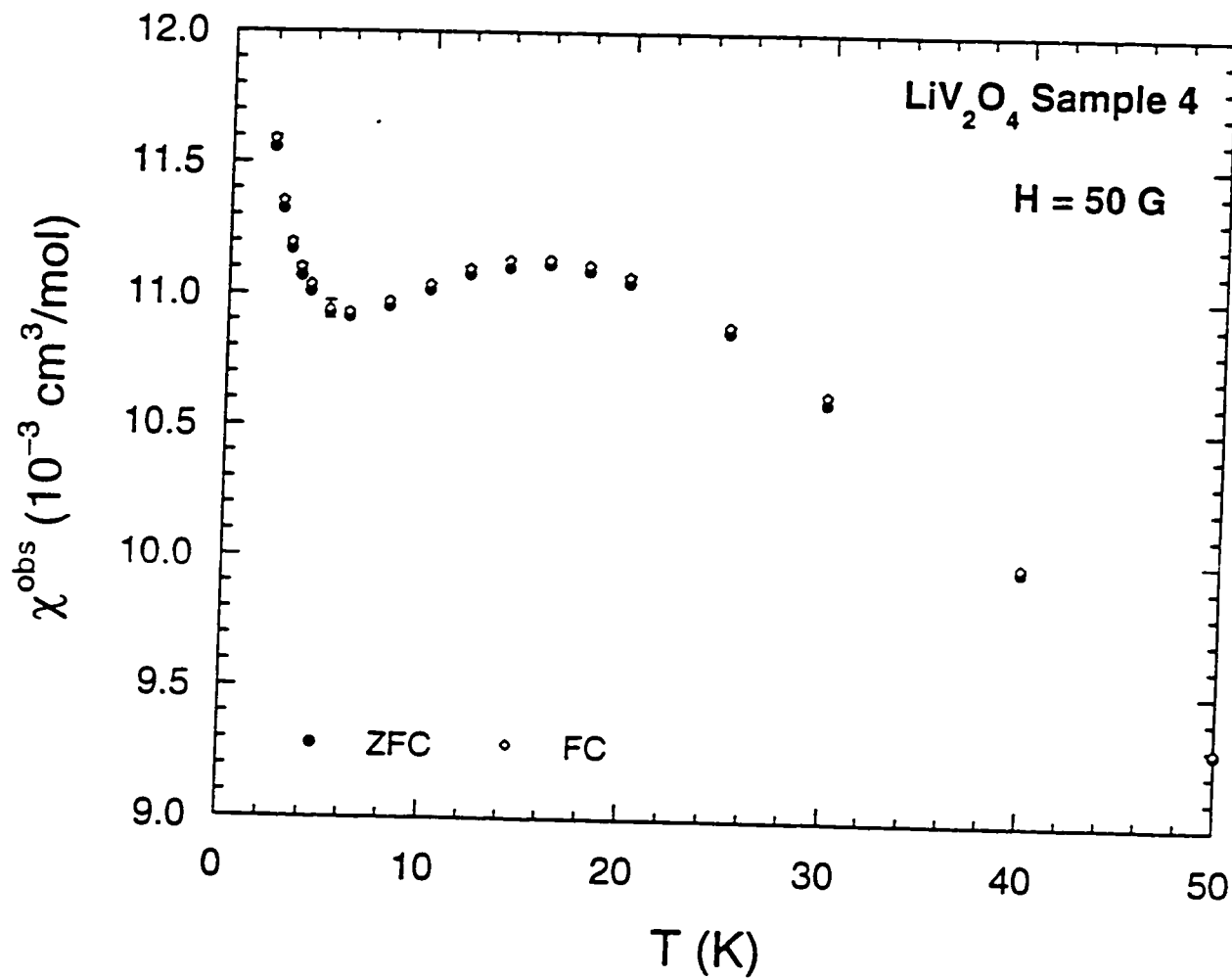


Figure 4.7 Observed magnetic susceptibility $\chi^{\text{obs}}(T) \equiv M^{\text{obs}}(T)/H$ versus temperature T in a low magnetic field $H = 50$ G of LiV₂O₄ sample 4 cooled in zero field (ZFC) and in the low field (FC).

4A is evidently different from that in the other samples. Except for the anomalous samples 4A and 4B, the $\chi(T=0)$ values were estimated from Figs. 4.8(a) and (b), neglecting the small residual increases at lowest T for samples 2, 6, 7 and 4B to be

$$\chi(0) = 9.8, 10.8, 9.6, 9.7, 10.0, 10.2, 10.2, 9.8 \times 10^{-3} \text{ cm}^3/\text{mol} \text{ (samples 1-7, 4B)} \quad (4.3)$$

Modeling of the intrinsic magnetic susceptibility

The Van Vleck susceptibility

The Van Vleck paramagnetic orbital susceptibility χ^{VV} may be obtained in favorable cases from the so-called K - χ analysis, i.e., if the transition metal NMR frequency shift K depends linearly on χ , with T an implicit parameter. One decomposes $\chi(T)$ per mole of transition metal atoms according to

$$\chi(T) = \chi^{\text{core}} + \chi^{\text{VV}} + \chi^{\text{spin}}(T) \quad (4.4)$$

We neglect the diamagnetic orbital Landau susceptibility, which should be small for d -electron bands [128]. The NMR shift is written in an analogous fashion as

$$K(T) = K^{\text{VV}} + K^{\text{spin}}(T) \quad (4.5)$$

a term K^{core} does not appear on the right-hand side of Eq. (4.5) because the absolute shift due to χ^{core} is expected to be about the same as in the Knight shift reference compound and hence does not appear in the shift measured with respect to the reference compound. Each component of K is written as a product of the corresponding component of χ and of the hyperfine coupling constant A as

$$K^{\text{VV}} = \frac{A^{\text{VV}}}{N_{\text{A}}\mu_{\text{B}}} \chi^{\text{VV}} \quad (4.6)$$

$$K^{\text{spin}} = \frac{A^{\text{spin}}}{N_{\text{A}}\mu_{\text{B}}} \chi^{\text{spin}} \quad (4.7)$$

Combining Eqs. (4.5), (4.6) and (4.7) yields

$$K = \frac{A^{\text{VV}}}{N_{\text{A}}\mu_{\text{B}}} \chi^{\text{VV}} + \frac{A^{\text{spin}}}{N_{\text{A}}\mu_{\text{B}}} \chi^{\text{spin}} \quad (4.8)$$

If $K(T)$ varies linearly with $\chi(T)$, then the slope is $A^{\text{spin}}/N_{\text{A}}\mu_{\text{B}}$ since χ^{VV} (and χ^{core}) is normally independent of T . We write the observed linear relation as

$$K = K_0 + \frac{A^{\text{spin}}}{N_{\text{A}}\mu_{\text{B}}} \chi \quad (4.9)$$

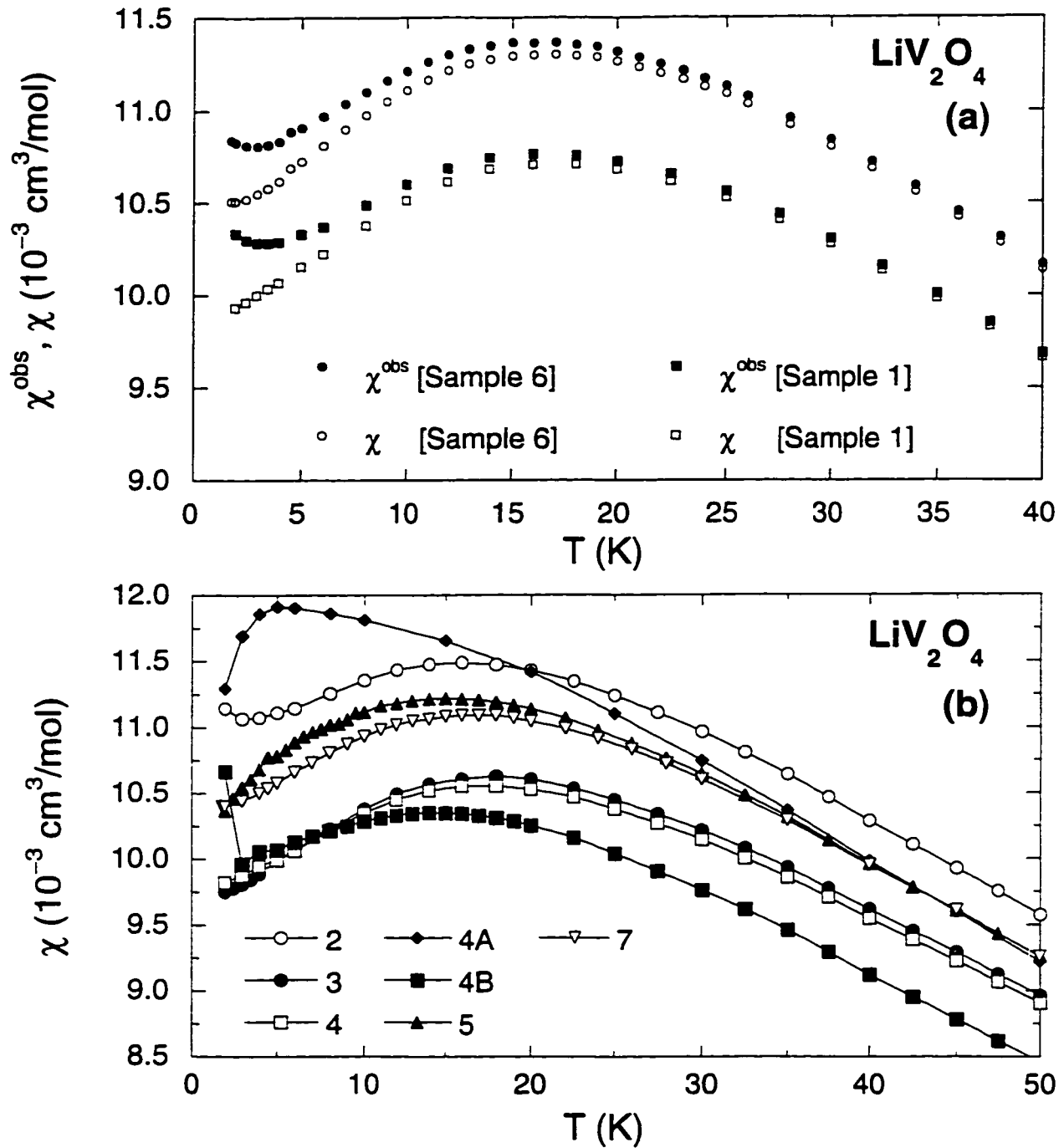


Figure 4.8 Observed susceptibilities χ^{obs} and derived intrinsic susceptibilities χ versus temperature T of (a) samples 1 and 6 and (b) samples 2, 3, 4, 5, 7, 4A and 4B. The solid lines are guides to the eye.

Setting the right-hand-sides of Eqs. (4.8) and (4.9) equal to each other gives

$$\chi^{\text{VV}} = \frac{N_{\text{A}}\mu_{\text{B}}K_{\text{o}} + A^{\text{spin}}\chi^{\text{core}}}{A^{\text{VV}} - A^{\text{spin}}} . \quad (4.10)$$

From ^{51}V NMR and $\chi(T)$ measurements, the K vs. χ relationship for LiV_2O_4 was determined by Amako *et al.* [90] and was found to be linear from 100–300 K, as shown in Fig. 4.9. Our fit to their data gave

$$K = 0.0117(4) - \left[17.08(21) \frac{\text{mol V}}{\text{cm}^3} \right] \chi \left(\frac{\text{cm}^3}{\text{mol V}} \right) . \quad (4.11)$$

shown as the straight line in Fig. 4.9. Comparison of Eqs. (4.9) and (4.11) yields

$$K_{\text{o}} = 0.0117(4) . \quad (4.12)$$

$$A^{\text{spin}} = -95.4(12) \text{ kG} . \quad (4.13)$$

The orbital Van Vleck hyperfine coupling constants for V^{+3} and V^{+4} are similar. For atomic V^{+3} , one has $A^{\text{VV}} = 403 \text{ kG}$ [129]. We will assume that A^{VV} in LiV_2O_4 is given [130] by that for atomic V^{+4} ,

$$A^{\text{VV}} = 455 \text{ kG} . \quad (4.14)$$

The core susceptibility is estimated here from Selwood's table [131], using the contributions [in units of $-10^{-6} \text{ cm}^3/(\text{mol ion})$] 1 for Li^{+1} , 7 for V^{+4} and 12 for O^{-2} , to be

$$\chi^{\text{core}} = -63 \times 10^{-6} \frac{\text{cm}^3}{\text{mol}} . \quad (4.15)$$

Inserting Eqs. (4.12), (4.13), (4.14) and (4.15) into (4.10) yields

$$\chi^{\text{VV}} = 2.48(9) \times 10^{-4} \frac{\text{cm}^3}{\text{mol}} . \quad (4.16)$$

Mahajan *et al.* [19] have measured the ^{51}V $K(T)$ for our LiV_2O_4 sample 2 from 78 to 575 K. Their data are plotted versus our measurement of $\chi^{\text{obs}}(T)$ for sample 2 from 74 to 400 K in Fig. 4.9. Applying the same K - χ analysis as above, we obtain

$$K_{\text{o}} = 0.0101(3) . \quad (4.17)$$

$$A^{\text{spin}} = -76.9(8) \text{ kG} , \quad (4.18)$$

$$\chi^{\text{VV}} = 2.22(6) \times 10^{-4} \frac{\text{cm}^3}{\text{mol}} . \quad (4.19)$$

where the linear fit of K vs. χ^{obs} is shown by the dashed line in Fig. 4.9.

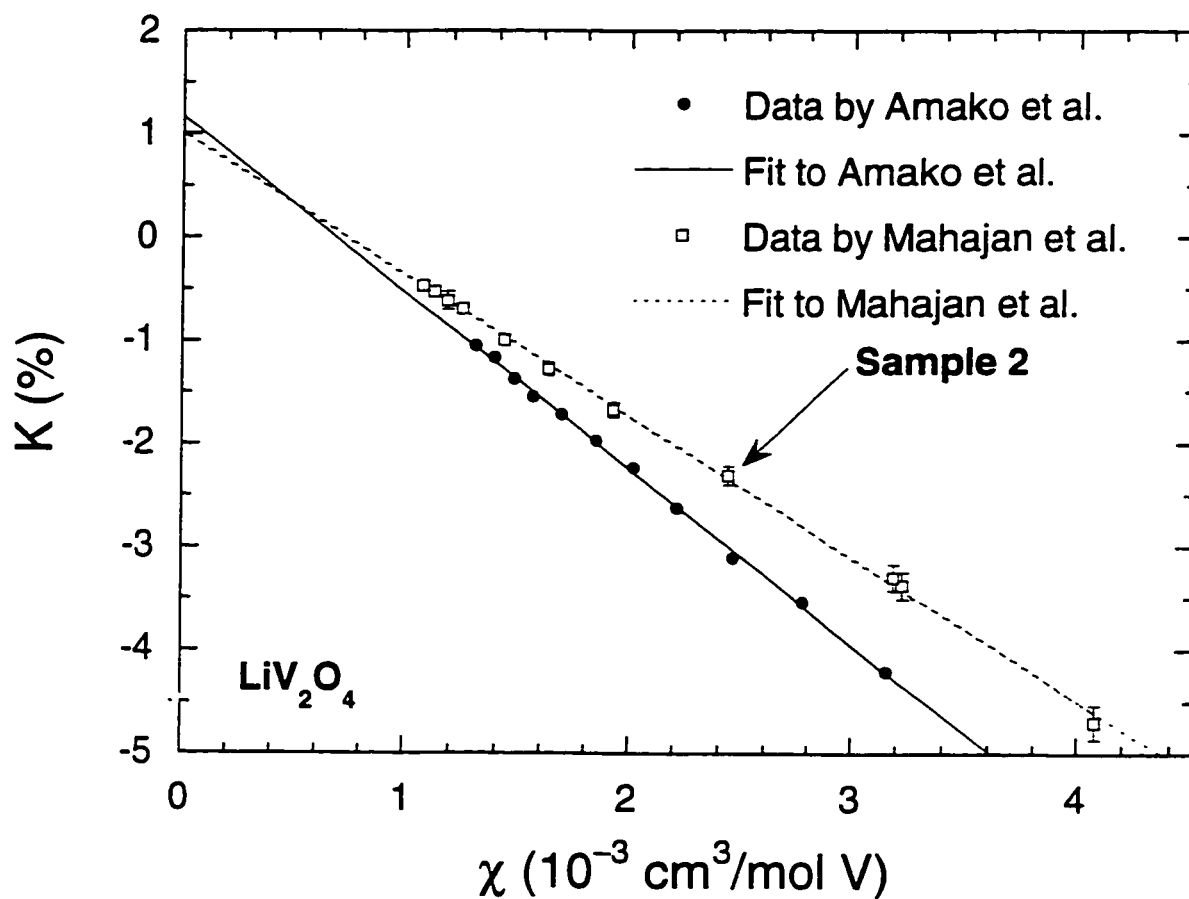


Figure 4.9 ^{51}V NMR Knight shift K versus observed magnetic susceptibility χ^{obs} for LiV_2O_4 by Amako *et al.* [8, 90] and by Mahajan *et al.* [19] for LiV_2O_4 sample 2. The solid and dashed lines are linear fits to the respective data according to Eq. (4.11).

We may compare our similar values of χ^{VV} for LiV_2O_4 in Eqs. (4.16) and (4.19) with those obtained from K - χ analyses of other oxides containing V^{+3} and V^{+4} . For stoichiometric V_2O_3 above its metal-insulator transition temperature of ~ 160 K. Jones [132] and Takigawa *et al.* [129] respectively obtained $\chi^{\text{VV}} = 2.10$ and $2.01 \times 10^{-4} \text{ cm}^3/(\text{mol V})$. Kikuchi *et al.* [133] obtained $\chi^{\text{VV}} = 0.92 \times 10^{-4} \text{ cm}^3/(\text{mol V})$ for LaVO_3 , whereas for VO_2 , Pouget *et al.* [130] obtained $\chi^{\text{VV}} = 0.65 \times 10^{-4} \text{ cm}^3/(\text{mol V})$.

High-temperature series expansion analysis of the susceptibility

Above ~ 50 K the monotonically decreasing susceptibility of LiV_2O_4 with increasing T has been interpreted by previous workers in terms of the Curie-Weiss law for a system of spins $S = 1/2$ and $g \approx 2$ [2, 5, 6, 7, 8, 9]. To extend this line of analysis, we have fitted $\chi(T)$ by the high-temperature series expansion (HTSE) prediction [88, 134] up to sixth order in $1/T$. The assumed nearest-neighbor (NN) Heisenberg Hamiltonian between localized moments reads

$$\mathcal{H} = J \sum_{(i,j)} \vec{S}_i \cdot \vec{S}_j \quad . \quad (4.20)$$

where the sum is over all nearest-neighbor pairs. J is the NN exchange coupling constant and $J > 0$ denotes AF interactions. A HTSE of $\chi_{\text{HTSE}}^{\text{spin}}(T)$ arising from this Hamiltonian up to the n^{max} -th order of $J/k_B T$ for general lattices and spin S was determined by Rushbrooke and Wood [88], given per mole of spins by

$$\frac{N_A g^2 \mu_B^2}{\chi_{\text{HTSE}}^{\text{spin}}(T) J} = \frac{3k_B T}{S(S+1)J} \sum_{n=0}^{n^{\text{max}}} b_n \left(\frac{J}{k_B T} \right)^n \quad . \quad (4.21)$$

where $b_0 \equiv 1$. The b_n coefficients for $S = 1/2$ up to sixth order ($n = 6$) are

$$\begin{aligned} b_1 &= \frac{z}{4} \quad , \quad b_2 = \frac{z}{8} \quad , \quad b_3 = \frac{z}{24} (1 - \frac{5p_1}{8}) \quad , \quad b_4 = \frac{z}{768} (13 - 5z - 15p_1 + 5p_2) \quad , \\ b_5 &= -\frac{z}{15360} (90z - 122 + 245p_1 - 60zp_1 - 45p_1^2 - 90p_2 + 25p_3) \quad , \\ b_6 &= \frac{z}{184320} (134z^2 - 783z + 713 + 908zp_1 - 2697p_1 - 106zp_1^2 + 1284p_1^2 - 234zp_2 \\ &\quad + 849p_2 - 291p_3 + 75p_4 - 288p_1p_2 - 51q - 8r) \quad . \end{aligned} \quad (4.22)$$

Here z is the nearest-neighbor coordination number, and p_n , q and r are so-called lattice parameters which depend upon the geometry of the magnetic lattice. The Curie Law corresponds to maximum order $n^{\text{max}} = 0$, and the Curie-Weiss Law to maximum order $n^{\text{max}} = 1$. For the B sublattice of a normal-spinel structure compound $\text{A}[\text{B}_2]\text{O}_4$, which is geometrically frustrated for AF interactions, the parameters are $z = 6$, $p_1 = 2$, $p_2 = 2$, $p_3 = 0$, $p_4 = 2$, $q = 0$, $r = 2$. For $S = 1/2$, Eq. (4.22) then yields

$$b_1 = \frac{3}{2} \quad , \quad b_2 = \frac{3}{4} \quad , \quad b_3 = -\frac{1}{16} \quad , \quad b_4 = -\frac{37}{128} \quad , \quad b_5 = \frac{43}{640} \quad , \quad b_6 = \frac{1361}{6144} \quad . \quad (4.23)$$

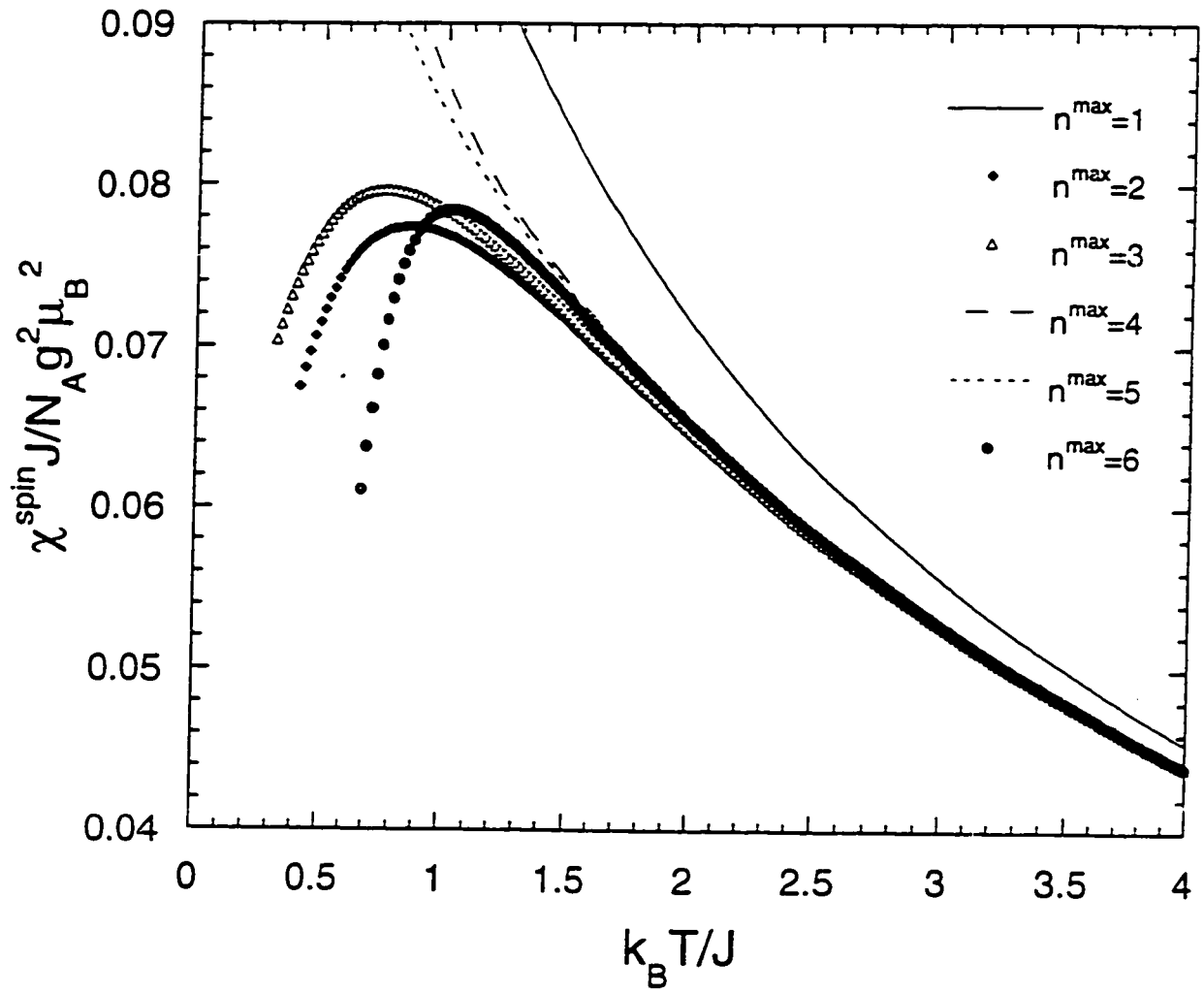


Figure 4.10 High-temperature series expansion predictions of $\chi_{\text{HTSE}}^{\text{spin}}$ versus temperature T [Eq. (4.21)] for the antiferromagnetically coupled spins $S = 1/2$ in the vanadium sublattice of LiV_2O_4 with $n^{\text{max}} = 1-6$.

Figure 4.10 illustrates the HTSE predictions of Eq. (4.21) for $S = 1/2$ using these b_n coefficients for $n^{\max} = 1$ to 6. The theoretical $\chi_{\text{HTSE}}^{\text{spin}}(T)$ predictions with $n^{\max} = 2, 3$ and 6 exhibit broad maxima as seen in our experimental $\chi(T)$ data. The prediction with $n^{\max} = 6$ is evidently accurate at least for $k_{\text{B}}T/J \gtrsim 1.6$; at lower T , the theoretical curves with $n^{\max} = 5$ and 6 diverge noticeably from each other on the scale of Fig. 4.23. Our fits given below of the experimental data by the theoretical $\chi^{\text{spin}}(T)$ prediction were carried out over temperature ranges for which $k_{\text{B}}T/J \gtrsim 1.6$. The Weiss temperature θ in the Curie-Weiss law is given for coordination number $z = 6$ and $S = 1/2$ by

$$\theta = -\frac{zJS(S+1)}{3k_{\text{b}}} = -\frac{3J}{2k_{\text{B}}} . \quad (4.24)$$

To fit the HTSE calculations of $\chi^{\text{spin}}(T)$ to experimental data, we assume that the experimentally determined intrinsic susceptibility $\chi(T)$ is the sum of a T -independent term χ_0 and $\chi_{\text{HTSE}}^{\text{spin}}(T)$,

$$\chi(T) = \chi_0 + \chi_{\text{HTSE}}^{\text{spin}}(T) . \quad (4.25)$$

with $\chi_{\text{HTSE}}^{\text{spin}}(T)$ given by Eq. (4.21) and the b_n coefficients for $S = 1/2$ in Eq. (4.23). The three parameters to be determined are χ_0 , g and J/k_{B} . The fitting parameters for samples 1–7, 4A and 4B using $n^{\max} = 6$, and for sample 1 also using $n^{\max} = 2$ and 3, are given in Table 4.2 for the 50–400 K and 100–400 K fitting ranges. The fits for these two fitting ranges for sample 1 and $n^{\max} = 6$ are shown in Fig. 4.11. Both g and J/k_{B} tend to decrease as the lower limit of the fitting range increases. The HTSE fits for all the samples yielded the ranges $C = N_{\text{A}}g^2\mu_{\text{B}}^2/(4k_{\text{B}}) = 0.36\text{--}0.48\text{ cm}^3\text{ K}/(\text{mol V})$ and $\theta = -20$ to -42 K. These ranges are in agreement with those reported previously (see Table 1.5). χ_0 was found to be sensitive to the choice of fitting temperature range. For the 50–400 K range, χ_0 was negative for some samples. Recalling the small negative value of the core diamagnetic contribution in Eq. (4.15) and the larger positive value of the Van Vleck susceptibility in Eqs. (4.16) and (4.19), it is unlikely that χ_0 [defined in Eq. (4.29)] would be negative. Negative values of χ_0 occur when the low- T limit of the fitting range is below 100 K, and may therefore be a spurious consequence of the crossover between the local moment behavior at high T and the HF behavior at low T .

To eliminate χ_0 as a fitting parameter, we fitted $d\chi/dT$ by the HTSE prediction for that quantity. In order to generate the experimental $d\chi/dT$, we first employed the following function to obtain an analytic expression for $\chi(T)$,

$$\chi(T) = \frac{a_1 + a_2T + a_3T^2 + a_4T^3 + a_5T^4}{a_6 + a_7T + a_8T^2 + a_9T^3 + T^4} . \quad (4.26)$$

The $\chi(T)$ of samples 1 and 6 for the entire T ranges 2–400 K and 1.8–400 K, respectively, can be fitted well by Eq. (4.26) and the a_n coefficients are listed in Table 4.3. The rms deviation of the fit from the

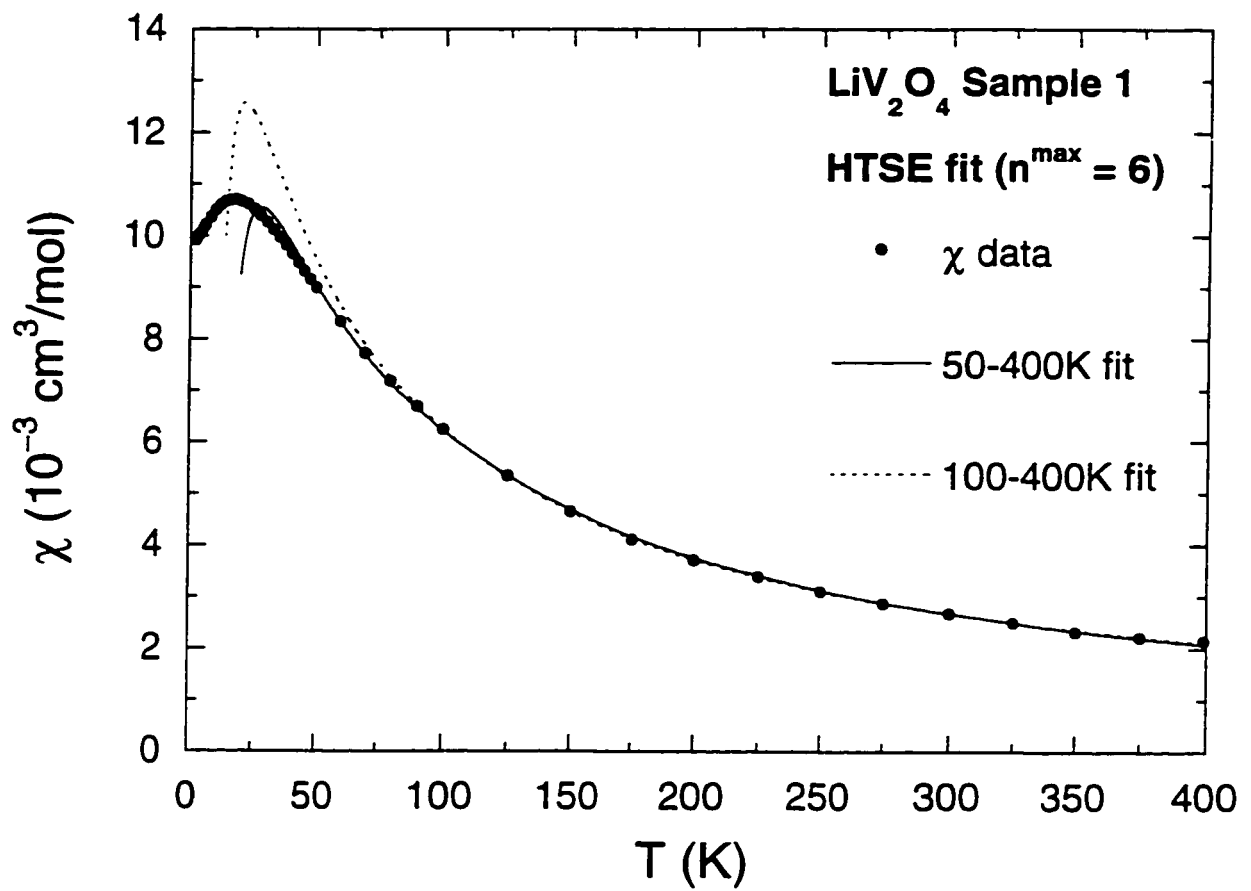


Figure 4.11 Intrinsic susceptibility χ versus temperature T for LiV_2O_4 sample 1 (filled circles) and fits (curves) by the high- T series expansion (HTSE) prediction to 6th order in $1/T$ for the 50–400 and 100–400 K temperature ranges.

Table 4.2 Results of high-temperature series expansion calculation fits to the experimental intrinsic magnetic susceptibility data for LiV_2O_4 . The temperature independent susceptibility, χ_0 , is in units of $10^{-4} \text{ cm}^3/\text{mol}$, and J/k_B is in K. The error in the last digit of a quantity is given in parentheses.

Sample No.	n^{max}	50–400 K			100–400 K		
		χ_0	g	J/k_B	χ_0	g	J/k_B
1	2	0.8(4)	2.17(1)	25.8(5)	2.7(3)	2.07(2)	20(1)
1	3	0.7(4)	2.18(2)	26.2(6)	2.6(3)	2.07(2)	20(1)
1	6	0.5(4)	2.19(2)	26.9(7)	2.6(3)	2.07(2)	20(1)
2	6	−0.2(5)	2.26(2)	26.7(8)	2.6(3)	2.11(2)	19(1)
3	6	−1.3(5)	2.23(2)	27.8(7)	1.4(3)	2.08(2)	20.5(8)
4	6	1.1(6)	2.16(3)	26.4(9)	4.1(5)	1.99(3)	17(2)
4A	6	−0.6(8)	2.20(3)	26.(1)	2.3(2)	2.05(1)	18.1(6)
4B	6	−0.7(5)	2.12(2)	26.2(8)	1.8(5)	1.97(3)	18(2)
5	6	1.2(7)	2.17(3)	25.(1)	4.9(7)	1.95(4)	13(2)
6	6	0.8(1)	2.251(6)	26.5(2)	3.3(7)	2.108(4)	18.4(2)
7	6	0.5(3)	2.20(1)	25.8(5)	3.0(1)	2.051(8)	17.5(4)

data for sample 1 (sample 6) is 0.29% (0.21%), while the maximum deviation is 1.3% (0.48%). Using Eq. (4.26), $d\chi/dT$ was computed and is plotted in Fig. 4.12 for sample 1. These data were fitted by $d\chi_{\text{HTSE}}^{\text{spin}}/dT$ obtained from the HTSE prediction Eq. (4.21) with $n^{\text{max}} = 6$, where the fitting parameters are now g and J/k_B . The fits were carried out over the same two T ranges as in Fig. 4.11: Table 4.4 displays the fitting parameters and the fits are plotted in Fig. 4.12. Of the two fitting ranges, the 100–400 K fit is the best fit inside the respective range, though it shows a large deviation from the data below this range. Using the fitting parameters, the HTSE $\chi^{\text{spin}}(T)$ is obtained from Eq. (4.21). According to Eq. (4.25), the difference between the experimental $\chi(T)$ and $\chi_{\text{HTSE}}^{\text{spin}}(T)$, $\delta\chi(T) = \chi(T) - \chi_{\text{HTSE}}^{\text{spin}}(T)$, should represent the T -independent contribution χ_0 . $\delta\chi(T)$ is plotted for sample 1 versus T in Fig. 4.13 for the 50–400 K and 100–400 K fit ranges. Again, the superiority of the 100–400 K fitting range to the other is evident, *i.e.*, χ_0 is more nearly constant for this fitting range. χ_0 for the 50–400 K fit range is negative within the range. This sign is opposite to that obtained in the first HTSE fitting results in Table 4.2. This inconsistency found in the fit using a low T limit below 100 K may again be due to changing physics in the crossover regime, which would invalidate the parameters. By averaging the χ_0 values for sample 1 in the range 100–400 K, we conclude that the T -independent contribution to the

susceptibility is

$$\chi_0 = 2.00(4) \times 10^{-4} \text{ cm}^3/\text{mol} \text{ (sample 1)} . \quad (4.27)$$

Similarly, for sample 6 we obtain

$$\chi_0 = 2.11(1) \times 10^{-4} \text{ cm}^3/\text{mol} \text{ (sample 6)} . \quad (4.28)$$

Table 4.3 Coefficients a_n in Eq. (4.26) in the fit to the intrinsic susceptibility of LiV_2O_4 sample 1 for the temperature range 2–400 K and of sample 6 for 1.8–400 K.

	sample 1	sample 6
a_1	6582.265	16550.251
a_2	-249.28006	-915.01623
a_3	32.222161	33.136264
a_4	0.66645683	0.62427567
a_5	0.00047520063	0.00063083797
a_6	672225.75	1606070.2
a_7	-29971.386	-102780.73
a_8	3467.6212	4270.2043
a_9	30.324884	6.8469583

Table 4.4 Parameters g and J/k_B obtained by fitting the temperature derivative of the experimental intrinsic susceptibility data by the temperature derivative of the HTSE spin susceptibility [Eq. (4.21)] with $n^{max} = 6$ for LiV_2O_4 samples 1 and 6. The error in the last digit of a quantity is given in parentheses.

Sample no.	50–400 K		100–400 K	
	g	J/k_B (K)	g	J/k_B (K)
1	2.275(3)	29.61(7)	2.103(2)	22.27(8)
6	2.402(4)	31.61(9)	2.174(3)	22.1(1)

In the itinerant plus localized moment model implicitly assumed in this section, χ_0 can be decomposed as

$$\chi_0 = \chi^{\text{core}} + \chi^{\text{VV}} + \chi^{\text{Pauli}} , \quad (4.29)$$

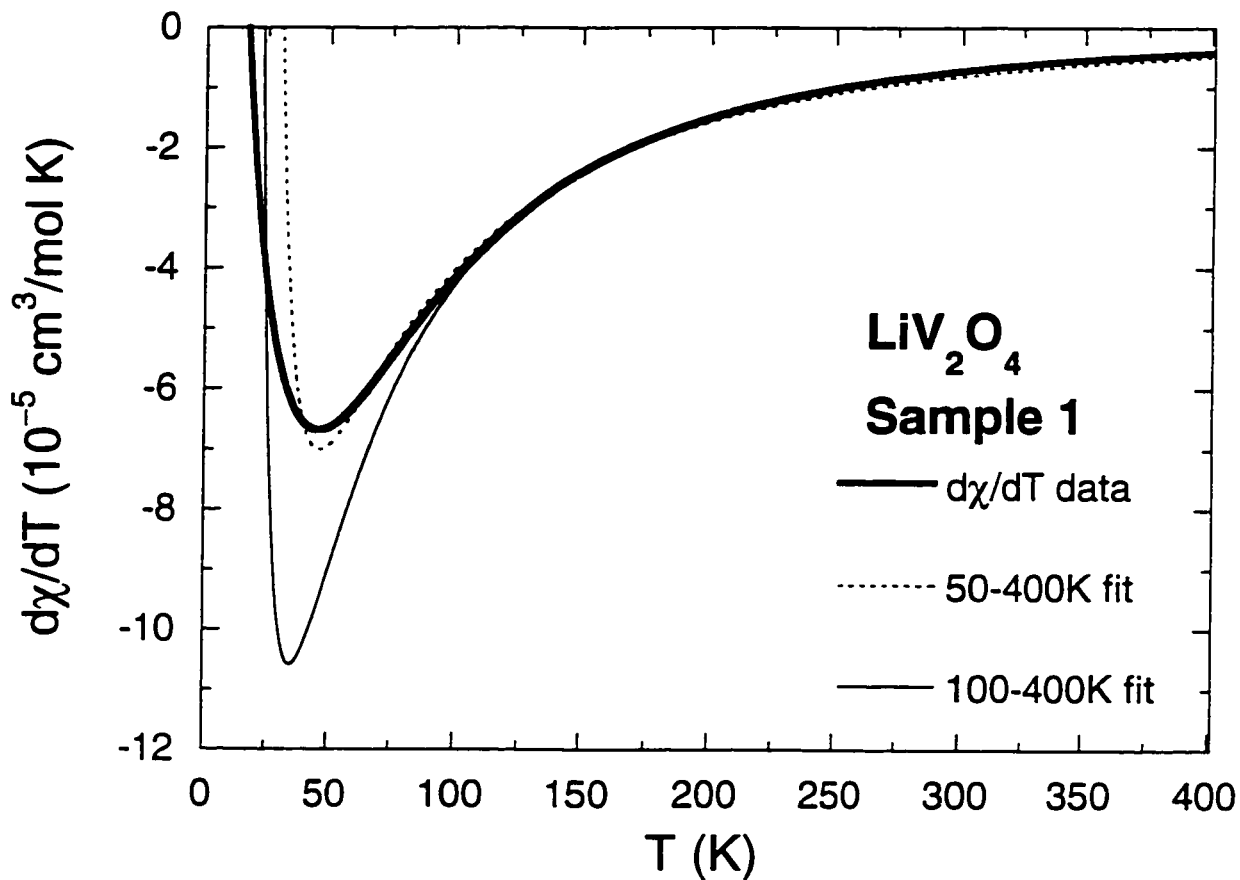


Figure 4.12 Temperature derivative of the experimental intrinsic susceptibility, $d\chi/dT$, for LiV_2O_4 sample 1 (heavy solid curve), generated using Eq. (4.26) with the coefficients a_n from Table 4.3. Fits by the T derivative of the HTSE prediction $d\chi^{\text{spin}}/dT$ in Eq. (4.21) are also shown for T ranges of 50–400 K (dashed curve) and 100–400 K (light solid curve).

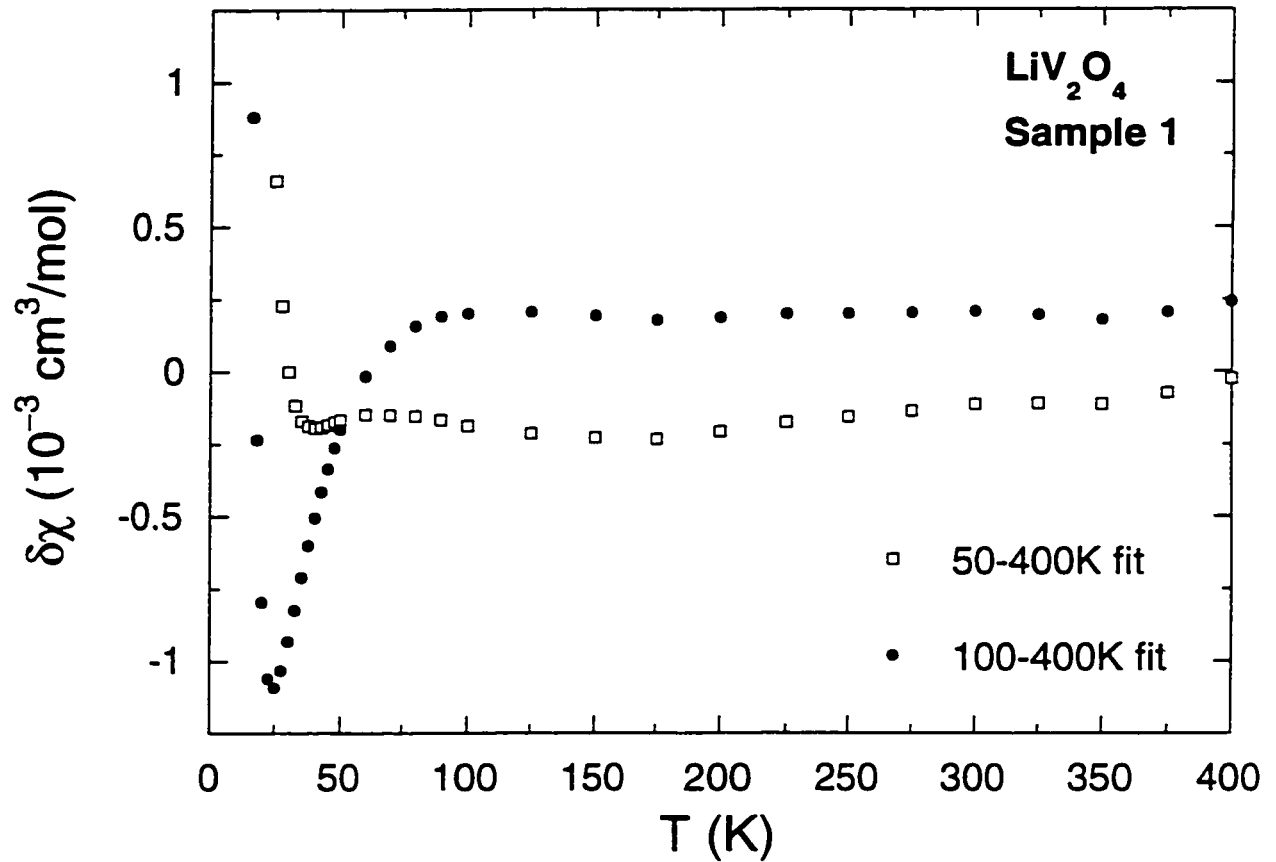


Figure 4.13 The differences between the experimental intrinsic susceptibility $\chi(T)$ of LiV_2O_4 sample 1 and the HTSE prediction χ^{spin} obtained from the T derivative analysis, $\delta\chi(T) \equiv \chi(T) - \chi^{\text{spin}}$, versus temperature T for the fitting T ranges of 50–400 K (open squares) and 100–400 K (filled circles). For a valid fit, these differences should be the T -independent susceptibility χ_0 .

where χ^{Pauli} is the temperature-independent Pauli spin susceptibility of the conduction electrons. Using the results in Eqs. (4.15), (4.19) and (4.27), for sample 1 we find

$$\chi^{\text{Pauli}} = 0.41(10) \times 10^{-4} \text{ cm}^3/\text{mol} \quad (\text{sample 1}) \quad . \quad (4.30)$$

For sample 6, we similarly obtained

$$\chi^{\text{Pauli}} = 0.52(7) \times 10^{-4} \text{ cm}^3/\text{mol} \quad (\text{sample 6}) \quad . \quad (4.31)$$

These χ^{Pauli} values are approximately four times smaller than that obtained for LiV_2O_4 by Mahajan *et al.* [19]. They used $\chi^{\text{obs}}(T)$ in the T range 100–800 K, combining our $\chi^{\text{obs}}(T)$ data to 400 K and those of Hayakawa *et al.* [9] to 800 K. By fitting these combined data by the expression $\chi^{\text{obs}}(T) = \chi_0 + 2C/(T - \theta)$, they obtained $\chi_0 = 5.45 \times 10^{-4} \text{ cm}^3/\text{mol}$. As shown above, the value of χ_0 is sensitive to the fitting temperature range. For LiTi_2O_4 , $\chi^{\text{Pauli}} \sim 2 \times 10^{-4} \text{ cm}^3/\text{mol}$ [4, 135] between 20 and 300 K, which is a few times larger than we find for LiV_2O_4 in Eqs. (4.30) and (4.31).

Crystal field model

The ground state of a free ion with one $3d$ electron is ${}^2D_{3/2}$ and has five-fold orbital degeneracy. The point symmetry of a V atom in LiV_2O_4 is trigonal. If we consider the crystalline electric field (CEF) seen by a V atom arising from only the six nearest-neighbor oxygen ions, the CEF due to a perfect oxygen octahedron is cubic (O_h symmetry), assuming here point charges for the oxygen ions. In this CEF the degeneracy of the five d orbitals of the vanadium atom is lifted and the orbitals are split by an energy “ $10Dq$ ” into a lower orbital t_{2g} triplet and a higher orbital e_g doublet. However, in LiV_2O_4 each V-centered oxygen octahedron is slightly distorted along one of the $\langle 111 \rangle$ directions [see Fig. 1.14(b)], as discussed in Chapter 1. This distortion lowers the local symmetry of the V atom to D_{3d} (trigonal) and causes a splitting of the t_{2g} triplet into an A_{1g} singlet and an E_g doublet. It is not clear to us which of the E_g or A_{1g} levels become the ground state, and how large the splitting between the two levels is. These questions cannot be answered readily without a knowledge of the magnitudes of certain radial integrals [136], and are not further discussed here [137]. However, this trigonal splitting is normally about an order of magnitude smaller than $10Dq$ [1]. In the following, we will examine the predictions for $\chi(T)$ of a d^1 or d^2 ion in a cubic CEF and compare with our experimental data for LiV_2O_4 .

Kotani [138] calculated the effective magnetic moment $\mu_{\text{eff}} \equiv p_{\text{eff}} \mu_B$ per d -atom for a cubic CEF using the Van Vleck formula [139]. The spin-orbit interaction is included, where the coupling constant

is λ . For an isolated atom $\mu_{\text{eff}}(T)$ is defined by

$$\chi(T) = \frac{N\mu_{\text{eff}}^2(T)}{3k_{\text{B}}T} . \quad (4.32)$$

where μ_{eff} is in general temperature-dependent and N is the number of magnetic atoms. With spin included, one uses the double group for proper representations of the atomic wavefunctions. Then in this cubic double group with one d -electron the six-fold (with spin) degenerate t_{2g} level splits into a quartet $\Gamma_8(t_{2g})$ and a doublet $\Gamma_7(t_{2g})$ [138, 140, 141]. The four-fold degenerate e_g level does not split and its representation is $\Gamma_8(e_g)$. For a positive λ as appropriate to a $3d$ atom with a less than half-filled d -shell, $\Gamma_8(t_{2g})$ is the ground state, and the first-order Zeeman effect does not split it: this ground state is non-magnetic. Kotani does not include in his calculations of μ_{eff} the possible coupling of $\Gamma_8(t_{2g})$ and $\Gamma_8(e_g)$, which have the same symmetry, and assumes that the cubic CEF splitting $10Dq$ is large enough to prevent significant mixing. On the other hand, the cubic double group with two d -electrons gives an orbitally nondegenerate, five-fold spin-degenerate, ground state with angular momentum quantum number $\mathcal{J} = 2$ which splits into five non-degenerate levels under a magnetic field. The spin-orbit coupling constant is $\lambda = +250 \text{ cm}^{-1}$ for d^1 (V^{+4}) and $+105 \text{ cm}^{-1}$ for d^2 (V^{+3}) [142]. The effective moment is defined from the observed molar susceptibility of LiV_2O_4 as

$$\chi^{\text{obs}}(T) = \chi_0 + \frac{2N_{\text{A}}[p_{\text{eff}}^{\text{obs}}(T)]^2\mu_{\text{B}}^2}{3k_{\text{B}}T} . \quad (4.33)$$

where χ_0 is given by Eq. (4.27). Kotani's results from the Van Vleck equations are

$$p_{\text{eff}}^{(1)} = \left[\frac{8 + (3x - 8)e^{-\frac{1}{2}x}}{x(2 + e^{-\frac{1}{2}x})} \right]^{1/2} \quad (4.34)$$

for the d^1 ion, and

$$p_{\text{eff}}^{(2)} = \left[\frac{3(\frac{5}{2}x + 15 + (\frac{x}{2} + 9)e^{-x} - 24e^{-\frac{3}{2}x})}{x(5 + 3e^{-x} + e^{-\frac{3}{2}x})} \right]^{1/2} \quad (4.35)$$

for the d^2 ion, where $x \equiv \lambda/k_{\text{B}}T$. Figure 4.14 shows $p_{\text{eff}}^{\text{obs}}$, $p_{\text{eff}}^{(1)}$ and $p_{\text{eff}}^{(2)}$ as a function of T . For comparison also shown is $p_{\text{eff}}^{(1+2)}$ obtained by assuming that $p_{\text{eff}}^{\text{obs}}(T)$ arises from an equal mixture of V^{+3} and V^{+4} localized moments. None of the three calculated curves agrees with the experimental data over the full temperature range. However, in all three calculations p_{eff} increases with T , in qualitative agreement with the data, perhaps implying the importance of orbital degeneracy in LiV_2O_4 and/or antiferromagnetic coupling between vanadium spins. The nearly T -independent $p_{\text{eff}}^{\text{obs}} \approx 1.8$ for $T \gtrsim 100 \text{ K}$ is close to the spin-only value $p_{\text{eff}} = g\sqrt{S(S+1)}$ with $S = 1/2$ and $g \approx 2$, as expected in the *absence* of orbital degeneracy.

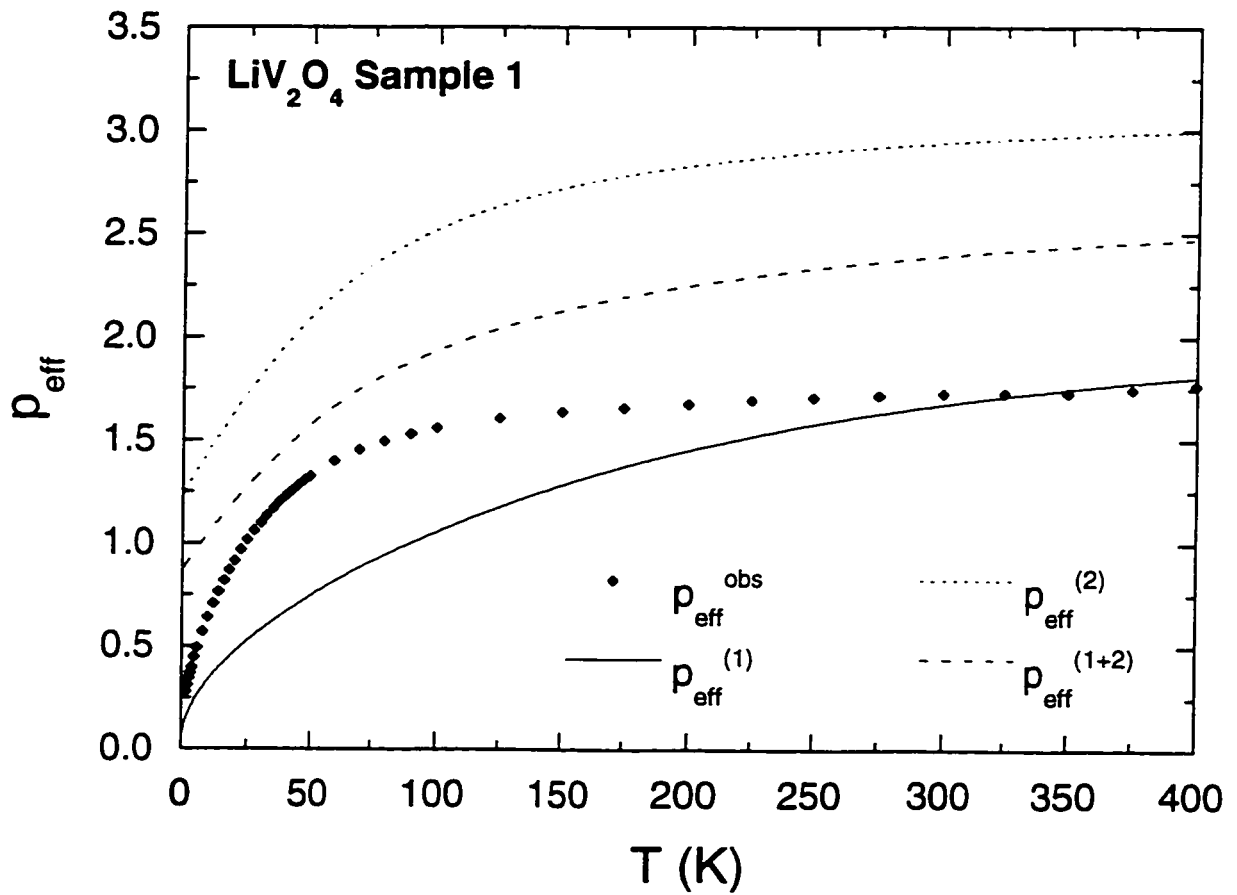


Figure 4.14 Observed effective magnetic moment in μ_B , $p_{\text{eff}}^{\text{obs}}$, versus temperature T of LiV_2O_4 sample 1 (filled diamonds). Also shown as the curves are the predictions $p_{\text{eff}}^{(1)}$ for d^1 ions and $p_{\text{eff}}^{(2)}$ for d^2 ions by Kotani [138], and $p_{\text{eff}}^{(1+2)}$ for an equal mixture of d^1 and d^2 ions.

Spin-1/2 Kondo model and Coqblin-Schrieffer model

$\chi^{\text{obs}}(T)$ data for f -electron HF compounds are often found similar to the predictions of the single-ion Kondo model [57, 143, 144, 145, 58] for spin $S = 1/2$ or its extension to $S > 1/2$ in the Coqblin-Schrieffer model [146, 147]. The zero-field impurity susceptibility $\chi_{\text{CS}}(T)$ of the Coqblin-Schrieffer model was calculated exactly as a function of temperature by Rajan [147]. His numerical results $\chi_{\text{CS}}(T)$ for impurity spin $\mathcal{J} = 1/2, \dots, 7/2$ show a Curie-Weiss-like $1/T$ dependence (with logarithmic corrections) for $T \gg T_{\text{K}}$, where T_{K} is the Kondo temperature. As T decreases, $\chi_{\text{CS}}(T)$ starts to deviate from the $1/T$ dependence, shows a peak at $T \approx 0.2T_{\text{K}}$ only for $\mathcal{J} \geq 3/2$, and levels off for $T \lesssim 0.2T_{\text{K}}$ for all \mathcal{J} .

In the zero temperature limit the molar susceptibility for $\mathcal{J} = S = 1/2$ (which corresponds to the $S = 1/2$ Kondo model) is [147]

$$\chi_{\text{CS}}(T \rightarrow 0) = \frac{0.10268 N_{\text{A}} g^2 \mu_{\text{B}}^2}{k_{\text{B}} T_{\text{K}}} . \quad (4.36)$$

Setting $g = 2$, and using the intrinsic $\chi(T \rightarrow 0) = 0.0049 \text{ cm}^3/(\text{mol V})$ for LiV_2O_4 sample 1 from Eq. (4.3), Eq. (4.36) yields the Kondo temperature

$$T_{\text{K}} = 32.1 \text{ K} . \quad (4.37)$$

On the other hand, if the g -value of 2.103 from Table 4.4 (100–400 K range) is employed instead, the Kondo temperature is

$$T_{\text{K}} = 35.5 \text{ K} . \quad (4.38)$$

The temperature dependence of the impurity susceptibility of the $S = 1/2$ Kondo model was obtained using accurate Bethe ansatz calculations by Jerez and Andrei [148]. We fitted these results by the following ratio of polynomials

$$\frac{\chi_{\text{CS}} k_{\text{B}} T_{\text{K}}}{N_{\text{A}} g^2 \mu_{\text{B}}^2} = \frac{a_1 + a_2 x + a_3 x^2 + a_4 x^3}{a_5 + a_6 x + a_7 x^2 + a_8 x^3 + x^4} . \quad (4.39)$$

where $x \equiv T/T_{\text{K}}$. This analytic form converges to a finite value for $T \rightarrow 0$, and approaches a Curie law ($\propto 1/T$) in the high- T limit, as required by the Kondo model. The coefficients a_n for the fitting range $0.012849 \leq x \leq 102.53$ are listed in Table 4.5. The numerical data of Jerez and Andrei and our fit to their data are plotted in Fig. 4.15. The rms deviation of the fit values from the Bethe ansatz calculation values is 0.13%, and the maximum deviation is found to be 1.0% at the upper limit $T/T_{\text{K}} = 102.53$. For the low- x range of 0.012849–9.5982 (relevant to a fit of the theory to our experimental data), the rms deviation is 0.01%, whereas the maximum deviation is 0.04% at $T/T_{\text{K}} = 8.8867$. Using the above-stated g -values and T_{K} from Eqs. (4.37) and (4.38), the $\chi_{\text{CS}}(T)$ calculations are compared with our

$\chi(T)$ data in Fig. 4.16. Note that in Fig. 4.16, both the T -independent χ_0 [Eq. (4.27)] and impurity susceptibilities are already subtracted from χ^{obs} . Although the T_K values in Eqs. (4.37) and (4.38) are comparable to those obtained from heat capacity analyses [11, 14], the $S = 1/2$ Kondo model predictions for $\chi(T)$ with these T_K values do not agree with our observed temperature dependence. This failure is partly due to the fact that our $\chi(T)$ exhibits a weak maximum whereas the $S = 1/2$ Kondo model calculation does not.

Table 4.5 Coefficients a_n in Eq. (4.39) in the fits to the theoretical data for the susceptibility vs. temperature of the $\mathcal{J} = S = 1/2$ Kondo model by Jerez and Andrei [148] and the Coqblin-Schrieffer model (for $\mathcal{J} > 1/2$) by Rajan [147]. Temperature ranges of the fits are in units of T_K , where T_K is the Kondo temperature.

T Range	$\mathcal{J} = 1/2$	$\mathcal{J} = 1$	$\mathcal{J} = 3/2$	$\mathcal{J} = 2$	$\mathcal{J} = 5/2$	$\mathcal{J} = 3$	$\mathcal{J} = 7/2$
	0.01–100	0.01–50	0.01–30	0.01–30	0.01–20	0.01–20	0.01–20
a_1	0.73154	0.25221	0.35665	0.60875	3.207	1.0982	1.6387
a_2	2.2266	0.618	1.3195	1.8565	3.8544	-0.9116	-2.0406
a_3	2.9967	3.2186	7.051	18.001	96.277	43.219	86.929
a_4	0.1992	0.51585	1.1	1.7213	2.3977	3.1439	4.1247
a_5	7.1161	0.61359	0.34579	0.29505	0.88917	0.1899	0.18853
a_6	21.571	1.5457	1.3861	1.0586	1.5409	-0.025662	-0.027465
a_7	38.441	6.8847	4.5961	4.8049	11.558	3.0354	3.2449
a_8	20.245	6.5961	7.3312	10.359	36.633	11.234	17.468

As noted above, the Coqblin-Schrieffer model for $\mathcal{J} \geq 3/2$ does give a peak in $\chi_{\text{CS}}(T)$. We fitted the digitized theoretical $\chi(T)$ curves for this model calculated by Rajan [147], for various T ranges of fits, by Eq. (4.39). The fitting coefficients a_n for $1 \leq \mathcal{J} \leq 7/2$ are listed in Table 4.5. We used the fitted curves to calculate the ratio

$$r(\%) = \frac{\chi_{\text{CS}}^{\text{peak}} - \chi_{\text{CS}}(0)}{\chi_{\text{CS}}(0)} \times 100 \quad . \quad (4.40)$$

where $\chi_{\text{CS}}^{\text{peak}}$ is the value of χ_{CS} at the peak. The calculations give $r = 2, 7, 11, 17$ and 22% for $\mathcal{J} = 3/2, 2, 5/2, 3$ and $7/2$, respectively. The observed value is $r = 8.2\%$ in sample 1, which is between the theoretical values for $\mathcal{J} = 2$ and $5/2$. Using the a_n coefficients for $\mathcal{J} = 2$ and $5/2$ from Table 4.5, we have fitted χ_{CS} to our $\chi(T)$ data of sample 1 for $T = 2\text{--}400\text{ K}$ with three free parameters, χ_0 , g and T_K . The fits are shown in Fig. 4.17 and the parameters are

$$\chi_0 = 2.3(3) \times 10^{-4} \text{ cm}^3/\text{mol} \quad , \quad g = 0.790(3) \quad , \quad T_K = 97.8(6) \text{ K} \quad (\mathcal{J} = 2) \quad , \quad (4.41)$$

$$\chi_0 = 6.9(9) \times 10^{-4} \text{ cm}^3/\text{mol} \quad , \quad g = 0.591(7) \quad , \quad T_K = 103(2) \text{ K} \quad (\mathcal{J} = 5/2) \quad . \quad (4.42)$$

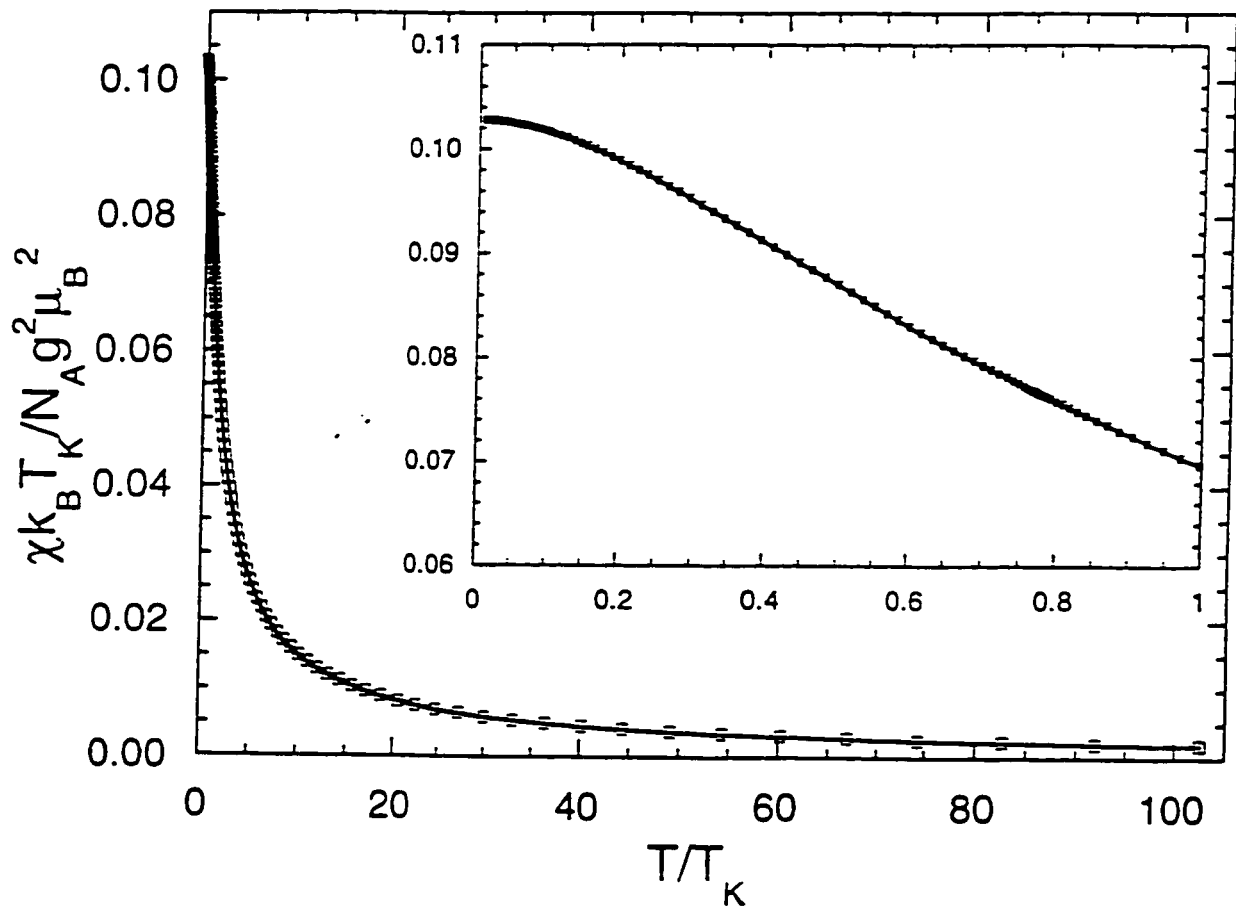


Figure 4.15 Bethe ansatz calculation of the magnetic susceptibility χ for the spin $S = 1/2$ Kondo model by Jerez and Andrei [148], exhibited in terms of the dimensionless reduced susceptibility $\chi k_B T_K / N_A g^2 \mu_B^2$, as a function of T/T_K , where T_K is the Kondo temperature. The inset shows an expanded plot at low temperatures.

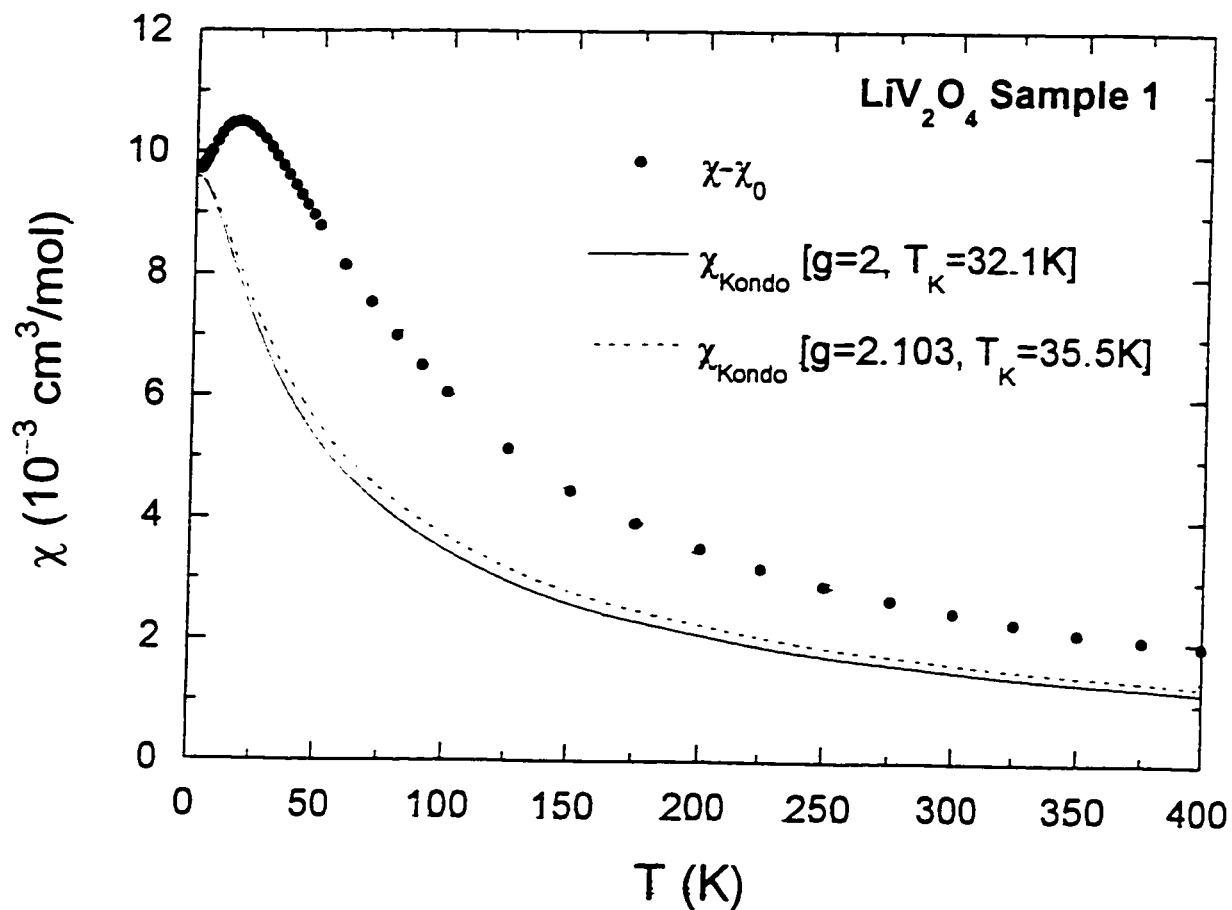


Figure 4.16 Temperature T -dependent part of the intrinsic magnetic susceptibility, $\chi - \chi_0$, versus T for LiV_2O_4 sample 1 (filled circles). Also shown as solid and dashed curves are the predictions of the spin $S = 1/2$ Kondo model for $(g, T_K) = (2, 32.1\text{K})$ and $(2.103, 35.5\text{K})$, respectively, where g is the g -factor and T_K is the Kondo temperature.

The $\mathcal{J} = 2$ curve fits our $\chi(T)$ data fairly well. However, the 1.5 d -electrons per V ion could not give rise to a \mathcal{J} value this large: the very small value of g is also considered highly unlikely.

On the basis of the above analysis we conclude that the Coqblin-Schrieffer model for $\mathcal{J} > 1/2$ and the $S = 1/2$ Kondo model cannot explain the intrinsic susceptibility of LiV_2O_4 over any appreciable temperature range.

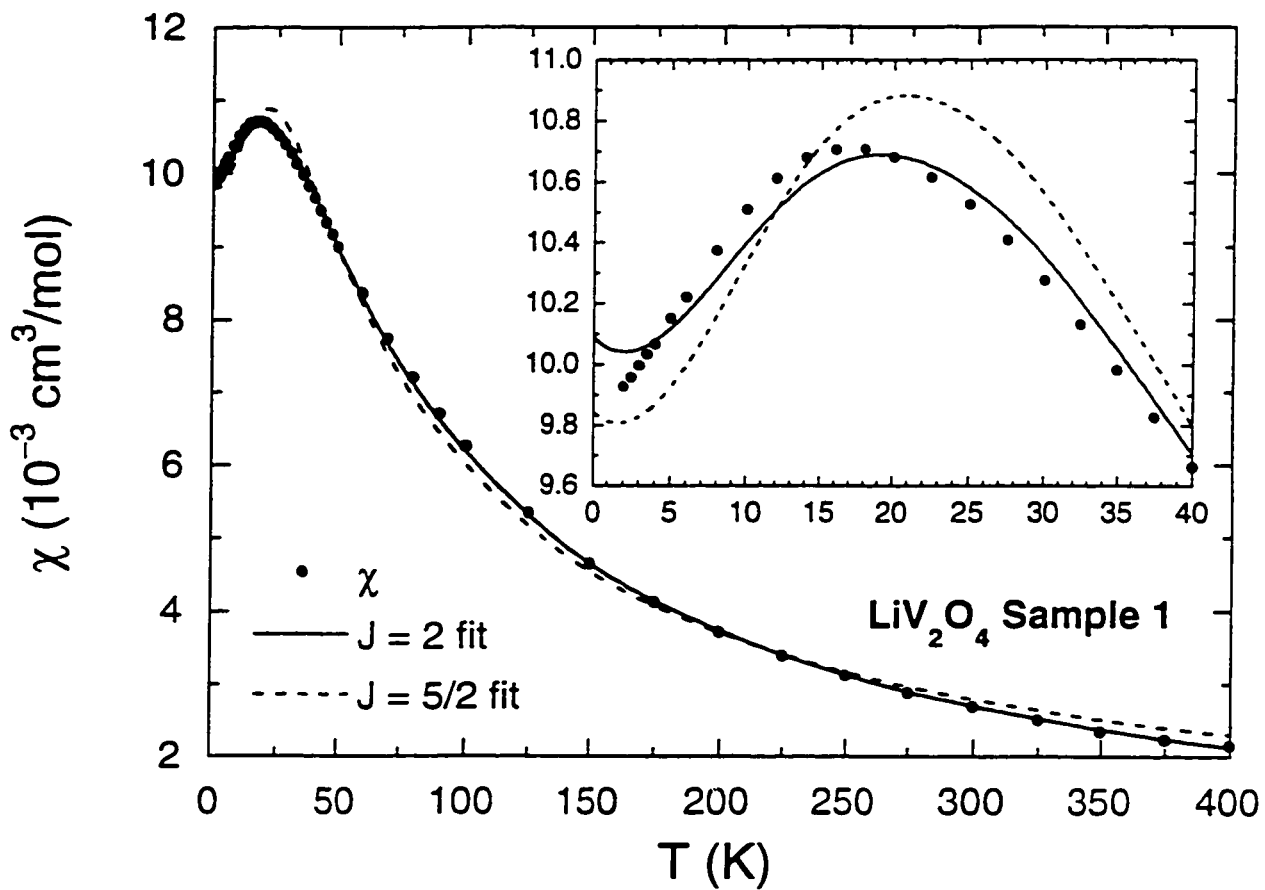


Figure 4.17 Intrinsic magnetic susceptibility χ of sample 1 versus temperature T and fits by the Coqblin-Schrieffer model prediction in Eq. (4.39) for spin $\mathcal{J} = 2$, and $5/2$, using the corresponding a_n coefficients in Table 4.5. The inset shows an expanded plot of the data and fits below 40 K.

5 RESISTIVITY

Resistivity measurements using powder samples

Resistivity $\rho(T)$ measurements of polycrystalline oxide samples are often misleading. They often display not only qualitatively incorrect temperature dependences but also quantitatively incorrect magnitudes. This uncertainty is usually caused by extra resistance coming from grain boundaries of powder samples. Therefore, the intrinsic electronic transport properties cannot be evidenced from such measurements on polycrystalline samples. Nevertheless, when a polycrystalline sample undergoes a transition to a superconducting state, a sharp drop in $\rho(T)$ at the transition temperature T_c may be usually observed.

For LiV_2O_4 the resistivity measurements on polycrystalline samples in the past showed semiconducting behaviors [9, 149]. We also observed a semiconducting behavior, partly due to bad contacts of platinum wires to powdery sample pellet surface. Superconductivity was not observed above 0.01 K from $\rho(T)$ measurements on a polycrystalline pellet (sample 3) [11].

Analysis of single crystal resistivity measurements

Despite the failure to show the metallic conductivity definitively from powder samples, single crystals of LiV_2O_4 showed metallic T dependences in the resistivity $\rho(T)$ as noted in Chapter 1. We digitized the published $\rho(T)$ data of Rogers *et al.* [3], which were plotted as $\log(\rho)$ vs. T , and replot here the data on linear scales in Fig. 5.1. Although $\rho(T)$ increases monotonically with T as expected for a metal, the magnitude of ρ is not as small as for typical metals ($O(\rho)=1 \mu\Omega \text{ cm}$) [150]: $58(1)$ and $638(18) \mu\Omega \text{ cm}$ at $T = 4$ and 299 K , respectively, for "Crystal 2". The resistance ratio for this crystal is $\rho(299 \text{ K})/\rho(4 \text{ K}) = 11$. In Fig. 5.1, a strong but smooth downturn in $\rho(T)$ occurs at $T \approx 30 \text{ K}$, evidently signifying the crossover to the heavy Fermi liquid regime with decreasing T .

In strongly correlated electron systems such as f -electron HF compounds, the low- T resistivity exhibits a T^2 dependence arising from Umklapp scattering processes between conduction electrons.

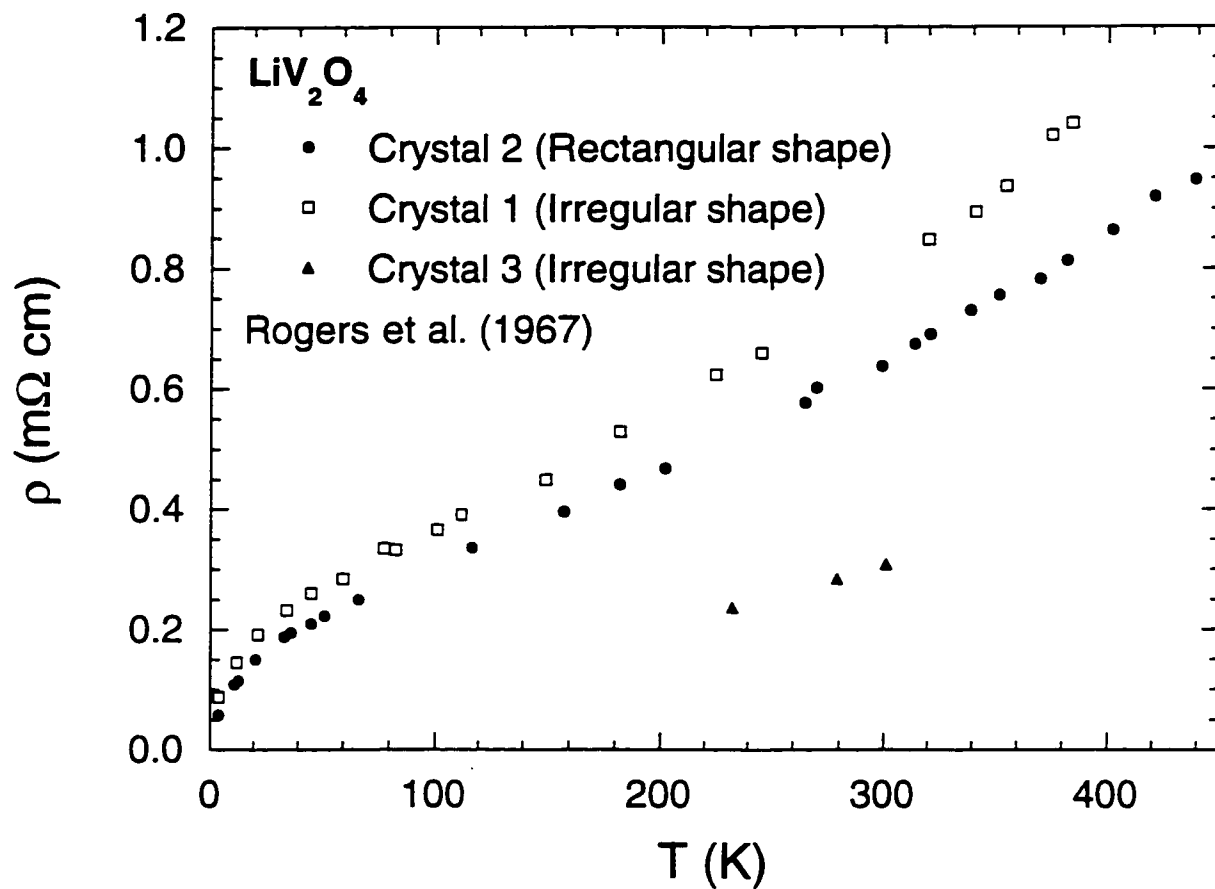


Figure 5.1 Electrical resistivity ρ of LiV_2O_4 single crystals versus temperature T , digitized from Fig. 1 of Rogers *et al.* [3]. Open squares, closed circles and closed triangles correspond to Crystals 1, 2 and 3, respectively. Crystal 2 had a rectangular shape, whereas the other two had irregular shapes. Only three data points are given in [3] for Crystal 3.

Combined with a residual resistivity ρ_0 , the resistivity at low T is written as

$$\rho(T) = \rho_0 + AT^2 \quad (5.1)$$

In 1986, a universal linear relation between A and γ^2 , the square of the electronic heat capacity coefficient at $T = 0$, was postulated for f -electron HF compounds via the so-called Kadowaki-Woods plot [66]. The proportionality constant they found was $(A/\gamma^2)_{\text{HF}} = 1.0 \times 10^{-5} \mu\Omega \text{ cm} (\text{mol K/mJ})^2$. Miyake *et al.* [151] subsequently deduced this proportionality constant theoretically, along with a corresponding value for common transition metals $(A/\gamma^2)_{\text{TM}} \simeq 0.4 \times 10^{-6} \mu\Omega \text{ cm} (\text{mol K/mJ})^2$. They concluded that the origin of the factor of 25 ratio between the A/γ^2 values for the two classes of compounds arises from different degrees of frequency dependences of the conduction-electron self-energy. Many-body effects yield the large proportionality constant for HF compounds. Yamada *et al.* [65] derived this proportional relationship in Fermi liquid theory using the periodic Anderson Hamiltonian.

Although there are not many low- T $\rho(T)$ data points available in Fig. 5.1 (the lowest T datum is at 4 K), we have fitted the lowest two data points for each of Crystals 1 and 2 by Eq. (5.1) to obtain very rough estimates of the T^2 coefficient A . For Crystal 1, we obtain $\rho_0 = 81 \mu\Omega \text{ cm}$ and $A = 0.45 \mu\Omega \text{ cm/K}^2$, whereas for Crystal 2 we get $\rho_0 = 50 \mu\Omega \text{ cm}$ and $A = 0.49 \mu\Omega \text{ cm/K}^2$. The fit for Crystal 2 is plotted as the solid curve in Fig. 5.2. If the value of A is estimated from the $(A/\gamma^2)_{\text{TM}}$ proportionality constant for transition metals using $\rho_0 = 50 \mu\Omega \text{ cm}$ and $\gamma(T = 1 \text{ K}) = 210 \text{ mJ}/[(\text{mol V}) \text{ K}^2]$, it is seen from the plot of Eq. (5.1) in Fig. 5.2 (dotted line) that the value of $(A/\gamma^2)_{\text{TM}}$ for transition metals evidently does not fit the experimental data. Using the average of the two values of A obtained above for LiV_2O_4 , $A = 0.47 \mu\Omega \text{ cm/K}^2$, this (A, γ) data point for LiV_2O_4 is on the straight line in a plot of A versus γ which many HF compounds cluster around as shown in Fig. 5.3.

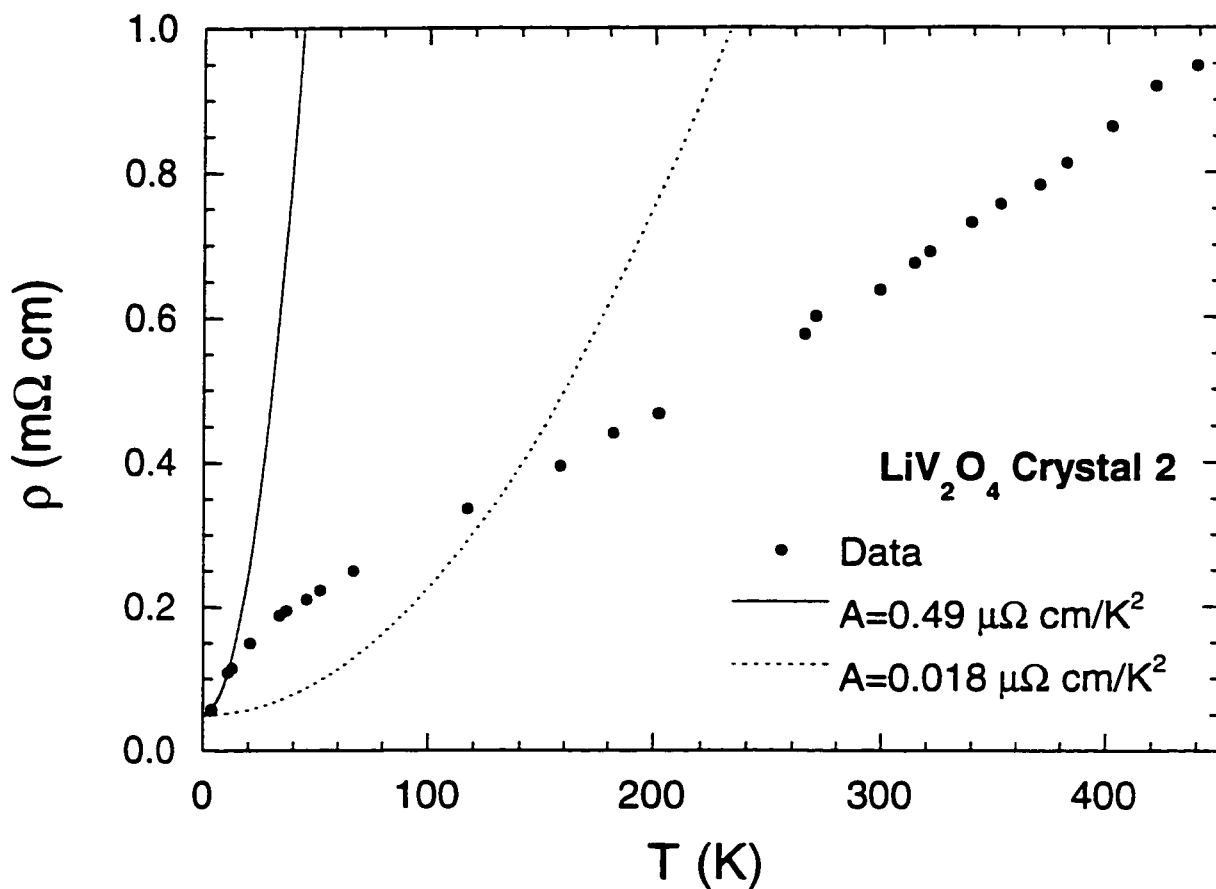


Figure 5.2 Electrical resistivity ρ of LiV₂O₄ “Crystal 2” versus temperature T , from Rogers *et al.* [3], and a fit (solid curve) to the lowest two data points by $\rho(T) = \rho_0 + AT^2$. The dotted line is a plot of the same expression for $\rho(T)$ but with a smaller value of A which was estimated assuming the proportionality constant A/γ^2 appropriate to ordinary transition metals.

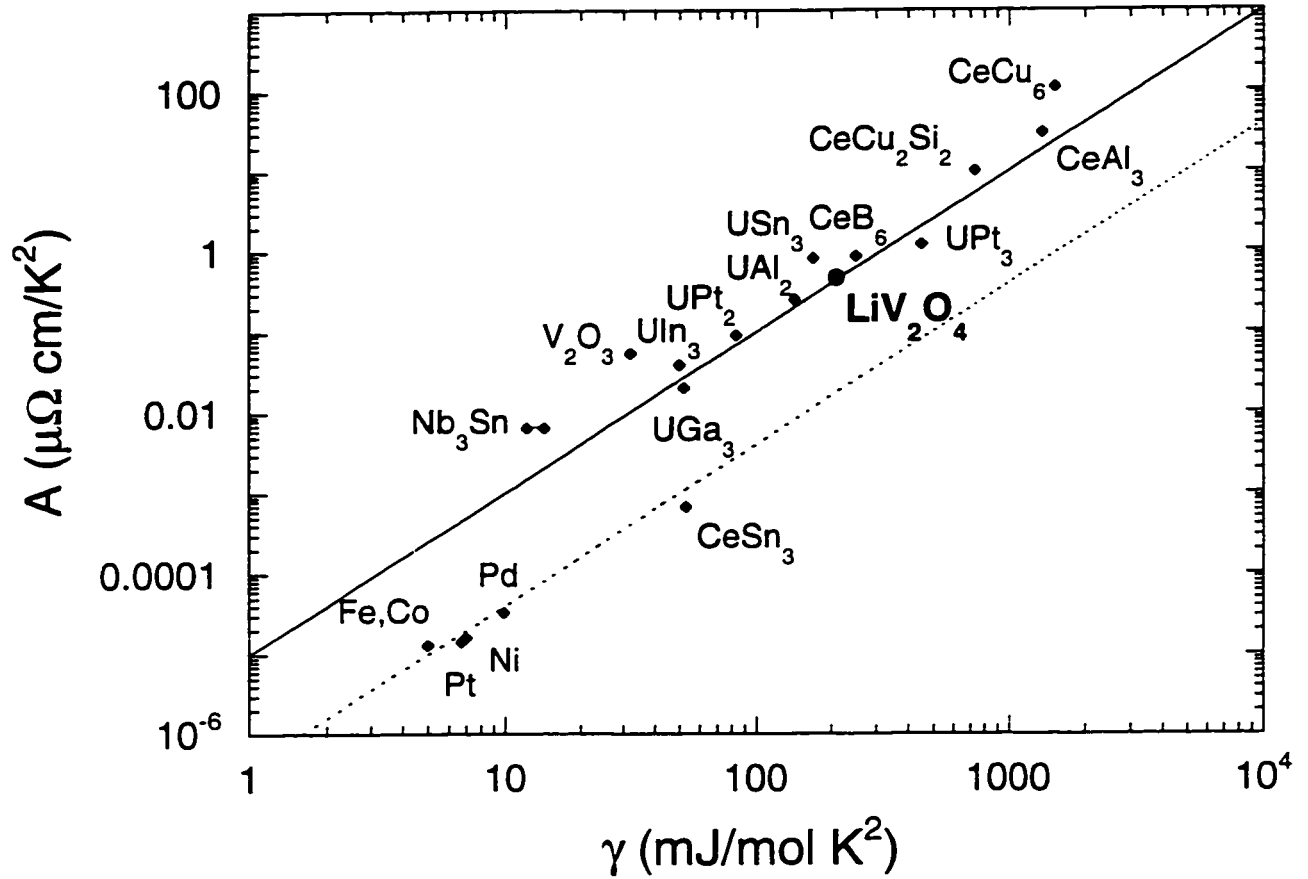


Figure 5.3 Kadowaki-Woods plot of the electrical resistivity T^2 coefficient A in Eq. (5.1) versus electronic heat capacity coefficient γ for LiV_2O_4 and various other transition metals and f -electron HF compounds. The solid straight line satisfies $(A/\gamma^2)_{\text{HF}} = 1.0 \times 10^{-5} \mu\Omega \text{ cm} (\text{mol K}/\text{mJ})^2$, the empirical relation found by Kadowaki and Woods [66] for strongly correlated electron systems. The dashed line represent the proportionality constant $(A/\gamma^2)_{\text{TM}} = 0.4 \times 10^{-6} \mu\Omega \text{ cm} (\text{mol K}/\text{mJ})^2$ for common transition metals [151].

6 HEAT CAPACITY

It is no exaggeration to say that heat capacity plays the most important role in the study of heavy fermion (HF) compounds. A large linear (*i.e.*, electronic) in T heat capacity at low temperature T is the first requirement for a material to be called a heavy fermion compound, because the large slope implies a large effective mass in the Fermi liquid picture.

The measurements were carried out under ambient pressure and no applied magnetic field using a conventional semiadiabatic pulse calorimeter from 1.2 to 108 K [152] by Dr. C. A. Swenson on samples provided by the author. Six LiV_2O_4 samples with varied but small amounts of magnetic and structural impurities were measured. In addition, in order to estimate the lattice contribution to the total observed heat capacity, isostructural nonmagnetic insulator spinel $\text{Li}_{4/3}\text{Ti}_{5/3}\text{O}_4$ and isostructural superconducting LiTi_2O_4 samples were measured. The absolute and relative accuracies of the measurements are, approximately, 3% and 1%, respectively. For LiV_2O_4 , the measurement accuracy was improved to $\sim 0.1\%$ at low T where the measured heat capacity is enhanced strongly due to the HF behavior. Some structural and magnetic properties of these samples from Rietveld refinements of powder x-ray diffraction patterns and magnetization versus applied magnetic field isotherm ($T = 2\text{--}6\text{ K}$) analyses are already tabulated in Tables 3.4 and 4.1, respectively. Theoretical modeling of the heat capacity data was done by Dr. D. C. Johnston and Dr. C. A. Swenson, and is described below. This chapter closely follows the draft of a paper in preparation [14].

Heat capacity measurement results

Overview

An overview of our isobaric heat capacity C_p measurements are given in Fig. 6.1 (a) for LiV_2O_4 sample 2 (run 2; 1.26–78 K) and sample 6 (1.16–108 K), along with the two titanium spinel $\text{Li}_{1+x}\text{Ti}_{2-x}\text{O}_4$ compounds ($x = 0$ and $1/3$; both up to 108 K). Shown in terms of C_p/T in Fig. 6.1(b), the peculiar strong upturn below $\sim 25\text{ K}$ is readily seen for LiV_2O_4 , while the LiV_2O_4 data above $\sim 30\text{ K}$ appear to be shifted by a constant from those of the Ti spinels. The data for both Ti spinels are in good agreement

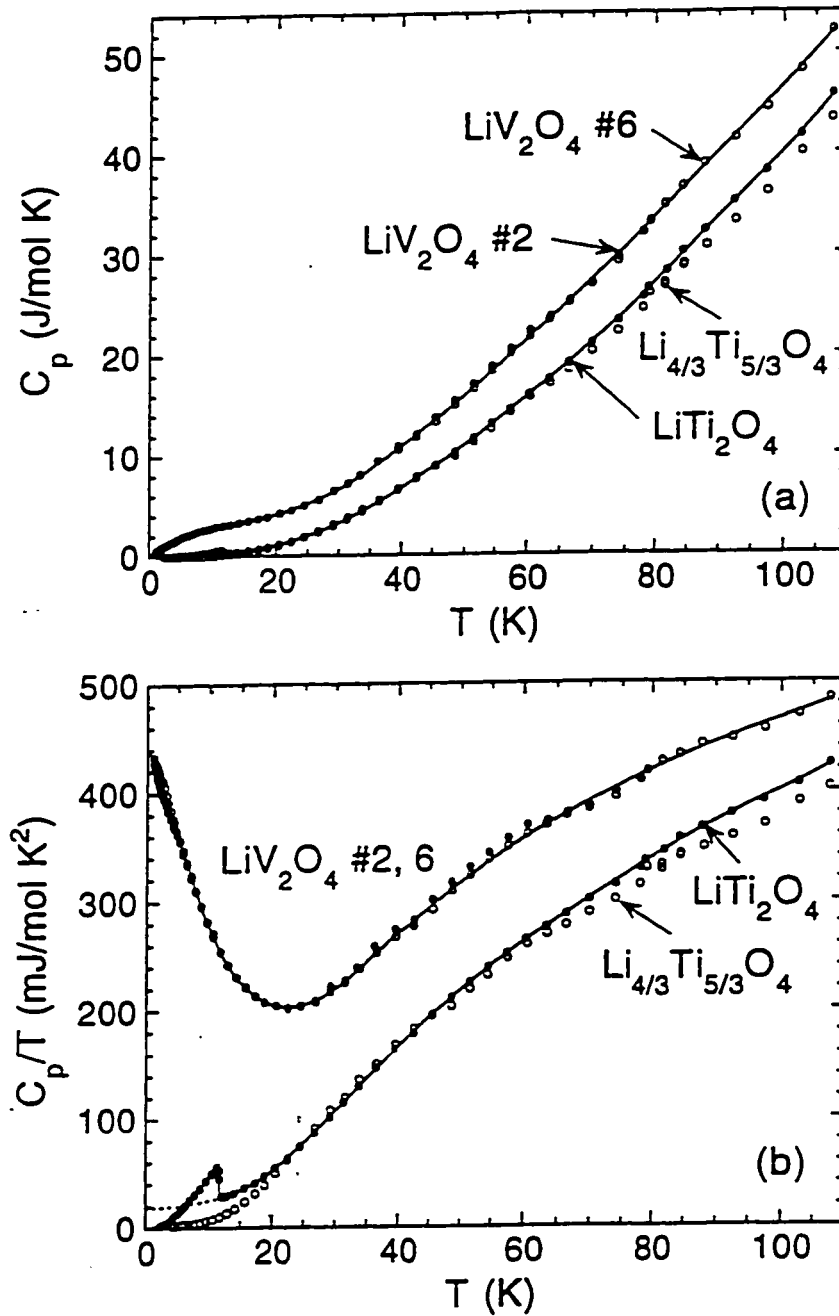


Figure 6.1 Overview of the molar isobaric heat capacity C_p (a) and C_p/T versus temperature T for LiV_2O_4 samples 2 and 6, as well as those of LiTi_2O_4 and $\text{Li}_{4/3}\text{Ti}_{5/3}\text{O}_4$. The solid curves are polynomial fits to the data for LiTi_2O_4 and $\text{Li}_{4/3}\text{Ti}_{5/3}\text{O}_4$. The solid curves are polynomial fits to the data for LiV_2O_4 and LiTi_2O_4 (in normal state), whereas the dashed curve in (b) is the inferred normal-state C_p/T for the superconducting LiTi_2O_4 below T_c .

with those of McCallum *et al.* [94]. In the following sections, the detailed theoretical modeling by Johnston *et al.* [14] on these measurements is reviewed.

$\text{Li}_{1+x}\text{Ti}_{2-x}\text{O}_4$ ($x = 0$ and $1/3$)

It should be noted that the $C_p(T)$ data of the two Ti spinels are slightly different. From Fig. 6.1(b), in the range between ~ 25 K and ~ 45 K, $\text{Li}_{4/3}\text{Ti}_{5/3}\text{O}_4$ shows larger C_p values than LiTi_2O_4 which is in the normal state in this T range (note $T_c = 11.8$ K; see below). Outside this T range, the relationship becomes opposite. The measured C_p of $\text{Li}_{4/3}\text{Ti}_{5/3}\text{O}_4$ is equal to the lattice heat capacity C^{lat} of this compound since the compound is an insulator (*i.e.* no electronic contribution C_e). On the other hand, LiTi_2O_4 has both C^{lat} and C_e contributions. Since C_e cannot be negative, one must conclude that these two Ti spinels have different lattice dynamics.

Superconducting Ti spinel LiTi_2O_4

The molar heat capacity C_p data of LiTi_2O_4 were fitted by the following power series for several temperature T segments:

$$C_p(T) = \sum_n A_n T^n \quad , \quad (6.1)$$

where the obtained coefficients A_n are given in Table 6.1. The fits to LiTi_2O_4 $C_p(T)$ are shown as solid curves in Fig. 6.1. C_p/T data and fits to them (solid curves) for LiTi_2O_4 are shown in Figs. 6.2 up to $T = 20$ K with respect to T (a) and T^2 (b) in which the sharp superconducting transition is clearly seen.

The normal-state heat capacity parameters γ and β are determined as follows. The heat capacity $C_p(T)$ of a conventional metal in its normal state at low $T \ll \theta_D$ is normally represented in terms of a linear electronic and cubic lattice (Debye) terms, where θ_D is the Debye temperature at $T = 0$. $C_p(T) = \gamma T + \beta T^3$. From Fig 6.2(b) one can easily see the invalidity of the linear relationship of C_p/T with respect to T^2 as long as the coefficient of the linear term, γ , is assumed T -independent. This is probably due to the insufficient approximation of $C^{\text{lat}}(T)$ by the Debye term at T_c . To remedy the problem, a T^5 term is added to $C_p(T)$, while γ is still assumed T -independent. Under these assumptions, the normal-state parameters γ and β were determined from the fit to the normal-state $C_p(T)$ from 14 to 19 K by

$$C_p(T) = A_1 T + A_3 T^3 + A_5 T^5 \quad , \quad (6.2)$$

where $\gamma = A_1$ and $\beta = A_3$. When inferring the normal-state $C_p(T)$ behavior of a superconducting compound, one has to preserve the entropy S in a given T range. In this case, the $C_p(T)$ for 14–19 K

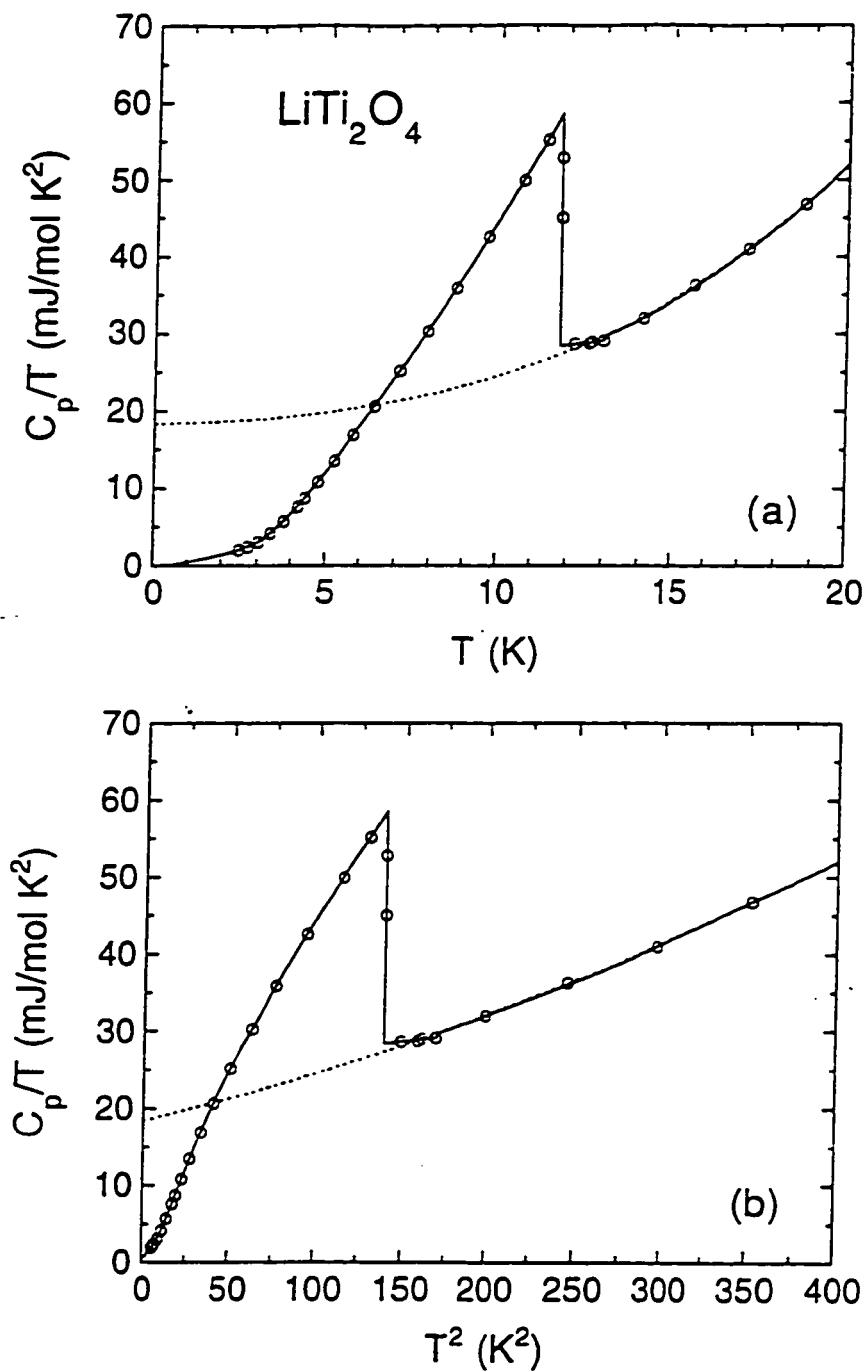


Figure 6.2 Expanded plots below 20K of the molar heat capacity divided by temperature C_p/T versus temperature T for LiTi_2O_4 from Fig. 6.1. The solid curves are fits to the data [Eq. (6.1) and Table 6.1], while the dashed curve is the estimated normal-state C_p/T [Eq. (6.1) and the last column in Table 6.1] from 0 to 19 K.

Table 6.1 Coefficients A_n in the power-series fitting function $C_p(T) = \sum_n A_n T^n$ for the measured C_p data [in units of mJ/(molK)] of LiTi_2O_4 in the given T ranges for fitting. The values of A_n given in the last column were obtained under a constraint of the entropy $S = 283.41$ mJ/(molK) at 13 K.

n	0-4 K	4-11.8 K	11.8-13 K	14-108 K	14-19 K
0	0	91.14920	21.2823	-835.1008	0
1	0	-68.14413	0.6003	267.5082	18.345
2	0	16.15982	0	-27.72682	0
3	0.4449394	-0.9316757	0	1.472060	0.053476
4	0	0.03530610	0	-0.03288067	0
5	-0.04713193	0	0	3.885628×10^{-4}	7.7680×10^{-5}
6	0	0	0	-2.351512×10^{-6}	0
7	5.417518×10^{-3}	0	0	5.732396×10^{-9}	0
8	0	0	0	0	0
9	-2.017705×10^{-4}	0	0	0	0
10	0	0	0	0	0
11	2.492636×10^{-6}	0	0	0	0

was determined by the fit using Eq. (6.2) in such a way that the value of S calculated from this fit matches at 13 K the measured entropy $S = 283.41$ mJ/(molK) which was derived using the fitting parameters in Table 6.1. The fit results are given in Figs. 6.2(a) and (b) and Table 6.1 (last column). The Debye temperature θ_D may be derived by using the relation $\theta_D = (12\pi^4 N_A r / \beta)^{1/3}$ [153], where N_A is the Avogadro number and r is the number of atoms per formula unit (in this case $r = 7$). The normal-state parameters for LiTi_2O_4 determined in this way are

$$\gamma = 18.4(1) \text{ mJ}/(\text{mol K}^2) \quad . \quad (6.3)$$

$$\beta = 0.054(1) \text{ mJ}/(\text{mol K}^4) \quad . \quad (6.4)$$

$$\theta_D = 632(4) \text{ K} \quad . \quad (6.5)$$

This γ value is slightly smaller than those 20-22 mJ/(molK²) reported previously [94, 135]. Including an additional T^7 term in Eq. (6.2), the fits for the T fitting range 14-17 K to 14-21 K yielded $\gamma = 18.97(12)$ mJ/(molK²) and $\beta = 0.0321(18)$ mJ/(molK⁴). This γ value is close to that in Eq. (6.5), but β is very different. This smaller β value gives a larger Debye temperature $\theta_D = 751(15)$ K, and the difference is discussed below in connection with θ_D values of the other Ti spinel $\text{Li}_{4/3}\text{Ti}_{5/3}\text{O}_2$.

Nonmagnetic insulating Ti spinel $\text{Li}_{4/3}\text{Ti}_{5/3}\text{O}_4$

In Fig. 6.3(a), C_p/T for $\text{Li}_{4/3}\text{Ti}_{5/3}\text{O}_4$ is plotted versus T^2 for $T \leq 20$ K. The small anomalous bump seen at ≈ 7 K is most likely an experimental artifact since it was present in all samples with small low- T heat capacity. The addenda contribution was recently remeasured, and the subsequent corrections are in progress at the present time. The electronic term $C_e = \gamma T$ does not exist in the insulating $\text{Li}_{4/3}\text{Ti}_{5/3}\text{O}_4$, and γ indeed appears to be zero for the data above $T \approx 7.8$ K where the anomalous bump occurs. Again, it is clear from the nonlinearity of C_p/T in Fig. 6.3(a) that the low- T approximation of $C^{\text{lat}}(T)$ by the T^3 Debye term is not sufficient. Therefore, the following fits were carried out to the data above the anomaly.

The first fit was to C_p/T versus T in Fig. 6.3(a) by

$$\frac{C_p}{T} = A_3 T^2 + A_5 T^4 \quad . \quad (6.6)$$

The upper limit of the fitting range was taken from 12 to 16 K, and the fitting results were found to be insensitive to the exact range. The parameters obtained from the 7.8–14 K fit range are

$$A_3 = \beta = 0.039(3) \text{ mJ}/(\text{mol K}^4) \quad . \quad A_5 = 2.3524 \times 10^{-4} \text{ mJ}/(\text{mol K}^6) \quad . \quad (6.7)$$

where $\theta_D = 704(19)$ K can be derived from β . The fit is shown as the solid curve in Fig. 6.3(a).

The second fit was to C_p/T^3 versus T in Fig. 6.3(b) in the 7.8–24.5 K fitting range by

$$\frac{C_p}{T^3} = A_3 + A_5 T^2 + A_7 T^4 \quad , \quad (6.8)$$

with parameters

$$A_3 = \beta = 0.03309(11) \text{ mJ}/(\text{mol K}^4) \quad . \quad A_5 = 3.274 \times 10^{-4} \text{ mJ}/(\text{mol K}^6) \quad . \quad A_7 = -2.935 \times 10^{-7} \text{ mJ}/(\text{mol K}^8) \quad . \quad (6.9)$$

This value of A_3 corresponds to $\theta_D = 744(1)$ K. The fit is given in a solid curve in Fig. 6.3(b). Furthermore, $\theta_D = 747(2)$ K was obtained from a fit including a T^6 term in Eq. (6.8). Including one additional higher order T^8 term, θ_D became 716(28) K.

Including rather conservative error bars from all these fits, the $T = 0$ Debye temperature θ_D is inferred to be

$$\theta_D = 718(30) \text{ K} \quad . \quad (6.10)$$

Debye temperature

We anticipate that the Debye temperature θ_D for LiTi_2O_4 is smaller than that for $\text{Li}_{4/3}\text{Ti}_{5/3}\text{O}_4$ for the following reasons. First of all, the larger molecular weight of LiTi_2O_4 may be responsible for

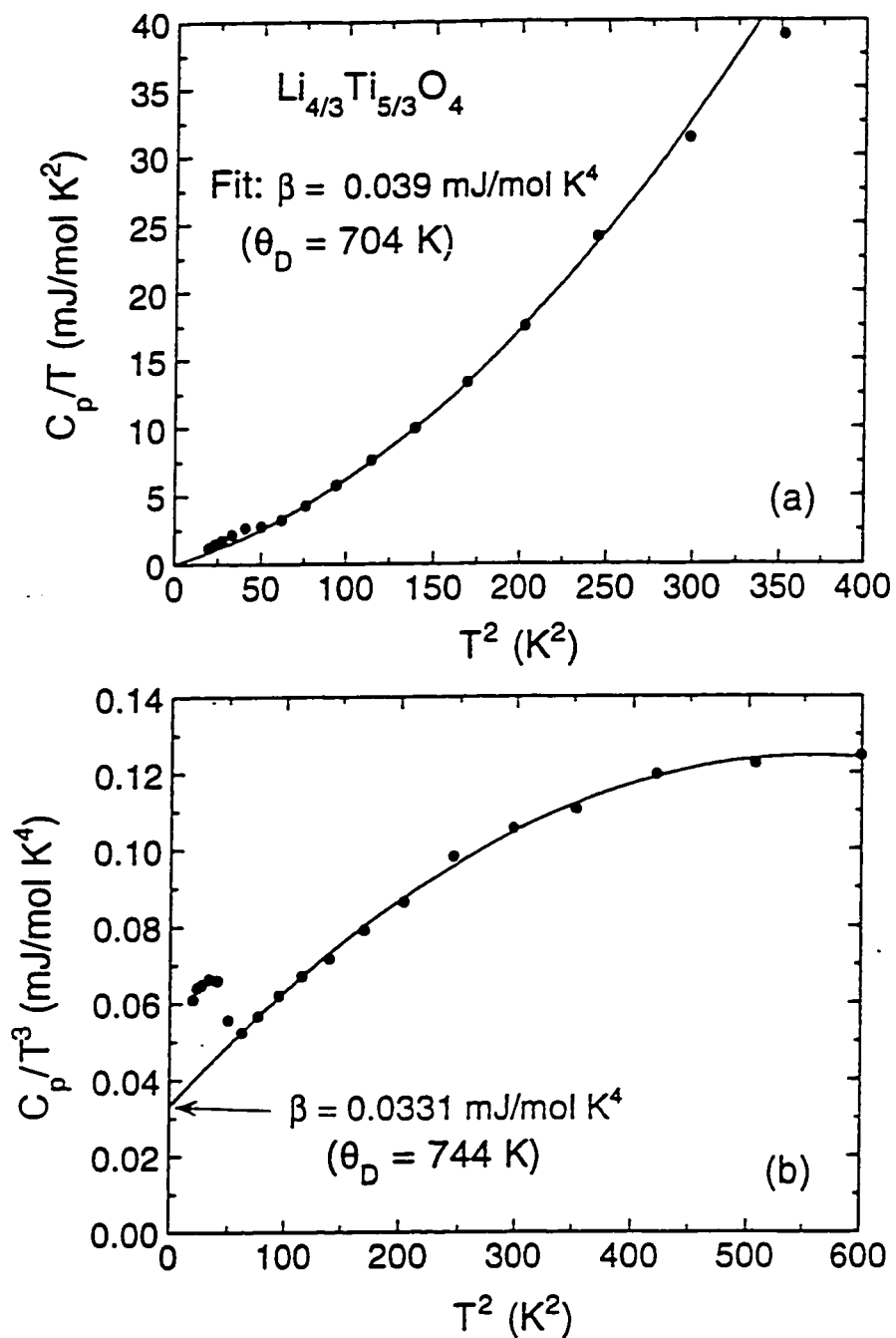


Figure 6.3 Molar heat capacity of $\text{Li}_{4/3}\text{Ti}_{5/3}\text{O}_4$ divided by temperature T . C_p/T (a), and C_p/T^3 (b), versus T^2 . The fits by Eqs. (6.6) and (6.8) are shown in a solid curve in (a) and (b), respectively.

the smaller θ_D since the Debye temperature is inversely proportional to the square root of the formula weight. Second the screening of interatomic electric forces by conduction electrons in LiTi_2O_4 would relax the lattice motion, in a sense, decreasing the "spring constant." This then yields a smaller θ_D .

However, the Debye temperatures for LiTi_2O_4 obtained in the two ways from the analyses of C_p differed by more than 100 K. The higher value of $\theta_D = 751$ K for LiTi_2O_4 exceeds $\theta_D = 718(30)$ K [Eq. (6.10)] for $\text{Li}_{5/3}\text{Ti}_{5/3}\text{O}_4$. This is opposite to what one expects from the reasons mentioned above. Uncertainty exists for $\text{Li}_{4/3}\text{Ti}_{5/3}\text{O}_4$ because of its structural disorder at the octahedral (16d) sites. This can be more easily seen if one realizes this insulating spinel is an intermediate spinel $\text{Li}[\text{Li}_{1/3}\text{Ti}_{5/3}]\text{O}_4$ in which one third of the 16d sites are occupied by Li, presumably at random. It is not clear how this influences the comparison of the θ_D values of the two Ti spinels. Therefore, since the two fits for LiTi_2O_4 were found to have similar quality, taking the two θ_D values into equal consideration, not being biased by the θ_D of $\text{Li}_{4/2}\text{Ti}_{5/3}\text{O}_4$, one obtains with conservative error bars

$$\theta_D = 700(70) \text{ K} \quad (6.11)$$

This uncertainty in C_p of LiTi_2O_4 does not have a significant effect when the lattice contribution of LiV_2O_4 to C_p is estimated since the C_p of LiV_2O_4 is much larger at low T than the inferred normal-state C_p of LiTi_2O_4 below T_c .

Along with this Debye temperature, some characteristic values of the two Ti spinels are summarized in Table 6.2.

Table 6.2 Characteristics of $\text{Li}_{1+x}\text{Ti}_{2-x}\text{O}_4$ samples.

a_0 (Å)	u	γ (mJ/molK ²)	θ_D (K)	T_c (K)	ΔT_c (K)	$\Delta C_p/\gamma T_c$ (mJ/molK ²)	Ref.
LiTi_2O_4							
8.4033(4)	0.2628(8)	18.7(4)	700(70)	11.8	$\lesssim 0.2$	1.62	[14]
8.4033(1)	0.26275(5)						[154]
8.41134(1)	0.26260(4)						[93]
8.407		21.4	685	11.7	1.2	1.59	[94]
		22.0	535	12.4	0.32	1.57	[135]
	0.26290(6) (300 K)						[155]
	0.26261(5) (6 K)						[155]
$\text{Li}_{4/3}\text{Ti}_{5/3}\text{O}_4$							
8.3589(3)	0.2625(3)	0	718(30)				[14]
8.35685(2)	0.26263(3)						[93]
8.359		0	610				[94]
		0.05	518				[135]

LiV₂O₄

Despite the above uncertainty in estimating θ_D for LiTi₂O₄, we expect that the lattice dynamics and $C^{\text{lat}}(T)$ of LiTi₂O₄ may reproduce those of LiV₂O₄ much better than Li_{4/3}Ti_{5/3}O₄. This is partly because LiTi₂O₄ with a normal spinel structure is structurally closer to the normal spinel LiV₂O₄, compared to the intermediate spinel Li_{4/3}Ti_{5/3}O₄. Also, the Ti normal spinel has a formula weight closer to that of the V spinel. Hence, the lattice heat capacity of LiV₂O₄ is assumed to be identical with that of LiTi₂O₄, and the small difference between the formula weights (3.5%) is neglected. The second assumption is reasonable since this 3.5% difference results in an even smaller difference in the Debye temperature ($\lesssim 1.8\%$), which is now close to the accuracy of measurements at high T . The electronic heat capacity $C_e(T)$ of LiV₂O₄ was determined by subtracting $C^{\text{lat}}(T)$ of LiTi₂O₄ from $C_p(T)$ of the former.

The $C_e(T)$ of LiV₂O₄ (samples 1 and 6) derived in this way is plotted as C_e versus T in Fig. 6.4(a) and C_e/T versus T in (b). An expanded C_e/T versus T plot below 9 K for LiV₂O₄ samples 1, 3 and 6 is displayed in Fig. 6.4(c). Sample 2 shows a small positive curvature in C_e/T below ~ 3 K, opposite to the behavior of samples 3 and 6. From Table 4.1, sample 2 has a larger magnetic impurity concentration (0.2%) than samples 3 (0.1%) and 6 (0.01%). Therefore, this positive curvature for sample 2 is a reflection of the larger magnetic impurity amount in the sample, and the other purer samples are believed to reflect intrinsic behaviors. Sample 6 shows a positive deviation from the other samples below 4 K, showing the similar sample dependency in the susceptibility (see Figs. 4.8). The cause of these quantitative differences is not known.

In order to estimate the $T = 0$ value of $\gamma(T) \equiv C_e/T$, fits to the C_e/T data for 1–9 K by the following polynomial were done for samples 3 and 6:

$$\frac{C_e}{T} = \gamma(0) + \sum_{n=1}^5 C_{2n} T^{2n} \quad . \quad (6.12)$$

where the obtained C_{2n} coefficients are listed in Table 6.3. The determined electronic heat capacity coefficients $\gamma(0)$ are

$$\gamma(0) = 426.7(6) \text{ mJ}/(\text{mol K}^2) \quad (\text{sample 3}) \quad , \quad (6.13)$$

$$\gamma(0) = 438.3(5) \text{ mJ}/(\text{mol K}^2) \quad (\text{sample 6}) \quad . \quad (6.14)$$

In Fig. 6.4(c) the fit curves for samples 3 and 6 are respectively given as the solid and dashed curves. These $\gamma(0)$ values are an order or more larger than values for conventional transition metal compounds.

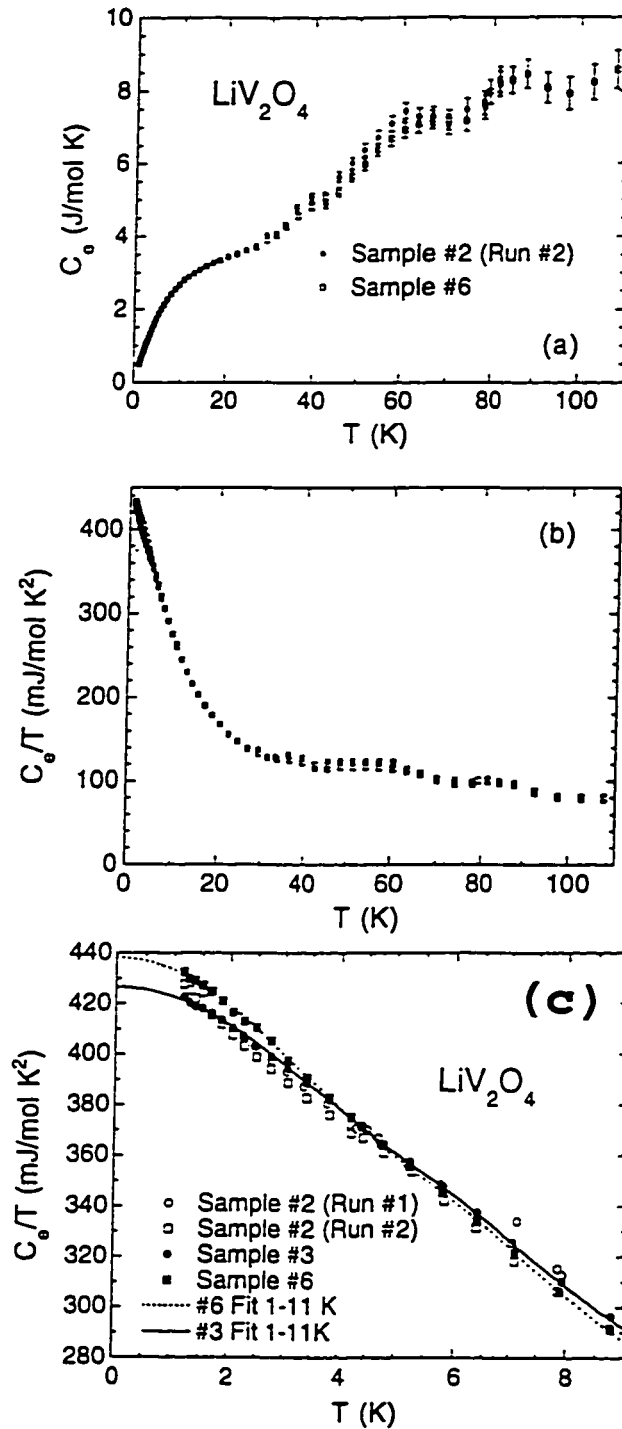


Figure 6.4 Inferred electronic heat capacity $C_e(T)$ of LiV_2O_4 samples 2 (runs 1 and 2) and 6 is plotted as C_e versus temperature T in (a) and C_e/T versus T in (b). Expanded plot of (b) below 9 K of LiV_2O_4 samples 2, 3 and 6 are given in (c). Polynomial fits to the 1.1–10 K data for samples 3 (solid curve) and 6 (dashed curve) are shown in (c).

Table 6.3 Coefficients C_n in the expression for the electronic heat capacity $C_e(T)/T = \sum_{n=0}^5 C_{2n} T^{2n}$ (in units of mJ/molK^2) for LiV_2O_4 samples 3 and 6 between 1.1 and 10 K.

C_{2n}	Sample 3	Sample 6
C_0	426.70(64)	438.33(48)
C_2	-4.15920	-5.32731
C_4	0.0922899	0.131312
C_6	-1.53307×10^{-3}	-2.17162×10^{-3}
C_8	1.28312×10^{-5}	1.76920×10^{-5}
C_{10}	-4.05676×10^{-8}	-5.43349×10^{-8}

In Fig. 6.5 the T -dependent electronic entropy with respect to that of the lowest $T = 1.16$ K, $S_e(T) - S_e(1.16 \text{ K})$ for LiV_2O_4 sample 6 is plotted. The observed large high- T values above ~ 65 K surpass the local moment prediction of the maximum spin entropy $2R \ln(2)$ (per mole of LiV_2O_4) for one spin $S = 1/2$ at each V site. R is the molar gas constant. For comparison, this value is given as a horizontal line in Fig. 6.5. An additional entropy from 0 to 1.16 K is $0.505 \text{ J}/(\text{mol K})$, which is found from extrapolating the C_e/T data from 1.16 K to 0 in Fig. 6.4(c).

The magnetically impure sample 4A shows an anomalous peak in C_p/T at about 29 K, as plotted in Fig. 6.6 along with the sample 2 data. Sample 4A also shows a larger upturn below 5 K. From Table 3.4 and Table 4.1, we have already shown some anomalous properties that sample 4A displayed. First of all, this sample contains the largest amount of impurity phase ($S_{\text{imp}} = 2$; 0.8 mol%), and the unsuccessful derivation of the intrinsic susceptibility $\chi(T)$ shape at low T may suggest some other complex magnetic mechanism. Next, the lattice constant of this sample is above 8.247 \AA which is one of the largest (next to sample 4B for which heat capacity measurements were not done). Recalling that this sample received an ice-water quenching from 725°C (see Chapter 3), there is a possibility to have some structural disorder, in particular, Li-V anti-site disorder which could cause this anomaly. Above the ‘‘background’’ a large amount of entropy $\Delta S \sim 0.9 \text{ J}/(\text{mol K}) \sim 0.16R \ln(2)$ is associated. There exist vanadium oxides V_4O_7 and V_5O_9 which have Néel temperatures of 33.3 and 28.8 K, respectively. However, these oxides cannot contribute to the extent of the observed anomalous peak, provided the concentration of such vanadium ‘‘impurity’’ phase is at or below the few percent level [156]. Therefore, it is likely that this behavior is inherent in this structurally and magnetically anomalous sample. Further study is needed to clarify the origin of this heat capacity anomaly at 29 K.

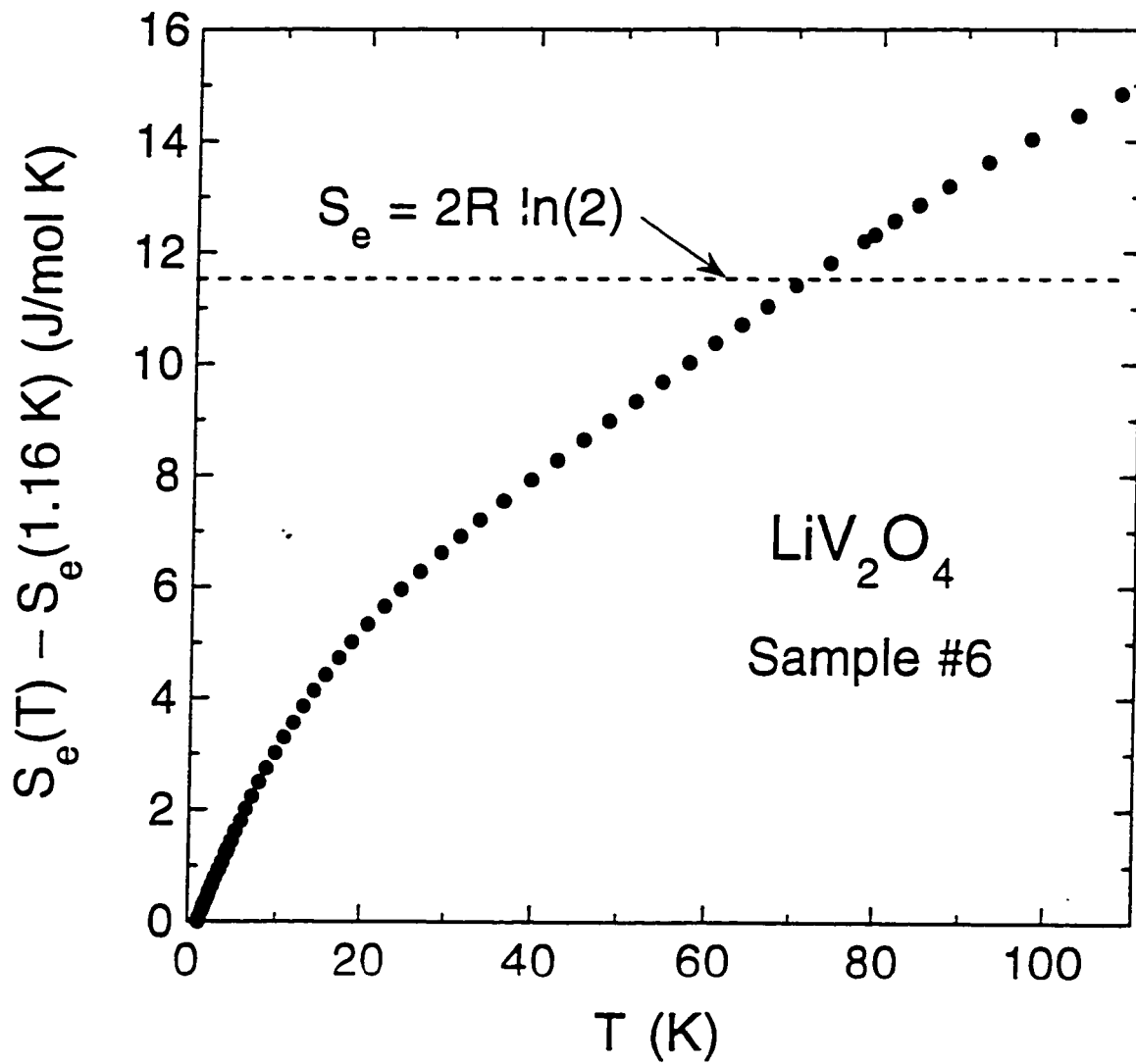


Figure 6.5 Electronic entropy with respect to that at the lowest temperature $T = 1.16 \text{ K}$. $S_e(T) - S_e(1.16 \text{ K})$, for LiV_2O_4 sample 6 versus temperature T .

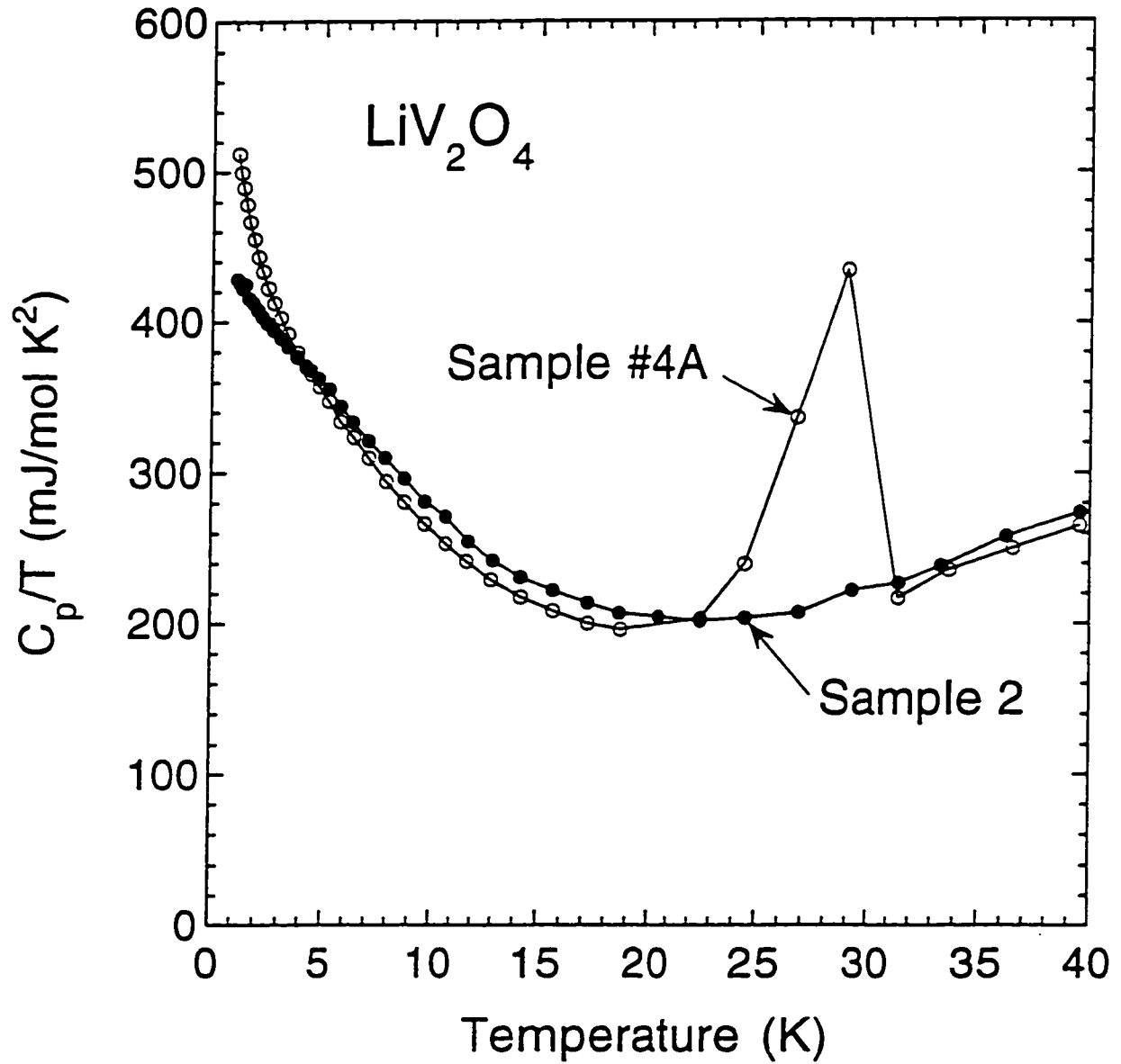


Figure 6.6 Observed molar heat capacity divided by temperature C_p/T versus temperature T for LiV_2O_4 sample 4A. The data of sample 2 are given for comparison. The solid lines are guides for the eye.

Theoretical modeling of electronic heat capacity of LiV_2O_4

Single-band spin $S = 1/2$ Fermi liquid

By introducing an interaction between electrons in the Fermi gas adiabatically, one can continuously transform to a Fermi liquid of quasiparticles. The forms of spin susceptibility χ and electronic heat capacity coefficient $\gamma \equiv C_e/T$ are not changed qualitatively. In the noninteracting Fermi gas, both quantities are independent of temperature T . On the other hand, the electron-electron interaction occurring in the Fermi liquid may alter the distribution function. Therefore, χ and γ are no longer T independent. Some important equations for the Fermi gas and liquid models are summarized in Table 6.4.

Table 6.4 Summary of equations of the density of states at the Fermi energy $\mathcal{D}(E_F)$, of the spin susceptibility χ , of the electronic heat capacity coefficient γ and of the Wilson ratio R_W for the Fermi gas (with superscripts "0") and Fermi liquid (without superscripts) models. The definitions of symbols are: m_e (m^*) = bare (effective) mass, $k_F = (3\pi^2 N_e/V)^{1/3}$ = Fermi wavevector, N_e = number of conduction electrons in volume V , $\mathcal{D}^\chi(E_F)$ [$\mathcal{D}^C(E_F)$] = density of states at the Fermi energy E_F probed by susceptibility (heat capacity) measurements, λ = electron-phonon coupling constant (ignored for the Wilson ratios), F_0^a = Landau parameter, and A_0^a = Fermi liquid scattering amplitude.

Fermi gas	Fermi liquid
$\mathcal{D}^0(E_F) = \frac{V m_e k_F}{\pi^2 \hbar^2}$	$\mathcal{D}^*(E_F) = \frac{V m^* k_F}{\pi^2 \hbar^2} = \frac{m^*}{m_e} \mathcal{D}^0(E_F)$
$\chi^0(0) = \frac{g^2 \mu_B^2}{4} \mathcal{D}^\chi(E_F) = \frac{g^2 \mu_B^2}{4} \mathcal{D}^0(E_F)$	$\chi(0) = \frac{g^2 \mu_B^2}{4} \mathcal{D}^\chi(E_F) = \frac{g^2 \mu_B^2}{4} \frac{\mathcal{D}^*(E_F)}{1+F_0^a}$
$\gamma^0 = \frac{\pi^2 k_B^2}{3} \mathcal{D}^C(E_F) = \frac{\pi^2 k_B^2}{3} (1+\lambda) \mathcal{D}^0(E_F)$	$\gamma(0) = \frac{\pi^2 k_B^2}{3} \mathcal{D}^C(E_F) = \frac{\pi^2 k_B^2}{3} (1+\lambda) \mathcal{D}^*(E_F)$
$R_W^0 = \frac{\mathcal{D}^\chi(E_F)}{\mathcal{D}^C(E_F)} = \frac{\mathcal{D}^0(E_F)}{\mathcal{D}^0(E_F)} = 1$	$R_W = \frac{4\pi^2 k_B^2 \chi(0)}{3g^2 \mu_B^2 \gamma(0)} = \frac{\mathcal{D}^\chi(E_F)}{\mathcal{D}^C(E_F)} = \frac{1}{1+F_0^a} = 1 - A_0^a$

In most of the literature about heavy fermion materials, the electron-phonon interaction is not taken into account. Therefore, we also neglect it here, so $\mathcal{D}^C(E_F) = \mathcal{D}^*(E_F)$.

For LiV_2O_4 , using

$$m_{\text{mol}} = \text{formula weight} = 172.82 \text{ g/mol} . \quad (6.15)$$

$$Z = \text{number of formula units in a unit cell} = 8 \quad . \quad (6.16)$$

$$a_0(12 \text{ K}) = \text{lattice parameter} = 8.2269 \text{ \AA} \quad [11]. \quad (6.17)$$

$$\rho^{\text{calc}}(12 \text{ K}) = \text{calculated mass density} = 4.123 \text{ g/cm}^3 \quad . \quad (6.18)$$

$$n = \text{number of conduction electrons per V atom} = 1.5 \quad . \quad (6.19)$$

the following quantities are derived

$$\frac{N_e}{V} = 4.310 \times 10^{22} \text{ cm}^{-3} \quad . \quad (6.20)$$

$$k_F = 1.0847 \text{ \AA}^{-1} \quad . \quad (6.21)$$

Then, using the value of $\gamma(0)$ for LiV_2O_4 sample 3 from Eq. (6.13) and $\chi(0) = 0.0100(2) \text{ cm}^3/\text{mol}$ [11], the equations in Table 6.4 yield

$$\mathcal{D}^C(E_F) = \mathcal{D}^*(E_F) = \left[0.5019 \frac{\text{states}}{\text{eV (V atom)}} \right] \left(\frac{m^*}{m_e} \right) = 90.6 \frac{\text{states}}{\text{eV (V atom)}} \quad . \quad (6.22)$$

$$\frac{m^*}{m_e} = 180.5 \quad . \quad (6.23)$$

$$E_F = \frac{\hbar^2 k_F^2}{2m_e} \left(\frac{m_e}{m^*} \right) = 24.83 \text{ meV} \quad . \quad (6.24)$$

$$T_F = \frac{E_F}{k_B} = 288.2 \text{ K} \quad . \quad (6.25)$$

$$R_W = 1.71 \quad . \quad (6.26)$$

$$F_0^a = -0.42 \quad . \quad (6.27)$$

$$A_0^a = -0.71 \quad . \quad (6.28)$$

In the Fermi liquid theory, a term proportional to $T \ln T$ is often included in addition to the linear term $\gamma(0)T$ in order to account for the T dependent $\gamma(T)$ [157, 158, 159]. That is,

$$C_e(T) = \gamma(0)T + \delta T^3 \ln\left(\frac{T}{T_0}\right) + \mathcal{O}(T^3) \quad . \quad (6.29)$$

where T_0 is the scaling temperature.

A Fermi liquid model of Engelbrecht and Bedell [160] formulates δ as

$$\delta_{\text{EB}} = \frac{3\pi^2}{5} \frac{\gamma(0)}{T_F^2} (A_0^a)^2 \left(1 - \frac{\pi^2}{24} A_0^a \right) \quad . \quad (6.30)$$

and requires that $|A_0^a| \leq 1$ and $-\frac{1}{2} \leq F_0^a < \infty$. The values of F_0^a from Eq. (6.27) and A_0^a from Eq. (6.28) for LiV_2O_4 both satisfy the requirements. From Eqs. (6.13), (6.25), (6.28), and (6.29), one obtains

$$\delta_{\text{EB}} = 0.0199 \frac{\text{mJ}}{\text{mol K}^4} \quad . \quad (6.31)$$

The formulation by Auerbach and Levin [161, 162] and Millis *et al.* [163, 164] for a heavy Fermi liquid is based upon a Kondo lattice model and yields

$$\delta_M = \frac{3\pi^2\gamma(0)}{20T_F^2} \left(1 - \frac{\pi^2}{12}\right) . \quad (6.32)$$

which for LiV_2O_4 gives

$$\delta_M = 0.00135 \frac{\text{mJ}}{\text{mol K}^4} . \quad (6.33)$$

Fits to the C_e/T data for LiV_2O_4 sample 3 were carried out using

$$\frac{C_e(T)}{T} = \gamma(0) + \delta T^2 \ln\left(\frac{T}{T_0}\right) + \epsilon T^3 . \quad (6.34)$$

The fitting was done with or without ϵ . It was found that the fitting parameters $\gamma(0)$, δ and T_0 depended upon the fitting T ranges (1.5–5, 10, 15, . . . , 30 K). The fits for the 1–5, 10, and 15 K T ranges with $\epsilon = 0$ and the 1–30 K range with $\epsilon \neq 0$ are plotted in Fig. 6.7. From these reasonably good fits, one obtains

$$\gamma(0) = 428 (2) \frac{\text{mJ}}{\text{mol K}^2} , \quad \delta = 1.9 (3) \frac{\text{mJ}}{\text{mol K}^4} . \quad (6.35)$$

which are similar to those found in the heavy fermion compound UPt_3 ($T_F = 289$ K and $m^*/m_e = 178$ [158]): $\gamma(0) = 429\text{--}450$ mJ/(molK²) and $\delta = 1.99$ mJ/(molK⁴) [39].

A large discrepancy is found between the experimental δ in Eq. (6.35) and the predicted δ in Eqs. (6.31) and (6.33). Millis [163] found a similar discrepancy for UPt_3 and gave some possible reasons. Also using Millis' [163] theoretical model, one estimates a much smaller Li Knight shift for LiV_2O_4 than the observed value ($\sim 0.04\%$ at room T), which is as small as that in a normal metal (0.00024% at room T [93]).

Quantum-disordered antiferromagnetically coupled metal

LiV_2O_4 shows a negative Weiss temperature from the susceptibility analysis done in Chapter 4, which indicates antiferromagnetic (AF) coupling between $S = 1/2$ vanadium spins. However, no magnetic long-range AF order has been found in pure LiV_2O_4 from heat capacity [14], NMR (Chapter 8: [19]) and muon-spin relaxation [11] measurements above 0.02 K. Quantum fluctuations may disorder a magnetic system in some circumstances. Zülicke and Millis [95] solved scaling equations and obtained the temperature dependence of $C_e(T)$ due to quantum fluctuations for a three-dimensional AF coupled metal which is not ordered. Their theory assumes that the magnetic system is close to the zero-temperature critical point which is defined as a transition point of an AF to quantum-disordered

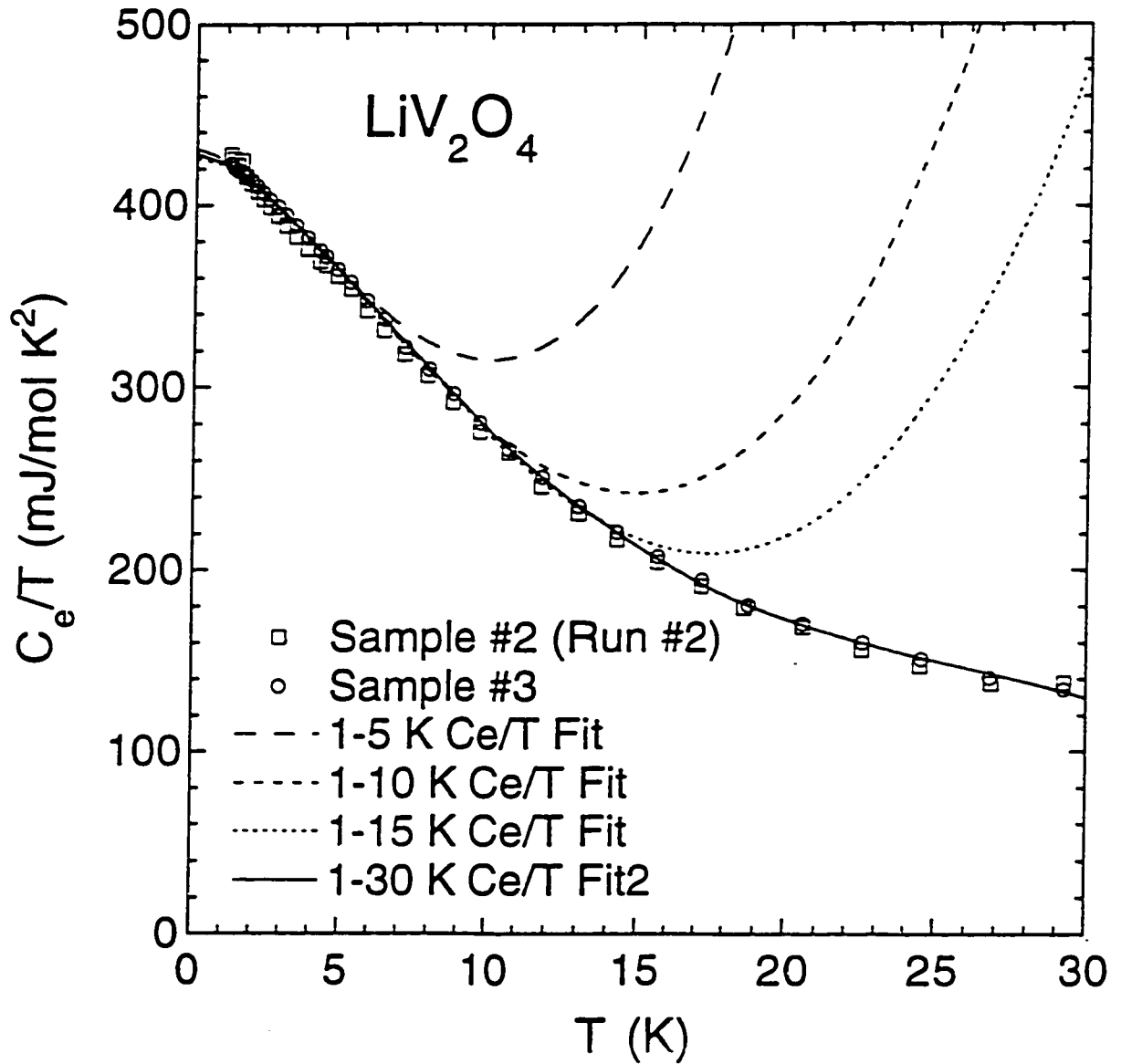


Figure 6.7 Electronic heat capacity divided by temperature, C_e/T , versus T for LiV_2O_4 sample 3. The C_e/T data are from Fig 6.4(c). The dashed curves are fits by Eq. (6.34) with $\epsilon = 0$ for 1-5, 10, and 15 K fitting T ranges. The solid curve is a 1-30 K fit with $\epsilon \neq 0$.

phase transition at $T = 0$. A single parameter called the control parameter r governs the zero- T transition for a given system. This r may depend on T , but also on other parameters such as pressure and stoichiometry of the material. The possible T dependence of r cannot be found unless another parameter called u is evaluated experimentally. Therefore, r is assumed to be a constant. LiV_2O_4 has the structural dimensionality $d = 3$, dynamical exponent $z = 2$ (for AF) and $N_0 = 3$ (for Heisenberg spin system) in their theory. The electronic heat capacity they predicted is

$$\frac{C_e}{T} = \gamma_0 - \frac{\alpha R N_0 \sqrt{r}}{6T^*} F\left(\frac{T}{rT^*}\right) . \quad (6.36)$$

where

$$F(x) = \frac{3\sqrt{2}}{\pi^2} \int_0^\infty dy \frac{y^2}{\sinh^2 y} \sqrt{1 + \sqrt{1 + 4x^2 y^2}} . \quad (6.37)$$

In Eq. (6.36) γ_0 is the electronic heat capacity coefficient at $T = 0$ from the Fermi liquid theory [$\gamma(0)$ above], and the second term is the correction due to quantum fluctuations. T^* is a characteristic temperature and R is the molar gas constant. The number α is a constant but cannot be determined from the theory. It is expected, however, to be on the order of the number of conduction electrons per formula unit. Therefore, $\alpha \sim 3$ is expected for LiV_2O_4 . The function $F(x)$ is defined in such a way that $F(0) = 1$.

In the disordered region in the parameter space, one can separate the quantum regime with $T \ll rT^*$ from the classical regime with $T \gg rT^*$, and the crossover between the two regimes is expressed as $T/T^* \sim r^{2/2}$. Non-integral, approximate equations of $F(x)$ in the low- T (quantum) and high- T (classical) limits are available in the original paper [95]. Here, the numerically generated $F(x)$ data for $x = 0-100$ were fitted by the following equation which is in agreement with both the low- T and high- T limiting forms

$$F(x) = \frac{1 + b_1 x^2 + b_2 x^3 + b_3 x^4 + b_4 x^5 + b_5 x^6}{1 + b_6 x^{2.5} + b_7 x^{3.5} + b_8 x^{4.5} + b_9 x^{5.5}} . \quad (6.38)$$

The fits yielded an rms deviation of 0.0019% and a maximum deviation of 0.017%, and the determined b_n coefficients are listed in Table 6.5.

Using this expression for $F(x)$, combined with Eq. (6.36), the fits to our C_e/T versus T data of LiV_2O_4 sample 3 (see Fig. 6.4(b)) were carried out for several fitting temperature ranges. Table 6.6 shows the determined fitting parameters γ_0 , α , r , T^* and the derived $\gamma(0)$ (see below). The goodness of fits are indicated in terms of χ^2/DOF , and are normally considered good when $\chi^2/\text{DOF} \ll 1$.

The fits with 1–20 K or higher ranges were found unacceptable. From Table 6.6 the following are the inferred parameters for LiV_2O_4 based upon the theory of Zülicke and Millis

$$\gamma_0 = 800(50) \frac{\text{mJ}}{\text{mol K}^2}, \quad \alpha = 2.65(9), \quad r = 0.40(6), \quad T^* = 18.9(4) \text{ K} . \quad (6.39)$$

Table 6.5 Coefficients b_n determined by a fit using Eq. (6.38) for the function $F(x)$ in Eq. (6.36) for the electronic heat capacity $C_e(T)$ of a three-dimensional antiferromagnetically coupled Fermi liquid [95].

n	b_n
1	-0.21375209
2	-52.743910
3	82.963105
4	381.62915
5	0.10383570
6	-13.440766
7	-68.625506
8	398.22865
9	0.10830681

The fits are given in Fig. 6.8 for 1-5, 1-10 and 1-15 K fitting ranges.

When $T = 0$, Eq. (6.36) becomes

$$\gamma(0) = \gamma_0 - \frac{\alpha R N_0 \sqrt{r}}{6T^2} . \quad (6.40)$$

since $F(0) = 1$, as defined. This equation states that quantum fluctuations decrease the observed $\gamma(0)$.

Using the parameters in Eq. (6.39), Eq. (6.40) gives

$$\gamma(0) = 430(1) \text{ mJ/mol K}^2 . \quad (6.41)$$

which is approximately a factor of two smaller than γ_0 in Eq. (6.39).

The $\alpha = 2.65$ is found to be close to the above expectation for LiV_2O_4 , $\alpha \sim 3$. However, the value of r suggests that LiV_2O_4 is not very close to the quantum critical point, and would not have long-range AF order induced by a small change of r via pressure or stoichiometry of the material. In fact, the zinc-doped system $\text{Li}_{1-x}\text{Zn}_x\text{V}_2\text{O}_4$ [83] for $0.2 \lesssim x \lesssim 0.9$ has shown spin-glass (*i.e.*, short-range) order, but does not show long-range order until the Zn concentration is as high as 0.95. In addition, one of our LiV_2O_4 sample (sample 3) showed spin-glass behavior detected by muon-spin relaxation measurements [11], which is believed to be caused by structural defects/disorder existing in the sample (see Chapter 3).

Spin-1/2 Kondo model

The single-impurity spin $S = 1/2$ Kondo model was solved by the numerical renormalization theory by Wilson [57] and by the other methods [143, 144, 145, 147, 58, 148, 165, 166]. These solutions are

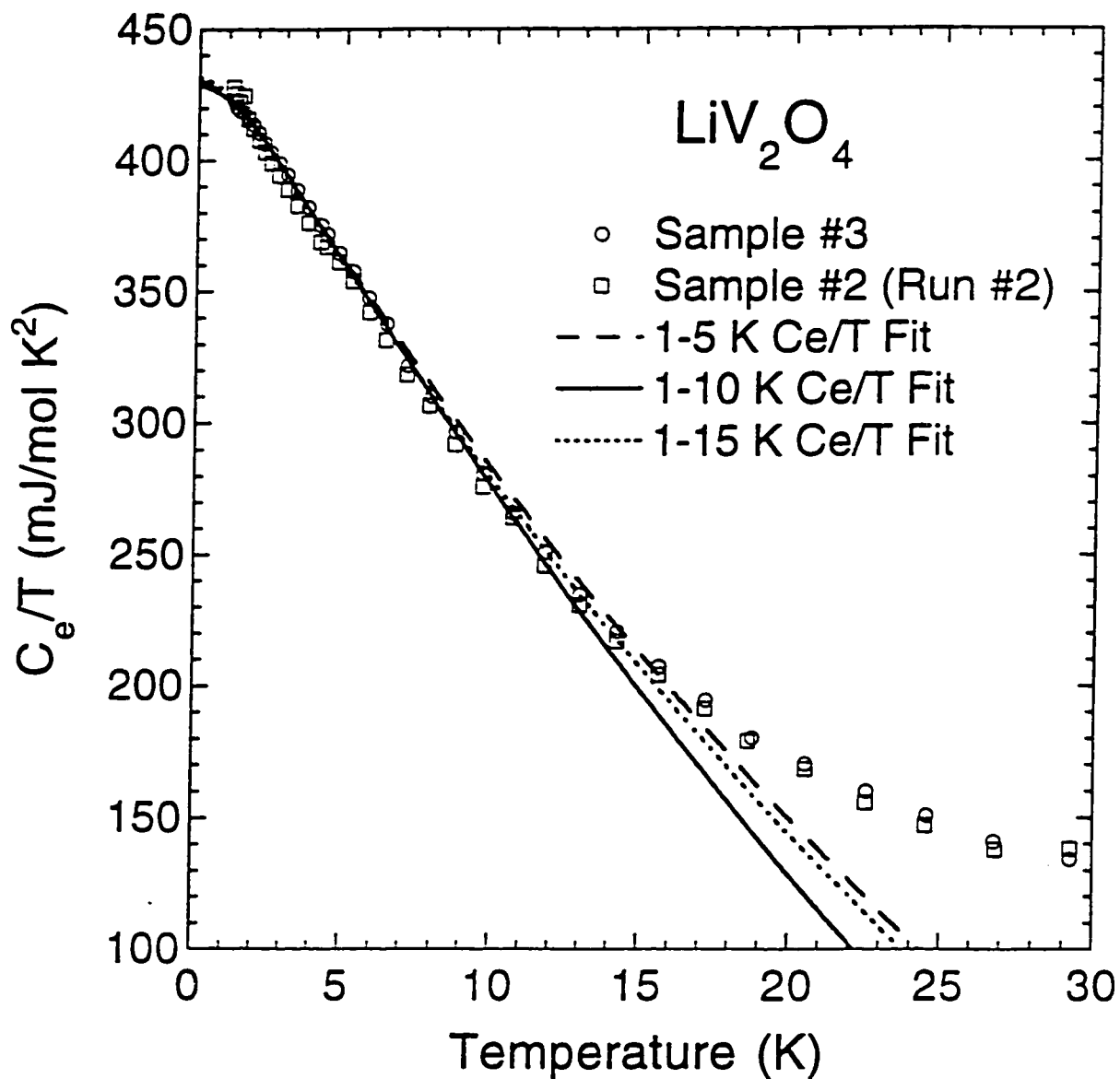


Figure 6.8 Electronic heat capacity divided by temperature C_e/T vs. T for LiV_2O_4 samples 2 and 3 from Fig. 6.4(b). Fits to the data for sample 3 by the theory of Zülicke and Millis [95] are also given for the fitting ranges 1–5 K (long-dashed curve), 1–10 K (solid curve) and 1–15 K (short-dashed curve). The fitting parameters are listed in Table 6.6.

Table 6.6 Fitting parameters in Eqs. (6.36) and (6.37) for the electronic heat capacity coefficient $\gamma(T) \equiv C_e(T)/T$ of LiV_2O_4 sample 3 by the theory of Zülicke and Millis [95] for several temperature ranges of the fit. The goodness of fit χ^2/DOF and the derived $\gamma(0)$ are also given. From the large values of χ^2/DOF , the 1–20 K and 1–25 K fits are unacceptable.

T range (K)	γ_0 (mJ/molK ⁴)	α	r	T^* (K)	χ^2/DOF	$\gamma(0)$ (mJ/molK ⁴)
1–5	770	2.57	0.374	19.1	0.014	429.6
1–10	862	2.78	0.473	18.3	0.059	428.5
1–15	760	2.61	0.343	19.3	0.027	431.5
1–20	642	2.41	0.178	20.9	1.97	440.0
1–25	541	2.35	0.033	23.9	9.95	467.3

very often represented in complex integral equations which cannot be easily fitted to experimental data.

However, Rajan [147] obtained the zero-temperature-limit value of the electronic heat capacity coefficient for $S = 1/2$ impurity spins. $\gamma(0)$ per mole of impurities is given by

$$\gamma(0) = \frac{\pi W N_A k_B}{6T_K} = \frac{5.61714 \text{ J/mol K}}{T_K} \quad (6.42)$$

where N_A is Avogadro's number and T_K is the Kondo temperature (Wilson's definition [57]). The number W is called the Wilson number [57] and is given [167, 168] by

$$W = \gamma e^{1/4} \pi^{-1/2} \approx 1.290\,268\,998 \quad (6.43)$$

where $\ln \gamma \approx 0.577\,215\,664\,902$ is Euler's constant.

To make use of Eq. (6.42) for $\gamma(0)$, an accurate Bethe ansatz calculation of $C_e(T)$ by Jerez and Andrei [148] was used. Their numerically calculated $C_e(T)$ and C_e/T versus $\log_{10}(T/T_K)$ are plotted respectively in Figs. 6.9(a) and (b) for $0.001 < T/T_K < 1000$. These data were parameterized by the equations

$$\frac{C_e(T)}{Nk_B} = f(t) \quad (6.44)$$

$$\frac{C_e(T)}{Nk_B T/T_K} = g(t) \equiv \frac{f(t)}{t} \quad (6.45)$$

$$f(t) = 0.675583268 \frac{t(1 + a_1 t + a_2 t^2 + a_3 t^3 + a_4 t^4)}{1 + a_5 t + a_6 t^2 + a_7 t^3 + a_8 t^4 + a_9 t^5} \quad (6.46)$$

where $t \equiv T/T_K$. The form of $f(t)$ in Eq. (6.46) was chosen as shown so that the zero- T limit of Eq. (6.42) is satisfied. Table 6.7 lists the derived a_n coefficients for both fits.

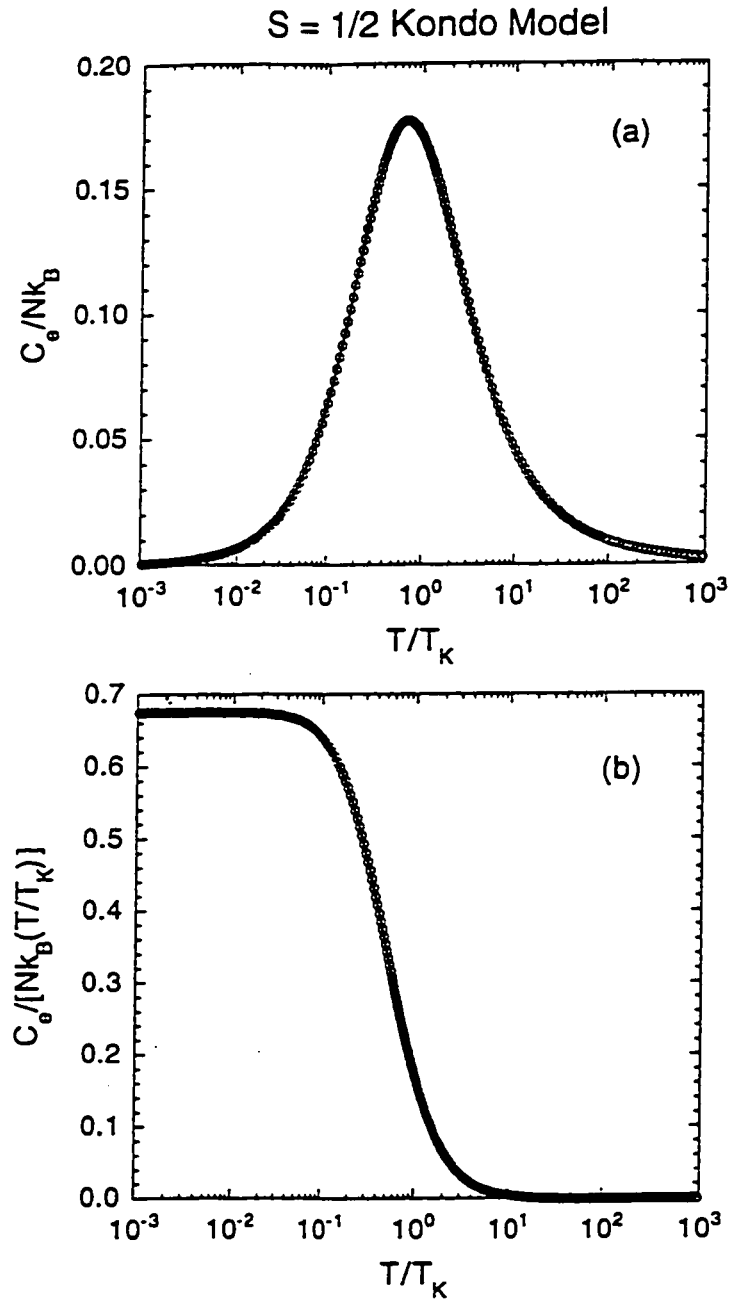


Figure 6.9 Accurate Bethe ansatz calculation of electronic heat capacity C_e (a) and C_e/T (b) of the $S = 1/2$ Kondo model, plotted versus $\log_{10}(T/T_K)$, where T is the temperature and T_K is the Kondo temperature [145, 148]. The fits to these data by Eqs. (6.44) and (6.45) are shown as solid curves in (a) and (b), respectively. The fitting parameters determined are listed in Table 6.7.

Table 6.7 Coefficients a_n in Eq. (6.46) in the fits to the Bethe ansatz prediction for the electronic heat capacity C_e and C_e/T versus temperature T of the $S = 1/2$ Kondo model by Jerez and Andrei [148].

a_n	$C_e(T)$ Fit	$C_e(T)/T$ Fit
a_1	9.1103933	6.8135534
a_2	30.541094	21.718636
a_3	2.1041608	2.3491812
a_4	0.0090613513	0.017533911
a_5	9.1164094	6.8158433
a_6	36.143206	27.663307
a_7	67.91795	48.229552
a_8	53.509135	40.216156
a_9	1.7964377	2.4863342

Fitting the theory to the experimental C_e/T data [Fig. 6.4(b)], Eqs. (6.45) and (6.46) yield

$$T_K^C = 26.4(1) \text{ K} \quad . \quad (6.47)$$

and from Eq. (6.42).

$$\gamma(0) = 426(2) \text{ mJ/mol K}^2 \quad . \quad (6.48)$$

Figures 6.10(a) and (b) present the fit as a solid curve, along with two dashed curves with slightly different values of $T_K = 25 \text{ K}$ and 28 K for comparison. It is clear that the low- T predicted C_e/T values are sensitive to the choice of T_K . The derived $\gamma(0) = 426 \text{ mJ/mol K}^2$ in Eq. (6.48) is in excellent agreement with those obtained in the previous two theories: 428 mJ/mol K^2 in Eq. (6.35) and 430 mJ/mol K^2 in Eq. (6.41). However, the high T ($\gtrsim 10 \text{ K}$) data are not fitted well, as seen in Fig. 6.10(b).

Local moment high-temperature description

The high-temperature series expansion (HTSE) analysis done in Chapter 4 for the intrinsic susceptibility data presents the formulation of magnetic heat capacity $C_m(T)$ based upon the same Hamiltonian [Eq. (4.20)]. The HTSE prediction of $C_m(T)$ given by Rushbrooke and Wood [88] is

$$\frac{C_m(T)}{Nk_B} = \frac{2z[S(S+1)]^2}{3t^2} \left(1 + \sum_{n=1}^{n^{\max}} \frac{c_n(S)}{t^n} \right) \quad . \quad (6.49)$$

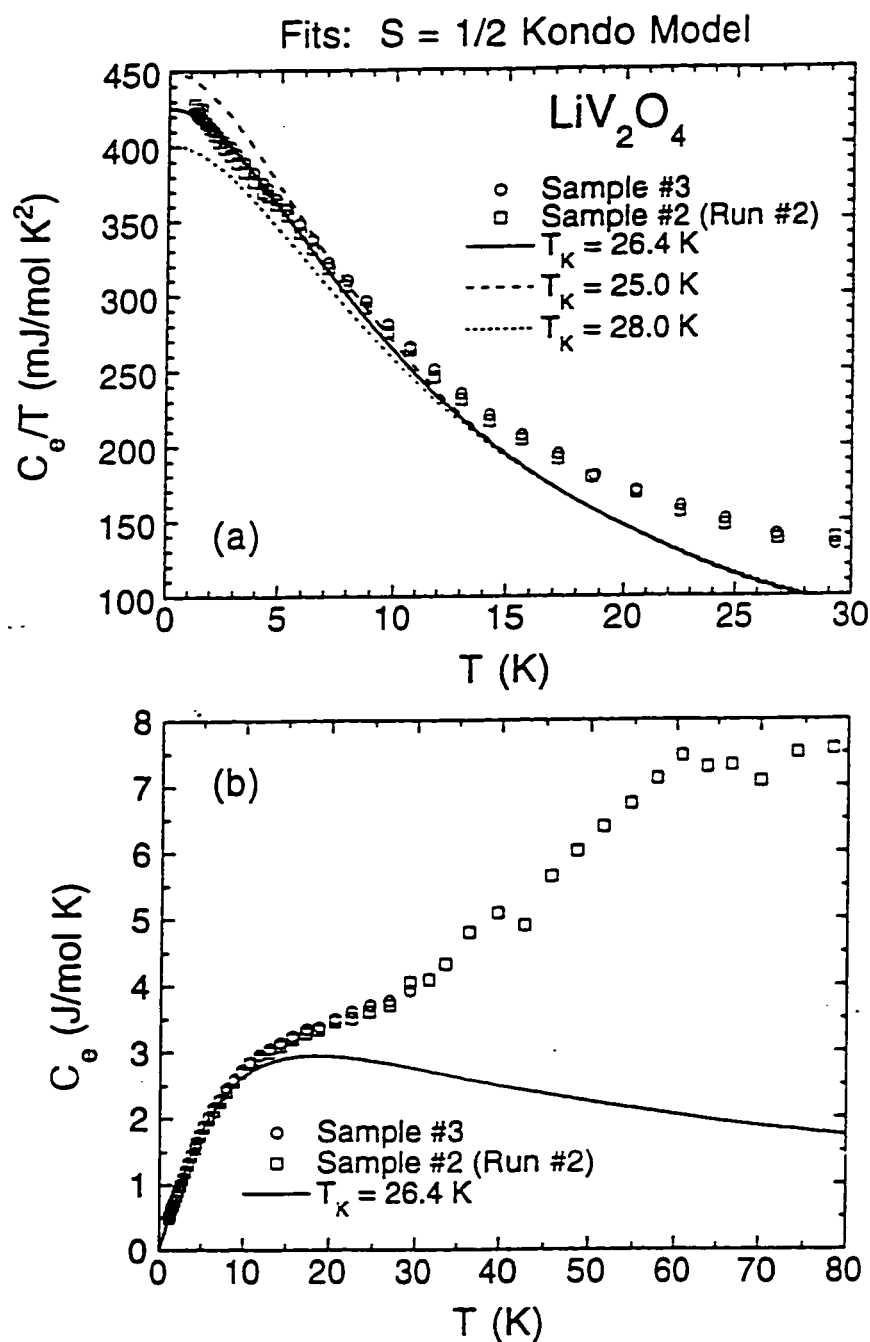


Figure 6.10 (a) Electronic heat capacity divided by temperature $C_e(T)/T$ data versus T (up to 30 K) for LiV_2O_4 sample 3 (open symbols) and a fit (solid curve) by the $S = 1/2$ Kondo model, Eqs. (6.46) and (6.47) with $T_K = 26.4$ K. Also for comparison the predictions for $T_K = 25.0$ K (long-dashed curve) and 28.0 K (short-dashed curve) are shown. (b) The same fit with $T_K = 26.4$ K is plotted in a wider T range to 80 K with the same data.

where $t \equiv k_B T/J$, and $z = 6$ is the coordination number of V by V in LiV_2O_4 . The c_n coefficients for $S = 1/2$ with $n^{\max} = 5$ are

$$c_1 = -\frac{1}{2} \quad , \quad c_2 = -\frac{23}{16} \quad , \quad c_3 = \frac{65}{48} \quad , \quad c_4 = \frac{1183}{768} \quad , \quad c_5 = -\frac{18971}{7680} \quad . \quad (6.50)$$

With these c_n coefficients the HTSE prediction $C_m(T)$ curve with $J/k_B = 20$ K (a typical value found in Chapter 4) is plotted in Fig. 6.11 with our experimental $C_e(T)$ for LiV_2O_4 sample 2 and 6. It is evident that the HTSE prediction $C_m(T)$ displays much lower values than the experimental data, and that the overall T dependence is much different. The $C_e(T)$ cannot be explained by the local-moment prediction over the T range of our measurements.

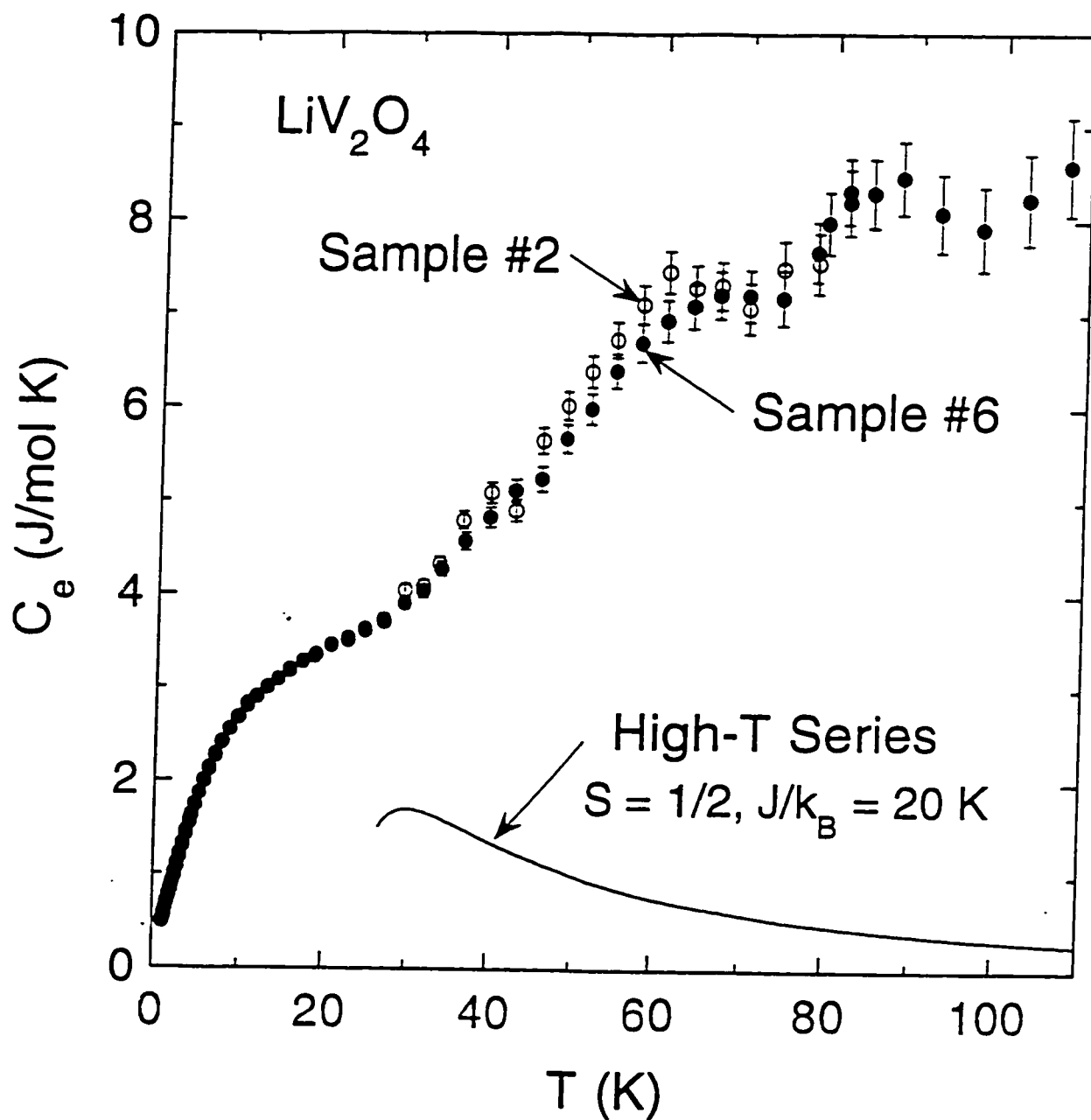


Figure 6.11 Comparison between the experimental $C_e(T)$ data of LiV_2O_4 samples 2 (run 2) and 6 [from Fig. 6.4(a)] and the high-temperature series expansion (HTSE) prediction of the magnetic heat capacity $C_m(T)$ ($n^{\max} = 5$) for the B sublattice of the normal spinel structure with $S = 1/2$ and c_n coefficients in Eq. (6.50). A typical value of $J/k_B = 20$ K was assumed.

7 THERMAL EXPANSION

The thermal expansion of our LiV_2O_4 polycrystalline samples was measured by the use of neutron diffraction and high-resolution capacitance dilatometry. The neutron diffraction study from 4 to 295 K was done by Dr. Jorgensen's group at Argonne National Laboratory and reported in [18]. The dilatometry measurements from 4.4 to 297 K were carried out by Dr. C. A. Swenson, the present discussion and modeling of these results closely follow that given by Dr. D. C. Johnston and Dr. C. A. Swenson in a paper in preparation [14]. In this chapter, the results of these two measurements are briefly introduced and a discussion in terms of the Grüneisen parameter Γ follows.

Neutron diffraction

Chmaissem *et al.* [18] measured the thermal expansion of our LiV_2O_4 sample 5 at the Argonne National Laboratory. No structural phase transition to a lower symmetry was observed down to 4 K. Also, no impurity phase was detected. This is contrary to our x-ray diffraction measurement result, as discussed in Chapter 3. The x-ray diffraction measurement on the same sample 5 showed the V_2O_3 impurity phase. The small negative neutron scattering length of vanadium might have been the cause of this difference. Nonetheless, we infer that the difference comes from sample dependence. This is because using the powder sample 5 on which the neutron diffraction was done we found no V_2O_3 peaks in a separate x-ray diffraction measurement. Although this "neutron" sample and the original "x-ray" sample are both sample 5, they are from different pieces of the same batch. This is believed to be the reason that causes these samples to have slightly different lattice parameter a_0 values, as discussed below.

Rietveld analyses of the neutron diffraction data at temperatures T from 4 to 295 K were done using the "GSAS" (General Structure Analysis System) [169]. The refinement results are given in Table 7.1.

The temperature variation of the lattice parameter a_0 is plotted in Fig. 7.1. The lattice parameter a_0 shows a continuous decrease from 295 K on cooling. The T dependence of a_0 becomes very weak from ~ 65 to ~ 20 K, then another decrease below ~ 20 K follows (see the inset of Fig. 7.1). This low- T

Table 7.1 Results of GSAS code Rietveld refinements of the neutron diffraction data for $T = 4$ 295 K (results for only selected T data are shown here). For the oxygen parameter u , the second choice of the origin for the space group $F\bar{d}3m$ is used, as in the Rietveld analysis results of the x-ray diffraction data (see Chapter 3), so that $u = 0.25$ for an ideal closed-packed oxygen array. The unit of the lattice parameter a_0 is Å, and that for the thermal displacement parameters B is Å².

T	295 K	250 K	200 K	150 K	100 K	50 K	15 K	4 K
a_0	8.24039(3)	8.23605(4)	8.23177(4)	8.22889(4)	8.22737(3)	8.22688(3)	8.22687(3)	8.22672(3)
$B(\text{Li})$	1.10(5)	1.08(6)	1.06(6)	0.85(6)	0.81(6)	0.79(6)	0.73(3)	0.72(3)
$B(\text{V})$	-0.29(6)	-0.32(8)	-0.24(8)	-0.24(8)	-0.45(7)	-0.50(5)	-0.46(5)	-0.50(5)
$B(\text{O})$	0.48(1)	0.41(2)	0.38(2)	0.33(2)	0.27(1)	0.27(1)	0.26(1)	0.24(1)
u	0.26127(2)	0.26128(3)	0.26118(3)	0.26114(3)	0.26110(3)	0.26112(3)	0.26114(2)	0.26111(2)
χ^2	1.550	1.300	1.268	1.256	1.314	1.298	1.523	1.297

decrease was found to be reproducible from repetitive measurements.

The slope of a_0 with respect to T is proportional to the thermal expansion coefficient. The linear thermal expansion coefficient α is defined

$$\alpha(T) = \frac{1}{\ell} \frac{d\ell}{dT} . \quad (7.1)$$

From the neutron diffraction analysis results, we have a decreasing $\alpha(T)$ from high T to ~ 65 K. The $\alpha(T)$ becomes nearly zero from ~ 65 to ~ 20 K where there is a very weak T variation of a_0 . Below ~ 20 K, $\alpha(T)$ rises again. These behaviors of $\alpha(T)$ were confirmed from the capacitance dilatometer measurements which are described below.

Capacitance dilatometry

The linear thermal expansion coefficient $\alpha(T)$ defined in Eq. (7.1) for LiV_2O_4 sample 6 was obtained from capacitance dilatometer measurements from 4.4 to 297 K [14]. Figure 7.2 shows $\alpha(T)$ and $\alpha(T)/T$ for the entire T range. LiV_2O_4 and the isostructural LiTi_2O_4 [170] have similar room- T values of α : 12.4×10^{-6} and $\approx 15.6 \times 10^{-6} \text{ K}^{-1}$, respectively. These values are comparable to α at room-temperature of elementary metals, as shown in Table 7.2. In addition, LiV_2O_4 shows a decreasing $\alpha(T)$ with decreasing T like conventional metals. However, unlike such metals which show a monotonically decreasing $\alpha(T)$ as $\alpha(T) = A_1T + A_3T^3$ at low T [171], $\alpha(T)$ of LiV_2O_4 shows an upturn below ~ 20 K after being nearly zero at about 23 K. This strong T dependence can be more readily seen when plotted as $\alpha(T)/T$ versus T (Fig. 7.2). The curve fitting by the following polynomial equation [Eq. (7.2)] was done for three T regions, and the A_n coefficients are listed in Table 7.3.

$$\alpha(T) = \sum_n A_n T^n . \quad (7.2)$$

The zero-temperature limit of α/T is identical to the coefficient A_1 determined from the lowest 0–14 K fitting range, and is found to be $2.002 \times 10^{-7} \text{ K}^{-2}$.

From the $\alpha(T)$ data set, the lattice parameter $a_0(T)$ may be generated by the integral $a_0(T) = a_0(0)[1 + \int_0^T \alpha(T')dT']$. Using the above fit Eq. (7.2) for $\alpha(T)$ with the A_n coefficients in Table 7.3, $a_0(T)$ was calculated assuming $a_0(0) = 8.226709 \text{ \AA}$. This zero- T lattice parameter value was chosen so that the calculated $a_0(4 \text{ K})$ becomes equal to that from the neutron diffraction measurements. These calculated $a_0(T)$ values based on the dilatometer measurements reproduces well the overall T variation of $a_0(T)$ from the neutron diffraction measurements, as shown in Figs. 7.3(a) and (b). The downturn of $a_0(T)$ for $T \lesssim 20$ K found in the neutron diffraction study is also seen in the derived $a_0(T)$ from

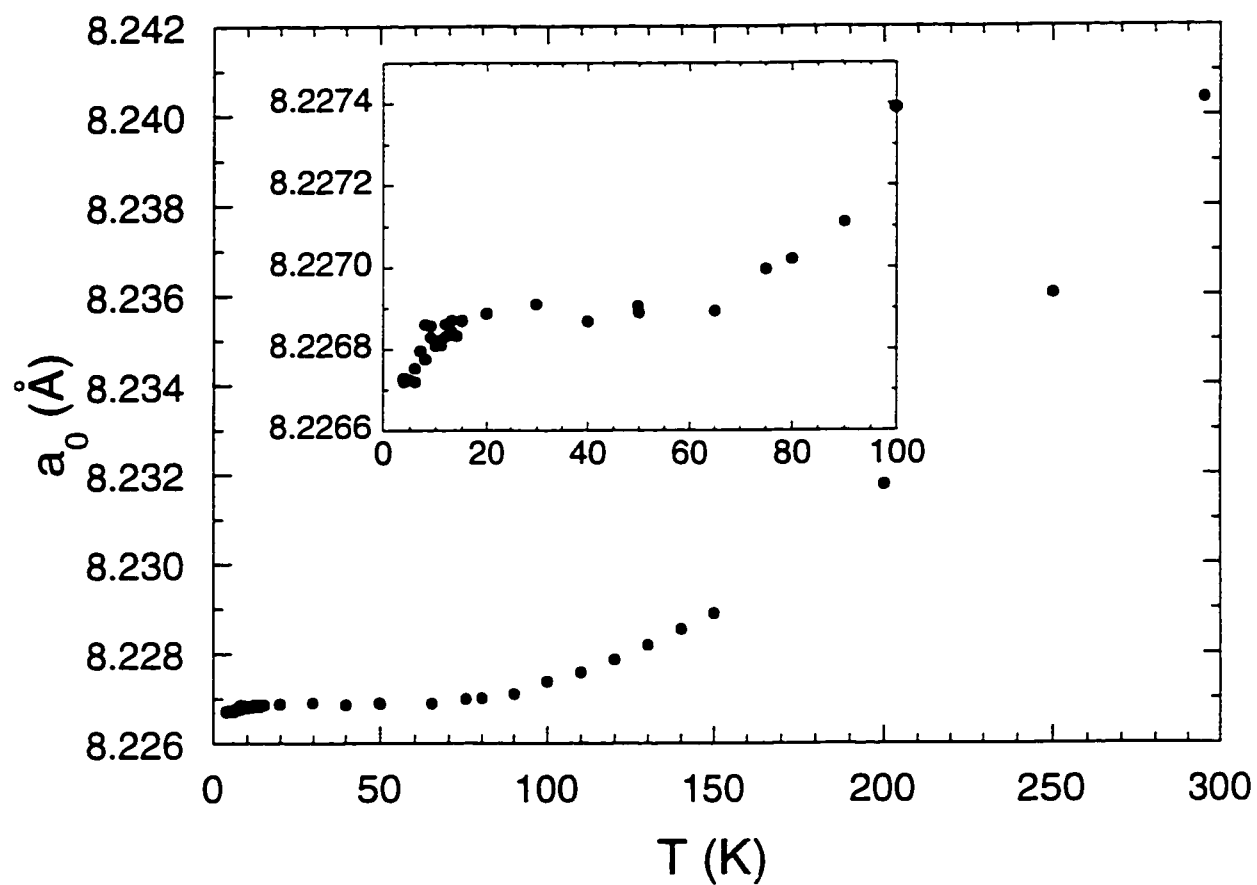


Figure 7.1 Lattice parameter a_0 versus temperature T for LiV_2O_4 sample 5 as determined from neutron diffraction measurements [18].

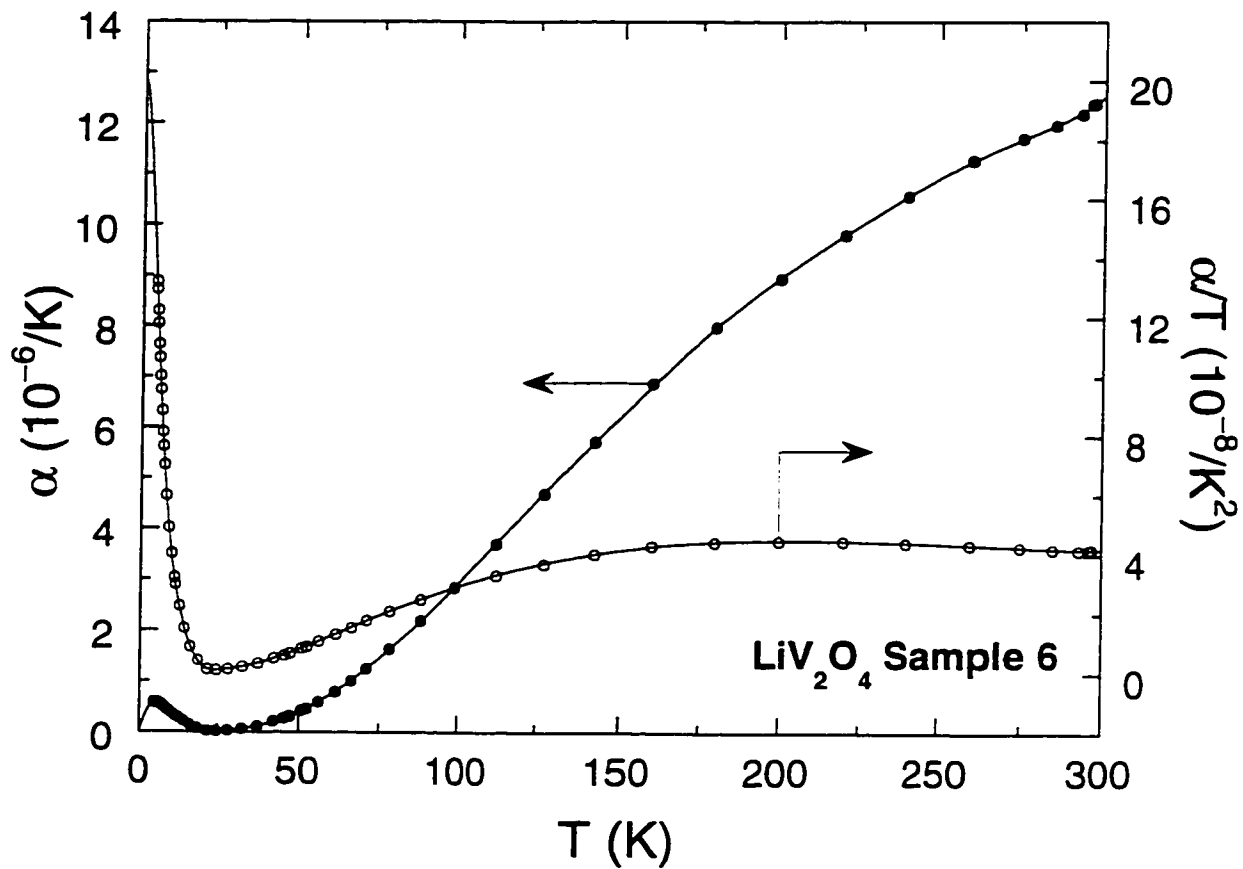


Figure 7.2 Linear thermal coefficient $\alpha(T)$ (left-hand scale) and $\alpha(T)/T$ (right-hand scale) versus temperature T for LiV_2O_4 sample 6, obtained from capacitance dilatometer measurements [14].

Table 7.2 Room-temperature values of linear thermal expansion coefficients of LiV_2O_4 [14], LiTi_2O_4 [170], and some elemental metals [171].

	α (10^{-6} K^{-1})
LiV_2O_4	12.4
LiTi_2O_4	≈ 15.6
Al	23.1
Ca	22.3
Cu	16.5
Au	14.2
Mg	24.8
Ag	18.9

the dilatometer measurements. The difference in sizes of the downturns from the two measurements differ by more than the accuracies of both measurements; hence, this difference may indicate a sample dependence. Sample 6 has shown its tendency to yield slightly larger values of the susceptibility and electronic heat capacity, as already mentioned in Chapters 4 and 6, respectively.

This enhanced behavior in $\alpha(T)/T$ below $\sim 20 \text{ K}$ may be seen in relation to that in $C_p(T)/T$, both indicating the crossover to the heavy fermion regime. Figure 7.4 illustrates this similarity clearly. To compare these similarly behaving quantities, one normally calculates the Grüneisen parameter Γ , which is the dimensionless, normalized ratio of the thermal expansion coefficient to the heat capacity. Using the volume thermal expansion β ($\beta = 3\alpha$ for a cubic material), the Grüneisen parameter is defined in the following Grüneisen relation (page 5a in [171])

$$\Gamma(T) = \frac{B_s V_m \beta(T)}{C_V(T)} \quad (7.3)$$

where B_s is the adiabatic bulk modulus and V_m is the molar volume. The heat capacity at constant volume $C_V(T)$ may be replaced with the observed, isobaric heat capacity $C_p(T)$ since these two heat capacity values differ from each other by less than 0.1% [14]. The volume thermal expansion coefficient $\beta(T)$ is usually considered to be the sum of electronic and lattice contributions as in the heat capacity; that is, $\beta = \beta_e + \beta^{\text{lat}}$ and $C_p = C_e + C^{\text{lat}}$. The Grüneisen relation is then given as

$$\Gamma(T) = B_s V_m \frac{\beta_e + \beta^{\text{lat}}}{C_e + C^{\text{lat}}} \quad (7.4)$$

from which we can readily see that we cannot simply assume Γ as a sum of Γ_e and Γ^{lat} ; the temperature

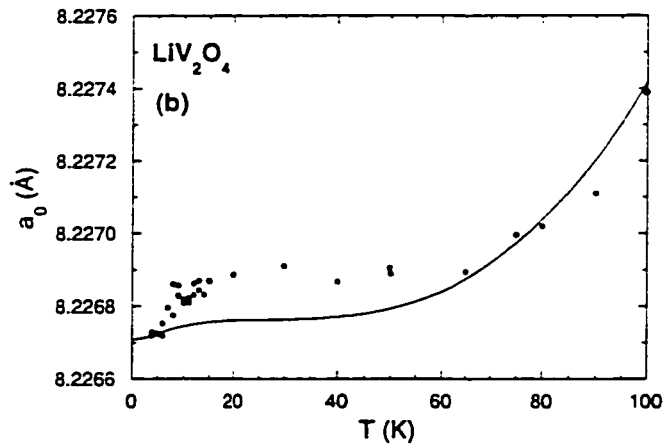
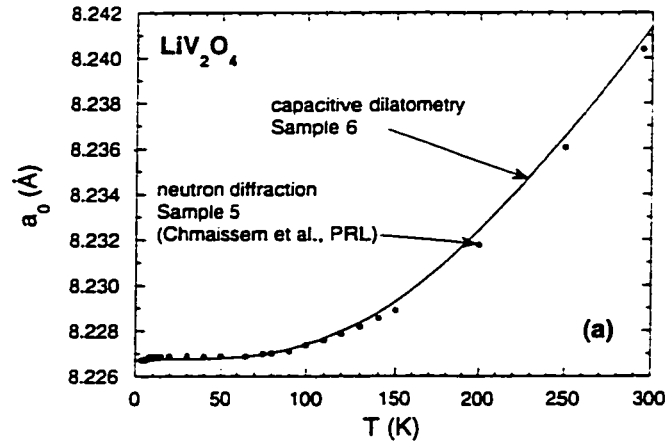


Figure 7.3 Comparison of the lattice parameter $a_0(T)$ for the entire temperature range (a) and up to 100 K (b) from the neutron diffraction measurements [18] and that derived from the linear thermal expansion coefficient $\alpha(T)$ by the integration given in the text. The neutron study used sample 5, while the dilatometry measurements used sample 6.

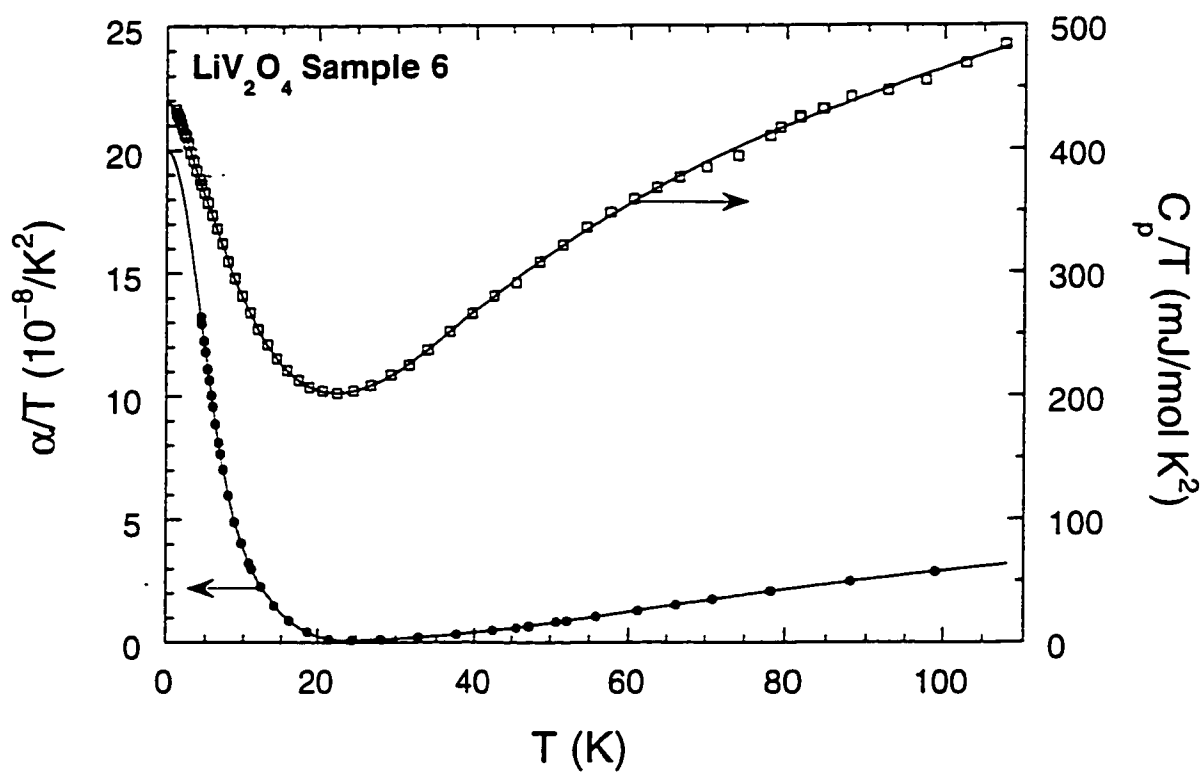


Figure 7.4 Linear thermal expansion coefficient divided by temperature α/T (left-hand scale) and observed heat capacity divided by temperature C_p/T (right-hand scale), versus T . The solid curves are fits to the respective data.

Table 7.3 Coefficients A_n of the power series Eq. (7.2) used to fit the observed linear thermal expansion coefficient $\alpha(T)$ (in units of K^{-1}) for LiV_2O_4 sample 6 in the three temperature ranges shown. The actual fitting range of the “0–14 K” range is 4.4–14 K, but the determined A_n coefficients in this range were used to extrapolate to $T = 0$.

n	0–14 K	14–24.5 K	24.5–297 K
0	0	8.18273×10^{-7}	-3.85093×10^{-7}
1	2.00162×10^{-7}	-4.14713×10^{-8}	6.03956×10^{-8}
2	0	-8.00360×10^{-10}	-3.55211×10^{-9}
3	-4.44102×10^{-9}	4.75726×10^{-11}	9.94538×10^{-11}
4	0	0	-1.36244×10^{-12}
5	5.40327×10^{-11}	0	1.11678×10^{-14}
6	0	0	-5.68546×10^{-17}
7	-3.76734×10^{-13}	0	1.75092×10^{-19}
8	0	0	-2.97738×10^{-22}
9	1.38751×10^{-15}	0	2.14217×10^{-25}
10	0	0	0
11	-2.08005×10^{-18}	0	0

dependences of components of β and C_p mix. White [172] showed that

$$\Gamma = \frac{\Gamma_e C_e + \Gamma^{\text{lat}} C^{\text{lat}}}{C_e + C^{\text{lat}}} . \quad (7.5)$$

Then from Eqs. (7.4) and (7.5) we have

$$\Gamma_e C_e + \Gamma^{\text{lat}} C^{\text{lat}} = B_s V_m (\beta_e + \beta^{\text{lat}}) . \quad (7.6)$$

so this indicates the need of $\beta^{\text{lat}}(T)$ from experiments to a corresponding insulating compound (*e.g.*, LiTi_2O_4 for LiV_2O_4) in order to separate out the two Grüneisen parameter contributions. Theoretically, for a metal, $\Gamma_e = 1 + [d \ln \mathcal{D}^*(E_F)/d \ln V]$ (page 10a in [171]), and $\Gamma^{\text{lat}} = -d \ln \theta_D(0)/d \ln V$. Therefore, Γ_e is the direct measure of the volume dependence of the mass-enhanced quasiparticle density of states at the Fermi level $\mathcal{D}^*(E_F)$. For the Fermi gas, $\Gamma_e = 2/3$, and for elemental nonmagnetic metals one has $\Gamma_e = 1.8$ (Al), 0.7 (Cu), 2.1 (Fe), 1.7 (Pb) and 2.4 (Pt) [173].

The Grüneisen parameter $\Gamma(T)$ was computed from the observed $\alpha(T)$ data in Fig. 7.2 and the fit to the observed $C_p(T)$ [14] (fitting coefficients not given in this dissertation). The bulk modulus was assumed to be $B_s = (2 \pm 0.4) \times 10^{11} \text{ N/m}^2$, which is the range shown by various similar compounds [14] including the mineral spinel MgAl_2O_4 [174]. Figure 7.5 shows the Grüneisen parameter $\Gamma(T)$ of

LiV_2O_4 sample 6. For the value extrapolated to $T = 0$, the fit to $\alpha(T)$ in Eq. (7.2) with the determined coefficients from Table 7.3 was used in combination with the fit to the $C_p(T)$. The estimated $\Gamma(0)$ is 11.5. In the limit of $T = 0$, the lattice contributions β^{lat} and C^{lat} become negligible, so $\Gamma(0) = \Gamma_e(0) = 11.5$. This value is intermediate between normal metals and f -electron heavy fermion compounds [e.g., 57 (CeCu₆), 150 (CeRu₂Si₂), 25 (URu₂Si₂), 34 (UBe₁₃), and 71 (UPt₃) [175]].

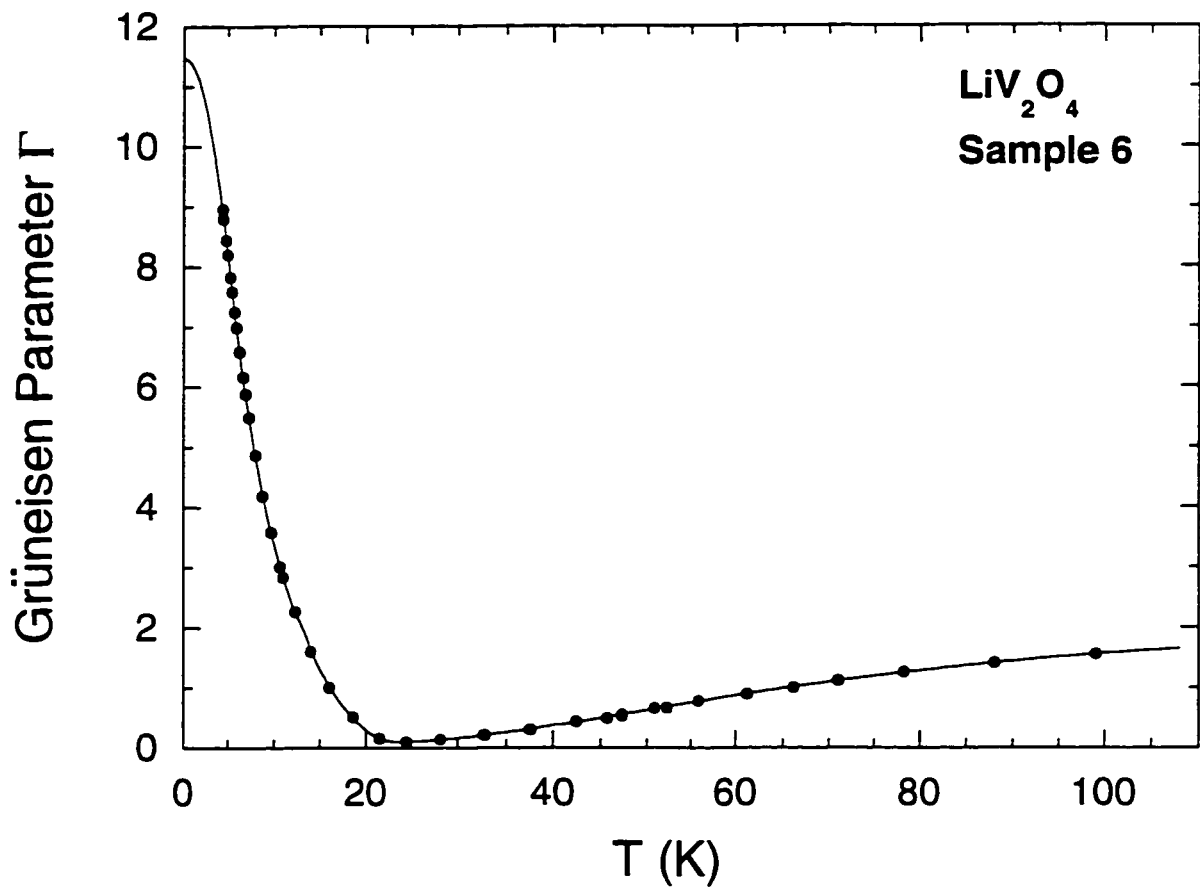


Figure 7.5 Grüneisen parameter Γ versus temperature T for LiV_2O_4 sample 6. The solid curve is an interpolation and extrapolation of the data (see text).

8 NUCLEAR MAGNETIC RESONANCE

In this chapter, the results analyses of ${}^7\text{Li}$ and ${}^{51}\text{V}$ nuclear magnetic resonance (NMR) studies of LiV_2O_4 done by Dr. F. Borsa's group are reviewed, based upon the recent publication by Mahajan *et al.* [19]. NMR plays an important role in describing how a magnetic system behaves microscopically in terms of several coupling mechanisms with nuclei. With respect to LiV_2O_4 , the ${}^7\text{Li}$ Knight shift K approximately varies linearly with the intrinsic susceptibility χ over the whole temperature T range measured. More specifically, Mahajan *et al.* obtained the hyperfine coupling constants from the slope of the shift versus the T dependent spin susceptibility $\chi^{\text{spin}}(T)$ in the high temperature regime. The ${}^7\text{Li}$ nuclear spin-lattice relaxation rate $1/T_1$ manifests the Korringa law ($1/T_1 \propto T$) below 5 K, indicative of the Fermi liquid state, and shows a crossover to high- T localized moment behavior above ~ 50 K. From the presence of only one observed ${}^{51}\text{V}$ line in the NMR spectrum, it is inferred that there is only one kind of V moment, eliminating the possibility of having two different magnetic moments on V^{+3} and V^{+4} on a time scale longer than that of NMR, *i.e.* 10^{-6} sec. In the following, major results from the published paper by Mahajan *et al.* are reviewed. This NMR work was done using five samples 1, 2, 4A, 4B and 6 of LiV_2O_4 .

Linewidths

${}^7\text{Li}$ linewidth

A nucleus with a nuclear spin larger than $I = 1/2$ has an electric quadrupole moment, and may interact with the electric field gradients that the surrounding charges create at the nuclear site only if the point symmetry of the nucleus site is non-cubic. The Li site in LiV_2O_4 is called the δa position, and its point symmetry is cubic. Therefore, there is no quadrupole effect in ${}^7\text{Li}$ NMR measurements. The ${}^7\text{Li}$ NMR linewidth Δ was obtained from the full width at half maximum (FWHM) of the free induction decay. The temperature T variation of Δ was found to be qualitatively similar to that of the susceptibility, as seen in Fig. 8.1. The width increases as T decreases from high T , and appears to be very weakly temperature dependent below ~ 30 K. This behavior is similar to that of the magnetic

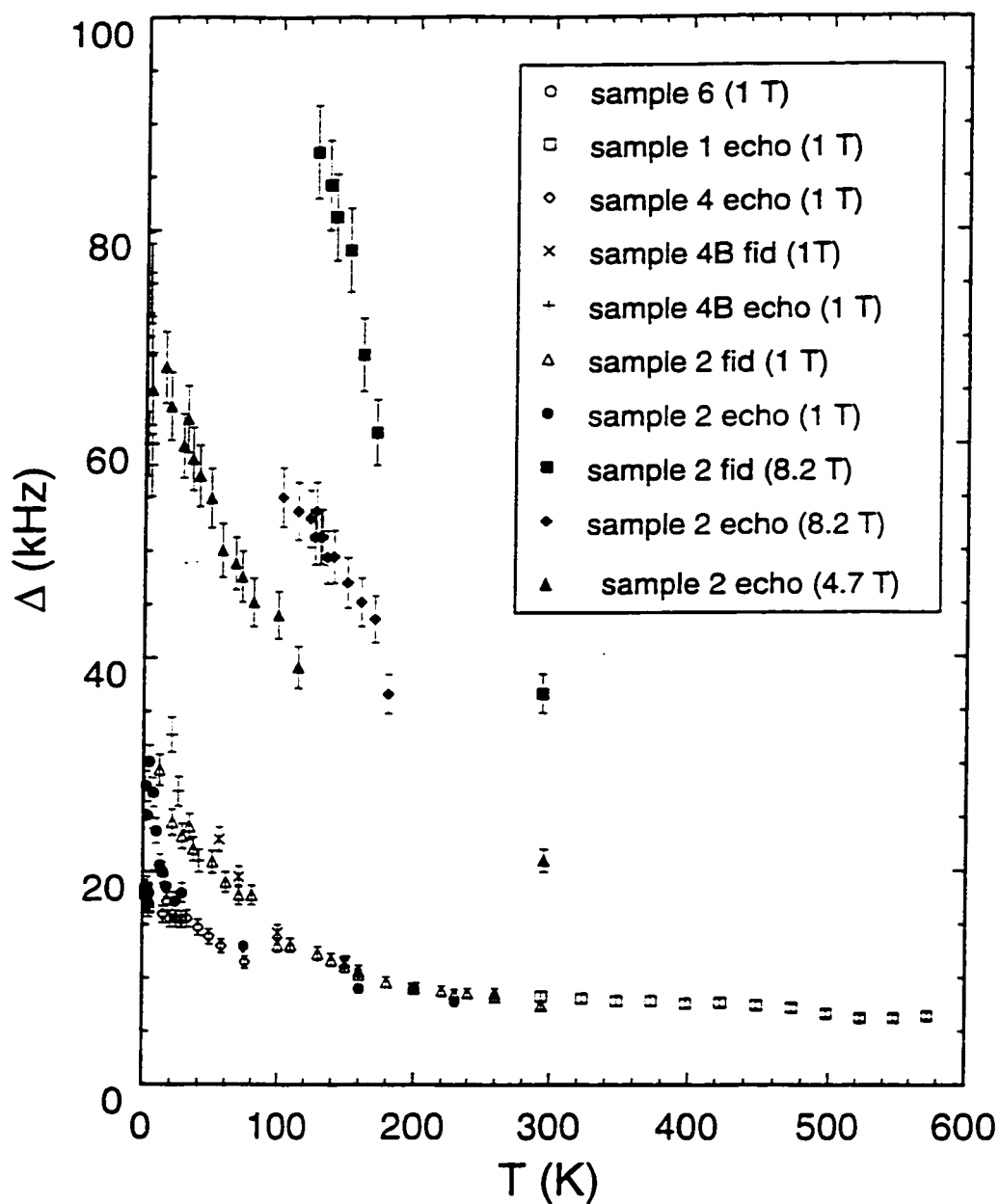


Figure 8.1 Temperature T dependences of ${}^7\text{Li}$ NMR linewidth Δ (FWHM) for five LiV_2O_4 samples. Δ was found to be larger as the applied field became larger, and Δ determined from the Fourier transform (FT) of the free induction decay (FID) shows a tendency to be larger than that from FT of the spin echo.

susceptibility. Also the linewidth Δ was found to be sample-dependent. The linewidth tends to be smaller for a sample with less magnetic impurities. In addition, for sample 2 the measurements were done under more than one value of applied field H , and the linewidth was found field-dependent. This suggests that the linewidth is due to inhomogeneities of local fields that the Li nucleus sees. These results agree well with previous work [97, 149].

^{51}V linewidth

The ^{51}V linewidth Δ was determined from the FWHM of the FT of the spin echo signal. Only one V site exists crystallographically in LiV_2O_4 , and is called the $16d$ site. The point symmetry of the site is trigonal. Since the ^{51}V nucleus has nuclear spin $I = 7/2$, quadrupole effects are therefore possible. However, the $\pi/2$ pulse length on the ^{51}V nuclei was found to be the same as that on the ^{27}Al nuclei in a reference solution under the same coil and power conditions (both nuclei has nearly the same nuclear gyromagnetic ratio γ). Hence, not only the central transition line (which corresponds to $I = \frac{1}{2} \leftrightarrow -\frac{1}{2}$) but all the six satellite lines ($\pm\frac{1}{2} \leftrightarrow \pm\frac{3}{2} \leftrightarrow \pm\frac{5}{2} \leftrightarrow \pm\frac{7}{2}$) were irradiated. In other words, all these lines are found to be so close to each other that the given pulse could not distinguish them but just saw only one line due to the overlap. Therefore, quadrupole effects can be neglected.

As in the ^7Li NMR, the temperature and field-dependent linewidth Δ was obtained from ^{51}V NMR, shown in Fig. 8.2. Only one ^{51}V line was observed. This implies that NMR did not distinguish between the two possible vanadium valence configurations V^{+3} and V^{+4} on the time scale longer than that of NMR (10^{-6} sec), so only one kind of V moment exists. The nuclear dipole-dipole interactions in pairs $^{51}\text{V}-^{51}\text{V}$ and $^{51}\text{V}-^7\text{Li}$ contribute to the observed ^{51}V linewidth a T and H independent term [176]. On the other hand, a T and H dependent contribution to the width comes from macroscopic field inhomogeneities due to the demagnetization effect of powder samples [177]. By assuming a Gaussian approximation, the ^{51}V linewidth can be written

$$\Delta_{\text{FWHM}} = 2.35 \sqrt{\langle \Delta\nu^2 \rangle_{\text{dip}} + \left(B\chi_V H \frac{\gamma}{2\pi} \right)^2} \quad (8.1)$$

where B is the fractional rms deviation of the local field generated by the applied field H , and $\gamma/2\pi = 1119.3 \text{ Hz/G}$. χ_V is the observed volume susceptibility, and $\chi_V = \chi^{\text{obs}} d/M$, where χ^{obs} is the molar susceptibility, $d = 4.105 \text{ g/cm}^3$ is the density, and $M = 173 \text{ g/mol}$ is the molar mass of LiV_2O_4 . With the lattice paramter $a = 8.24 \text{ \AA}$, the Van Vleck formula [176] gives

$$\begin{aligned} \langle \Delta\nu^2 \rangle_{\text{dip}} &= \langle \Delta\nu^2 \rangle_{\text{V-V}} + \langle \Delta\nu^2 \rangle_{\text{V-Li}} \\ &= 4.6 \times 10^7 \text{ Hz}^2 + 0.41 \times 10^7 \text{ Hz}^2 \end{aligned} \quad (8.2)$$

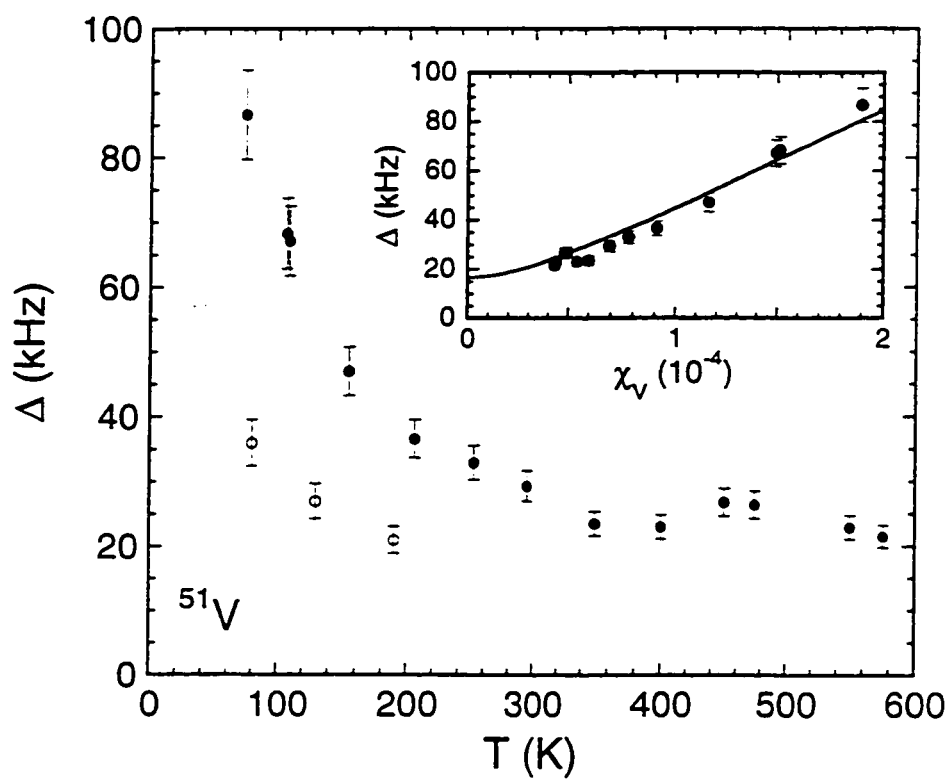


Figure 8.2 ^{51}V NMR linewidth Δ versus temperature T for LiV_2O_4 sample 2. The linewidth was determined from the Fourier transform of the spin echo signal under magnetic fields of 1.5 T (open circles) and 4.7 T (filled circles). The inset shows the latter data set plotted as a function of the dimensionless volume spin susceptibility χ_V^{spin} . The solid curve is Eq. (8.1) with $B = 3.6$.

$$= 5.0 \times 10^7 \text{ Hz}^2 .$$

A fit of Eq. (8.1) to the observed linewidth yielded $B = 3.6$, and the fit is drawn as the solid curve in the inset of Fig. 8.2. The demagnetization effect can give rise to $B = 4\pi \cdot 0.114 = 1.43$, assuming closely-packed spheroids. It is suggested that, since the symmetry of the V site is not cubic, the dipolar sum inside the Lorentz sphere can give an additional contribution to B to yield this difference. From this analysis, one finds that the above mean-square width from dipolar interactions in Eq. (8.1) is much smaller at low T and high H than the other contribution from macroscopic field inhomogeneities due to the demagnetization effects of powder samples [the second term in the square root in Eq. (8.1)]. For instance, a rough calculation using $B = 3.6$, $\chi^{\text{obs}} = 0.01 \text{ cm}^3/\text{mol}$ at low T and $H = 47 \text{ kG}$ (data points were actually taken under this field) gives

$$\left(B\chi_V H \frac{\gamma}{2\pi} \right)^2 = 2.02 \times 10^9 \text{ Hz}^2 . \quad (8.3)$$

This value is 44 times larger than the above dipolar contribution. Having this dominating magnetization term, one can conclude that no more useful information can be drawn from the linewidth analysis than those already obtained from the susceptibility analyses, since $\Delta(T)$ should behave the same way as the susceptibility. This conclusion holds for the ${}^7\text{Li}$ linewidth, too. Further analysis of linewidths is not given.

Knight shifts

${}^7\text{Li}$ Knight shift

The Knight shift K obtained from ${}^7\text{Li}$ NMR is shown versus T in Fig. 8.3. It is quite clear that the T variation of the shift appears very similar to that of the intrinsic susceptibility $\chi(T)$. A Curie-Weiss-like behavior at high $T \gtrsim 50 \text{ K}$ is observed, and $K(T)$ shows a weak T dependence at low T with a broad maximum at $T \approx 25\text{--}30 \text{ K}$. Figure 8.4 indicates the approximately linear relationship of the shift with the T -dependent, local moment susceptibility $\chi^{\text{loc}}(T)$ above 100 K (see below). From the analyses of intrinsic susceptibilities $\chi(T)$, the Curie constants C expected for $S = 1/2$ and $g \approx 2$ were obtained in Chapter 4. As mentioned before, this suggests that $\approx 1d$ -electron per V atom is localized and the remaining 0.5 d -electrons/V are itinerant. This view is taken here for the analyses of Knight shifts.

There are five different possible magnetic contributions to Knight shifts [178, 179]. The first one is a direct magnetic dipole-dipole coupling of the ${}^7\text{Li}$ nuclear spin to the V local electron spin. The

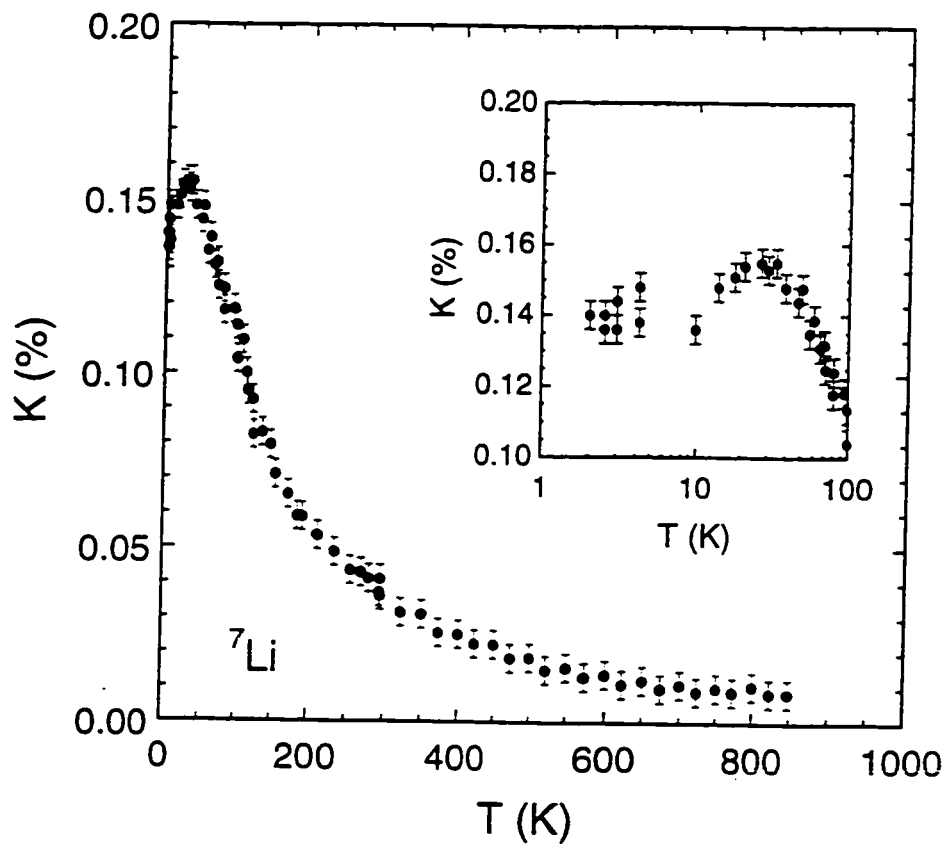


Figure 8.3 ${}^7\text{Li}$ Knight shift K versus temperature T of LiV_2O_4 . In the inset the data below 100 K is shown.

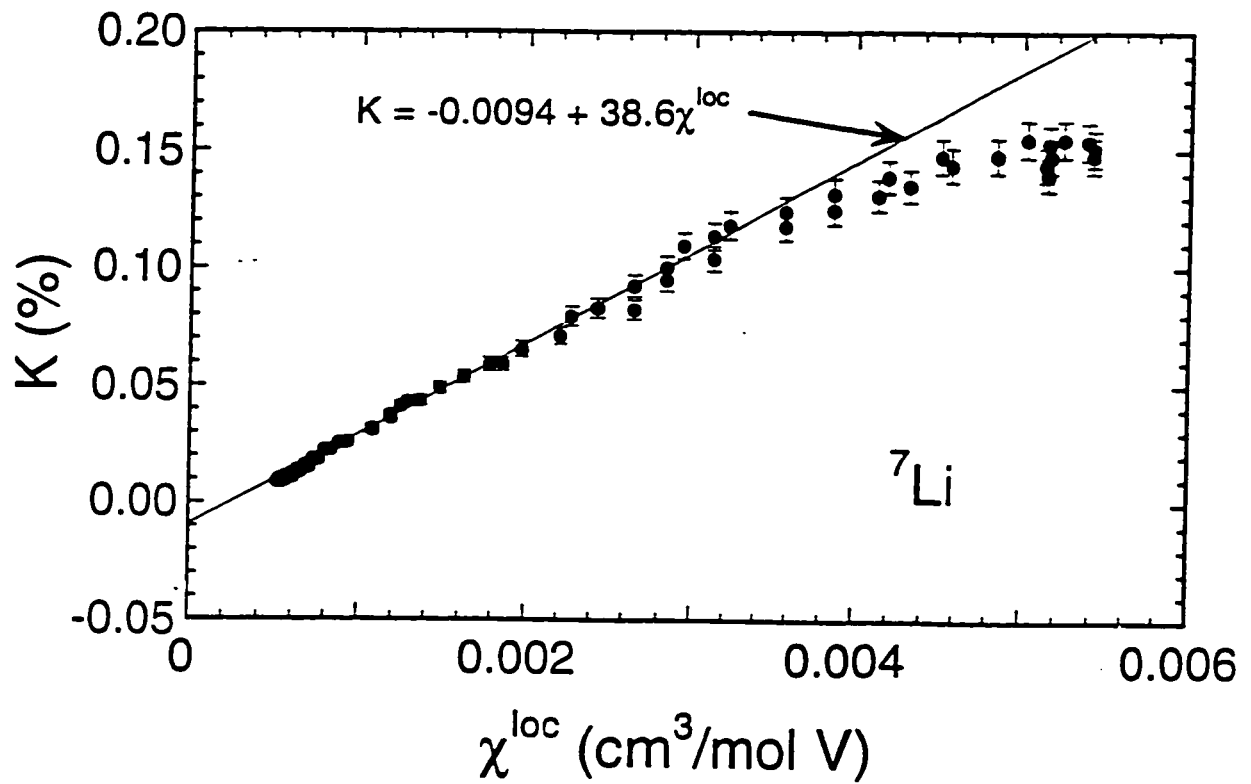


Figure 8.4 ⁷Li Knight shift K versus the local magnetic susceptibility χ^{loc} for sample 6 of LiV_2O_4 .

Hamiltonian in this case is

$$\mathcal{H}_{\text{dip}} = -\gamma_e \gamma_n \hbar^2 \vec{I} \cdot \left[\frac{\vec{S}}{r^3} - 3 \frac{\vec{r}(\vec{S} \cdot \vec{r})}{r^5} \right] . \quad (8.4)$$

Various symbols used in this and following equations are defined as follows: electron spin magnetic moment $\vec{\mu}_e = -g\mu_B \vec{S} = -\gamma_e \hbar \vec{S}$, where g is the g -value of the electron, μ_B is the Bohr magneton, \vec{S} is the electron spin angular momentum in units of \hbar , γ_e is the electron gyromagnetic ratio, and \hbar is the Planck constant divided by 2π ; the nuclear spin magnetic moment $\vec{\mu}_n = g_n \mu_n \vec{I} = \gamma_n \hbar \vec{I}$, where g_n , μ_n , \vec{I} and γ_n are the nuclear equivalents of the above defined electron quantities; \vec{r} is the position vector of an electron with respect to the origin where a nucleus is situated, and $r \equiv |\vec{r}|$; $\vec{\ell}$ (used below) is the electron orbital angular momentum in units of \hbar . This dipole-dipole coupling yields a zero net contribution to the Knight shift for an isotropic g -value. If there exists an anisotropy in the g -value, the dipolar contribution to the shift is proportional to $g_{\parallel}^2 - g_{\perp}^2$ [180]. For this cubic system, there can be no anisotropy in the g -value for the ${}^7\text{Li}$ in cubic point symmetry and hence this dipole-dipole interaction cannot give rise to the observed Knight shift.

The second interaction that can contribute to the Knight shift is the so-called Fermi contact interaction. This is due to the Zeeman-like interaction of the nuclear spin I with the effective magnetic field that an electron at the nucleus site may create. Therefore, only unpaired s -electrons can give rise to this Fermi contact interaction. The Hamiltonian is

$$\mathcal{H}_{\text{Fc}} = \frac{8\pi}{3} \gamma_e \gamma_n \vec{I} \cdot \vec{S} \delta(\vec{r}) . \quad (8.5)$$

where $\delta(\vec{r})$ is the Dirac delta function.

The d -electrons have a zero probability of existing at the site of a nucleus (origin), so the Fermi contact interaction in the above, direct sense is not possible. However, the d -electrons can indirectly produce a same Fermi contact effect. The d -electrons can polarize the core electrons in a closed shell and the paired outer conduction electrons, which then interact with the nuclear spin by the ordinary Fermi contact term.

The third contribution to the shift is due to the orbital motion of conduction electrons induced by an applied external field. This orbital motion creates an effective magnetic field at the nuclear site, and the nuclear spin I interacts with the effective field. In this way, the orbital moment of electrons can couple with the nuclear spin I by

$$\mathcal{H}_{\text{orb}} = \gamma_e \hbar \frac{\vec{\mu}_n \cdot \vec{\ell}}{r^3} . \quad (8.6)$$

The fourth contribution is due to the Landau diamagnetic susceptibility χ^{Landau} of conduction electrons. The Knight shift due to this is proportional to χ^{Landau} . But χ^{Landau} is negligibly small for

d -electron systems [128]. Therefore, this term is neglected in the following analyses.

Finally, a contribution to the Knight shift can arise from the exchange coupling of the Li nuclear spin I to the V spins. Each Li has 4 oxygens as nearest neighbors, and each of these oxygens is bonded to 3 vanadium atoms. Hence, there are 12 V atoms whose spins can couple with one Li nuclear spin by exchange interactions.

The observed magnetic susceptibility $\chi^{\text{obs}}(T)$ is written for high T ($\gtrsim 50$ K) as

$$\chi^{\text{obs}}(T) = \chi^{\text{VV}} + \chi^{\text{core}} + \chi^{\text{spin}}(T) \quad . \quad (8.7)$$

where χ^{VV} is the orbital Van Vleck susceptibility and χ^{core} is the core diamagnetic susceptibility. Both of these are temperature T independent. $\chi^{\text{spin}}(T)$ is the spin susceptibility which can be further decomposed in a picture of local moments in metals according to

$$\chi^{\text{spin}}(T) = \chi^{\text{Pauli}} + \chi^{\text{loc}}(T) \quad . \quad (8.8)$$

where χ^{Pauli} is the Pauli paramagnetic susceptibility of conduction electrons, and $\chi^{\text{loc}}(T)$ is T -dependent susceptibility of local moments. Dropping the dipolar and Landau diamagnetic contributions, the ^7Li Knight shift K can be given as

$$\begin{aligned} K(T) &= K^{\text{VV}} + K^{\text{Pauli}} + K^{\text{loc}}(T) \\ &= 2 \frac{A^{\text{VV}}}{N_{\text{A}} \mu_{\text{B}}} \chi^{\text{VV}} + 2 \frac{A^{\text{Pauli}}}{N_{\text{A}} \mu_{\text{B}}} \chi^{\text{Pauli}} + 12 \frac{A^{\text{loc}}}{N_{\text{A}} \mu_{\text{B}}} \chi^{\text{loc}}(T) \quad . \end{aligned} \quad (8.9)$$

where the A 's are the respective hyperfine coupling constants. All of these susceptibilities are in units of cm^3 per mole of vanadium atoms. The factors of 2 in Eq. (8.10) are to take into account for the fact that there are two V atoms per formula unit of LiV_2O_4 . A^{VV} is neglected because of the orbital singlet Li ion.

The K - χ analysis was done in Ref. [19] using the local moment susceptibility $\chi^{\text{loc}}(T)$, not the total, observed susceptibility $\chi^{\text{obs}}(T)$. Combining the three T -independent susceptibility terms into one term as χ_0 , and assuming the validity of the Curie-Weiss law for the local moment contribution $\chi^{\text{loc}}(T)$, the measured susceptibility χ^{obs} was fitted by Mahajan *et al.* [19] to the following equation

$$\chi^{\text{obs}}(T) = \chi_0 + \frac{2C}{T - \theta} \equiv \chi_0 + \chi^{\text{loc}}(T) \quad . \quad (8.10)$$

in the T range of 100–800 K, using the combined data set of χ^{obs} of our own data [17] and that (high T part) of Hayakawa *et al.* [9], yielding (see [181])

$$\chi_0 = 2.72 \times 10^{-4} \text{ cm}^3 / (\text{mol V}) \quad , \quad (8.11)$$

$$C = 0.329 \text{ cm}^3 \text{ K}/(\text{mol V}) \quad . \quad (8.12)$$

$$\theta = -12.86 \text{ K} \quad . \quad (8.13)$$

These fit results enabled Mahajan *et al.* to plot $K(T)$ versus $\chi^{\text{loc}}(T)$, T being an implicit variable, in Fig. 8.4. A straight line fit was done and the fit curve is shown in Fig. 8.4. From the slope, they found

$$A^{\text{loc}} = 0.18(1) \text{ kG} \quad . \quad (8.14)$$

and from the y (here K) intercept,

$$K_0 = -0.0094 \% \quad . \quad (8.15)$$

It is necessary to know the Pauli susceptibility χ^{Pauli} in order to determine the hyperfine coupling constant A^{Pauli} from the intercept. From the K - χ analysis by Kondo *et al.* [17] using the ^{51}V Knight shift and the observed susceptibility χ^{obs} for LiV_2O_4 sample 2, the orbital Van Vleck susceptibility was found in Eq. (4.19)

$$\chi^{\text{VV}} = 1.11(3) \times 10^{-4} \text{ cm}^3/(\text{mol V}) \quad . \quad (8.16)$$

Using the core diamagnetic contribution $\chi^{\text{core}} = -31.5 \times 10^{-6} \text{ cm}^3/(\text{mol V})$, from the equation $\chi_0 = \chi^{\text{VV}} + \chi^{\text{core}} + \chi^{\text{Pauli}}$ and Eq. (8.11) we obtained

$$\chi^{\text{Pauli}} = 1.64 \times 10^{-4} \text{ cm}^3/(\text{mol V}) \quad . \quad (8.17)$$

This value is close to that of an isostructural superconducting LiTi_2O_4 [$\chi^{\text{Pauli}} \sim 1 \times 10^{-4} \text{ cm}^3/(\text{mol Ti})$] [4, 135]. From this estimate, we determine the hyperfine coupling constant of ^7Li nuclei with conduction electrons

$$A^{\text{Pauli}} = -1.60 \text{ kG} \quad . \quad (8.18)$$

This value is roughly 1% of the atomic hyperfine coupling constant for $2s$ conduction electrons of Li metal (122 kG) [179]. Having mostly d -character in a conduction band, this small size is not unexpected. The negative sign in Eq. (8.18) implies antiferromagnetic exchange interaction between the V d conduction electrons and the $1s$ core electrons of Li on the polarization. The small size of A^{loc} can be explained by the fact that the lithium is located far from the vanadium site where the local moments reside, so there is very little overlap of the V wavefunctions to the lithium s orbitals.

^{51}V Knight shift

^{51}V Knight shift K versus temperature T is shown in Fig. 8.5. The observed shift is negative throughout, and its T dependence appears to be very similar to that of the susceptibility. This is again

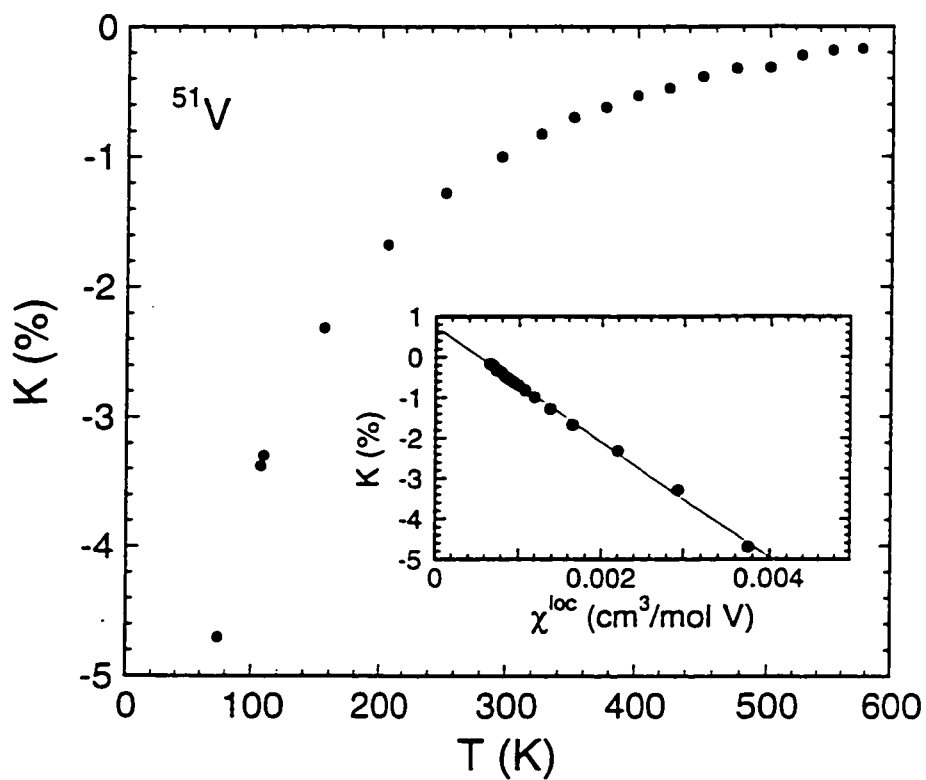


Figure 8.5 ^{51}V Knight shift K versus temperature T of LiV_2O_4 sample 2 (3-3). In the inset K is plotted as a function of the local moment susceptibility χ^{loc} using the data of sample 6 (12-1).

proved by plotting, in the inset of Fig. 8.5, the shift K as a function of the local moment susceptibility $\chi^{\text{loc}}(T)$, displaying the linear relationship above 74 K. Therefore, the linear fit was carried out again as shown in the inset. Like the case of ${}^7\text{Li}$, the dipolar contribution is neglected and the equation for K in terms of the on-site hyperfine coupling terms is

$$K(T) = \frac{B^{\text{VV}}}{N_A \mu_B} \chi^{\text{VV}} + \frac{B^{\text{Pauli}}}{N_A \mu_B} \chi^{\text{Pauli}} + \frac{B^{\text{loc}}}{N_A \mu_B} \chi^{\text{loc}}(T) . \quad (8.19)$$

where the B 's are the on-site hyperfine coupling constants. Unlike the ${}^7\text{Li}$ K case, the orbital Van Vleck contribution could not be neglected. Therefore, it is not evident how to determine separately the hyperfine coupling constants B^{VV} and B^{Pauli} from the K -intercept K_0 in a linear fit. The V core polarization by unpaired $V d$ electrons is negative and expected to dominate B^{Pauli} . But K_0 was found to be positive, $K_0 = 0.74 \text{ kG}$ from the fit. Thus, Mahajan *et al.* inferred that the positive orbital Van Vleck term in Eq. (8.19) should be larger in magnitude than the second term. It is still possible to determine the other hyperfine coupling constant B^{loc} from the slope of the fit. They found

$$B^{\text{loc}} = -79 \text{ kG} . \quad (8.20)$$

which agrees well with $B^{\text{loc}} = -74 \text{ kG}$ determined by Onoda *et al.* [149]. In addition, the hyperfine coupling constant of vanadium metal, $B^{\text{loc}} = -112 \text{ kG}$, is also close and has the same sign [179].

Nuclear spin-lattice relaxation rates

${}^7\text{Li}$ nuclear spin-lattice relaxation rate

The recovery of the nuclear magnetization after a $\pi/2$ pulse was found to follow single-exponential behavior over the whole temperature region (1.5–800 K), from which the determination of the ${}^7\text{Li}$ nuclear spin-lattice relaxation rate $1/T_1$ was made. Figure 8.6(a) shows the T dependence of $1/T_1$ for sample 2. The nuclear spin-lattice relaxation rate has a maximum at $T \approx 50 \text{ K}$ which separates the T regions into two distinguishable parts. In the low T region ($T \lesssim 10 \text{ K}$), the relaxation rate shows a linear decrease with decreasing T , as can be seen more clearly in the expanded plot in Fig. 8.6(b). In this T region, it should be noted that both the Knight shift and the intrinsic susceptibility become nearly independent of T . On the other hand, in the higher T region, as T increases, $1/T_1$ decreases monotonically. As opposed to the rich temperature variation of LiV_2O_4 , the isostructural (*i.e.* cubic spinel), superconducting LiTi_2O_4 follows only a linear T dependence (Korringa relation) from 20 to 300 K which is typical of metals in the normal (metallic and paramagnetic) phase [92]. The room temperature value of $1/T_1$ of LiV_2O_4 is enhanced strongly, by a factor of about 100, compared with

that of LiTi_2O_4 . In the following sections, the results in the low- T and high- T regions are discussed separately.

Low temperature ${}^7\text{Li}$ relaxation rate

For all five LiV_2O_4 samples measured, the linear T dependence in the ${}^7\text{Li}$ nuclear spin-lattice relaxation rate $1/T_1$ was observed below 4K, as shown in Fig. 8.6(b). It is remarkable to see this phenomena in samples 2 and 4B, both of which are not as magnetically pure as the other three and show a Curie-like upturn at low T in the observed susceptibilities. (Note that magnetic impurity concentrations are listed for all five samples in Table 8.1.) Therefore, small amounts of magnetic impurities/defects are not capable of suppressing this robust Fermi liquid behavior. The slope $1/T_1 T = 2.25 \text{ sec}^{-1} \text{ K}^{-1}$ of the vanadium spinel (samples 1 and 6) is much larger than the corresponding value of $5.6 \times 10^{-4} \text{ sec}^{-1} \text{ K}^{-1}$ for LiTi_2O_4 [92].

In a simple metal in which the Fermi contact coupling is the only source for Knight shifts and relaxation rates, the so-called Korringa relation holds well [179]. The relation is written

$$K^2 T_1 T = S \quad . \quad (8.21)$$

where for ${}^7\text{Li}$,

$$S \equiv \left(\frac{\gamma_e}{\gamma_n} \right)^2 \frac{\hbar}{4\pi k_B} = 1.74 \times 10^{-6} \text{ sec K} \quad . \quad (8.22)$$

From this relation and due to the nearly constant K , one may anticipate that the Korringa ratio $K^2 T_1 T / S$ will be constant for $T \lesssim 10 \text{ K}$ for LiV_2O_4 . This was indeed observed, as shown in Fig. 8.7, which indicates characteristics of the Fermi liquid state of LiV_2O_4 in the low T region. The nearly constant ratio for $T \lesssim 10 \text{ K}$ is about 0.5, close to the values for normal metals [179]. The ratio for all the five LiV_2O_4 samples measured, as well as the Korringa product $(T_1 T)^{-1}$, are summarized in Table 8.1. The Korringa ratios are normally (with a few exceptions) greater than unity for d band metals [178, 179]. For f -electron heavy fermion compounds such as CeAl_3 [91] $\text{YbNi}_2\text{B}_2\text{C}$ [182], CePd_2In [183], and CeCuGe_2 [184], the linear T dependence of the relaxation rate $1/T_1$ was observed. But it was only for CeAl_3 that the Korringa ratio could be determined [91]. The temperature dependence of the ratio from ${}^{27}\text{Al}$ NMR on this compound appears to be qualitatively the same as that of LiV_2O_4 , but the size of the ratio for CeAl_3 , $\approx 2-3$, is a few times larger.

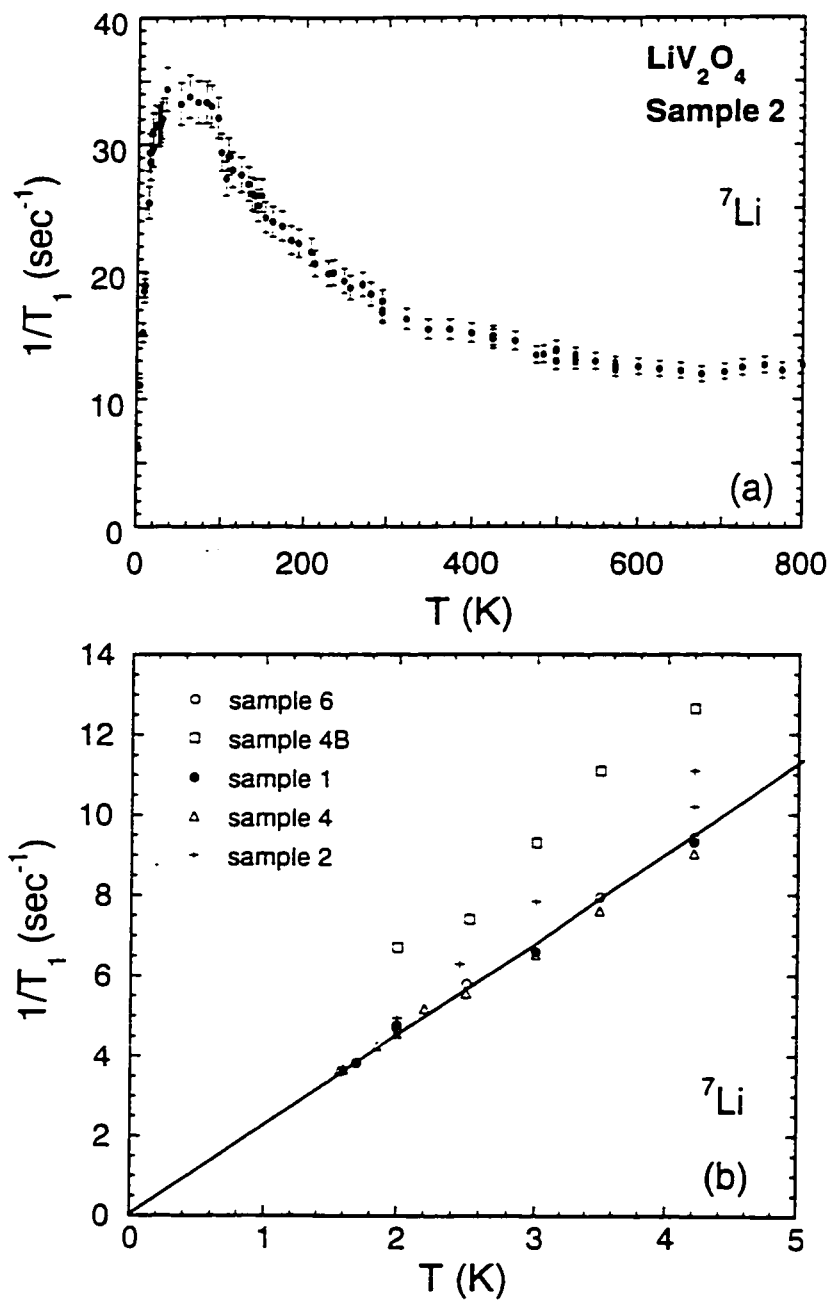


Figure 8.6 (a) ${}^7\text{Li}$ nuclear spin-lattice relaxation rate $1/T_1$ versus temperature T for sample 2 for $T = 1.5\text{--}800$ K. (b) An expanded plot for low T (< 4.2 K) for all five samples. The Korringa law with $1/T_1 T = 2.25 \text{ sec}^{-1} \text{ K}^{-1}$ is shown as a straight line.

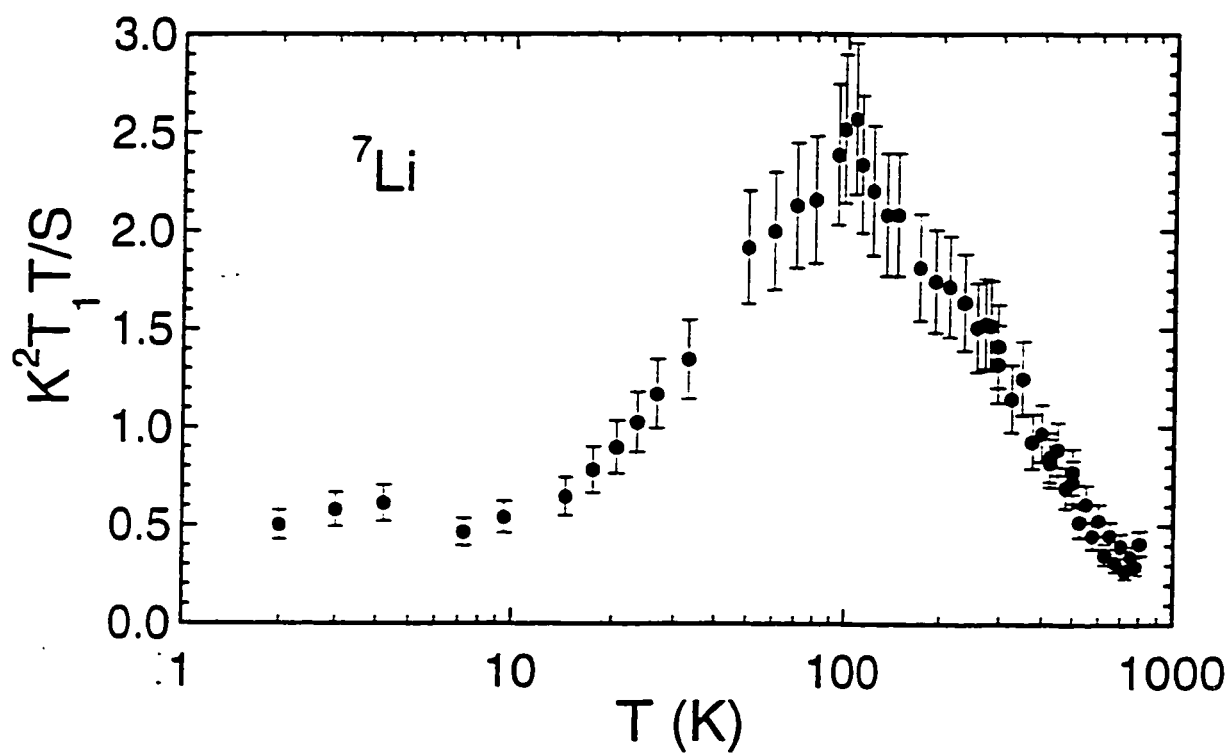


Figure 8.7 Korrington ratio $K^2 T_1 T / S$ versus temperature T for LiV_2O_4 sample 2, determined from ${}^7\text{Li}$ NMR, where $S = 1.74 \times 10^{-6}$ sec K.

Table 8.1 Summary of the $1/T_1T$ values and the Korringa ratios K^2T_1T/S , obtained from the low T (1.5–4.2 K) ${}^7\text{Li}$ NMR data. Magnetic impurity concentrations, found under the assumptions of impurity spin $S_{\text{imp}} = 2$ and impurity g -value $g_{\text{imp}} = 2$, are also listed. The error in the last digit of a quantity is given in parentheses.

Sample Name	Alternative Name	f_{imp} (mol %)	$(T_1T)^{-1}$ ($\text{sec}^{-1} \text{K}^{-1}$)	K^2T_1T/S
1	4-0-1	0.03	2.25(5)	0.55(1)
2	3-3	0.35	2.5(1)	0.50(1)
4	3-3-q1	0.08	2.20(5)	0.57(1)
4B	3-3-a2	1.2	3.0(1)	0.42(1)
6	12-1	0.02	2.25(5)	0.55(1)

High temperature ${}^7\text{Li}$ relaxation rate

A metallic compound with local magnetic moments may have two contributions to the nuclear spin-lattice relaxation rate $1/T_1$. First of all, being metallic, LiV_2O_4 has a relaxation process proportional to T (*i.e.*, Korringa type) by conduction electrons. Second, the relaxation occurs due to the local field fluctuations which are induced by V spin fluctuations. A rough estimate of the Korringa term can be made using the temperature independent K_0 obtained in Eq. (8.15), which is the Knight shift in the high T limit from the linear K - χ fit. Given $K_0 = -0.0094\%$ from Eq. (8.15) and $S = 1.74 \times 10^{-6} \text{ sec K}$ from Eq. (8.22), the Korringa product $1/T_1T$ is estimated

$$\frac{1}{T_1T} = \frac{K_0^2}{S} = 5(1) \times 10^{-3} \text{ sec}^{-1} \text{ K}^{-1} \quad (8.23)$$

The isostructural compound LiTi_2O_4 has no local moments, and its Korringa product for $20 \leq T \leq 300 \text{ K}$ is $5.6 \times 10^{-4} \text{ sec}^{-1} \text{ K}^{-1}$ [92], roughly ten times smaller than that of LiV_2O_4 . This indicates that the above estimate in Eq. (8.23) is too large. Therefore, we neglect the Korringa contribution to the relaxation rate up to 800 K, and the following analysis is done with the spin fluctuation term only.

Moriya [185] derived the following equation for the nuclear spin-lattice relaxation rate due to spin fluctuations

$$\frac{1}{T_1} = \frac{2k_{\text{B}}T}{N_{\text{A}}^2 \hbar^2} \left(\frac{\gamma_{\text{n}}}{\gamma_{\text{e}}} \right)^2 \sum_{\vec{q}} |A_{\vec{q}}|^2 \left(\frac{\chi''(\vec{q}, \omega_{\text{L}})}{\omega_{\text{L}}} \right) \quad (8.24)$$

where here the total hyperfine coupling constant $A \equiv A_{\vec{q}}$ is assumed to be wave-vector \vec{q} independent. χ'' is the imaginary part of the dynamic susceptibility, and ω_{L} is the Larmor frequency. To make a comparison to our uniform susceptibility (both ω_{L} and $\vec{q} = 0$), the summation in Eq. (8.24) can be

written in the limit of $\omega_L \rightarrow 0$ as $N_A \chi_{\text{at}}^{\text{loc}} \tau / 2\pi$, where $\chi_{\text{at}}^{\text{loc}}$ is the uniform local moment susceptibility per mole, and τ is the relaxation time of the local moment. The total hyperfine coupling constant should contain contributions from both exchange hyperfine coupling of Li nuclei to the V local moments and direct dipole-dipole coupling to them. Assuming that these two coupling mechanisms are not correlated with each other, the square of the total hyperfine coupling constant is

$$A^2 = 12(A^{\text{loc}})^2 + (A^{\text{dip}})^2 \quad . \quad (8.25)$$

The first term on the right-hand side of Eq. (8.25) describes the transferred hyperfine contributions from the 12 nearest-neighbor V moments around one Li nucleus, whereas the second term is the "total" electromagnetic dipolar hyperfine coupling constant due to all the surrounding V spins. $A^{\text{loc}} = 180\text{G}$ has already been obtained in Eq. (8.14). A^{dip} was obtained by Mahajan *et al.* to be 2.58kG [19].

Substituting these coupling constants and the other fundamental constants into Eq. (8.24) and rearranging the equation, we now have

$$\frac{1}{\tau} = 1.73 \times 10^{14} \chi^{\text{loc}} T_1 T \quad . \quad (8.26)$$

A calculation of $1/\tau$ as a function of T from T_1 data was made possible by utilizing the Curie-Weiss susceptibility from Eq. (8.10). The results are given in Fig. 8.8. A $T^{0.5}$ dependence of $1/\tau$ has been obtained theoretically by Cox *et al.* [186] for the relaxation rates of $4f$ local moments in ordinary f -electron heavy fermion compounds. Experimentally YbCuAl [186], CeCu₂Ge₂ [184], and YbNi₂B₂C [187] f -electron heavy fermion compounds satisfy the $T^{0.5}$ prediction for $1/\tau$. A fit of the derived $1/\tau$ values for LiV₂O₄ was carried out, and the $T^{0.5}$ dependence agrees well with data for $T = 200\text{--}800\text{K}$, as Fig. 8.8 shows. A $T^{0.6}$ dependence was found to fit better when lower T data were included in the fit.

An analysis of this local spin fluctuation rate $1/\tau$ may give ideas about the sizes of (exchange) coupling constants of a V local moments. For this analysis, a phenomenological model was employed for room temperature and above. The fluctuation rate $1/\tau$ can be written

$$\frac{1}{\tau} = \frac{1}{\tau_d} + \frac{1}{\tau_{\text{ex}}} \quad . \quad (8.27)$$

The first term $1/\tau_d$ represents the fluctuation rate of a local (impurity) spin due to conduction electrons, given by the following Korringa-like expression [188]

$$\frac{1}{\tau_d} = \left(\frac{4\pi}{\hbar} \right) k_B T (J\rho(\epsilon_F))^2 = \Gamma_0 T \quad , \quad (8.28)$$

where J indicates the coupling constant of the spin to the conduction band, and $\rho(\epsilon_F)$ is the density of states per spin direction at the Fermi level. The second term $1/\tau_{\text{ex}}$ represents the spin fluctuation

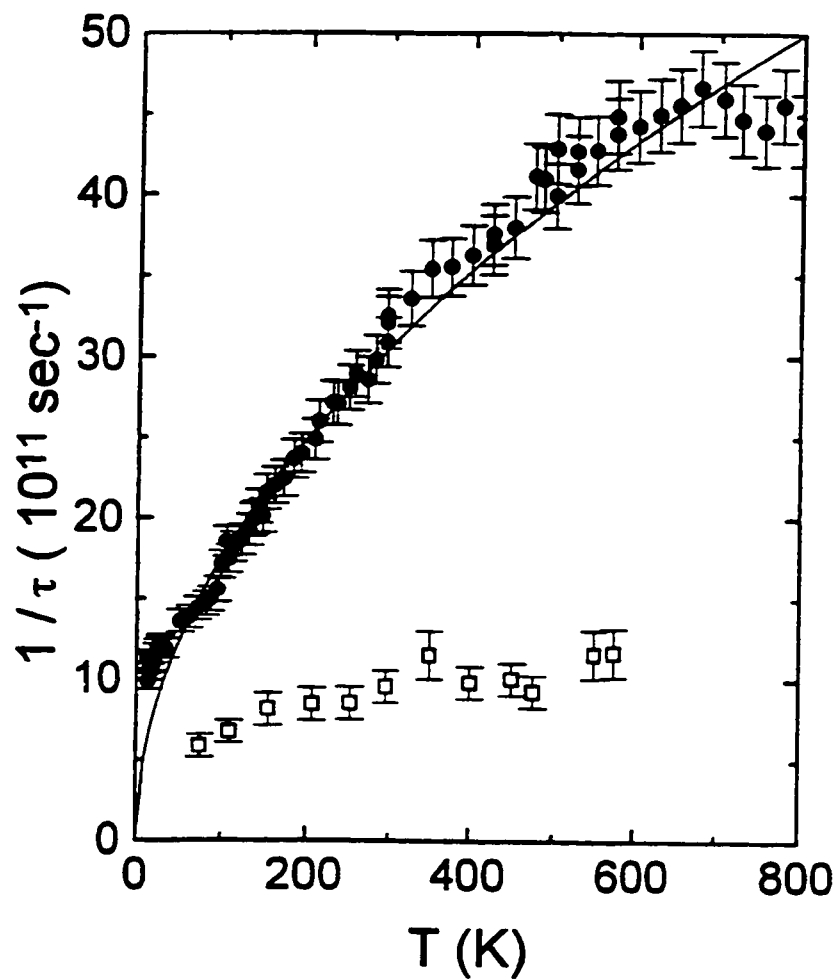


Figure 8.8 Local electronic V moment fluctuation rate $1/\tau$ as a function of temperature T , calculated from the observed ${}^7\text{Li}$ (dots) and ${}^{51}\text{V}$ (open squares) nuclear spin-lattice relaxation rates $1/T_1$ using Eqs. (8.26) and (8.40), respectively. A fit by a $T^{0.5}$ dependence based upon Cox *et al.* [186] is shown by a solid curve.

rate arising from the local moment spin-spin exchange interaction. The high temperature limit for this term is given by Moriya [185] as

$$\frac{1}{\tau_{\text{ex}}} = \frac{\omega_{\text{ex}}}{2\pi} = \Gamma_1 \quad . \quad (8.29)$$

where ω_{ex} is defined via

$$\omega_{\text{ex}}^2 = \frac{8J_{\text{ex}}^2 z S(S+1)}{3\hbar^2} \quad . \quad (8.30)$$

J_{ex} is the exchange coupling constant from a Heisenberg Hamiltonian in the form $2J_{\text{ex}}\vec{S}_i \cdot \vec{S}_j$ for a pair of nearest-neighbor spins, and z is the number of nearest neighbor spins. A linear fit of $1/\tau$ versus T by Eqs. (8.27), (8.28) and (8.29) for the 300–700 K data points yields

$$\Gamma_0 = 4.4(10) \times 10^9 \text{ sec}^{-1} \text{ K}^{-1} \quad . \quad (8.31)$$

$$\Gamma_1 = 1.9(3) \times 10^{12} \text{ sec}^{-1} \quad . \quad (8.32)$$

Equation (8.28) then yields $|J|\rho(\epsilon_F) = 0.05$. Recalling that the Pauli paramagnetic susceptibility χ^{Pauli} is expressed as

$$\chi^{\text{Pauli}} = \frac{(g\mu_B)^2}{2} \rho(\epsilon_F) \quad . \quad (8.33)$$

the value of χ^{Pauli} in Eq. (8.17) yields with $g = 2$

$$\rho(\epsilon_F) = 2.54 \frac{\text{states}}{\text{eV} - V - \text{spin direction}} \quad . \quad (8.34)$$

Then the coupling constant $|J|$ can be determined to be

$$|J| = 19.7(2) \text{ meV} \quad . \quad (8.35)$$

or $|J_{\text{ex}}|/k_B = 229 \text{ K}$. From Eqs. (8.29), (8.30) and (8.32), we find for $S = 1/2$ and $z = 6$ (6 nearest neighbor V atoms to a given V atom)

$$|J_{\text{ex}}| = 2.3(4) \text{ meV} \quad . \quad (8.36)$$

or $|J_{\text{ex}}|/k_B = 27 \text{ K}$. It is worthwhile to note a few things about the coupling constants. First, one can express the Weiss temperature θ in terms of $|J_{\text{ex}}|$. In the mean field approximation, we have

$$|\theta| = \frac{2zS(S+1)|J_{\text{ex}}|}{3k_B} = 81 \text{ K} \quad ; \quad (8.37)$$

this value is not very close to the Weiss temperature of 12.86 K (in magnitude) in Eq. (8.13). Second, this model suggests that the coupling of the V moment to the conduction electron band is more than one order of magnitude stronger than that between the local moments.

The above method was employed to reanalyze the ^{209}Bi relaxation rate for the heavy fermion compound YbBiPt [182]. The obtained coupling constants are

$$|J| \approx 80 \text{ meV} \quad . \quad (8.38)$$

assuming $\rho(\epsilon_F) = 1 \text{ states}/(\text{eV} \cdot \text{V-spin direction})$. and

$$|J_{\text{ex}}| = 9.5 \text{ meV} \quad . \quad (8.39)$$

Once again, $|J|$ is one order of magnitude larger than $|J_{\text{ex}}|$. In addition, from the work on CeAl_3 [91], $|J_{\text{ex}}| = 10 \text{ meV}$ may be inferred. These results indicate that the exchange coupling between local moments in LiV_2O_4 is ~ 4 times smaller than corresponding values for f -electron heavy fermion compounds.

^{51}V nuclear spin-lattice relaxation rate

The ^{51}V nuclear spin-lattice relaxation rate $1/T_1$ was obtained by successfully fitting the recovery of the spin echo signal by a single exponential. This single exponential fit was possible for the whole temperature T range, 74–575 K. A lower T measurement than 74 K was not possible due to the loss of signal which was caused by the very short spin-spin relaxation time T_2 . The measurement results are given in Fig. 8.9, along with the data of Fujiwara *et al.* [97] and Onoda *et al.* [149]. Throughout the measurement T range, the relaxation time T_1 was found to be very short (20–50 μsec). The room temperature data from the three groups are in good agreement, while at the lower temperature some disagreement is seen. Mahajan *et al.* did not observe a signal at low T ($< 74 \text{ K}$). On the other hand, the successful detection of the signal in this T region by continuous wave techniques (at low fields, $H < 1.5 \text{ T}$) [149] implies that the ^{51}V T_1 and/or T_2 are so short that the dead time of the receiver hides the free induction decay completely. From this, both relaxation rates are inferred to be $T_{1,2} \leq 5 \mu\text{sec}$ at low T .

In the same way as in the previous section, an attempt was made to extract information about the V electronic spin fluctuation rate from the ^{51}V $1/T_1$. It is reasonable to assume that the hyperfine coupling of the ^{51}V nuclei with their own local moment electrons is the major contribution to ^{51}V T_1 . Then using $|B^{\text{loc}}| = 79 \text{ kG}$ from Eq. (8.20) for the hyperfine coupling A in Eq. (8.24), the following equation was derived for generating the values of V local spin fluctuation rate $1/\tau$ in Fig. 8.8

$$\frac{1}{\tau} = 7.47 \times 10^{16} \chi^{\text{loc}} T_1 T \quad , \quad (8.40)$$

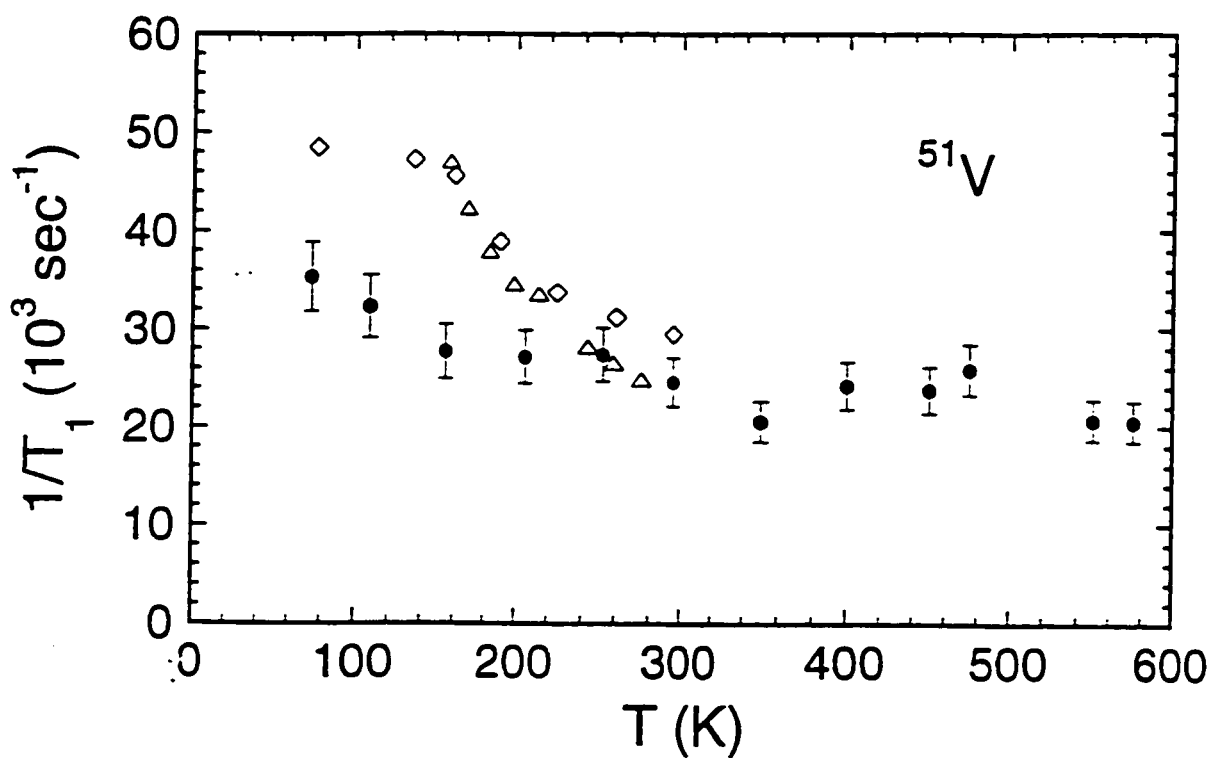


Figure 8.9 ^{51}V nuclear spin-lattice relaxation rate $1/T_1$ versus temperature T . The data of Mahajan *et al.* for sample 6 [19] are shown as filled circles, along with those of Fujiwara *et al.* [97] (open triangles) and of Onoda *et al.* [149] (open diamonds).

in which the Curie-Weiss susceptibility in Eq. (8.10) was used again. In Fig. 8.8 the two data sets of $1/\tau$ should ideally be the same, since both are the same fluctuation of the V local moment. Although the overall temperature dependences appear to be similar, the quantitative disagreement is obvious. This may be caused by the simple model itself, and/or the neglected contributions to T_1 such as the Korringa term.

9 SUMMARY AND DISCUSSIONS

Throughout this dissertation, intriguing properties of LiV_2O_4 have been presented and analyzed. This strongly correlated electron compound exhibits a crossover with decreasing temperature T from localized magnetic moment behavior to heavy Fermi liquid behavior. This crossover has been observed through magnetic susceptibility, nuclear magnetic resonance, heat capacity, and thermal expansion measurements on high-purity polycrystalline LiV_2O_4 samples. In this final chapter, while brief summaries from preceding chapters are given, our current understanding and outlook for appropriate interpretations of the observed crossover in LiV_2O_4 are stated.

In Chapter 3, the preparative method and characterization of our LiV_2O_4 and $\text{Li}_{1+x}\text{Ti}_{2-x}\text{O}_4$ ($x = 0$ and $1/3$) samples were described. The LiV_2O_4 samples were found to be single-phase or to have only on the order of a percent of V_2O_3 or V_3O_5 impurity phase from the x-ray diffraction measurements (Figs. 3.1 and 3.2). From the Rietveld refinements of the x-ray diffraction data, the lattice a_0 and oxygen u parameters were determined for each sample (Tables 3.4 for LiV_2O_4 and 6.2 for $\text{Li}_{1+x}\text{Ti}_{2-x}\text{O}_4$). Due to the weak scattering of x-ray from lithium, it was impossible to determine whether vacancies occur in the Li and/or V sites. Introductions of the Rietveld refinement method and of the computer program RIETAN-97J were also given. From the low- T x-ray [11] and neutron [11, 18] diffraction measurements, it was found that LiV_2O_4 retains the cubic normal spinel structure down to 4 K, with no evidence for any structural transition (see Chapters 2 and 7).

Our magnetically purest samples 1 and 6 clearly showed a broad shallow maximum in the observed magnetic susceptibility $\chi^{\text{obs}}(T)$ at $T \approx 16$ K, with small Curie-like upturns below ~ 5 K. Field-cooled and zero-field-cooled magnetization measurements with $H = 10\text{--}100$ G did not reveal any evidence for static spin-glass ordering from 2 to 50 K in any of the seven samples measured. At $T \gtrsim 50$ K, $\chi^{\text{obs}}(T)$ showed local magnetic moment behavior for all samples. Low- T isothermal magnetization versus applied magnetic field $M^{\text{obs}}(H)$ data were analyzed, and the parameters of the paramagnetic impurities giving rise to the Curie-like upturn in $\chi^{\text{obs}}(T)$ were determined, assuming that a single type of impurity is present. Using these parameters, the intrinsic susceptibility $\chi(T)$ was obtained and

found to be essentially the same in all samples but two (4A and 4B). Surprisingly, the spin S_{imp} of the paramagnetic impurities was found to be large, $S_{\text{imp}} = 3/2$ to 4 depending on the sample, suggesting the presence of variable amounts of ferromagnetically coupled vanadium spin defect clusters in the samples.

The high- T (above ~ 50 K) localized magnetic moment picture was tested using the high-temperature series expansion (HTSE) prediction for the spin susceptibility of the $S = 1/2$ vanadium sublattice of the spinel structure. The Curie constant C and Weiss temperature θ determined from the HTSE fits were found to be similar to those obtained in the past using the Curie-Weiss law to fit the high- T susceptibility data for LiV_2O_4 . Using the values of the Van Vleck susceptibility obtained from the K - χ analyses, the Pauli susceptibility contribution to the temperature-independent susceptibility χ_0 was derived and found to be small, comparable to that of LiTi_2O_4 . The Van Vleck formulas for the paramagnetic susceptibility of V^{+3} , V^{+4} and an equal mixture, assuming that each V ion is in a cubic crystalline electric field, failed to describe the T dependence of the observed effective magnetic moment. However, for the high- T “localized moment” region, the effective moment is in agreement with the spin-only value.

At low T , muon spin relaxation [11] (not detailed here) and nuclear magnetic resonance (NMR) measurements did not detect static magnetic ordering in our purest sample of LiV_2O_4 to 0.02 K, and in any of seven samples to 1.5 K, respectively. The low- T behaviors observed in the intrinsic susceptibility $\chi(T)$, electronic heat capacity coefficient $\gamma(T)$, and ^7Li NMR measurements are similar to those of the heaviest mass f -electron heavy fermion (HF) compounds. The nearly T -independent and relatively large ($\sim 10^{-2}$ cm³/mol) $\chi(T)$ below ~ 30 K with a broad peak at ≈ 16 K may be viewed as reflecting the disappearance of the V magnetic moment via Kondo screening by conduction electrons, and the formation of a Fermi liquid with an enhanced mass. The value of $\gamma(1\text{ K}) = 0.42\text{ J/molK}^2$ for LiV_2O_4 [11, 14] is, to our knowledge, the largest among existing transition metal compounds, surpassing those of predecessors such as $(\text{Y}_{0.97}\text{Sc}_{0.03})\text{Mn}_2$ ($\approx 0.2\text{ J/molK}^2$ [16, 189]) and V_{2-x}O_3 (0.07 J/molK^2 [85]). Not only do we infer a large quasiparticle effective mass ($m^*/m_e \approx 180$) from this large γ , but the rapidly decreasing $\gamma(T)$ is also indicative of a similarity to f -electron HF compounds. The ^7Li Knight shift K becomes nearly T independent below about 4.2 K [19], and simultaneously the nuclear spin-lattice relaxation rate $1/T_1$ has a linear T dependence in this low- T range. These two observations from ^7Li NMR demonstrate that the Korringa law holds, another indication that LiV_2O_4 is a Fermi liquid at low T .

Although our neutron diffraction study did not show any structural transition to 4 K, structural evidence for the crossover to the HF regime with decreasing $T < 20$ K was found from the remarkable T

dependence of the thermal expansion at low T [18]. This was confirmed through capacitance dilatometer measurements [14]. The linear thermal expansion coefficient divided by T , α/T , indicated a strong upturn below ≈ 25 K which was correlated with the strong increase of γ in the same T region. The derived, normalized ratio of α to C_e (which is identical to $(\alpha/T)/\gamma$), called the Grüneisen parameter $\Gamma(T)$, showed a strong enhancement below ≈ 25 K, and reaches $\Gamma(0) = 11.5$. At $T = 0$, the observed $\Gamma(0)$ becomes equal to the electronic Grüneisen parameter $\Gamma_e(0)$. Compared with a typical value of ~ 2 for a normal elemental metal and that of f -electron HF compounds, this $\Gamma_e(0)$ is intermediate, but still indicates that the crossover to the HF regime a stronger influence on the thermal expansion than on the heat capacity.

The electrical resistivity $\rho(T)$ shows a metallic behavior, monotonically decreasing upon cooling, shown by Rogers *et al.* [3] in 1967. We were lately informed that for the first time in more than 30 years Urano *et al.* [190] qualitatively reproduced the metallic $\rho(T)$ of Rogers *et al.* by measurements on a single crystal of LiV_2O_4 . The observed downturn of $\rho(T)$ below ≈ 30 K in the data of Rogers *et al.* may be an indication that LiV_2O_4 transforms to the coherent state at lower T . The T^2 dependence of $\rho(T)$ is characteristic of the coherent, *i.e.* Fermi liquid state. Though not low enough T data are available, our rough estimate of the T^2 coefficient A satisfies the proportional relationship of A to γ^2 (see the Kadowaki-Woods plot in Fig. 5.3) that f -electron HF compounds follow.

The Wilson ratio $R_W \sim 1$ of HF compounds may be visually seen in a plot of $\chi(0)$ versus $\gamma(0)$ since R_W is the normalized ratio of these two quantities. Figure 9.1 shows this plot, which includes data for LiV_2O_4 , many f -electron HF materials, some elemental metals and other superconducting or metallic oxide compounds [14]. It is seen that LiV_2O_4 is situated in the middle of the f -electron HF and intermediate-valent compound cluster.

From all these observations we conclude that the HF behaviors of LiV_2O_4 are like those of f -electron HF systems. However, we have found difficulties to self-consistently describe both $\chi(T)$ and $C_e(T)$ in terms of the dilute-impurity $S = 1/2$ Kondo and $S \geq 1$ Coqblin-Schrieffer models. This suggests that there might be a completely different mechanism responsible for these HF behaviors in LiV_2O_4 and in the f -electron systems, or there might be some additional mechanism(s) that makes this d -electron system more complex than conventional f -electron HF systems.

In conventional f -electron heavy fermion compounds, local f -electron orbitals and conduction electron states in non- f bands hybridize only weakly, resulting in a many-body scattering resonance of the conduction electrons by the local moments near the Fermi energy E_F , a large density of quasiparticle state $D^*(E_F)$, and hence a large quasiparticle effective mass, electronic specific heat coefficient and

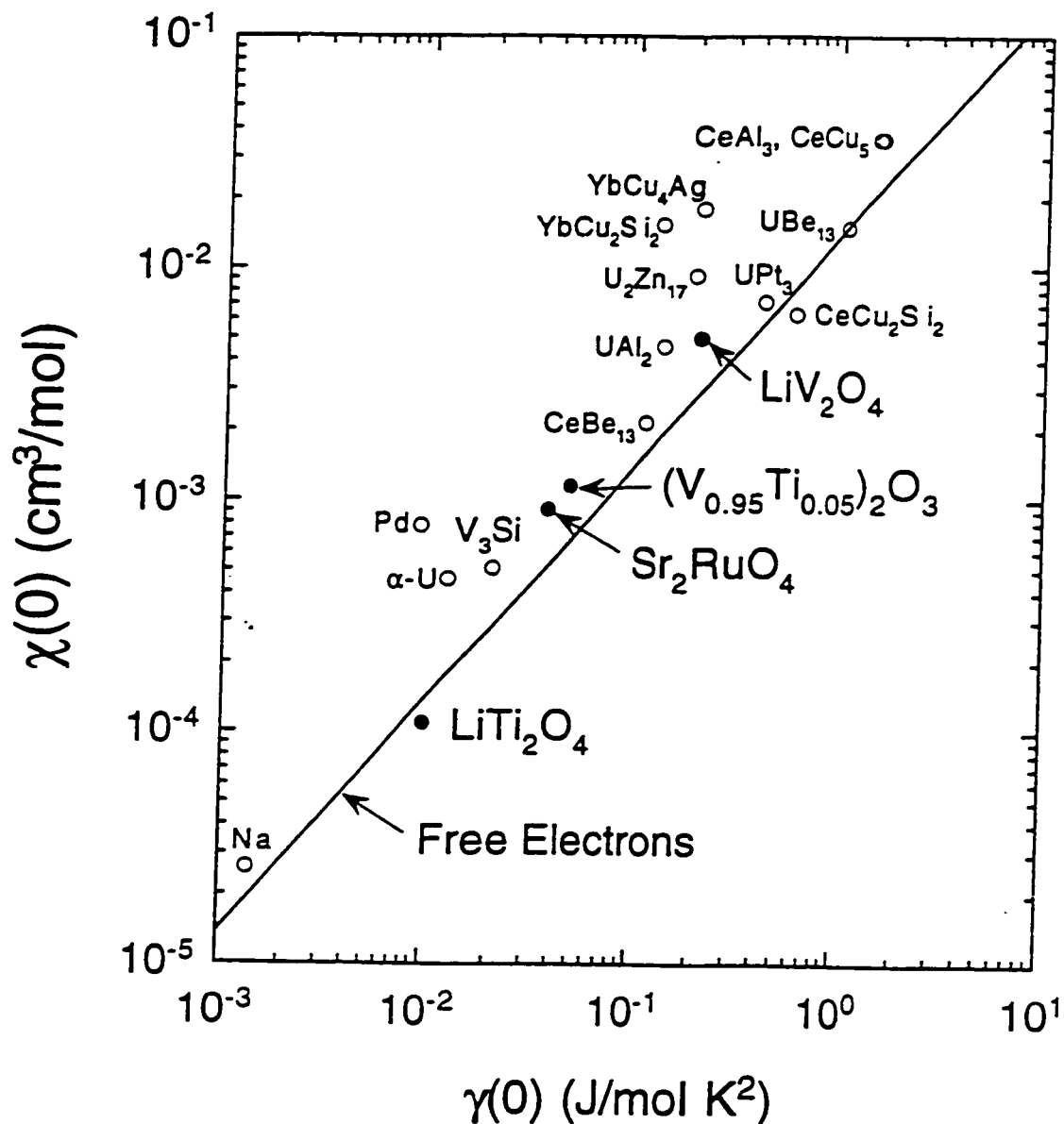


Figure 9.1 Magnetic susceptibility $\chi(0)$ versus electronic heat capacity coefficient $\gamma(0)$ at zero temperature for several *f*-electron heavy fermion (HF) compounds, *d*-electron metallic oxides and some elemental metals [14], after [191]. “mol” stands for a mole of *d* or *f* atoms in the respective compounds.

magnetic spin susceptibility at low T . Screening of $S = 1/2$ local moments by surrounding conduction electrons leads to a nonmagnetic ground state and a saturating spin susceptibility as $T \rightarrow 0$. We tested several models for $\chi(T)$ which assume the presence of local magnetic moments in LiV_2O_4 ($S = 1/2$ per V) interacting weakly with the conduction electrons. In these models, the itinerant and localized electrons must both occupy t_{2g} orbitals (or bands derived from these orbitals), rather than orbitals of more distinct character. One can still imagine a scenario [192] in which the HF behaviors of LiV_2O_4 at low T arise in a way similar to that of the f -electron HF compounds, if the following conditions are fulfilled: (i) the trigonal component of the CEF causes the A_{1g} orbital singlet to lie below the E_g orbital doublet; (ii) one of the 1.5 d -electrons/V is localized in the ground A_{1g} orbital due to electron-electron correlations; (iii) the remaining 0.5 d -electron/V occupies the E_g doublet and is responsible for the metallic character; and (iv) the band(s) formed from the E_g orbitals hybridize only weakly with the A_{1g} orbital on each V ion. This scenario involves a kind of orbital ordering; a more general discussion of orbital ordering effects is given below.

In the rest of this chapter, two important concepts, geometrical frustration and orbital ordering which may be important in relation to the similar “heavy-electron” compound $(\text{Y}_{0.97}\text{Sc}_{0.03})\text{Mn}_2$ are discussed.

The geometric frustration for antiferromagnetic ordering inherent in the V sublattice of LiV_2O_4 may be important to the mechanism for HF behaviors of this compound at low T . Such frustration inhibits long-range magnetic ordering and enhances quantum spin fluctuations and (short-range) dynamic spin ordering [10, 193, 194]. These effects have been verified to occur in the C15 fcc Laves phase intermetallic compound $(\text{Y}_{0.97}\text{Sc}_{0.03})\text{Mn}_2$, in which the Y and Sc atoms are nonmagnetic and the Mn atom substructure is identical with that of V in LiV_2O_4 . In $(\text{Y}_{0.97}\text{Sc}_{0.03})\text{Mn}_2$ Shiga *et al.* discovered quantum magnetic moment fluctuations with a large amplitude ($\mu_{\text{rms}} = 1.3\mu_{\text{B}}/\text{Mn}$ at 8 K) in their polarized neutron scattering study [195]. They also observed a thermally-induced contribution, with $\mu_{\text{rms}} = 1.6\mu_{\text{B}}/\text{Mn}$ at 330 K. Further, Ballou *et al.* [16] inferred from their inelastic neutron scattering experiments the presence of “short-lived 4-site collective spin singlets”, thereby suggesting the possibility of a quantum spin-liquid ground state. A recent theoretical study by Canals and Lacroix [194] by perturbative expansions and exact diagonalization of small clusters of a $S = 1/2$ frustrated pyrochlore antiferromagnet [196] found a spin-liquid ground state and an AF spin correlation length of less than one interatomic distance at $T = 0$.

$(\text{Y}_{0.97}\text{Sc}_{0.03})\text{Mn}_2$ has some similarities in properties to those of LiV_2O_4 . No magnetic long-range ordering was observed above 1.4 K [16, 195]. Similar to LiV_2O_4 , it shows a large electronic specific heat

coefficient $\gamma(0) \approx 160\text{--}200 \text{ mJ/molK}^2$ [16, 189]. However, the T dependences of the susceptibility [197] and γ [189] are very different from those seen in LiV_2O_4 and in the heaviest f -electron heavy fermion compounds. $\chi^{\text{obs}}(T)$ does not show the Curie-Weiss-like behavior at high T , but rather increases with increasing T [197]. $\gamma(T)$ is nearly independent of T up to $\sim 6.5 \text{ K}$ [189]. Replacing a small amount of Mn with Al, Shiga *et al.* [198] found spin-glass behavior in $(\text{Y}_{0.95}\text{Sc}_{0.05})(\text{Mn}_{1-x}\text{Al}_x)_2$ with $x \geq 0.05$. The susceptibility for $x = 0.15$ shows a Curie-Weiss-like behavior above $\sim 50 \text{ K}$. The partial removal of the geometric frustration upon substitution of Al for Mn leads to spin-glass ordering below $\sim 50 \text{ K}$ (for $x = 0.1$) [198]. This might be analogous to that in our sample 3 in which structural defects evidently ameliorated the frustrated V-V interactions, leading to spin-glass ordering below $\sim 0.8 \text{ K}$. Hence, it is of great interest to carry out similar neutron scattering measurements on LiV_2O_4 to test for similarities and differences in the spin excitation properties.

The magnetic properties of materials can be greatly influenced when the ground state has orbital degeneracy in a high-symmetry structure. Such degenerate ground state orbitals can become energetically unstable upon cooling. The crystal structure is then deformed to a lower-symmetry to achieve a lower-energy, non-orbitally-degenerate ground state (Jahn-Teller theorem) [199]. Energetically some occupied orbitals are split from the originally degenerate levels to have lower energy. This kind of orbital ordering accompanied with a structural distortion is called the cooperative Jahn-Teller effect [199]. The driving force for this effect is the competition between CEF and the lattice energies. Orbital ordering may also be caused by spin exchange interactions in a magnetic system with orbital-degenerate ground state [199, 200]. The orbital (and charge) degrees of freedom may couple with those of spins in such a way that certain occupied orbitals become energetically favorable, and consequently the degeneracy is lifted. As a result, the exchange interaction becomes spatially inhomogeneous [200, 201]. For example, Pen *et al.* [200] showed that the degenerate ground states in the geometric frustrated, V triangular lattice Heisenberg antiferromagnet LiVO_2 can be lifted by a certain static orbital ordering. However, the presence of orbital degeneracy or near-degeneracy suggest that dynamical orbital-charge-spin correlations may be important to the physical properties of LiV_2O_4 . It is not yet known theoretically whether such dynamical correlations can lead to a HF ground state and this scenario deserves further study.

In conclusion, thus far we and collaborators have experimentally demonstrated heavy fermion behaviors of LiV_2O_4 characteristic of the heaviest mass f -electron HF systems from magnetization [11], heat capacity [11, 14], nuclear magnetic resonance [11, 19], thermal expansion [14, 18], and muon spin relaxation [11] measurements. Our higher-purity samples made this discovery of the HF behaviors in

LiV_2O_4 possible. High-quality single crystals without structural defects or magnetic impurities are in great demand. While the observed heavy fermion behaviors should be checked using such crystals, inelastic neutron scattering experiments are vital for profound understanding of the magnetic excitations in this *d*-electron heavy fermion compound. This strongly correlated metal provides a challenge to theorists to provide an applicable theory which may elucidate the nature of the observed heavy electron mass in LiV_2O_4 , and the reason(s) that the properties of this compound are so radically different from those of the isostructural superconductor LiTi_2O_4 .

APPENDIX. RIETAN-973 INPUT FILE EXAMPLE

```

#***** (Beginning of the input file for LiV2O4 sample 4A)*****
# Title (CHARACTER*80)
LiV2O4 sample 6 (3-3-q2)(sk4164) (LiV2O4, V2O3 impurity) 'Sample4A.ins'

NBEAM = 0! Neutron powder diffraction.
NBEAM = 1! Conventional X-ray powder diffraction (characteristic X rays).
NBEAM = 2! Synchrotron X-ray powder diffraction.

NMODE = 0: Rietveld analysis of powder diffraction data.
NMODE = 1! Calculation of powder diffraction intensities (plus simulation).

NPRINT = 0! Minimal output.
NPRINT = 1! Standard output.
NPRINT = 2! Detailed output.
NPRINT = 0

If NBEAM = 1 then
TNAME = 'Cu': Radiation ('Cr', 'Fe', 'Co', 'Cu', 'Mo', or 'Ag').
R12 = 0.497: I(K-alpha2)/I(K-alpha1).
CTHM = 0.8009: (cos(2*alpha))**2 for the monochromator (alpha: Bragg angle).

NTRAN = 0: Reflection (Bragg-Brentano) geometry.
NTRAN = 1! Transmission geometry.
end if

```

If NBEAM > 0 then

Real chemical species plus '/'

'Li' 'V' 'O' /

end if

Information about phases {

Phase No. 1: LiV₂O₄

PHNAME1 = 'LiV₂O₄': Phase name (CHARACTER*25)

VNS1 = 'I-227-2':(Vol. No.)-(Space group No.)-(Setting No.) in Int. Tables.

LSPSYM1 = 0: Information on the space group is read from the data base.

INDIV1 = 0! The overall isotropic thermal parameter (Q) is input.

INDIV1 = 1: Isotropic and/or anisotropic thermal parameters are input.

NPROR1 = 0! Preferred orientation is not corrected.

NPROR1 = 1! Plate crystals (Sasa-Uda function).

NPROR1 = 2! Needle-like crystals (Sasa-Uda function).

NPROR1 = 3: March-Dollase function.

IH1 = 1:

IK1 = 0: → Preferred-orientation vector. hp. kp. lp.

IL1 = 0:

LSUM1 = 0! No summation when calculating the March-Dollase function.

LSUM1 = 1: Summation when calculating the March-Dollase function.

IHA1 = 1:

IKA1 = 1: → Anisotropic-broadening axis, ha, ka, la.

ILA1 = 1:

Phase No. 2: V2O3

PHNAME2 = 'V2O3': Phase name (CHARACTER*25)

VNS2 = 'I-167-2':(Vol. No.)-(Space group No.)-(Setting No.) in Int. Tables.

LSPSYM2 = 0: Information on the space group is read from the data base.

INDIV2 = 0! The overall isotropic thermal parameter (Q) is input.

INDIV2 = 1: Isotropic and/or anisotropic thermal parameters are input.

NPROR2 = 0! Preferred orientation is not corrected.

NPROR2 = 1! Plate crystals (Sasa-Uda function).

NPROR2 = 2! Needle-like crystals (Sasa-Uda function).

NPROR2 = 3: March-Dollase function.

IH2 = 0:

IK2 = 0: → Preferred-orientation vector. hp, kp, lp.

IL2 = 1:

LSUM2 = 0: No summation when calculating the March-Dollase function.

LSUM2 = 1! Summation when calculating the March-Dollase function.

IHA2 = 0:

IKA2 = 0: → Anisotropic-broadening axis. ha, ka, la.

ILA2 = 1:

} Information about phases

Labels. A(I)'s, and ID(I)'s {

```
# Global parameters
# Peak-shift parameters. Z. Ds. and Ts
SHIFT 3.58927E-2 0.0 0.0 100
# Background parameters. bj (j = 0-11)
BKGD 3.80044 -3.61998 3.06328 -2.22331 0.990238 -2.09748E-1
0.0 0.0 0.0 0.0 0.0 0.0 111111000000
# Parameters for phase No. 1 (LiV2O4)
# Scale factor. s
SCALE1 2.60639E-5 1
# Gaussian profile parameters. U. V. W. and P
GAUSS1 2.86861E-3 -4.35888E-3 2.78049E-3 0.0 1110
# Lorentzian profile parameters. X. Xe. Y. and Ye
LORENTZ1 1.00194E-4 0.0 8.47082E-2 0.0 1010
# Asymmetry parameter. As
ASYM1 0.110906 1
# Unused parameters (dummy)
VACANT1 0.0 0.0 00
# Preferred-orientation parameters. r or (p1 and p2)
PREF1 0.9 0.0 10
# Lattice parameters and overall isotropic thermal parameter. Q
CELQ1 8.24704 8.24704 8.24704 90.0 90.0 90.0 0.0 1000000
# Label/species. g. x. y. z. B. and refinement identifiers (ID)
Li/Li 1.0 0.125 0.125 0.125 1.1 00000
V1/V 1.0 0.5 0.5 0.5 0.420345 00001
O1/O 1.0 0.262044 0.262044 0.262044 0.48 01220
# Parameters for phase No. 2 (V2O3)
# The inputs of lattice parameters, fractional coordinates and betas are
# taken from W. Robinson, Acta Cryst. (1975). B31, 1153.
```

```

SCALE2 8.55836E-7 1
# Gaussian profile parameters. U. V. W. and P
GAUSS2 2.86861E-3 -4.35888E-3 2.78049E-3 0.0 2220
# Lorentzian profile parameters. X. Xe. Y. and Ye
LORENTZ2 1.00194E-4 0.0 8.47082E-2 0.0 2020
# Asymmetry parameter. As
ASYM2 0.110906 2
# Unused parameters (dummy)
VACANT2 0.0 0.0 00
# Preferred-orientation parameters. r or (p1 and p2)
PREF2 1.13267 0.0 10
# Lattice parameters and overall isotropic thermal parameter. Q
CELQ2 4.94066 4.94066 13.8957 90.0 90.0 120.0 0.0 1010000
# Label/species. g. x. y. z. B. and refinement identifiers (ID)
V2/V 1.0 0.0 0.0 0.34634 5.67E-3 5.67E-3 1.9E-4 2.835E-3 0.0
0.0 0000000000
O2/O 1.0 0.3122 0.0 0.25 4.9E-3 7.6E-3 5.0E-4 3.8E-3 4.0E-4 8.0E-4 0000000000
} end of labels. A(I)'s. and ID(I)'s

```

Linear constraints for parameters with ID(I) = 2 {

A(O1.y)=A(O1.x)

A(O1.z)=A(O1.x)

A(GAUSS2.1)=A(GAUSS1.1)

A(GAUSS2.2)=A(GAUSS1.2)

A(GAUSS2.3)=A(GAUSS1.3)

A(LORENTZ2.1)=A(LORENTZ1.1)

A(LORENTZ2.3)=A(LORENTZ1.3)

A(ASYM2.1)=A(ASYM1.1)

}end of linear constrains

NEXC = 0! Use all the intensity data.

NEXC = 1: Skip some intensity data.

If NEXC = 1 then

Excluded 2-theta regions {

15.00 19.98

}

end if

If NMODE = 0 then

NRANGE = 0: Refine the background.

NRANGE = 1! Fix the background.

NPAT = 0! Do not create any file storing diffraction intensities.

NPAT = 1! Create a PostScript file for Rietveld-refinement patterns.

NPAT = 2! Create a Macplot/RietPlot file for Rietveld-refinement patterns.

NPAT = 3! Create a DMPLOT file for Rietveld-refinement patterns.

NPAT = 4! Create a SigmaPlot file for Rietveld-refinement patterns.

NPAT = 5! Create an Igor Pro file for Rietveld-refinement patterns.

NPAT = 5

end if

If NMODE = 0 or NPAT > 0 then

PC = 9.0: Profile cut-off.

end if

If NMODE = 0 then

NLESQ = 0: Marquardt method (recommended in most cases).

NLESQ = 1! Gauss-Newton method.

NLESQ = 2! Conjugate-direction method.

NESD = 0: Standard deviations are estimated by the conventional method.

NESD = 1! Standard deviations are estimated by Scott's method.
end if

If NLESQ <= 1 then

NAUTO = 0! Refine all the variable parameters simultaneously.

NAUTO = 1! Refine incrementally (specify variable parameters).

NAUTO = 2! Refine incrementally (automatic: recommended in most cases).

NAUTO = 3! In addition to NAUTO = 2. check convergence to the global min.

NAUTO = 3

NCYCL = 20: Maximum number of cycles.

CONV = 0.0001: Small positive number used for convergence judgement.

NCONV = 3: Number of cycles used for convergence judgement.

NC = 0: No nonlinear constraints are imposed.

NC = 1! Nonlinear constraints are imposed.

TK = 5000.0: Penalty parameter.

FINC = 20.0: Factor by which TK is multiplied when TK is increased.

MITER = 6: Maximum number of iterations.

STEP = 0.04: Coefficient to calculate the initial step interval.

ACC = 1.0E-6: Small positive number used for convergence judgement.

end if

If NLESQ <= 1 and NAUTO = 1 then

Parameters to be refined in each cycle plus '/' {

BKGD.1 BKGD.2 BKGD.3 BKGD.4 BKGD.5 BKGD.6. BKGD.7 BKGD.8 /

CELLQ.1 /

}

end if

If NLESQ = 2 then

MITER = 6: Maximum number of iterations.

STEP = 0.04: Coefficient to calculate the initial step interval.

ACC = 1.0E-6: Small positive number used for convergence judgement.

NC = 0: No nonlinear constraints are imposed.

NC = 1! Nonlinear constraints are imposed.

TK = 5000.0: Penalty parameter.

end if

If NC = 1 then

Nonlinear constraints imposed on interatomic distances and bond angles

For Series numbers of distances/angles, refer to outputs of ORFFE.

Nonlinear constraints {

Ser.No. Expctd.val. Deviation

}

end if

NUPDT = 0: Variable parameters in the input file remain unchanged.

NUPDT = 1! Variable parameters are updated in the packing mode.

NUPDT = 2! Variable parameters are updated in the overwriting mode.

NFR = 0: No file is created which stores FOURIER data.

NFR = 1! File #21 is created which stores FOURIER data for phase #1.

NFR = 2! File #21 is created which stores FOURIER data for phase #2.

NDA = 0: No file is created which store ORFFE data.

NDA = 1! File #9 is created which store ORFFE data for phase #1.

NDA = 2! File #9 is created which store ORFFE data for phase #2.

If NDA > 0 then

ORFFE instructions {

201 2 28 }

end if

If NMODE = 0 and NPAT = 1 then

X0 = 6.5: X coordinate of the origin.

Y0 = 7.0: Y coordinate of the origin.

FACFIG = 0.35: Magnification factor for graphic output (0.35 for ND).

INC = 0: Increase per scale division of the ordinate (0 for default).

end if

#***** (End of the input file)*****

BIBLIOGRAPHY

- [1] S. Krupička and P. Novák. *Ferromagnetic Materials*, edited by E. P. Wohlfarth (North-Holland, New York, 1982). Vol. 3. Ch. 4.
- [2] D. C. Johnston, T. Ami, F. Borsa, M. K. Crawford, J. A. Fernandez-Baca, K. H. Kim, R. L. Harlow, A. V. Mahajan, L. L. Miller, M. A. Subramanian, D. R. Torgeson, and Z. R. Wang, in *Springer Series in Solid-State Sciences*, Vol. 119. "Spectroscopy of Mott Insulators and Correlated Metals", edited by A. Fujimori and Y. Tokura (Springer-Verlag, Berlin and Heidelberg, 1995), pp. 241–254.
- [3] D. B. Rogers, J. L. Gillson, and T. E. Gier, *Solid State Commun.* **5**, 263 (1967).
- [4] D. C. Johnston, *J. Low Temp. Phys.* **255**, 145 (1976).
- [5] H. Kessler and M. J. Sienko, *J. Chem. Phys.* **55**, 5414 (1971).
- [6] Y. Nakajima, Y. Amamiya, K. Ohnishi, I. Terasaki, A. Maeda, and K. Uchinokura, *Physica C* **185–189**, 719 (1991).
- [7] B. L. Chamberland and T. A. Hewston, *Solid State Commun.* **58**, 693 (1986).
- [8] F. Takagi, K. Kawakami, I. Maekawa, Y. Sakai, and N. Tsuda, *J. Phys. Soc. Jpn.* **56**, 444 (1987).
- [9] T. Hayakawa, D. Shimada, and N. Tsuda, *J. Phys. Soc. Jpn.* **58**, 2867 (1989).
- [10] P. W. Anderson, *Phys. Rev.* **102**, 1008 (1956).
- [11] S. Kondo, D. C. Johnston, C. A. Swenson, F. Borsa, A. V. Mahajan, L. L. Miller, T. Gu, A. I. Goldman, M. B. Maple, D. A. Gajewski, E. J. Freeman, N. R. Dilley, R. P. Dickey, J. Merrin, K. Kojima, G. M. Luke, Y. J. Uemura, O. Chmaissem, and J. D. Jorgensen, *Phys. Rev. Lett.* **78**, 3729 (1997).
- [12] A. Aharony, R. J. Birgeneau, A. Coniglio, M. A. Kastner, and H. E. Stanley, *Phy. Rev. Lett.* **60**, 1330 (1988).

- [13] A. P. Ramirez. *Annu. Rev. Mater. Sci.* **24**, 453 (1994).
- [14] D. C. Johnston, C. A. Swenson, and S. Kondo (unpublished).
- [15] K. Andres, J. E. Graebner, and H. R. Ott. *Phys. Rev. Lett.* **35**, 1779 (1975).
- [16] R. Ballou, E. Lelièvre-Berna, and B. Fåk. *Phys. Rev. Lett.* **76**, 2125 (1996).
- [17] S. Kondo, D. C. Johnston, and L. L. Miller, (unpublished).
- [18] O. Chmaissem, J. D. Jorgensen, S. Kondo, and D. C. Johnston. *Phys. Rev. Lett.* **79**, 4886 (1997).
- [19] A. V. Mahajan, R. Sala, E. Lee, F. Borsa, S. Kondo, and D. C. Johnston. *Phys. Rev. B* **57**, 8890 (1998).
- [20] A. Wold and K. Dwight. *Solid State Chemistry: Synthesis, Structure, and Properties of Selected Oxides and Sulfides* (Chapman & Hall, New York, 1993).
- [21] K. Hirakawa, H. Ikeda, H. Kadowaki, and K. Ubukoshi. *J. Phys. Soc. Jpn.* **52**, 2882 (1983).
- [22] K. Hirakawa, H. Kadowaki, and K. Ubukoshi. *J. Phys. Soc. Jpn.* **54**, 3526 (1985).
- [23] A. Tauber, W. M. Moller, and E. Banks. *J. Solid State Chem.* **4**, 138 (1972).
- [24] A. P. Ramirez, G. P. Espinosa, and A. S. Cooper. *Phys. Rev. Lett.* **64**, 2070 (1990).
- [25] S.-H. Lee, C. Broholm, M. F. Collins, L. Heller, A. P. Ramirez, Ch. Kloc, E. Bucher, R. W. Erwin, and N. Laceyvic. *Phys. Rev. B* **56**, 8091 (1997).
- [26] A. H. Cooke, R. Lazenby, F. R. McKim, J. Owen, and W. P. Wolf. *Proc. R. Soc. London A* **250**, 97 (1959).
- [27] S. Hov, H. Bratsberg, and A. T. Skjeltorp. *J. Magn. Magn. Mater.* **15–18**, 455 (1980).
- [28] P. K. Baltzer, P. J. Wojtowicz, M. Robbins, and E. Lopatin. *Phys. Rev.* **151**, 367 (1966).
- [29] J. A. Mydosh. *Spin Glasses, An Experimental Introduction* (Taylor and Francis, London, 1993).
- [30] *Physics of Random Systems*, edited by Y. Haseda (Physical Society of Japan, Tokyo, 1981). Ch. 7.
- [31] S. Nagata, P. H. Keesom, and H. R. Harrison. *Phys. Rev. B* **19**, 1633 (1979).
- [32] Z. Fisk, D. W. Hess, C. J. Pethick, D. Pines, J. L. Smith, J. D. Thompson, and J. O. Willis. *Science* **239**, 33 (1988).

- [33] G. R. Stewart, *Rev. Mod. Phys.* **56**, 755 (1984).
- [34] For reviews, see, *e.g.*, J. M. Lawrence, P. S. Riseborough, and R. D. Parks, *Rep. Prog. Phys.* **44**, 1 (1981); N. B. Brandt and V. V. Moshchalkov, *Adv. Phys.* **33**, 373 (1984); P. Schlottmann, *Phys. Rep.* **181**, 1 (1989); N. Grewe and F. Steglich, Ch. 97 in *Handbook on the Physics and Chemistry of Rare Earths*, Vol. 14, eds. K. A. Gschneidner, Jr. and L. Eyring (Elsevier, Amsterdam, 1991), pp. 343–474; G. Aeppli and Z. Fisk, *Comments Cond. Mat. Phys.* **16**, 155 (1992); M. Loewenhaupt and K. H. Fischer, Ch. 105 in *Handbook on the Physics and Chemistry of Rare Earths*, Vol. 16, eds. K. A. Gschneidner, Jr. and L. Eyring (Elsevier, Amsterdam, 1993), pp. 1–105; A. Amato, *Rev. Mod. Phys.* **69**, 1119 (1997).
- [35] A. C. Hewson, *The Kondo Problem to Heavy Fermions* (Cambridge University Press, Cambridge, 1993).
- [36] Y. Ōnuki and T. Komatsubara, *J. Magn. Magn. Mater.* **63 & 64**, 281 (1987).
- [37] A. Ishihara, *Electron Liquids* (Springer-Verlag, Berlin, 1993), p. 145.
- [38] H. R. Ott, H. Rudigier, Z. Fisk, J. O. Willis, and G. R. Stewart, *Solid State Commun.* **53**, 235 (1985).
- [39] G. R. Stewart, Z. Fisk, J. O. Willis, and J. L. Smith, *Phys. Rev. Lett.* **52**, 679 (1984).
- [40] C. D. Bredle, S. Horn, F. Steglich, B. Lüthi, and R. M. Martin, *Phys. Rev. Lett.* **52**, 1982 (1984).
- [41] W. Lieke, U. Rauchschwalbe, C. B. Bredle, F. Steglich, J. Aarts, and F. R. de Boer, *J. Appl. Phys.* **53**, 2111 (1982).
- [42] H. R. Ott, H. Rudigier, Z. Fisk, and J. L. Smith, *Phys. Rev. Lett.* **50**, 1595 (1983).
- [43] G. R. Stewart, Z. Fisk, and M. S. Wire, *Phys. Rev. B* **30**, 482 (1984).
- [44] J. J. M. Franse, P. H. Frings, A. de Visser, and A. Menovsky, *Physica B* **126**, 116 (1984).
- [45] A. de Visser, J. J. M. Franse, and A. Menovsky, *J. Magn. Magn. Mater.* **43–47**, 43 (1984).
- [46] H. R. Ott, H. Rudigier, P. Delsing, and Z. Fisk, *Phys. Rev. Lett.* **52**, 1551 (1984).
- [47] J. O. Willis, Z. Fisk, R. M. Aikin, M. W. McElfresh, J. D. Thompson, E. Zirngiebl, J. A. O'Rourke, and J. L. Smith, *J. Appl. Phys.* **61**, 4373 (1987).

- [48] G. K. White and S. B. Woode. *Philos. Trans. R. Soc. London A* **251**, 273 (1959).
- [49] F. E. Hoare and J. C. Matthews. *Proc. R. Soc. London A* **212**, 137 (1952).
- [50] D. Martin. *Phys. Rev.* **124**, 438 (1961).
- [51] R. T. Schumacher and W. E. Vehse. *J. Phys. Chem. Solids* **24**, 297 (1963).
- [52] W. E. Lawrence and J. W. Wilkins. *Phys. Rev. B* **7**, 2317 (1973). [This value of A was theoretically obtained in this paper.]
- [53] H. H. Hill, in *Plutonium 1970 and Other Actinides*, edited by W. N. Miner (American Institute of Mining, New York, 1970), p. 2.
- [54] J. Kondo. *Prog. Theor. Phys.* **32**, 37 (1964).
- [55] A. A. Abrikosov. *Physics* **2**, 5 (1965).
- [56] K. Yosida and A. Okiji. *Prog. Theor. Phys.* **34**, 505 (1965).
- [57] K. Wilson. *Rev. Mod. Phys.* **47**, 773 (1975).
- [58] A. M. Tsel'ick and P. B. Wiegmann. *Adv. Phys.* **32**, 453 (1983).
- [59] N. Kawakami and A. Okiji. *Phys. Lett.* **86A**, 483 (1981).
- [60] A. Okiji and N. Kawakami. *J. Appl. Phys.* **55**, 1931 (1984).
- [61] K. Yosida and A. Yoshimori, in *Magnetism*, edited by H. Suhl (Academic Press, New York, 1973), Vol. 5.
- [62] K. Yamada. *Electronic Correlations* (Iwanami, Tokyo, 1993).
- [63] J. Friedel. *Nuevo Cimento Suppl.* **2**, 287 (1958).
- [64] W. P. Kirk, in *McGraw-Hill Encyclopedia of Physics* (McGraw-Hill, New York, 1993), second edition, p. 650.
- [65] K. Yamada, K. Hanzawa, and K. Yosida. *Prog. Theor. Phys.* **76**, 621 (1986).
- [66] K. Kadowaki and S. B. Woods. *Solid State Commun.* **58**, 507 (1986).
- [67] G. Blasse. *Philos. Res. Rep. Suppl.* **3** (1964).

- [68] *International Tables for Crystallography* (Kluwer Academic, Dordrecht, 1987), Vol. A.
- [69] R. D. Shannon, *Acta Cryst. A* **32**, 751 (1976).
- [70] *Science Dictionary*, 4th Edition, edited by R. Kubo, S. Nagakura, H. Iguchi, and H. Esawa (Iwanami Shoten, Tokyo, 1987).
- [71] Y. Gao, K. Myrtle, M. Zhang, J. N. Reimers, and J. R. Dahn, *Phys. Rev. B* **54**, 16670 (1996).
- [72] W. P. Wolf, *Rep. Prog. Phys.* **24**, 212 (1961).
- [73] D. B. Rogers, R. J. Arnett, A. Wold, and J. B. Goodenough, *J. Phys. Chem. Solids* **24**, 347 (1963).
- [74] J. B. Goodenough, G. Dutta, and A. Manthiram, *Phys. Rev. B* **43**, 10170 (1991).
- [75] A. Fujimori, K. Kawakami, and N. Tsuda, *Phys. Rev. B* **38**, 7889 (1988).
- [76] M. Abbate, F. M. de Groot, J. C. Fuggle, A. Fujimori, Y. Tokura, Y. Fujishima, O. Strebel, M. Domke, G. Kaindl, J. van Elp, B. T. Thole, G. A. Sawatzky, M. Sacchi, and N. Tsuda, *Phys. Rev. B* **44**, 5419 (1991).
- [77] S. Satpathy and R. M. Martin, *Phys. Rev. B* **36**, 7269 (1987); S. Massidda, J. Yu, and A. J. Freeman, *ibid.* **38**, 11352 (1988).
- [78] B. Reuter and J. Jaskowsky, *Angew. Chem.* **72**, 209 (1960).
- [79] B. Reuter and J. Jaskowsky, *Ber. Bunsenges. Phys. Chem.* **70**, 189 (1966).
- [80] D. B. Rogers, J. B. Goodenough, and A. Wold, *J. Appl. Phys.* **35**, 1069 (1964).
- [81] E. Pollert, *Czech. J. Phys. B* **23**, 468 (1973); *Krist. Tech.* **8**, 859 (1973).
- [82] D. Arndt, K. Müller, B. Reuter, and E. Riedel, *J. Solid State Chem.* **10**, 270 (1974).
- [83] Y. Ueda, N. Fujiwara, and H. Yasuoka, *J. Phys. Soc. Jpn.* **66**, 778 (1997).
- [84] M. B. Maple, C. L. Seaman, D. A. Gajewski, Y. Dalichaouch, V. B. Barbetta, M. C. de Andrade, H. A. Mook, H. G. Lukefahr, O. O. Bernal, and D. E. MacLaughlin, *J. Low Temp. Phys.* **95**, 225 (1994).
- [85] S. A. Carter, T. F. Rosenbaum, P. Metcalf, J. M. Honig, and J. Spalek, *Phys. Rev. B* **48**, 16341 (1993).

- [86] W. Trinkl, U. Weilhhammer, S. Corsépius, T. Schreiner, E.-W. Scheidt, and G. R. Stewart, *Phys. Rev. B* **54**, 1163 (1996).
- [87] P. H. Frings, J. J. M. Franse, F. R. de Boer, and A. Menovsky, *J. Magn. Magn. Mater.* **31-34**, 240 (1983).
- [88] G. S. Rushbrooke and P. J. Wood, *Mol. Phys.* **1**, 257 (1958).
- [89] Muhtar, F. Takagi, K. Kawakami, and N. Tsuda, *J. Phys. Soc. Jpn.* **57**, 3119 (1988).
- [90] Y. Amako, T. Naka, M. Onoda, H. Nagasawa, and T. Erata, *J. Phys. Soc. Jpn.* **59**, 2241 (1990).
- [91] M. J. Lysak and D. E. MacLaughlin, *Phys. Rev. B* **31**, 6963 (1985).
- [92] M. Itoh, Y. Hasegawa, H. Yasuoka, Y. Ueda, and K. Kosuge, *Physica C* **157**, 65 (1989).
- [93] M. Dalton, D. P. Tunstall, J. Todd, S. Arumugam, and P. P. Edwards, *J. Phys.: Condens. Matter* **6**, 8859 (1994).
- [94] R. W. McCallum, D. C. Johnston, C. A. Luengo, and M. B. Maple, *J. Low Temp. Phys.* **25**, 177 (1976): (unpublished).
- [95] U. Zülicke and A. J. Millis, *Phys. Rev. B* **51**, 8996 (1995).
- [96] G. M. Luke, A. Keren, L. P. Le, D. Wu, Y. J. Uemura, D. A. Bonn, L. Taillefer, and J. D. Garrett, *Phys. Rev. Lett.* **71**, 1466 (1993).
- [97] N. Fujiwara, Y. Ueda, and H. Yasuoka, *Physica B*, **239**, 237 (1997).
- [98] Y. Ueda (private communication).
- [99] F. Izumi, in *The Rietveld Method*, edited by R. A. Young (Oxford University Press, Oxford, 1993), Ch. 13.
- [100] H. M. Rietveld, *Acta Crystallogr.* **22**, 151 (1967).
- [101] H. M. Rietveld, *J. Appl. Crystallogr.* **2**, 65 (1969).
- [102] R. A. Young, in *The Rietveld Method*, edited by R. A. Young (Oxford University Press, Oxford, 1993), Chs. 1 and 2 (the latter by the inventor, Dr. Rietveld).
- [103] F. Izumi, H. Asano, T. Ishigaki, E. Takayama-Muromachi, Y. Uchida, N. Watanabe, and T. Nishikawa, *Jpn. J. Appl. Phys.* **26**, L649 (1987).

- [104] G. Calestani and C. Rizzoli. *Nature (London)*. **328**, 606 (1987).
- [105] F. Izumi. *Rigaku-Denki Journal* **27**, 18 (1996).
- [106] F. Izumi. in *Applications of Synchrotron Radiation to Materials Analysis*, edited by H. Saisho and Y. Gohshi (Elsevier, Amsterdam, 1996), Ch. 7.
- [107] P. Thompson, D. E. Cox, and J. B. Hastings. *J. Appl. Crystallogr.* **20**, 79 (1987).
- [108] G. K. Wertheim, M. A. Butler, K. W. West, and D. N. E. Buchanan. *Rev. Sci. Instrum.* **45**, 1369 (1974).
- [109] M. M. Hall, Jr., V. G. Veeraraghavan, H. Rubin, and P. G. Winchell. *J. Appl. Crystallogr.* **10**, 66 (1977).
- [110] F. Izumi. *A Rietveld-Refinement Program RIETAN-94 for Angular-Dispersive X-Ray and Neutron Powder Diffraction (RIETAN manual)*, (1996) (available at <http://www.nirim.go.jp/izumi/rietan/angle.dispersive/manual.pdf>).
- [111] C. J. Howard. *J. Appl. Crystallogr.* **15**, 615 (1982).
- [112] Y. Sasa and M. Uda. *J. Solid State Chem.* **18**, 63 (1976).
- [113] H. Toraya and F. Marumo. *Mineral. J.* **10**, 211 (1981).
- [114] A. March. *Z. Kristallogr.* **81**, 285 (1932).
- [115] W. A. Dollase. *J. Appl. Crystallogr.* **19**, 267 (1986).
- [116] E. Prince, in *The Rietveld Method*, edited by R. A. Young (Oxford University Press, Oxford, 1993), Ch. 3.
- [117] R. J. Hill, in *The Rietveld Method*, edited by R. A. Young (Oxford University Press, Oxford, 1993), Ch. 5.
- [118] G. Fujinawa, in *Fifth Short Course on X-Ray Analysis, "X-Ray Rietveld Analysis"*, (The Japan Society of Analytical Chemistry, Tokyo, 1996), Ch. 3.
- [119] F. Izumi, in *Fifth Short Course on X-Ray Analysis, "X-Ray Rietveld Analysis"*, (The Japan Society of Analytical Chemistry, Tokyo, 1996), Ch. 2.
- [120] G. Caglioti, A. Paoletti, and F. P. Ricci, *Nucl. Instrum. Methods* **35**, 223 (1958).

- [121] F. Izumi (private communication).
- [122] Y. Ueda, J. Kikuchi, and H. Yasuoka, *J. Magn. Magn. Mater.* **147**, 195 (1995).
- [123] S. Nagata, P. H. Keesom, and S. P. Faile, *Phys. Rev. B* **20**, 2886 (1979).
- [124] A. H. Lacerda, *et al.* (unpublished).
- [125] Yu. M. Belyakov, V. A. Perelyaev, A. K. Chirkov, and G. P. Shveikin, *Russ. J. Inorg. Chem.* **18**, 1789 (1973).
- [126] T. Palanisamy, J. Gopalakrishnan, and M. V. C. Sastri, *J. Solid State Chem.* **9**, 273 (1974).
- [127] J. Gendell, R. M. Cotts, and M. J. Sienko, *J. Chem. Phys.* **37**, 220 (1962).
- [128] R. M. White, *Quantum Theory of Solids*, 2nd Edition (Springer Verlag, Berlin, 1983) [From Eq. (3.97) on p. 96, $\chi_L = -(m/m_b)^2 \chi^{\text{Pauli}}/3$, where m_b is the band mass. So χ_L is expected to be negligibly small for d -electron system whose band width is normally narrow (*i.e.* m_b is large).]
- [129] M. Takigawa, E. T. Ahrens, and Y. Ueda, *Phys. Rev. Lett.* **76**, 283 (1996).
- [130] J. P. Pouget, P. Lederer, D. S. Schreiber, H. Launois, D. Wohlleben, A. Casalot, and G. Villeneuve, *J. Phys. Chem. Solids* **33**, 1961 (1972).
- [131] P. W. Selwood, *Magnetochemistry*, 2nd Edition (Interscience, New York, 1956), p. 78.
- [132] E. D. Jones, *Phys. Rev.* **137**, A978 (1965).
- [133] J. Kikuchi, H. Yasuoka, Y. Kokubo, Y. Ueda, and T. Ohtani, *J. Phys. Soc. Jpn.* **65**, 2655 (1996).
- [134] For a review, see G. S. Rushbrooke, G. A. Baker, and P. J. Wood, in *Phase Transitions and Critical Phenomena*, edited by C. Domb and M. S. Green (Academic Press, London, 1974), Vol. 3, Ch. 5.
- [135] J. M. Heintz, M. Drillon, R. Kuentzler, Y. Dossmann, J. P. Kappler, O. Durmeyer, and F. Gautier, *Z. Phys. B* **76**, 303 (1989).
- [136] M. Gerloch, J. Lewis, G. G. Phillips, and P. N. Queded, *J. Chem. Soc. (A)*, 1941 (1970).
- [137] S. Kondo (unpublished).
- [138] M. Kotani, *J. Phys. Soc. Jpn.* **4**, 293 (1949).

- [139] J. H. Van Vleck. *Theory of Electric and Magnetic Susceptibilities* (Oxford University Press, London, 1932).
- [140] C. J. Ballhausen. *Introduction to Ligand Field Theory* (McGraw-Hill, New York, 1962), p. 68.
- [141] T. M. Dunn. *Some Aspects of Crystal Field Theory* (Harper & Row, New York, 1965), Ch. 3.
- [142] T. M. Dunn. *Trans. Faraday Soc.* **57**, 1441 (1961).
- [143] H. R. Krishna-murthy, J. W. Wilkins, and K. G. Wilson. *Phys. Rev. B* **21**, 1003 (1980).
- [144] H. R. Krishna-murthy, J. W. Wilkins, and K. G. Wilson. *Phys. Rev. B* **21**, 1044 (1980).
- [145] V. T. Rajan, J. H. Lowenstein, and N. Andrei. *Phys. Rev. Lett.* **49**, 497 (1982).
- [146] B. Coqblin and J. R. Schrieffer. *Phys. Rev.* **185**, 847 (1969).
- [147] V. T. Rajan. *Phys. Rev. Lett.* **51**, 308 (1983).
- [148] A. Jerez and N. Andrei (1997, unpublished).
- [149] M. Onoda, H. Imai, Y. Amako, and H. Nagasawa. *Phys. Rev. B* **56**, 3760 (1997).
- [150] N. W. Ashcroft and N. D. Mermin. *Solid State Physics* (Saunders College, Philadelphia, 1976).
- [151] K. Miyake, T. Matsuura, and C. M. Varma. *Solid State Commun.* **71**, 1149 (1989).
- [152] C. A. Swenson. *Phys. Rev. B* **53**, 3669 (1996).
- [153] E. S. R. Gopal. *Specific Heats at Low Temperatures* (Plenum, New York, 1966).
- [154] R. J. Cava, D. W. Murphy, S. Zahurak, A. Santoro, and R. S. Roth. *J. Solid State Chem.* **53**, 64 (1984).
- [155] D. P. Tunstall, J. R. M. Todd, S. Arumugam, G. Dai, M. Dalton, and P. P. Edwards. *Phys. Rev. B* **50**, 16541 (1994).
- [156] G. D. Khattak, P. H. Keesom, and S. P. Faile. *Phys. Rev. B* **18**, 6181 (1978).
- [157] C. J. Pethick and G. M. Carneiro. *Phys. Rev. A* **7**, 304 (1973).
- [158] C. J. Pethick, D. Pines, K. F. Quader, K. S. Bedell, and G. E. Brown. *Phys. Rev. Lett.* **57**, 1955 (1986).

- [159] G. Baym and C. Pethick, *Landau Fermi Liquid Theory* (John Wiley & Sons, New York, 1991).
- [160] J. R. Engelbrecht and K. S. Bedell, *Phys. Rev. Lett.* **74**, 4265 (1995).
- [161] A. Auerbach and K. Levin, *Phys. Rev. Lett.* **57**, 877 (1986).
- [162] A. Auerbach and K. Levin, *Phys. Rev. B* **34**, 3524 (1986).
- [163] A. J. Millis, *Phys. Rev. B* **36**, 5420 (1987).
- [164] A. J. Millis and P. A. Lee, *Phys. Rev. B* **35**, 3394 (1987).
- [165] L. N. Oliveira and J. W. Wilkins, *Phys. Rev. Lett.* **47**, 1553 (1981).
- [166] H.-U. Desgranges and K. D. Schotte, *Phys. Lett.* **91A**, 240 (1992).
- [167] N. Andrei and J. H. Lowenstein, *Phys. Rev. Lett.* **46**, 356 (1981).
- [168] J. W. Rasul and A. C. Hewson, *J. Phys. C: Solid State Phys.* **17**, 3337 (1984).
- [169] A. C. Larson and R. B. VonDreele, General Structure Analysis System, University of California (1985–1990).
- [170] U. Roy, K. Petrov, I. Tsolovski, and P. Peshev, *Phys. Stat. Sol. (a)* **44**, K25 (1977).
- [171] *Thermophysical Properties of Matter*, Vol. 12, "Thermal Expansion", edited by Y. S. Touloukian, R. K. Kirby, R. E. Taylor, and P. D. Desai (IFI/Plenum, New York, 1975).
- [172] G. K. White, *Nature (London)* **187**, 927 (1960).
- [173] J. G. Collins and G. K. White, in *Progress in Low Temperature Physcs*, edited by C. J. Gorter (North Holland, Amsterdam, 1964), Ch. 9.
- [174] M. B. Kruger, J. H. Nguyen, W. Caldwell, and R. Jeanloz, *Phys. Rev. B* **56**, 1 (1997).
- [175] A. de Visser, J. J. M. Franse, and J. Flouquet, *Physica B* **161**, 324 (1989).
- [176] A. Abragam, *Principles of Nuclear Magnetism* (Oxford University Press, New York, 1961).
- [177] L. E. Drain, *Proc. Phys. Soc. (London)* **80**, 138 (1962).
- [178] Y. Masuda, *Fundamentals of Nuclear Magnetic Resonance* (in Japanese) (Maruzen, Tokyo, 1985).

- [179] G. C. Carter, L. H. Bennett, and D. J. Kahan, in *Metallic Shifts in NMR*, Progress in Materials Science, Vol. 20, edited by B. Chalmers, J. W. Christian, and T. B. Massalski (Pergamon Press, Oxford, 1977).
- [180] H. M. McConnell and R. E. Robertson, *J. Chem. Phys.* **29**, 1361 (1958).
- [181] This temperature-independent susceptibility χ_0 cannot be easily determined with precision because of its small size. There also is a question about the validity of the Curie-Weiss law when using it to a fit to the susceptibility including very high T data points ($T > 400$ K). In fact, Muhtar *et al.* interpreted their data assigning two different values of the Curie constant C to describe the lower ($T < 500$ K) and higher ($T > 500$ K) temperature susceptibility. Our χ_0 was determined, presumably more precisely, by making use of the temperature derivative of the high temperature series expansion susceptibility for $S = 1/2$, as shown in the preceding chapter. χ_0 was found to be smaller than that Mahajan *et al.* [19]. This result would consequently alter the subsequent results such as χ^{Pauli} .
- [182] A. P. Reyes, L. P. Le, R. H. Heffner, E. T. Ahrens, Z. Fisk, and P. C. Canfield, *Physica B* **206–207**, 332 (1995).
- [183] P. Vonlanthen, J. L. Gavilano, B. Ambosini, D. Heisenberg, F. Hullinger, and H. R. Ott, *Z. Phys. B* **102**, 347 (1997).
- [184] N. Buttgen, R. Böhmer, A. Krimmel, and A. Loide, *Phys. Rev. B* **53**, 5557 (1996).
- [185] T. Moriya, *Prog. Theor. Phys.* **16**, 23 (1956).
- [186] D. L. Cox, N. E. Bickers, and J. W. Wilkins, *J. Appl. Phys.* **57**, 3166 (1985).
- [187] R. Sala, E. Lee, F. Borsa, and P. C. Canfield, *Phys. Rev. B* **56**, 6195 (1997).
- [188] R. E. Walstedt and A. Narath, *Phys. Rev. B* **6**, 4118 (1972).
- [189] H. Wada, M. Shiga, and Y. Nakamura, *Physica B* **161**, 197 (1989).
- [190] C. Urano, *et al.* (unpublished).
- [191] B. A. Jones *et al.*, Fig. 1 in P. A. Lee, T. M. Rice, J. W. Serene, L. J. Sham, and J. W. Wilkins, *Comments Cond. Mat. Phys.* **12**, 99 (1986).
- [192] J. B. Goodenough (1997, private communication).

- [193] J. Villain, R. Bidaux, J. P. Carton, and R. Conte, *J. Phys. (Paris)* **41**, 1263 (1980).
- [194] B. Canals and C. Lacroix, *Phys. Rev. Lett.* **80**, 2933 (1998).
- [195] M. Shiga, H. Wada, Y. Nakamura, J. Deportes, B. Ouladdiaf, and K. R. A. Ziebeck, *J. Phys. Soc. Jpn.* **57**, 3141 (1988), and references therein.
- [196] B. D. Gaulin, J. N. Reimers, T. E. Mason, J. E. Greedan, and Z. Tun, *Phys. Rev. Lett.* **69**, 3244 (1992).
- [197] H. Nakamura, H. Wada, K. Yoshimura, M. Shiga, Y. Nakamura, J. Sakurai, and Y. Komura, *J. Phys. F* **18**, 981 (1988).
- [198] M. Shiga, K. Fujisawa, and H. Wada, *J. Phys. Soc. Jpn.* **62**, 1329 (1993).
- [199] K. I. Kugel' and D. I. Khomskii, *Sov. Phys. JETP* **37**, 725 (1973).
- [200] H. F. Pen, J. van den Brink, D. I. Khomskii, and G. A. Sawatzky, *Phys. Rev. Lett.* **78**, 1323 (1997).
- [201] S. Marini and D. I. Khomskii, Report cond-mat/9703130.

ACKNOWLEDGMENTS

I am grateful to my adviser Dr. David C. Johnston for his guidance and patience during the course of my Ph. D. study. Being his student has been such a precious experience to me. I have learned much from his deep insight to physics.

I would like to extend my appreciation to Dr. L. L. Miller, Dr. C. A. Swenson, Dr. F. Borsa, Dr. A. I. Goldman, Dr. M. B. Maple, Dr. Y. J. Uemura, Dr. O. Chmaissem, and Dr. J. D. Jorgensen. I am indebted to them for their collaborations about this work on LiV_2O_4 .

I would also like to thank my physics friends and colleagues Dr. A. V. Mahajan, Dr. F. C. Chou, Dr. Z. R. Wang, Dr. B. K. Cho, Dr. D. Vaknin, Dr. S. J. Lee, Dr. C. Detlefs, Dr. S. Kycia, Dr. T. Gu, A. H. M. Z. Islam, Dr. P. C. Canfield, Z. Jang, Dr. A. Abd El-Hady, J. E. Chang, Dr. T. Pe, Dr. J. L. Stanford, Dr. D. Allen, Dr. H. Eisaki, Dr. I. Inoue, Dr. F. Izumi, Dr. H. Takagi, Dr. Y. Ueda, Dr. N. Fujiwara, Dr. Yasuoka, and N. Ichikawa.

My thanks are also extended to non-physics friends, but too many to name them all here. Their support and encouragement deserve my deep appreciation.

Last but not least, my deepest appreciation to my wife Mihoko and son Kazuho for their continuous support and patience cannot be expressed well in words. I am also thankful to my parents, parents-in-law and my sister.

The work at Ames Laboratory was performed under Contract No. W-7405-Eng-82 with the U.S. Department of Energy. This work was supported by the Director of Energy Research, Office of Basic Energy Sciences.